Ultrafast Photoprotection Mechanisms and the Extraterrestrial Survivability of Adenine

by

Nicholas Lee Evans

(Under the direction of Susanne Ullrich)

Abstract

Electronic excited state relaxation dynamics of ammonia and adenine have been investigated by ultrafast time-resolved photoelectron and photoion spectroscopy. The ammonia investigation has determined that relaxation of $\nu_2' = 0$ - 5 levels of NH_3 ($\tilde{A}$) yields low kinetic energy H-atom dissociation products within 150 fs of initial excitation. Quantum tunneling through the NH_3 ($\tilde{A}$) state energy barrier is observed as a lengthened dissociation timescale for the $\nu_2' = 1$ level and a high kinetic energy feature in the H-atom spectrum of the $\nu_2' =$ 0 and 2 levels. Measurement of adenine's photoelectron spectrum has determined that the $S_2(\pi\pi^*) \rightarrow S_1(n\pi^*) \rightarrow S_\circ$ relaxation time decreases from 1032 to 700 fs as excitation energies increase from 4.7 to 6.2 eV. Participation of the $S_3(\pi\sigma^*)$ state is indicated for excitation energies above 5.2 eV.

A separate investigation of the interstellar survivability of adenine has shown that previously reported lifetimes are decreased, up to 30%, when the charged particle component of the Galactic Cosmic Radiation is considered. This result does not exclude the survival of adenine in small icy grains over the lifetime of star forming molecular clouds.

Index words: Femtosecond Pulse Generation and Measurement, Time-resolved Spectroscopy, Electronic Excited State Dynamics, Ultraviolet Photoprotection Mechanisms, Interstellar Chemistry

ULTRAFAST PHOTOPROTECTION MECHANISMS AND THE EXTRATERRESTRIAL SURVIVABILITY OF ADENINE

by

NICHOLAS LEE EVANS

B.S., East Carolina University, 2004
M.S., East Caroliina University, 2005

A Dissertation Submitted to the Graduate Faculty
of The University of Georgia in Partial Fulfillment
of the
Requirements for the Degree

DOCTOR OF PHILOSOPHY

ATHENS, GEORGIA

2013

Ultrafast Photoprotection Mechanisms and the Extraterrestrial Survivability of Adenine

by

Nicholas Lee Evans

Approved:

Major Professor: Susanne Ullrich

Committee: Willliam M. Dennis
Henning H. Meyer

Electronic Version Approved:

Dean Maureen Grasso
Dean of the Graduate School
The University of Georgia
August 2013

ACKNOWLEDGEMENTS

Acknowledgement is made to the National Science Foundation (Award No. CHE-0924456) and the Donors of the American Chemical Society Petroleum Research Fund (ACS-PRF No. 44110-G6) for partial support of this research. Also, thanks go to the UGA Graduate School and the UGA Department of Physics and Astronomy for their support of my research collaboration with the University of Hawaii.

I would like to thank my advisor, Susanne Ullrich, and the remaining members of the ultrafast spectroscopy group. I wish you well in your future research endeavours. I thank all of my co-authors including: Hui Yu, Amanda Brioullette, Garreth Roberts, Adam Chatterley, Vasilios Stavros, Chris Bennett, and Ralf Kaiser. I thank the staff and faculty at the UGA Department of Physics and Astronomy, with special thanks to the department head, Bill Dennis, for his support throughout my time at UGA.

Athens GA would not have been the same without all my friends in the physics, disc golf, and climbing communities.

Lastly, and most importantly, I thank my parents. All of my accomplishments are due to their hard work and loving support. I only hope that I get the chance to pass on the values they have instilled in me. I love you both very much.

Contents

List of Figures

List of Tables

CHAPTER 1

INTRODUCTION AND LITERATURE REVIEW

An explanation of the UV photophysics of adenine is required to understand how this important biomolecule was incorporated into living organisms during the biogenesis period on the early Earth. Biogenesis occurred around 4 billion years ago, before formation of the stratospheric ozone layer, which blocks the most harmful part of the Sun's ultraviolet (UV) spectrum. However, many organic molecules are destroyed by absorption of UV radiation. Incorporation of organics into biological systems must have occurred with strong selection of UV photostable molecules. The heterocyclic DNA base molecules (adenine, thymine, guanine, cytosine) and the set of 20 amino acids are considered to be the building blocks of modern living organisms. Each of the base molecules [see Ref 1] have displayed a remarkable ability to handle UV radiation through internal energy redistribution (IER) without being destroyed. It is by these IER mechanisms that important biomolecules survived the harsh UV radiation environment on the early Earth and were incorporated into living organisms.

This thesis is dedicated to the study of mechanisms and rates of non-radiative electronic relaxation by IER of gas-phase molecules using modern femtosecond time-resolved spectroscopy. Chapter 2 focuses on describing molecular photophysical processes including: absorption and emission of light and electronic excited state relaxation mechanisms. Chapter 3 deals with modern spectroscopic techniques capable of measuring such processes and details of the experiments performed during completion of the PhD program. Results from measurements carried out on the molecules ammonia and adenine have been published as peer reviewed journal articles and are included in Chapters 4 - 6. Details of the photophysics specific to each molecule are reserved for Chapters 4 - 6. A brief review of the literature will be given in this introductory chapter. Lastly, a study of the survivability of adenine under charged particle irradiation in interstellar environments and implications to astrobiological chemistry has been published in collaboration with the NASA astrobiological institute at the University of Hawaii and is presented in Chapter 7.

1.1 AMMONIA AND ADENINE LITERATURE

The well-studied [2 - 9] molecule ammonia (NH_3) is used to characterize our experimental approach in Chapters 4 - 5. Ammonia is a benchmark molecule in which fast pre-dissociation [2 - 5] and quantum tunneling [6 - 9] of excited state vibrational levels is observed. The UV absorption spectrum [4] of the first electronic excited state, NH_3 ($\tilde{A}$), extends from 216 - 170 nm and displays a long progression in the out-of-plane bend (umbrella) vibrational mode, ν_2'. The NH_3 ($\tilde{A}$) state is characterized as an nσ^* state and its potential energy surface is repulsive in the N-H stretch coordinate with a small barrier to dissociation. The repulsive nature of NH_3 ($\tilde{A}$) allows fast predissociation of vibrational levels at excitation energies above the dissociation barrier. Absorption linewidth measurements find evidence of NH_3 ($\tilde{A}$) state lifetimes of <75 fs. [4, 5] Excitation of NH_3 ($\tilde{A}$) below the dissociation barrier results in lengthened timescales [4 - 6, 8, 9] and a high H-atom kinetic energy (KE) emission feature, which is indicative of planar dissociation following tunneling through the barrier. Literature reports of the exact barrier height vary by ~0.5 eV. [10]

The ammonia work in Chapters 4 - 5 is intended to: 1) measure the NH_3 ($\tilde{A}$) lifetime by a direct time-resolved method, 2) find evidence of tunneling through the NH_3 ($\tilde{A}$) barrier by measrement of H-atom emission timescales and KE distributions, and 3) substantiate our experimental methods utilized in the investigation of H-atom dissociation *via* the nσ^* state.

In Chapter 6, the electronic excited state dynamics of the purine nucleobase adenine are investigated. The UV photophysics of adenine is perhaps the most well-studied of the DNA bases. [11] Several excited states have been identified [12 -14] in the vapor phase UV absorption spectrum, which spans the ∼200 - 300 nm range. [15] Three reaction paths have been proposed based on theoretical characterization of the excited state potential energy surfaces and conical intersections between them. [16 - 21] Non-adiabatic dynamics simulations have predicted the role of each pathway in the ultrafast deactivation of adenine. [22 - 27] Relaxation along three main coordinates have been described as: 1) a ring puckered coordinate, 2) an out-of-plane distortion coordinate, and 3) an N-H bond dissociation coordinate. The predicted percentage of molecules evolving along each path and the relaxation lifetimes are both strongly dependent on which theoretical model is used, and differences between models is based on their description of the potential energy surfaces. [22] Most models predict that paths 1) or 2) are dominant at excitation energies below 5.2 eV and overestimate the relaxation lifetimes when compared to experimental data. [22]

A bimodal relaxation mechanism, with time constants of approximately 0.1 and 1 ps, has been observed by time-resolved experimental methods including gas-phase total ion yield (TRIY), [28 - 32] photoelectron spectroscopy (TRPES), [29, 33 - 36] H-atom KE release (TKER), [37 - 40] and solution phase transient absorption. [41] The long time constant is attributed to an nπ^* state accessed from the initially excited $\pi\pi^*$ state along paths 1) or 2). [28, 33 - 35] The short time constant has been attributed to both a $\pi\pi^*/\mathrm{S}_\circ$ conical intersection along path 1) and to a repulsive $\pi\sigma^*$ state along path 3). [33 - 40] Relaxation *via* the $\pi\sigma^*$ state is a very efficient mechanism found throughout many heterocyclic molecules. [42] However, contradictory experimental results have been obtained regarding the participation of the $\pi\sigma^*$ state. Time-resolved ion yield measurements utilizing H-atom substitution techniques show no evidence of $\pi\sigma^*$ relaxation at 267 nm, [28, 29] whereas time-resolved photoelectron spectroscopy experiments have indicated $\pi\sigma^*$ relaxation at 267 nm [33 - 35] but not at 250 or 277 nm. [33, 34] H-atom emission measurements have identified $\pi\sigma^*$ relaxation at 267, [39] 243, [40] 200, [38] and 226 - 233 nm. [37]

The adenine work in Chapter 6 is meant to clarify the energetic onset of $\pi\sigma^*$ relaxation through an excitation wavelength dependent study using time-resolved photoelectron spectroscopy. Identification of the $\pi\sigma^*$ state is obtained by inspection of photoelectron emission timescales and kinetic energy distributions at varying excitation energies. Also, measurements of H-atom KE distributions allow verification of the $\pi\sigma^*$ state participation.

Lastly, an investigation of the survivability of adenine in interstellar environments is reported in Chapter 7. Interstellar chemistry is driven by the UV and charged particle component of the Galactic Cosmic Radiation (GCR). Small icy grains exist in cold molecular clouds, and typically consist of a silicate/carbonaceous core covered with water (H_2O), carbon monoxide (CO), carbon dioxide (CO_2), ammonia (NH_3), methane (CH_4), formaldehyde (H_2CO), methanol (CH_3OH), and carbonyl sulfide (OCS). [43] The interaction of the GCR with these icy grains results in the synthesis and simultaneous destruction of a widely varied chemical inventory. Build-up of large quantities of certain species is determined by the ratio of production and destruction rates. Laboratory experiments have shown that amino acids and nucleobases can be created by UV photolysis, [44 - 49] electron irradiation, [50 - 52] proton (H^+) irradiation, [53] and highly-charged heavy ion irradiation [54] of interstellar ice analogs. In Chapter 7 the destruction rate of adenine by the charged particle component of the GCR is measured. Comparison is made to the UV destruction rate, [55] and the half-life of adenine in several astrophysical environments is calculated. Astrobiological implications, including the possibility of extraterrestrial adenine delivery to early Earth, are discussed.

1.2 REFERENCES

[1] C. E. Crespo-Hernandez, B. Cohen, P. M. Hare and B. Kohler, Chem. Rev., 2004, 104, 1977.

[2] C. A. de Lange, in Advances in Chemical Physics, 2001, ed. I. Prigogine and S. A. Rice, John Wiley and Sons, Inc., New York, vol. 117, p. 1.

[3] M. N. R. Ashfold, D. H. Mordaunt and S. H. S. Wilson, in Advances in Photochemistry, 1996, ed. D. C. Neckers, D. H. Volman and G. vonBunau, John Wiley and Sons, Inc., New York, vol. 21, p. 217.

[4] V. Vaida, M. I. McCarthy, P. C. Engelking, P. Rosmus, H.-J. Werner and P. Botschwina, J. Chem. Phys., 1987, 86, 6669.

[5] L. D. Ziegler, J. Chem. Phys., 1985, 82, 664.

[6] J. Biesner, L. Schnieder, G. Ahlers, X. Xie, K. H. Welge, M. N. R. Ashfold and R. N. Dixon, J. Chem. Phys., 1989, 91, 2901.

[7] A. Bach, J. M. Hutchison, R. J. Holiday and F. Fleming Crim, J. Chem. Phys., 2002, 116, 9315.

[8] J. Ma, X. Zhu, H. Guo, and D. R. Yarkony, J. Chem. Phys., 2012, 137, 22A541.

[9] K. Giri, E. Chapman, C. S. Sanz, and G. Worth, J. Chem. Phys., 2011, 135, 044311.

[10] H. Akagi, K. Yokoyama and A. Yokoyama, J. Chem. Phys., 2003, 118, 3600.

[11] C. Z. Bisgaard, H. Satzger, S. Ullrich and A. Stolow, Chem. Phys. Chem., 2009, 10, 101.

[12] N. J. Kim, G. Jeong, Y. S. Kim, J. Sung, S. K. Kim and Y. D. Park, J. Chem. Phys., 2000, 113, 10051.

[13] E. Nir, C. Plutzer, K. Kleinermanns and M. deVries, Eur. Phys. J. D., 2002, 20, 317.

[14] D. C. Luhrs, J. Viallon and I. Fischer, Phys. Chem. Chem. Phys., 2001, 3, 1827.

[15] L. B. Clark, G. G. Peschel and I. Tinoco Jr., J. Phys. Chem., 1965, 69, 3615.

[16] A. J. Broo, Phys. Chem. A., 1998, 102, 526.

[17] A. L. Sobolewski and W. Domcke, Eur. Phys. J. D., 2002, 20, 369.

[18] C. M. Marian, J. Chem. Phys., 2005, 122, 104314.

[19] S. Perun, A. L. Sobolewski, and W. Domcke, J. Am. Chem. Soc., 2005, 127, 6257.

[20] L. Blancafort, J. Am. Chem. Soc., 2006, 128, 210.

[21] L. Serrano-Andres and M. Merchan, J. Photochem. Photobiol. C., 2009, 10, 21.

[22] M. Barbatti, Z. Lan, R, Crespo-Ortero, J. J. Szymczak, H. Lischka, and W. Thiel, J. Chem.. Phys., 2012, 137, 22A503.

[23] E. Fabiano and W. Thiel, J. Phys. Chem. A., 2008, 112, 6859.

[24] M. Barbatti, A. J. A. Aquino, J. J. Szymczak, D. Nachtigallova, P. Hobza, and H. Lischka, Proc. Natl. Acad. Sci. U.S.A., 2010, 107, 21453.

[25] M. Barbatti, J. J. Szymczak, A. J. A. Aquino, D. Nachtigallova, and H. Lischka, J. Chem. Phys., 2011, 134, 014304.

[26] A. N. Alexandrova, J. C. Tully, and G. Granucci, J. Phys. Chem. B., 2010, 114, 12116.

[27] Y. Lei, S. Yuan, Y. Dou, Y.Wang, and Z.Wen, J. Phys. Chem. A., 2008, 112, 8497.

[28] C. Canuel, M. Mons, F. Piuzzi, B. Tardivel, I. Dimicoli, and M. Elhanine, J. Chem. Phys., 2005, 122, 074316.

[29] C. Canuel, M. Elhanine, M. Mons, F. Piuzzi, B. Tardivel and I. Dimicoli, Phys. Chem. Chem. Phys., 2006, 8, 3978.

[30] D. C. Luhrs, J. Viallon, and I. Fischer, Phys. Chem. Chem. Phys., 2001, 3, 1827.

[31] H. Kang, B. Jung, and S. K. Kim, J. Chem. Phys., 2003, 118, 6717.

[32] K. L. Wells, G. M. Roberts and V. G. Stavros, Chem. Phys. Lett., 2007, 446, 20.

[33] S. Ullrich, T. Schultz, M. Z. Zgierski, and A. Stolow, Phys. Chem. Chem. Phys., 2004, 6, 2796.

[34] S. Ullrich, T. Schultz, M. Z. Zgierski, and A. Stolow, J. Am. Chem. Soc., 2004, 126, 2262.

[35] H. Satzger, D. Townsend, M. Z. Zgierski, S. Patchkovskii, S. Ullrich, and A. Stolow, Proc. Natl. Acad. Sci. U.S.A., 2006, 103, 10196.

[36] H. Satzger, D. Townsend, and A. Stolow, Chem. Phys. Lett., 2006, 430, 144.

[37] M. G. D. Nix, A. L. Devine, B. Cronin, and M. N. R. Ashfold, J. Chem. Phys., 2007, 126, 124312.

[38] K.L. Wells, D. Hadden, M.G.D. Nix and V.G. Stavros, J. Phys. Chem. Lett., 2010, 1, 993.

[39] M. Zierhut, W. Roth and I. Fischer, Phys. Chem. Chem. Phys., 2004, 6, 5178.

[40] I. Hunig, C. Plutzer, K. A. Seefeld, D. Louwenich, M. Nispel and K. Kleinermanns, Chem. Phys. Chem., 2004, 5, 1427.

[41] B. Cohen, P. M. Hare, and B. Kohler, J. Am. Chem. Soc., 2003, 125, 13594.

[42] M. N. R. Ashfold, G. A. King, D. Murdock, M. G. D. Nix, T. A. A. Oliver and A. G. Sage, Phys. Chem. Chem. Phys., 2010, 12, 1218.

[43] E. L. Gibb, D. C. B. Whittet, A. C. A. Boogert and A. G. G. M. Tielens, ApJSS, 2004, 151, 35.

[44] M. P. Bernstein, J. P. Dworkin, S. A. Sandford, G. W. Cooper and L. J. Allamandola, Nature, 2002, 416, 401.

[45] G. M. Munoz Caro, U. J. Meierhenrich, W. A. Schutte, B. Barbier, A. Arcones Segovia, H. Rosenbauer, W. H. P. Thiemann, A. Brack and J. M. Greenberg, Nature, 2002, 416, 403.

[46] M. Nuevo, Y. -J. Chen, T. -S. Yih, W. -H. Ip, H. -S. Fung, C. -Y. Cheng, H. -R Tsai and C. -Y, R Wu, Adv. Space Res., 2007, 40, 1628.

[47] M. Nuevo, G. Auger, D. Blanot and L. dHendecourt, Orig. Life Evol. Biosph., 2008, 38, 37.

[48] M. Nuevo, S. N. Milam, S. A. Sandford, J. E. Elsila and J. P. Dworkin, Astrobiology, 2009, 9, 683.

[49] M. B. Simakov and E. A. Kuzicheva, Adv. Space Res., 2005, 36, 190.

[50] D. Caceres, M. Bertin, A. Lafosse, A. Domaracka, D. Pliszka and A. Azaria, AIP Conference Proceedings, 2006, 876, 112.

[51] P. D. Holtom, C. J. Bennett, Y. Osamura, N. J. Mason and R. I. Kaiser, ApJ, 2005, 626, 940.

[52] A. Lafosse, M. Bertin, A. Domaracka, D. Pliszka, E. Illenberger and R. Azria, Phys. Chem. Chem. Phys., 2006, 8, 5564.

[53] K. Kobayashi, T. Kasamatsu, T. Kaneko, J. Koike, T. Oshima,T. Saito and H. Yanagawa, Adv. Space Res., 1995, 16, 21.

[54] S. Pilling, E. Seperuelo Duarte, E. F. da Silveira, E. Balanzat, H. Rothard, A. Domararcka and A. Boduch, e-print Archive, Astrophysics, 2009, 1.

[55] Z. Peeters, O. Botta, S. B. Charnley, R. Ruiterkamp and P. Ehrenfreund, ApJ, 2003, 593, L129.

CHAPTER 2

PHOTOPHYSICAL PRINCIPLES

2.1 MOLECULAR PHOTOSTABILITY

Scientific analysis of ionization by light absorption may be traced back to the second half of the 19^{th} century with the observation of what is now known as the photovoltaic effect by Becquerel [1] and the photoelectric effect by Hertz. [2] Subsequent investigations by Thomson [3] and Lenard [4] led to further understanding of these effects, specifically that electrons are emitted from materials by the absorption of light and that the energy of these electrons is related to the frequency of the incident light. Einstein gave a mathematical treatment of the photoelectric effect in his Nobel Prize winning paper published in 1905. [5] This paper utilized Planck's [6, 7] idea of light being comprised of energy quanta whose magnitude is proportional to the lights frequency. Einstein stated that absorption of a single photon causes emission of a single electron if the photon energy is above some threshold value, E_t, which is a characteristic of individual materials. The resulting electron energy can be calculated from the, now very famous, equation

$$\mathrm{E}_e = hf \text{ —}\mathrm{E}_t,$$

where h is the proportionality constant (now known as Planck's constant) and f is the frequency. The idea of light quantization, as well as the experimental observations, contradicted Maxwell's theory of classical wave behavior which predicted that the electron energy be dependent on the light intensity. Einsteins postulate was not well accepted until Millikan was able to provide a quantitative measurement of Planck's constant in 1916. [8] The idea of quantization led to the wave-particle duality interpretation of radiation and to the quantum revolution of modern physics.

We now understand that the electron emission from molecules in the gas phase observed in Lenard's experiments [4] is due to ionization, and the threshold energy is the binding energy (BE), also known as the ionization potential (IP). The BE is the magnitude of energy required to free an outer shell electron in the ground state from the attractive Coulomb potential of the nucleus. The BE of atoms and small molecules is typically in the 5 - 15 eV range - corresponding to ultraviolet (UV) or vacuum ultraviolet (VUV) parts of the electromagnetic spectrum ($\sim$250 - 50 eV). Lenard observed direct ionization by a single photon of energy above the IP threshold. This mechanism is now termed above threshold ionization.

Below threshold photons can also be absorbed, however this mechanism does not lead directly to ionization. Instead, multiple photon absorption is required for ionization. As observed in the spectrographs of Fraunhoffer in 1814, absorption or emission of visible light appears as discrete dark or bright lines. [9] Some 40 years later, Kirchoff and Bunsen [10] determined that substances with different chemical compositions have unique absorption and emission spectra. This discovery ushered in the era of experimental chemical analysis by optical spectroscopy. Bohr [11] offered a model of the atom based on electrons residing in stationary states that was able to explain the quantized nature of the observed spectra. Absorption or emission of energy packets (photons) whose energy exactly matches the energy between the participating electronic states causes an electron transition between stationary states. Bohrs model of quantized electron orbitals was able to explain the empirical Balmer formula for the hydrogen atom spectrum and was the basis of what is now known as the old quantum theory.

In the electronic ground state, electrons lie in the lowest possible energy configuration. Below threshold photon absorption produces an electronic excited state by elevation of one electron to a higher energy orbital. Excited electronic states are considered less stable against photoionization and photochemical reactions than are ground state configurations for several reasons. First, excited states are more chemically reactive than the ground state. Excited electrons are located farther from the nucleus and are more loosely bound by the Coulomb potential which affords more favorable bonding with surrounding atoms. Second, excited states are more easily ionized by photon absorption than is the ground state. The required photon energy is the difference between the IP and the excited state energy instead of the difference between the IP and the ground state energy - the latter typically being several eV larger. The resultant photoion is highly susceptible to chemical reactions due to the free valence shell charge. Chemical reactions serve to produce new molecular species and are thought of here as destroying the original species. The chemical reaction rate, and therefore the destruction rate, of excited states and photoions is increased in comparison to the electronic ground state, and the longer a molecule resides in an excited state, the more likely it is to be destroyed by chemical reactions.

Relaxation from an electronic excited state to the molecular ground state serves as a protection mechanism from photochemical destruction. Excited state relaxation can occur by radiative photon emission, by non-radiative vibrational energy exchange with the surrounding environment (collisional cooling), or by non-radiative internal electronic energy redistribution (IER) through vibrational coupling. The rate at which a molecule relaxes to the ground state is dependent on the number of available relaxation mechanisms as well as the probability of each occurring. Radiative relaxation typically occurs on ns timescales and collisional cooling rates are strongly dependent on the surrounding environment. Relaxation by IER can occur on timescales shorter than 1 x 10^{-12} s and is considered an extremely efficient means of photoprotection. Investigation of the relaxation mechanisms is therefore directly related to molecular photostability and overall survivability under photolysis.

2.2 ELECTRONIC EXCITED STATE RELAXATION MECHANISMS

Electronic states of small molecules have vertical excitation energies of the order of several eV and are populated by absorption of UV photons. Upon each electronic excited state lies a manifold of vibrational levels and upon each vibrational level lies a manifold of rotational levels. Spacing between adjacent levels is on the order of 1.0, 0.1, and 0.001 eV for electronic, vibrational, and rotational states, respectively. For a non-linear molecule with n atoms, the number of vibrational modes is $N_v = 3n - 6$. The number of available vibrational (and rotational) modes increases with n, and the discrete nature of atomic absorption spectra is eventually washed out by the increasing number of states. The wide energetic bandwidth, typical of large molecule absorption features, is indicative of short excited state lifetimes. This assertion is based on the time/energy uncertaintity principle, $\Delta t\ \Delta E \geq \hbar/2$, which reveals an inverse relationship between time and energy. Simply put, the number of ro-vibrational levels acts to both broaden the absorption bands and to facilitate fast relaxation through producing many IER pathways.

It is important to clarify the notation used to describe electronic states throughout this work. Electrons lie in molecular orbitals that are linear combinations of atomic orbitals (LCAO). A bond between two atoms with electrons in s atomic orbitals creates a σ molecular orbital in which the electron probability density resides along the axis between the bonding nuclei. A bond between two atoms with electrons in p atomic orbitals creates a π molecular orbital in which the electron probability density resides above and below the axis between the bonding nuclei. Non-bonding electrons lie in n molecular orbitals. Electronic excited states are created by promotion of an electron in the highest occupied molecular orbital (HOMO) into the lowest unoccupied molecular orbital (LUMO). The LUMO states are represented by the notation σ^*, π^* and n^* and are refered to as anti-bonding states. An electronic excited state is characterized by both the HOMO and the LUMO, and the notation (xy^*) represents excitation of an x-type electron into a y^*-type anti-bonding orbital. Excited states of $\pi\pi^*$,

$n\pi^*$, $\pi\sigma^*$, and $n\sigma^*$ character are encountered in this work. Further, the notation S$_1$($\pi\pi^*$) represents the lowest energy singlet excited state.

As described above, excited electronic states must be able to relax quickly as to avoid potentially dangerous photochemical reactions. Non-radiative relaxation by IER occurs when electronic energy is redistributed into one or many secondary modes. Several IER mechanisms, including 1) internal conversion (IC), 2) intersystem crossing (ISC), and 3) internal vibrational energy redistribution (IVR) are described here in reference to Fig 2.1. Photoxcitation from the singlet ground state, S$_\circ$, to the $\nu = 2$ vibrational level of the second excited singlet state, S$_2$, is represented by the solid arrow. Transitions from S$_2$ to the first singlet S$_1$, and first triplet T$_1$ excited states are represented by dashed lines. Both IC and ISC involve adiabatic transitions from a high-lying electronic level to a lower electronic level with high vibrational excitation. IC proceeds between states with the same spin (i.e. S$_2$($\nu = 2$) $\rightarrow$ S$_1$($\nu = 6$)) whereas ISC happens between different spin states (i.e. S$_1$($\nu = 6$) $\rightarrow$ T$_1$($\nu = 7$)). Vibrational and electronic level changes occur simultaneously during IC and ISC relaxation. In contrast, IVR involves transitions between two vibrational levels within a single electronic state. Relaxation to the ground state may occur through several sequential steps involving IC, ISC, and IVR. In the Fig 2.1 example, S$_2$($\nu = 2$) $\rightarrow$ S$_\circ$ relaxation may occur by, 1) S$_2$($\nu = 2$) $\rightarrow$ S$_1$($\nu = 6$) $\rightarrow$ S$_1$($\nu = 1$) $\rightarrow$ S$_\circ$($\nu = 10$) or by, 2) S$_2$($\nu = 2$) $\rightarrow$ S$_1$($\nu = 6$) $\rightarrow$ S$_1$($\nu = 1$) $\rightarrow$ T$_1$($\nu = 7$) $\rightarrow$ T$_1$($\nu = 2$) $\rightarrow$ S$_\circ$($\nu = 4$). These mechanisms are known to be extremely efficient, and can occur on sub picosecond (ps) timescales in organic heterocycles [12, 13].

Characterization of excited state potential energy surfaces (PESs) can be used to predict possible relaxation mechanisms and can serve as an intuitive illustration of excited state dynamics. Excitation to an electronic excited state creates a non-stationary quantum ensemble of states. One may visualize an excited state wave packet traveling along the PES in search of a minimum energy configuration. The wavepacket trajectory determines the excited state relaxation mechanism and depends on many parameters including the initial excitation energy, the initial state PES topography, and interactions between the initial

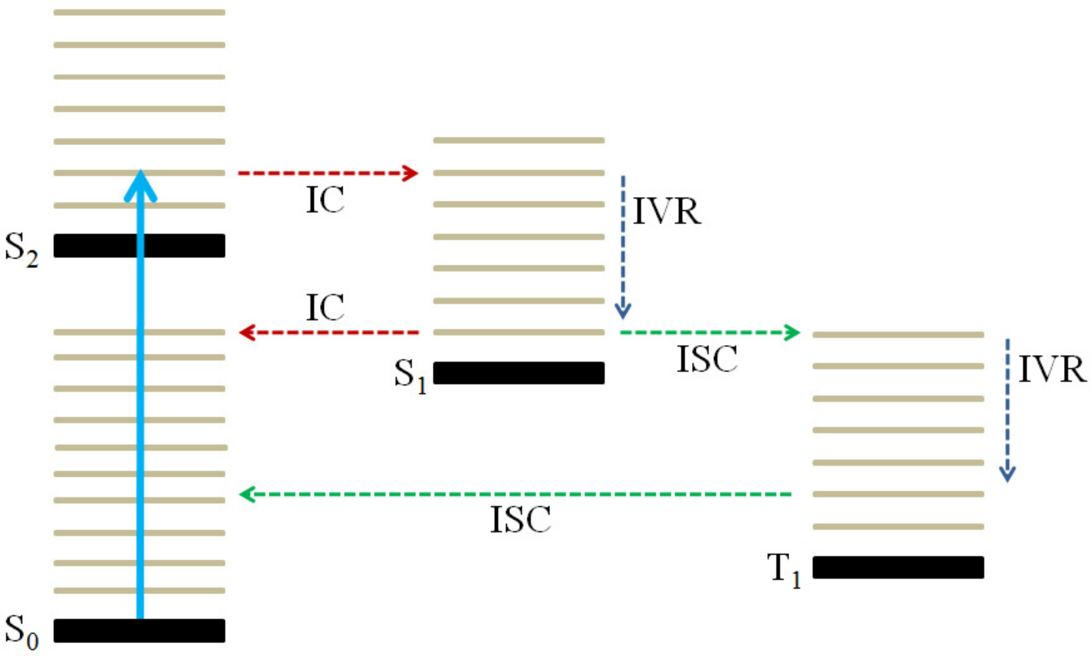

Figure 2.1: Diagram of excited state relaxation mechanisms. Black lines are electronic states and grey lines are vibrational levels. $S_\circ$ - singlet ground state; S_1 and S_2 - singlet excited states; T_1 - triplet excited state; IC - internal conversion; ISC - intersystem crossing; IVR - internal vibrational energy redistribution.

state and other excited states. Accurate PES determination is critical to the understanding of excited state relaxation. Multi-dimensional PESs are calculated by solving the time-independent Schrodinger equation using the Born-Oppenheimer approximation, in which electronic and nuclear motions are treated independently. First, the nuclear geometry is fixed at the equilibrium geometry, and the electric potential is calculated. Then, the geometry is changed in a step-by-step fashion, with the potential being calculated at each step, until all stable configurations have been assessed. The potential energy points are then fit with a multi-dimensional function to represent the PES. Multi-dimensional PES calculations are not always possible for large molecules due to the computational cost of dealing with a large number of atomic coordinates. Instead, preferred atomic motion dimensions, or reaction coordinates, are determined and the PES is calculated while only varying the atomic geometry in this coordinate. The resultant PESs are displayed as a function of the reaction coordinate in a manner similar to Fig 2.2. For simplicity, multi-dimensional PESs are often represented as a 1-D cut along the reaction coordinate as in Fig 2.2. Here, the ground, $S_\circ$, and two excited states, $S_1(\pi\pi^*)$ and $S_2(\pi\sigma^*)$, are shown as a function of the length, R, of one bond.

Conical intersections (CIs) are created when excited states are coupled by IC or ISC and state-to-state transfer can occur at these geometries. PES CIs are depicted by green rings in Fig 2.2. Calculation of the exact PES topography near the CI determines how the relaxation proceeds. However, this calculation can be difficult because in the region of the CI the nuclear and electronic motions are coupled and the Born-Oppenheimer approximation breaks down. The situation is even more complicated by the fact that multiple CIs can exist along different reaction coordinates and that multiple wavepacket trajectories are available at each CI.

A simple photoexcitation to ground state relaxation mechanism can be understood in reference to Fig 2.2. Excitation from the ground state $S_\circ$ to a vibrational mode of the bound first excited state $S_1(\pi\pi^*)$ is represented by the blue vertical arrow. The second excited state $S_2(\pi\sigma^*)$ is repulsive in R. Two CIs are formed in this picture - first between $S_1(\pi\pi^*)$ and $S_2(\pi\sigma^*)$, CI1, and second between $S_2(\pi\sigma^*)$ and $S_\circ$, CI2. As labeled in Fig 2.2, two different trajectories are possible at CI1 and three at CI2. At CI1, the wavepacket may avoid CI1 and continue along $S_1(\pi\pi^*)$ where it eventually reaches a turning point and returns toward the $S_1(\pi\pi^*)$ minimum (path 1), or it may cross onto the $S_2(\pi\sigma^*)$ surface by IC and move toward CI2 (path 2). At CI2, the wavepacket may avoid CI2 and continue along $S_2(\pi\sigma^*)$ until it reaches the dissociation limit (path 3), cross to the $S_\circ$ surface and continue toward dissociation (path 4), or cross to the $S_\circ$ surface and trend toward the $S_\circ$ minimum (path 5). One possible ground state relaxation mechanism may proceed by crossing from $S_1(\pi\pi^*)$ to $S_2(\pi\sigma^*)$ at CI1 and then from $S_2(\pi\sigma^*)$ to $S_\circ$ at CI2. If the CIs favor these crossings then ground state repopulation may occur very quickly and an efficient photoprotection

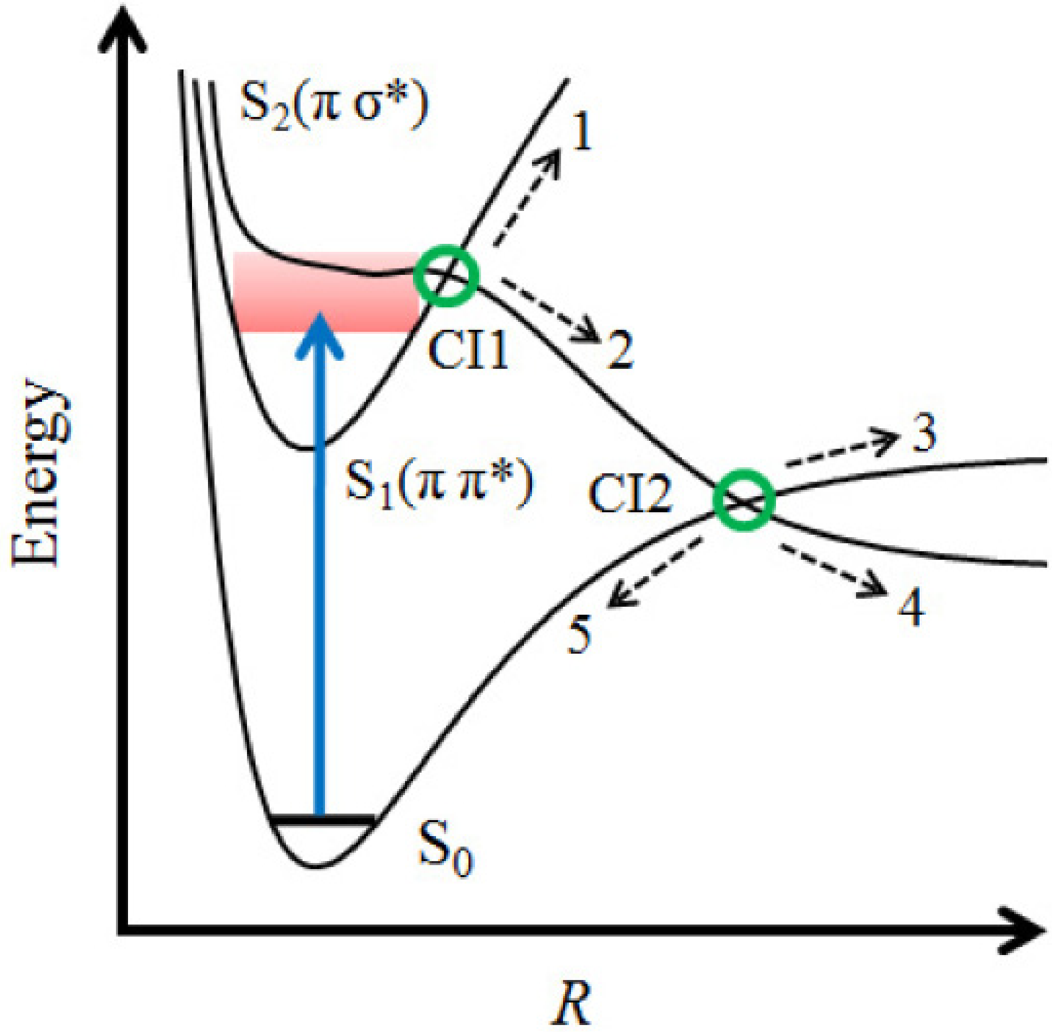

Figure 2.2: Schematic of one-dimensional potential energy surfaces. Ground, $S_\circ$, and two excited state surfaces, $S_1(\pi\pi^*)$ and $S_2(\pi\sigma^*)$, are shown as a function of a bond length coordinate, R. Excitation to a vibrational level of the $S_1(\pi\pi^*)$ state is represented by the vertical blue arrow. Two conical intersections, CI1 and CI2, create five separate relaxation paths shown by dashed arrows.

mechanism is created. However, it is possible that CI1 is avoided and the molecule remains in $S_1(\pi\pi^*)$ where it is susceptible to photochemical destruction. It is also possible that paths 3 or 4 are favored at CI2 and the molecule continues toward dissociation. The portion of trajectories evolving along each path and the rate of transfer between states is highly dependent on the shape of each CI and the geometry at which the molecule approaches each CI.

In the example relaxation mechanism of Fig 2.2, the initially excited $S_1(\pi\pi^*)$ bound state can only return to $S_\circ$ by way of the repulsive $S_2(\pi\sigma^*)$ state. The repulsive nature of the $\pi\sigma^*$ state is due to anti-bonding σ^* electrons lying between the nuclei. As first proposed by Domke and Sobelewski, [14, 15] σ^* states can offer an extremely efficent relaxation path, whereby energy is transfered into an X—H stretch coordinate, where X is typically N or O. As in Fig 2.2, a $\pi\sigma^*/S_\circ$ CI may be formed at extended X—H bond lengths that offers a ground state repopulation mechanism. Alternatively, paths 3 and 4 in Fig 2.2 can lead to cleavage of the X—H bond. The repulsive nature of these states offers an ultrafast mechanism for either ground state repopulation or H-atom emission The role of repulsive σ^* states is a major theme of this thesis due to their seemingly ubiquitous nature in organic molecules. [12, 13] In fact, both ammonia and adenine exhibit a σ^* state that forms a CI with the ground state at extended N—H bond lengths.

2.3 REFERENCES

[1] H. Becquerel 1839, Comptes Rendus, 9, 561.

[2] H. Hertz 1887, Annalen der Physik, 267, 983.

[3] J. J. Thomson, 1899, Philosophical Magazine, 48, 547.

[4] P. Lenard 1902, Ann. Phys., 313, 149.

[5] A. Einstein 1905, Annalen der Physik, 17, 132.

[6] M. Planck 1900, Annalen der Physik, 1, 719.

[7] M. Planck 1901, Annalen der Physik, 4, 553.

[8] R. A. Millikan 1916, Phys. Rev., 7, 355.

[9] J. Fraunhofer 1814, Denkschriften der Koniglichen Akademie der Wissenschaften zu Munchen, 5 193.

[10] G. Kirchhoff 1860, Annalen der Physik, 185, 275.

[11] N. Bohr 1914, Nature, 92, 231.

[12] M. N. R. Ashfold, G. A. King, D. Murdock, M. G. D. Nix, T. A. A. Oliver and A. G. Sage 2010, Phys. Chem. Chem. Phys. 12, 1218.

[13] M. N. R. Ashfold, B. Cronin, A. L. Devine, R. N. Dixon and M. G. D. Nix 2006, Science, 312, 1637.

[14] A. L. Sobolewski, W. Domcke, C. Dedonder-Lardeux and C. Jouvet 2002, Phys. Chem. Chem. Phys., 4, 1093.

[15] A. L. Sobolewski and W. Domcke 2000, Chem. Phys., 259, 181.

CHAPTER 3

EXPERIMENT

3.1 TECHNIQUES

Absorption linewidth measurements exhibited the first evidence of ultrafast excited state relaxation. Linewidth and lifetimes are related through the time-energy uncertaintity principle, $\Delta t\ \Delta E \geq \hbar/2$. The energy spread, or line broadening, of an absorption feature is inversely proportional to the lifetime of the absorbing state. Development of the narrow line (1 cm^{-1} resolution) laser allowed determination of ps and sub-ps lifetimes, however indirect lifetime measurements by linewidth absorption measurement suffer from many experimental problems such as Doppler, power, and pressure broadening. Suitable experimental construction, including use of vacuum chambers and molecular beams, helps alleviate many technical issues. Nevertheless, lifetime measurements of this type are still considered an indirect approach.

Time-resolved Pump-probe Spectroscopy

Time-resolved pump-probe spectroscopy allows more direct measurements of excited state lifetimes by probing the population distribution in real-time. The pump-probe method involves a) population of electronic excited state by the pump laser pulse, b) dynamical evolution of the initial excited state, c) ionization of relaxation products by the probe pulse, and d) detection of ionization products at varying delays between pump and probe pulses. The photophysics of a generic heterocycle are used as an example in Fig 3.1.

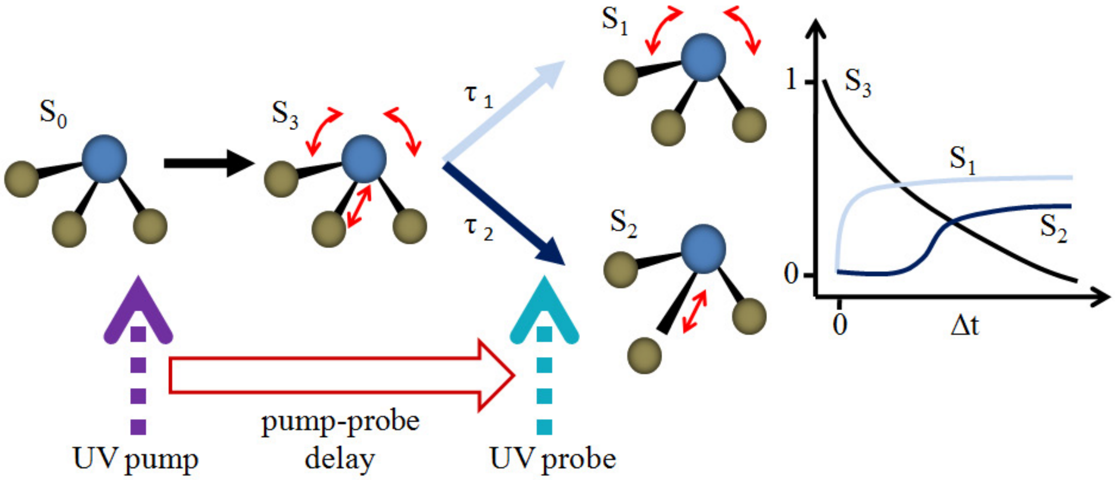

Figure 3.1: Schematic of pump-probe spectroscopy. The S_4 excited state is pumped from the $S_\circ$ ground state by a UV fs pulse. Relaxation into three channels, labeled S_1, S_2, and S_3 occurs with rates τ_1, τ_2, and τ_3, respectively. A time delayed UV fs probe promotes ionization of each species, and ionization product intensities are measured as a function of pump-probe delay, Δt. The inset shows the Δt dependence of the ionization intensity of each product from which the molecular dynamics can be extracted.

In Fig 3.1 a UV pump pulse populates the S_3 electronic state through excitation of the $S_\circ$ ground state. The pump wavelength is carefully selected for resonant excitation of specific excited states within each molecule under study. Excited state relaxation occurs after initial excitation, and two relaxation paths are available as indicated in Fig 3.1. The S_3 population can decay into each of the S_1 and S_2 atates with varying formation times (τ_1, τ_2). Relaxation products are ionized by the time-delayed probe pulse. Photoions and photoelectrons created by the probe are collected and are analyzed by mass or energy. The electronic states S_1 - S_3 can be identified by the resulting mass or energy spectra. Details of state identification are given in the following sections. Variations of the mass or energy spectra as a function of the pump-probe delay, Δt, indicate the population distribution of each state during the relaxation process. This experimental technique produces two-dimensional (2-D) data, which allows simulatneous identification of excited states, based on mass or energy spectra, and population transfer rates, based on Δt dependent spectral evolution. Measurement of this 2-D data has an advantage over frequency resolved experiments. Here, the real-time population distribution is measured, wheras the frequency resolved measurements infer dynamics from linewidth measurements. However, these measurements lack rotational resolution due to the bandwidth of the femtosecond (fs) pump and probe pulses.

Consider again the example of Fig 3.1, whereby states S_1 - S_3 can be uniquely identified through spectral measurements. The integrated intensity of each state is shown as a function of Δt in the inset. The initial S_3 population, shown in black, decays into each of the other states, depicted in blue. This over simplified plot still contains a wealth of information. The S_3 relaxation rate is evident from the black decay curve, and the S_1 and S_2 formation times (τ_1, τ_2) are determined from the blue rise curves. The S_1 (light blue) and S_2 (dark blue) curves rise abruptly to a plateau. However, the S_2 (dark blue) curve has a substantially delayed rise, indicating that it may be a secondary relaxation product.

Utilization of 2-D data to analyze the spectroscopic and dynamic fingerprint of excited state dynamics is common to the experimental techniques used throughout this thesis, time-resolved ion yield (TRIY), time-resolved photoelectron spectroscopy (TRPES), and time-resolved total kinetic energy release (TR-TKER). Discussion of each technique will proceed in the following sections with the idea of analyzing energetic and dynamic information simultaneously already in mind.

Time-resolved Ion Yield

TRIY spectroscopy is quite similar to the situation described in the previous section in that each relaxation product is directly ionized by the probe and is detected separately. TRIY is particularly well suited to study photofragmentation [1 - 3] whereby excited state relaxation produces small fragments of the parent molecule; each of which can be correlated with a specific electronic state. A general photofragmentation reaction is described as

$$h\nu + \mathrm{ABC} \rightarrow \mathrm{ABC}^* \rightarrow \mathrm{AB} + \mathrm{C} \rightarrow \mathrm{A} + \mathrm{B} + \mathrm{C},$$

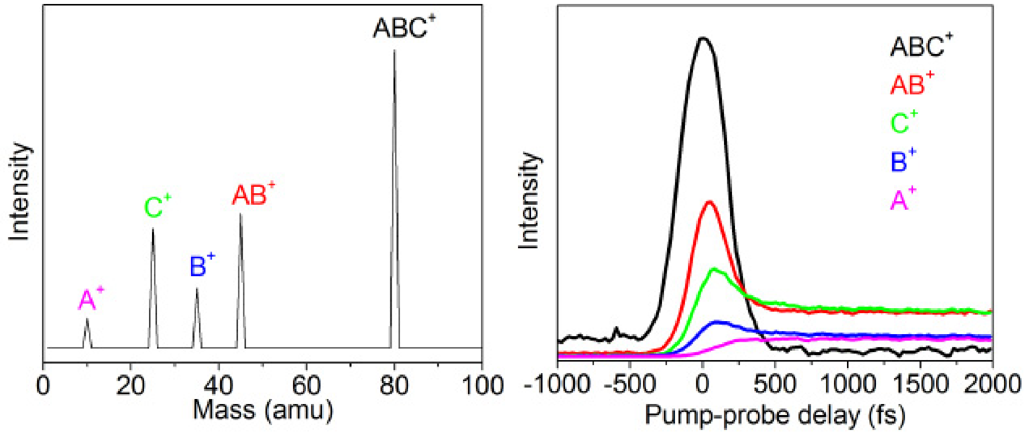

Figure 3.2: Results from a generic TRIY experiment. Left - fragmentation mass spectrum; right - pump-probe delay traces. Combination of mass and timing information allows identification of ABC decay within 250 fs proceeding by a C loss mechanism.

where $h\nu$ is the excitation photon and ABC is a generic triatomic molecule. The ABC* excited state is populated by absorption of $h\nu$ and subsequently dissociates into AB + C and then into A + B + C co-fragments. In TRIY, the dissociated co-fragments are ionized by a time-delayed probe pulse and are detected seperately by mass spectroscopy. In this example, co-fragments AB and C are detected first, followed by detection of A, B, and C separately. Timescales for production of each fragment are extracted and a step-by-step relaxation mechanism is revealed.

The mass spectrum and delay traces of ABC are shown in Fig 3.2 to illustrate the TRIY technique. The mass spectrum allows identification of the major fragments labeled in Fig 3.2. Comparison can be made to other experimental fragmentation spectra and to theoretically suggested fragmentation pathways for assignment. A fragmentation mechanism (see equation above) can be suggested from the mass spectrum in Fig 3.2. A gate around each mass peak in the left panel is integrated at all pump-probe delays to produce the transients in the right panel of Fig 3.2. Transients for each peak in the mass spectrum are presented and color coded. The ABC^+, AB^+, and C^+ delay traces show a peak near $\Delta t = 0$ fs - evidence that these three species are produced within the first 250 fs of excitation. The ABC^+ trace decays to the baseline quickly while the other fragments persist to longer times. Therefore, the ABC parent has decayed into the other fragments within 500 fs.The A^+ trace rises more slowly than the others - indicating that it may be a secondary product of ABC relaxation. Combination of the mass fragmentation spectrum and the pump-probe delay traces lead to the following relaxation mechanism: 1. ABC decays quickly by C loss, 2. AB Decays into A and B on a delayed timescale. Fits are made of each delay trace to quantify the destruction (ABC) or production (AB, A, B, and C) rates.

Time-resolved Photoelectron Spectroscopy

Collection of multiple ionization products, including ions (TRIY) and photoelectrons (TRPES), provides a comprehensive picture of the excited state dynamics. The general procedure of TRPES involves measurement of photoelectron KE to facilitate direct identification of cationic energy levels followed by correlation of measured cationic levels with excited states through Frank-Condon and ionization correlation arguments. The time-resolved pump-probe technique follows the variation of the photoelectron KE spectrum, therefore allowing the excited state population change to be measured in real-time. The general TRPES measurement technique will be described first, followed by a description of ionic and excited state identification.

A diagram of the TRPES measurement technique is given in Fig 3.3. In this example, the $\nu' = 7$ vibrational level of the S_2 electronic excited state is populated by ground state absorption of a UV fs pump pulse represented by the blue arrow. Absorption may occur from one of the manifold of ground state levels, but a single level is shown in Fig 3.3 for clarity. A secondary probe pulse (pink) promotes ionization with enough energy to reach the $\nu = 6$ level of the ionic state. The system falls into an energetically available cationic vibrational level and emits a photoelectron, whose energy is the difference between the total pump-probe photon energy minus the cationic energy level. The photoelectron KE is represented by green and red arrows for two possible vibrational levels of the cation in Fig 3.3, and a representative photoelectron KE spectrum is given in the inset. The energy conservation equations for this system are

$$h\nu_{pump} + \mathrm{A} = \mathrm{A}^*$$

$$\mathrm{A}^* + h\nu_{probe} = \mathrm{A}^+ + \mathrm{KE}(\mathrm{e}^-),$$

where the excited state A^* is populated by absorption of the pump and the cation A^+ is created by the probe. The conservation equations shows that measurement of $\mathrm{KE}(\mathrm{e}^-)$ allows direct identification of cationic energy levels.

The focus of TRPES is to measure electronic relaxation of the A^* excited state through IER on fs timescales. Such a reconfiguration is represented in 3.3 as a change from the S_2 $\nu' = 7$ level (left) to the S_1 $\nu' = 5$ level (right) with characteristic timescale, τ. In the example above, absorption of the probe occurred from the initial state with zero time delay between pump and probe, $\Delta\mathrm{t} = 0$. Alternatively, a time delayed probe (pink arrow at right) promotes ionization from the relaxed state (S_1 $\nu' = 2$) with energetic access to only the $\nu = 2$ cationic level. Again, the system falls into one of the available cationic levels and a photoelectron is emitted with KE represented by the dark blue arrow. The electron KE spectrum of the relaxed state is given in the inset and shows marked differences from the spectrum of the initially excited state. KE spectra are measured as the pump-probe delay is varied, and observation of the KE spectrum evolution allows determination of an excited state reconfiguration.

Cationic energy levels are determined by the measurement of photoelectron KE. Unfortunately no information about the rotational/vibrational/electronic character of these levels is extracted directly from the simple KE measurement. Comparison must be made to high-resolution frequency resolved experiments and *ab initio* calculations to afford assignment of specific ionic states. As first suggested by Domke [4, 5] assigning the cationic level distribution can give information about the excited state population if the allowed/preferred transitions from the exited state to the ion are known. The strict dipole allowed transi-

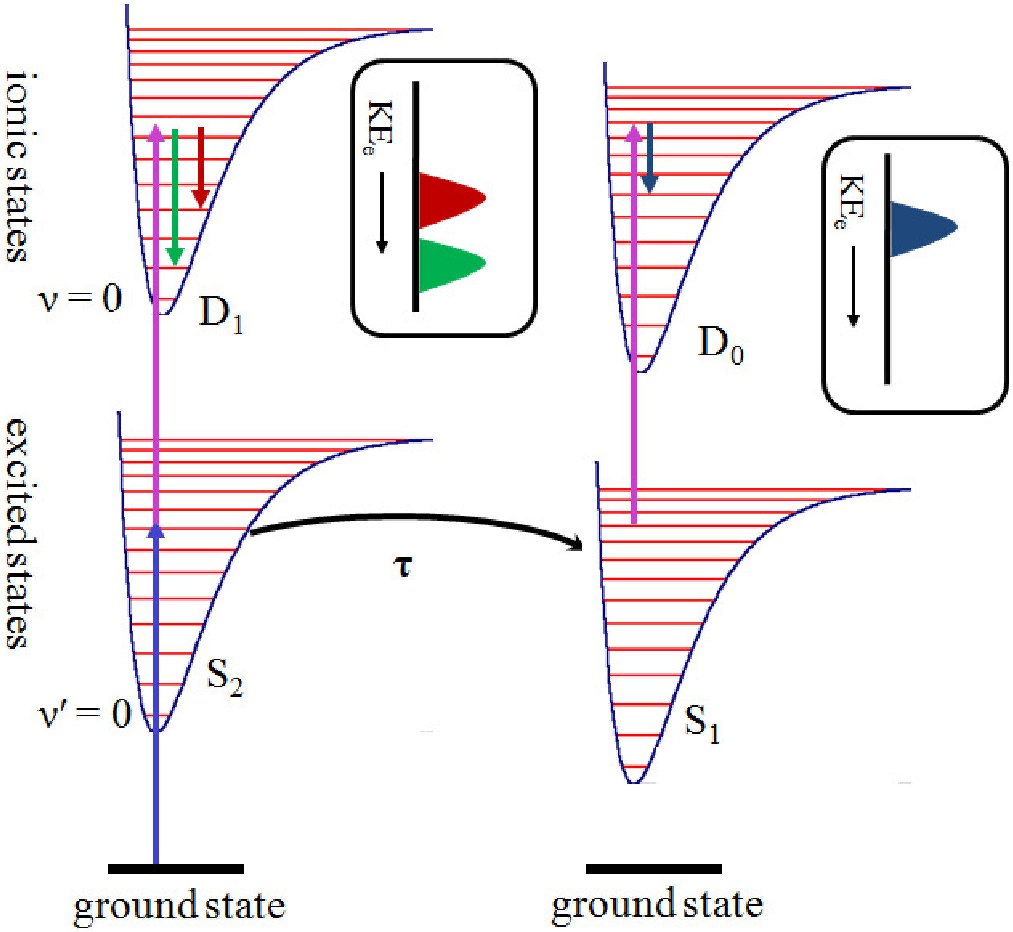

Figure 3.3: Schematic of the TRPES experimental technique. The ground, electronic excited and ionic states are shown at $\Delta t = 0$ (left) and at some time, τ, later (right). Vibrational energy levels of the excited (ν') and ionic (ν) states are shown as red lines. Ground state vibrational levels are omitted for clarity. Absorption of pump (blue) and probe (pink) pulses is represented by vertical arrows. Emission of electrons during the probe induced ionization is represented by the green, red, and dark blue arrows. The electron KE distribution changes during relaxation as shown in the inset and by the magnitude of the electron emission vectors.

tion rules ($\Delta S = 0$, ΔL and $\Delta J = 0, \pm 1$) can often be overcome in molecular transitions because of rotational/vibrational angular momentum coupling. Therefore, simple selection rules cannot be used to uniquely identify a transition. Instead, preferred transitions can be determined by calculation of the transition moment, $P = <\Psi'|\mu|\Psi>$, and the transition probability P^2. Here, μ is the dipole operator, and $|\Psi>$ and $|\Psi'>$ are the initial and final state wavefunctions, respectively. The total wavefunctions contain nuclear ($|\Psi_n>$), electronic ($|\Psi_e>$), vibrational ($|\Psi_v>$), and rotational ($|\Psi_r>$) components. The nuclear components can be factored out under the Born-Oppenheimer approximation that electronic motion occurs instantaneously when compared to the slow motion of heavy nuclei. The transition moment can be re-written as

$$P = <\Psi'_e|\mu|\Psi_e> <\Psi'_v|\Psi_v> <\Psi'_r|\Psi_r>.$$

The first term is the electric dipole transition strength. The last two terms, known as Franck-Condon and Honl-London factors, respectively, determine the intensity of a ro-vibrational transition between two fixed electronic levels. The most likely vibrational transition occurs when the overlap between $|\Psi'_v>$ and $|\Psi_v>$ is a maximum - a statement of the Frank-Condon principle. [6, 7] Explicit calculation of Franck-Condon factors reveals a simplified guiding principle - the wavefunction overlap is generally maximized for transitions in which the vibrational symmetry of the excited state is preserved in the ion. This means that measurement of ionic vibrational levels allows correlation with vibrational levels of the electronic state.

Time-resolved Total Kinetic Energy Release Spectroscopy

As previously discussed, investigation of σ*-mediated relaxation dynamics is paramount to the study of biomolecule photophysics. The repulsive nature of σ^* states offers an efficient route to the ground state or to H-atom dissociation. Therefore, collection of time and energy resolved H-atom emission spectra by TR-TKER provides an excellent tool for measuring σ^* relaxation dynamics and final product energy distributions.

During σ*-mediated excited state relaxation, electronic energy may be transferred into an X—H stretch mode by IER. Electronic energy transfer can lead to large amplitude H motion with enough energy to promote X—H bond cleavage. The relaxation leaves a free H-atom and a still vibrationally or electronically excited neutral parent minus one H-atom (P′). Energy transferred into the stretch coordinate is carried away as H-atom KE. The initial excited state energy is then shared between H-atom KE and the energy (internal and kinetic) of the P′ co-fragment. The initial excitation energy is generally known, and measurement of H-atom KE allows determination of the co-fragment internal energy distribution following

$$\mathrm{E}(\mathrm{P}')_{internal} = h\nu_{pump} — \mathrm{D}_{\circ} — \mathrm{KE(H)} — \mathrm{KE}(\mathrm{P}'),$$

where $\mathrm{h}\nu_{pump}$ is the excitation energy, $\mathrm{D}_{\circ}$ is the dissociation energy, KE(H) is the measured H-atom KE, and KE(P′) is the parent minus H KE. The last term can be neglected by momentum convervation arguments if the parent is much heavier than the emitted H-atom. This is often the case and allows $\mathrm{E}(\mathrm{P}')_{internal}$ to be determined from measurement of KE(H).

Free H-atoms are ionized in TR-TKER experiments and the ions are collected in a magnetic bottle energy spectrometer. Multi-photon absorption is required to overcome the 13.6 eV ionization potential of atomic H. Here, resonance enhanced multi-photon ionization (REMPI) *via* the H(2s) state is utilized. The H(2s) state (10.2 eV) is excited by two photons at 243.1 nm (5.1 eV) and a third 243.1 nm photon promotes ionization. This 2 + 1 photon REMPI probe offers much higher ionization probability than other non-resonant techniques.

3.2 APPARATUS

A major part of performing successful time-resolved spectroscopy measurements is the maintenance and operation of the experimental apparatus. During a typical experiment UV fs pump and probe pulses are generated by a commercially available laser system, and are directed into a vacuum chamber where they intersect a gaseous molecular beam containing the species under study. Ionization products of the laser/molecule interaction are collected and analyzed by ion and electron spectrometers. A detailed description of the 1) fs laser system, 2) molecular beam source, 3) ion and electron spectrometers, and 4) data acquisition and analysis systems will be given in this chapter. Specifics of each experiment are given in the experimental section of each published paper in Chapters 4 - 6.

Femtosecond Pulse Production

Measurement of fs timescale excited state dynamics by pump-probe spectroscopy requires laser pulses of temporal duration on the same scale. fs laser technology can be traced back to early colliding-pulse organic dye lasers, [8] but their impracticality and low efficiency restricted their research applications. The benchmark development of non-linear titanium sapphire (Ti:Sa) crystals as a gain medium allowed production of sub 100 fs pulses in a robust and efficient manner. [9, 10] Improvement of Ti:Sa technology in the following two decades has led to the commercial availability of high-power and highly flexible laser systems.

The optical layout used in the present pump-probe measurements is based on a Coherent Inc. Ti:Sa oscillator and regenerative amplifier pair as diagramed in Figs 3.4 - 3.6. The 800 nm 130 fs seed pulse originates in the diode pumped MIRA oscillator and is amplified in the LEGEND-HE amplifier to over 3 mJ/pulse. The amplified beam is split and converted to final UV wavelengths of 200 - 400 nm by one of three devices. Two Coherent Inc. optical parametric amplifiers (OPA; TOPAS-C and OPERA) provide tunable (230 - 320 nm) pulses while a homebuilt fourth harmonic ($4h\nu$) box provides fixed wavelengths of 200, 267, and 400 nm. After UV conversion, the pulses are combined at a dichroic optic and are sent to the spectrometer where they intersect a molecular beam of the species under study. The pump-probe delay is varied by changing the path length of one of the beams using a computer controlled motorized optical delay stage. Pulses from two of the three sources are used in a pump-probe measurement and three possible arrangements are shown in Figs 3.4 - 3.6. A general idea of fs pulse production and UV conversion in relation to our Coherent Inc. system is given here.

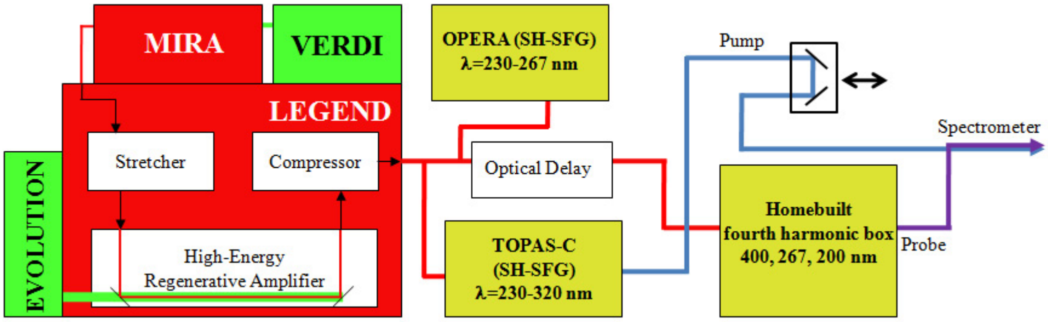

Figure 3.4: Optical layout for TOPAS-C plus fourth harmonic pump-probe scheme.

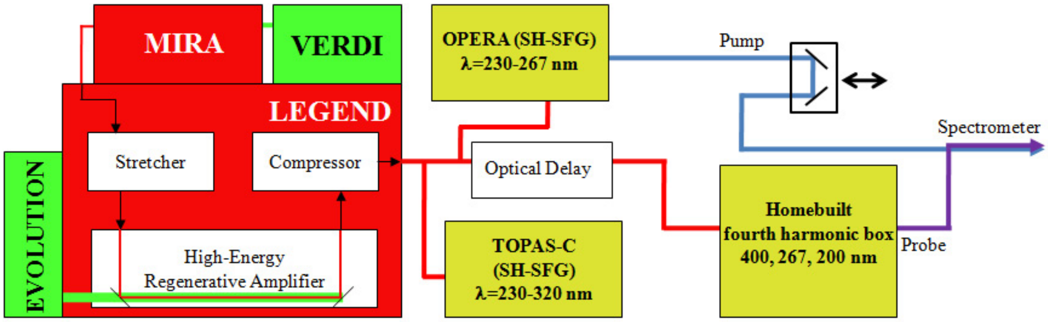

Figure 3.5: Optical layout for OPERA plus fourth harmonic pump-probe scheme.

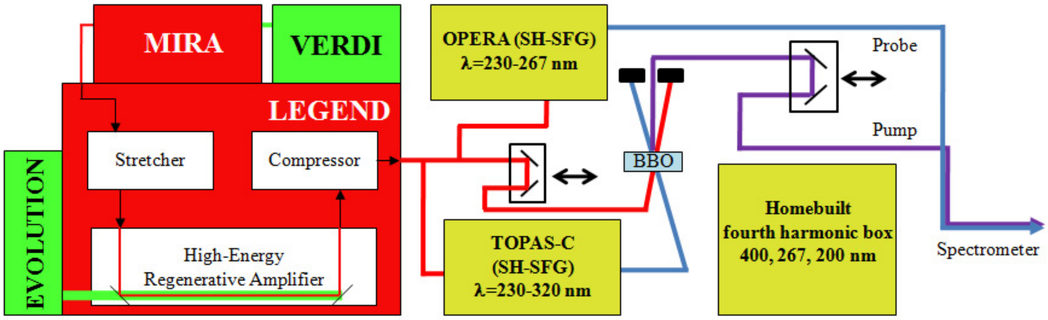

Figure 3.6: Optical layout for TOPAS-C DUV plus OPERA pump-probe scheme.

One requirement for generation of fs pulses is the simultaneous propagation of many longitudinal modes of different wavelength through the lasing cavity. Also, the phase between the longitudinal must be fixed to achieve constructive interference, a process called mode locking. Superposition of mode locked waves creates a large peak intensity ($\mathrm{I} \sim n\ \mathrm{E}_{\circ}^{2}$) within a short temporal duration ($\tau \sim (n\ \Delta\lambda)^{-1}$). Here, n is the number of longitudinal modes determined by the lasing medium gain profile width, $\mathrm{E}_{\circ}$ is the electric field amplitude of each mode, and $\Delta\lambda$ is the spacing between modes given by the resonator length. The pulse intensity increases with the number of modes, while the pulse duration decreases. The pulse bandwidth is determined from $BW \sim n\Delta\lambda$, and the relationship between bandwidth and temporal duration is

$$\tau \sim \frac{\lambda_{\circ}^{2}}{(n\Delta\lambda)c},$$

where $\lambda_{\circ}$ is the central wavelength and c is the speed of light.

Ultrafast Near-infrared Laser System

The fs pulse derives from the diode pumped MIRA oscillator. The VERDI V5 pump laser provides 5 W of continuous wave (CW) power to the Ti:Sa crystal inside the MIRA. The VERDI works by generating 1064 nm output from a diode array and fiber coupling it to an Nd:Yag crystal where it is frequency doubled to 532 nm. Population inversion in the MIRA's Ti:Sa crystal is promoted by absorption of the VERDI output. The wide gain profile of Ti:Sa extends over ∼ 400 nm [11] and provides a large number of longitudinal modes required for fs pulse generation. The MIRA design utilizes passive mode locking using a self-focusing mechanism based on the Kerr effect. Passive mode locking involves no mechanical cavity length variation to fix the phase. Instead a Kerr-lens and optical slit combination allows only the mode locked waves to propagate through the cavity. The Kerr-lens is formed from a non-linear material whose index of refraction is modified by intense electric fields. The spatial distribution of laser beam intensity creates an index of refraction gradient along the radial direction of the non-linear material, thus creating the same effect as a traditional lens.

The index of refraction change only occurs for the large electric field intensities produced by mode locked pulses. The mode locked portion of the beam is focused through an adjustable width slit by the Kerr-lens, while the CW portion is unfocused and is blocked by the slit. At the time of pulse initiation, only a few of the cavity modes are in phase and are passed by the Kerr-lens/slit combination. However, the mode locked intensity is quickly amplified upon successive trips through the gain medium and the Kerr-lens. The mode locked MIRA output is an $\sim$500 mW beam of $\sim$130 fs pulses centered at 800 nm with $\geq$10 nm bandwidth. The pulse repetition rate of 76 MHz leads to an energy of $\sim$7 nJ/pulse. Approximately 300 mW of the MIRA output are used to seed the amplifier; the residual is used for pulse diagnostics.

Before UV conversion, the seed pulses are amplified to about 3 mJ/pulse in a kHz rate LEGEND amplifier. Key elements of the amplifier are 1) a pulse stretcher and matched compressor, 2) an EVOLUTION pump laser, and 3) a Ti:Sa regenerative amplifier cavity. The seed is temporally stretched by three orders of magnitude at a high precision holographic diffraction grating before entering the Ti:Sa regenerative amplifier cavity. The EVOLUTION is a Nd:YLF laser providing 20 W of pump power at 527 nm in 250 ns pulses at 1 kHz. Interaction of the pump laser and the Ti:Sa crystal creates a high-power 1 kHz train of 250 ns pulses centered at 800 nm. Seed pulses arriving at the Ti:Sa crystal in time with the pump pulse will be amplified. However, the repetition rate mismatch (76 MHz to 1 kHz) means that most seed pulses will not encounter a pump pulse. When a seed pulse is precisely timed with the maximum of the pump intensity, it is injected into the amplifier cavity by means of a pockel cell. A pockel cell is essentially a $\lambda/4$ plate that is activated by a high voltage pulse. The pockel cell, in combination with an appropriate polarizer allows seed pulses to enter the cavity only when a high voltage pulse is present. Timing between the pump pulse and the pockel cell high voltage pulse is controlled by an adjustable synchronous delay generator (SDG). The injected seed passes through the cavity and the Ti:Sa crystal several times before maximum amplification occurs. A second pockel cell allows the amplified seed out of the cavity in a manner similar to the injection technique. Amplified pulses are then recompressed by a grating which reverses the action of the stretcher and the final fs pulse is created. Precisely matched stretcher and compressor gratings should theoreticalyl result in compression to the original pulse duration. However, spectral dispersion due to transmissive optics in the amplifier cavity typically results in a longer output pulse than the input. The compressor grating angle is adjusted to compensate for this spectral dispersion. Typical LEGEND output is ∼3.5 mJ/pulse centered at 800 nm with ≥10 nm bandwidth and ∼150 fs pulse duration.

Ultraviolet Pulse Conversion

Conversion of the 800 nm amplifier pulses into tunable UV wavelengths occurs by non-linear sum frequency mixing in barium borate oxide (BBO) crystals. Non-linear interactions will be described here and are common to the TOPAS-C, OPERA, and $4h\nu$ box conversion tools, although small differences will be described below.

The electric field of a laser pulse causes polarization of dipoles inside a solid. Radiation from the dipole field can create a new signal field at a different frequency if the electric field intensity is very intense, as is often the case with fs pulses. The laser field can be written as

$$\epsilon(\mathrm{t}) = 1/2\ \mathrm{E}(\mathrm{t})\ \exp\ (i\ \omega \mathrm{t}),$$

and the polarization can be expanded as

$$\mathrm{P} = \epsilon_{\circ}(\chi^{(1)}\epsilon + \chi^{(2)}\epsilon^2 + \chi^{(3)}\epsilon^3 + ...),$$

where ϵ is the electric field amplitude, $\chi^{(i)}$ is the i^{th} order susceptibility, and $\epsilon_{\circ}$ is the permittivity of free space. The magnitude of the susceptibility constant decreases at higher orders meaning that the non-linear terms only become important at large field strengths. Considering the second-order term alone leads to

$$\epsilon^2(\mathrm{t}) = 1/4\ \mathrm{E}(\mathrm{t})^2\ \exp\ (i\ 2\omega \mathrm{t}).$$

It is clear in this simplified picture that the polarization field oscillates at twice the frequency of the input field. This process is known as second harmonic generation (SHG) and is the most commonly used frequency conversion mechanism - occuring in the TOPAS-C, OPERA, $4h\nu$ box, and pulse measurement devices.

The combination of two beams of different frequencies in a non-linear medium is called sum frequency generation (SFG). The induced polarization is due to the field from both beams. We must now consider an electric field with both spatial and frequency components

$$\epsilon(\vec{r},\ \mathrm{t}) = 1/2\ \mathrm{E}_1 \exp\ (\mathrm{i}\ (\omega_1\ \mathrm{t}\ \text{-}\ \vec{k_1}\cdot\ \vec{r})) + 1/2\ \mathrm{E}_2 \exp\ (\mathrm{i}\ (\omega_2\ \mathrm{t}\ \text{-}\ \vec{k_2}\cdot\ \vec{r})),$$

where $\vec{k_1}$ and $\vec{k_2}$ are wave vectors of each beam. Again, consider the second order electric field. The first few terms are the SHG equations written above, and the remaining terms are of the form

$$\epsilon^2(\vec{r},\ \mathrm{t}) \sim 1/4\ \mathrm{E}_1\ \mathrm{E}_2 \exp\ (i\ (\omega_1 + \omega_2)\ \mathrm{t}\ \text{-}\ (\vec{k_1} + \vec{k_2})\cdot\ \vec{r}).$$

Here, the signal frequency is the sum of the input frequencies. SFG occurs in the TOPAS-C, OPERA, and $4h\nu$ box.

In both SHG and SFG, the input and signal beam propagate through the non-linear material together. The signal and input beams must oscillate with the same phase to eliminate destructive interference. This is the condition of phase matching which can be written as

$$\vec{k_\circ} = \pm\ \vec{k_1} \pm \vec{k_2},$$

where $\vec{k_\circ}$ is the signal wavevector. Practically, this means that the signal and input beams must travel through the non-linear medium at the same group velocity. This may seem unreasonable, as the index of refraction of a material, and therefore the speed of light in that material, is a function of frequency. However, a birefringent material, such as BBO, has different refractive indices along each crystal axis. Adjusting the angle between the laser input and the crystal axes allows the phase matching condition to be satisfied.

Having knowledge of non-linear frequency conversion interactions permits the discussion of the UV conversion apparatus used in the laboratory here. Conversion of the 800 nm amplifier output into UV wavelengths is required for one-photon excitation of electronic states, and is achieved using a home-built $4h\nu$ box and two seperate OPA's. A diagram of the $4h\nu$ box is given in Fig 3.7. Approximately 700 mW of the 800 nm fundamental is used.

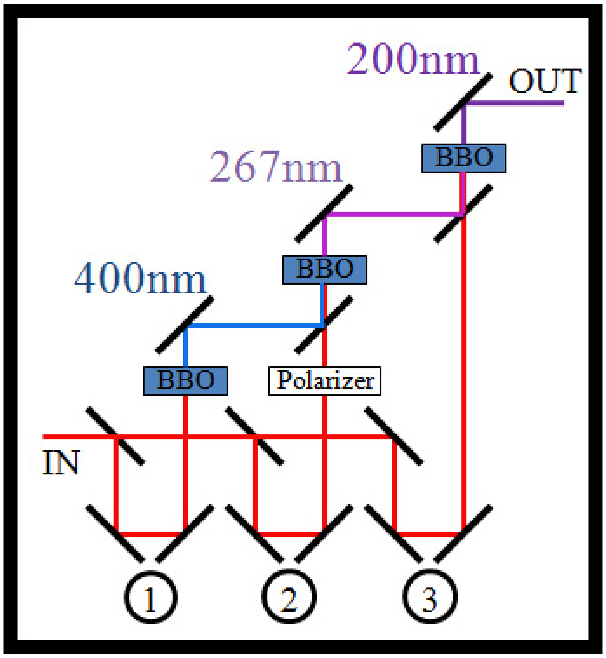

Figure 3.7: Diagram of home-built fourth harmonic conversion box. The 800 nm input is split into three conversion steps. 400, 267, and 200 nm are produced by SHG, SFG, and SFG interactions, respectively in three seperate BBO crystals. The 800 nm polarization is rotated by 90° in stage 2.

The input is split and the conversion takes place in three stages. Stages 1, 2, and 3 utilize 200, 200, and 300 mW, respectively. At the first stage, the fundamental is frequency doubled by SHG in BBO, and ∼80 mW of 400 nm is produced. At the second stage, ∼30 mW of 267 nm is produced by 800 + 400 nm SFG in a second BBO crystal. The second stage 800 nm passes a $\lambda/2$ polarizer to match the 400 nm polarization. Also, the 800 nm pathlength is adjusted to match the 400 nm timing at the mixing crystal. In the last stage, ∼5 mW of 200 nm is produced by 800 + 267 nm SFG in a third BBO crystal. The third stage 800 nm pathlength is adjusted to match the 267 nm timing at the mixing crystal. The phase matching angle of each BBO is adjsted to optimize the desired wavelength output.

The Coherent Inc. TOPAS-C and OPERA OPA's provide tunable wavelengths (230 - 1600 nm) for the pump-probe experiment, although the UV range (230 - 300 nm) is typically

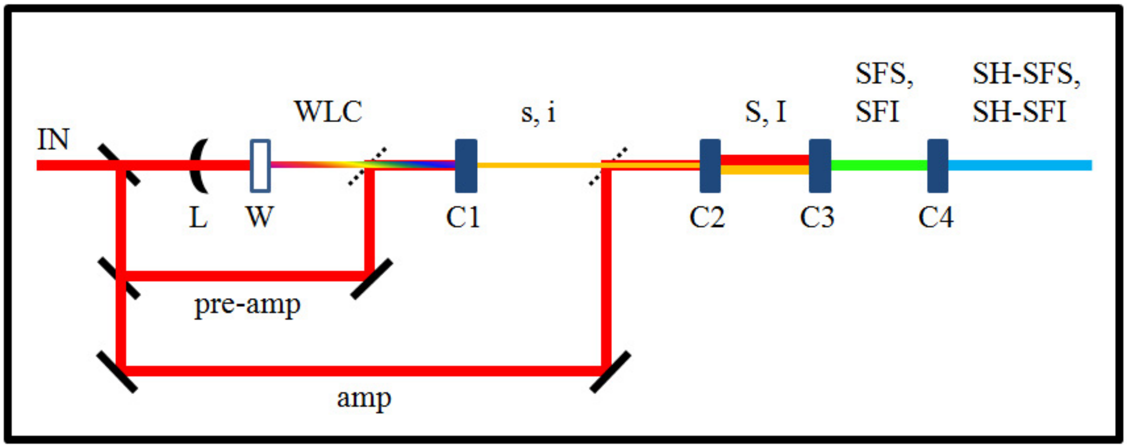

Figure 3.8: Diagram of optical parametric amplifier. White light (WLC), pre-amp, and amplifier paths are used to create tunable UV pulses. Non-linear interactions include: s, i - un-amplified signal and idler; S, I - amplified signal and idler; SFS, SFI - sum frequency of signal and idler; SH-SFS, SH-SFI - second harmonic sum frequency of the signal and idler. Optical elements include: L - lens; W - sapphire window; C1-C4 - non-linear crystals.

utilized. The beam geometry of each device is different, but the general idea of OPA can be understood in reference to Fig 3.8. The 800 nm input is split into three stages: the white light generation stage, the pre-amp stage, and the amplifier stage. Over 80% of the input power is directed into the main amplifier stage. Approximately 1% of the input is focused into a sapphire window (W) to create a white light supercontinuum (WLC). The WLC has an extremely wide bandwidth, extending from ∼400 - 1600 nm. The OPA signal is created by amplification of the WLC's IR range (1200 - 1600 nm) in the pre-amp and amp stages. In the pre-amp stage, the WLC is combined with the second 800 nm beam in a BBO crystal (C1). The 800 nm timing and the phase matching angle of C1 are adjusted to optimize a specific wavelength of the WLC. The resulting IR signal, s, is represented by the thin orange line in Fig 3.8. The pre-amplified signal beam has only 1 μJ/pulse energy and must be amplified further before UV conversion. The OPA idler, i, wavelength (1600 -2600 nm) is also created in C1 by difference frequency generation. The following amplification and UV conversion steps are discussed in terms of the signal interactions but can occur with the idler as well. In the amplifier stage, s is overlapped with the main 800 nm beam in BBO crystal, C2. The 800 nm timing and C2 angle are adjusted to optimize the signal power. The amplified signal, S, is represented by the thick orange line in Fig 3.8. Up to 100 μJ/pulse are produced in the amplifier stage for UV conversion. The first conversion stage involves SFG of the residual 800 nm beam with the amplified signal in a BBO crystal, C3. The angle of C3 is adjusted to optimize the SFG of the signal (SFS). The final conversion occurs by SHG of the SFS (SH-SFS) in a BBO crystal, C4. Again the angle of C4 is adjusted to produce up to 35 μJ/pulse of the SH-SFS interaction between 235 - 266 nm.

Femtosecond Pulse Measurement

It can be a difficult task to measure the temporal duration of the fs pulses used here to study excited state dynamics. In fact, an entire scientific field of ultrafast pulse measurement has developed along with fs pulse generation technology. [12] The extremely detailed measurement of complicated pulses shorter than 10 fs has been achieved but this level of measurement is not generally required here. Instead, basic pulse duration measurements are used as a diagnostic of laser system performance and timing resolution of the pump-probe experiment. A description is given here for three pulse measurement devices: intensity autocorrelator (AC), frequency resolved optical gate (FROG), and transient grating FROG (TG-FROG).

Measurement of some event in time requires a measurement device with a shorter temporal duration. This is not possible for fs pulses as a shorter event is not available. Instead, the fs pulse is used to measure itself by autocorrelation or FROG measurements. The key to this measurement is that the pulse is split into two copies which are subsequently overlapped in a non-linear material. The timing between the copies is varied and the response of the non-linear material is measured as a function of the time between pulses, Δt. An AC measurement records the intensity of the SHG signal generated in a BBO crystal.

The autocorrelation signal can be written as

$$\mathrm{AC}(\Delta \mathrm{t}) = \int_{-\infty}^{\infty} \mathrm{I}_1(\tau)\ \mathrm{I}_2(\tau - \Delta \mathrm{t})\ \mathrm{d}\tau,$$

where τ is the input pulse width and I_1 and I_2 are the intensities of each pulse. The SHG signal is only created when both pulses are overlapped in the crystal - Δt is within τ, and measuring AC(Δt) yields information about the pulse width. The FWHM duration of the input pulse can be obtained from the AC measurement only if a pulse shape is assumed. The FWHM of the autocorrelation signal is 1.41 times the pulse duration for Gaussian and 1.54 times the pulse duration for sech^2 pulse shapes.

A pulse cannot be uniquely identified by an AC measurement because of phase-shift, translation, and time-reversal ambiguities. [13] Instead, FROG measurements spectrally disperse the AC signal and allow retrieval of a unique pulse. The spectral and temporally resolved FROG measurement allows the relationship between time and fequency to be measured simultaneously. The FROG signal can be written as

$$\mathrm{I}(\Delta \mathrm{t}, \omega) = |\int_{-\infty}^{\infty} \mathrm{E}_1(\tau)\ (\mathrm{E}_2(\tau - \Delta \mathrm{t}))^2\ \mathrm{d}\tau|^2.$$

Calculating the field E(τ) from the measured FROG intensity involves solving the two-dimensional phase retrieval problem. [13] The exact pulse retrieval algorithm is outside the scope of this thesis, however a program developed by the Trebino group is utilized to analyze FROG measurements.

Measurement of UV pulses can be more difficult because BBO crystals do not exhibit favorable transmission characteristics or non-linear responses in this wavelength range. Instead a transient grating FROG (TG-FROG) is utilized. A three pulse geometry is utilized in TG-FROG measurements. Two of the pulses are temporally synchronized and are focused into a 3 mm thick Zinc Selenide (ZnSe) window. The synchronized pulses create a spatial variation of refractive index in the ZnSe by the Kerr effect. A refractive index grating is created with line spacing equal to the wavelength of the input pulse. The grating is only formed when the two synchronized pulses are present, thus a transient grating. The final pulse is then scanned over the transient grating by adjusting the timing between it and the

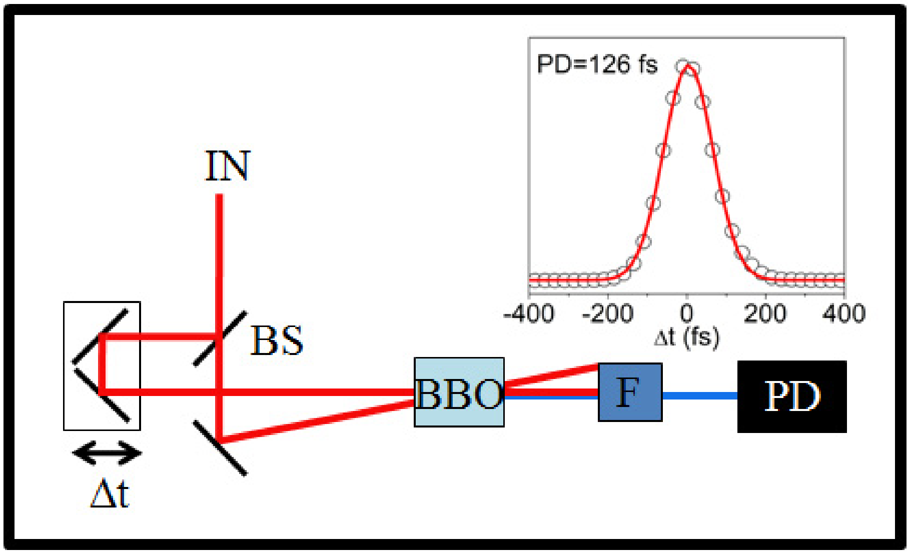

Figure 3.9: Diagram of intensity autocorrelator. BS - 50/50 beam splitter; Δt - variable time delay; BBO - SHG crystal; F - second harmonic filter; PD - photodiode detector.

synchronized pulses. The TG-FROG signal is created by diffraction from the grating of the time-delayed pulse. The signal results at a different angle than the input beams and is isolated by a spatial mask. A spectrometer measures the spectrum of the TG-FROG signal as a function of Δt, and an algorithm similar to the FROG retrieval code is used to determine the input pulse duration.

The intensity autocorrelator geometry is shown in Fig 3.9. The input pulse is divided into two equal intensity pulses by a 50/50 dichroic beam splitter (BS). Both pulses are routed through a BBO crystal where the SHG AC signal is created. One of the pulses travels through an optical delay stage that changes the time-delay, Δt, between pulses. The AC signal is isolated by a colored glass bandpass filter (F) and its intensity is measured as a function of Δt by a photodiode detector (PD). An AC measurement of a 126 fs 800 nm amplifier pulse is shown in the inset of Fig 3.9.

The optical setup of a FROG device is the same as the AC in Fig 3.9 but the PD is replaced by an Ocean Optics HR-4000 fiber spectrometer. The spectrometer resolution

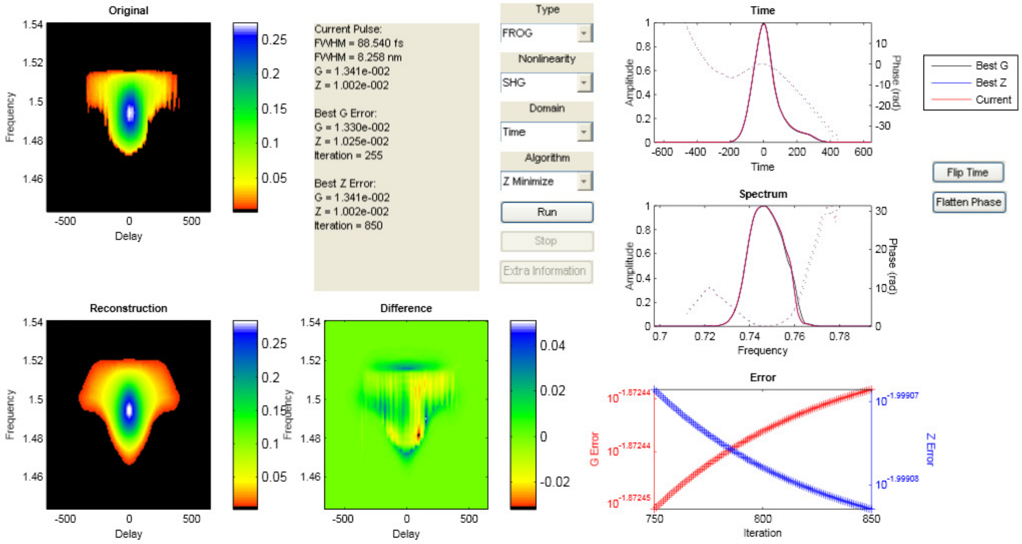

```
Current Pulse:
FWHM = 88.540 fs
FWHM = 8.258 nm
G = 1.341e-002
Z = 1.002e-002

Best G Error:
G = 1.330e-002
Z = 1.025e-002
Iteration = 255

Best Z Error:
G = 1.341e-002
Z = 1.002e-002
Iteration = 850
```

Type: FROG
Nonlinearity: SHG
Domain: Time
Algorithm: Z Minimize

Figure 3.10: Plots of pulse retrieval from SHG-FROG measurement of 800 nm pulse. Color plots show the measurement (top), retrieved pulse (bottom), and the difference between the two (center). Integration over the time (top) and frequency (bottom) axes are shown at right. The retrived FWHM = 88 fs corresponds to a pulsewidth of 124 fs.

is 0.02 nm. The spectrally dispersed SHG signal intensity is measured as a function of Δt. The resulting 2-D measurement is shown at the top left of Fig 3.10. The 2-D phase retrieval algorithm produces the reconstructed pulse shown at the bottom left of Fig 3.10. The measured and retrieved pulses show intensity differences (bottom center of Fig 3.10) of $\leq 10\%$ of the total signal. Integration of the reconstructed pulse over time or frequency domains yields the time and spectrum plots at the right of Fig 3.10. The 'wing' structure of the measured pulse causes the bump at positive times in the top plot and the non-symmetric shape of the spectrum plot. The width of the time trace (top) reveals FWHM = 88 fs - corresponding to a Gaussian pulse of 124 fs duration.

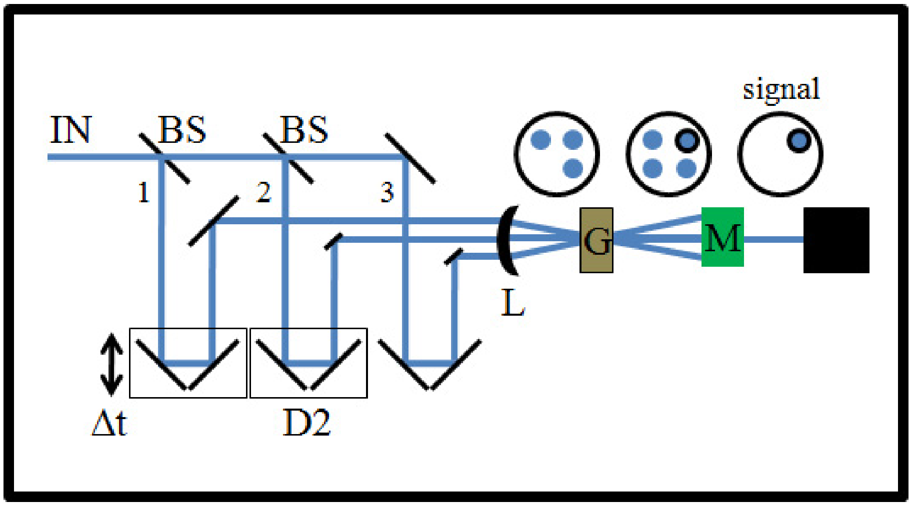

Figure 3.11: Diagram of TG-FROG. BS - beam splitter; Δt - variable time delay; D2 - fixed delay to synchronize beams 2 and 3; G - non-linear medium in which the transient grating is produced by beams 2 and 3; M - TG-FROG signal mask; S - spectrometer.

The TG-FROG optical setup is given in Fig 3.11. The input is split into 3 separate paths, and each is focused (L) into a ZnSe window (G). The input beams are arranged at three points of a box-car geometry as shown in the inset of Fig 3.11. Pulses 2 and 3 are synchronized at G by adjusting pulse 2 delay (D2) to create the transient grating. Pulse 1 is scaned over the grating by the variable delay, Δt. The TG-FROG signal is spatially offset from the input pulses by diffraction from the transient grating. The signal is isolated by a spatial mask (M) and is detected by the spectrometer. An example TG-FROG measurement of a 400 nm pulsecreated in the $4h\nu$ box is given in Fig 3.12. The 2-D color contour plot shows the ~5 nm bandwidth. This is half of the 800 nm bandwidth, and the reduction is caused by the SHG process that created the 400 nm pulse. In the right panel of Fig 3.12, a Gaussian fit (red line) of the integrated data (circles) reveals a pulsewidth of 143 fs.

Pulse measurements of the type described above are used as a diagnostic of the laser system performance and the timing resolution of our pump-probe experiment. The intensity AC is the workhorse device in the lab as it allows pulsewidth measurements to be made in

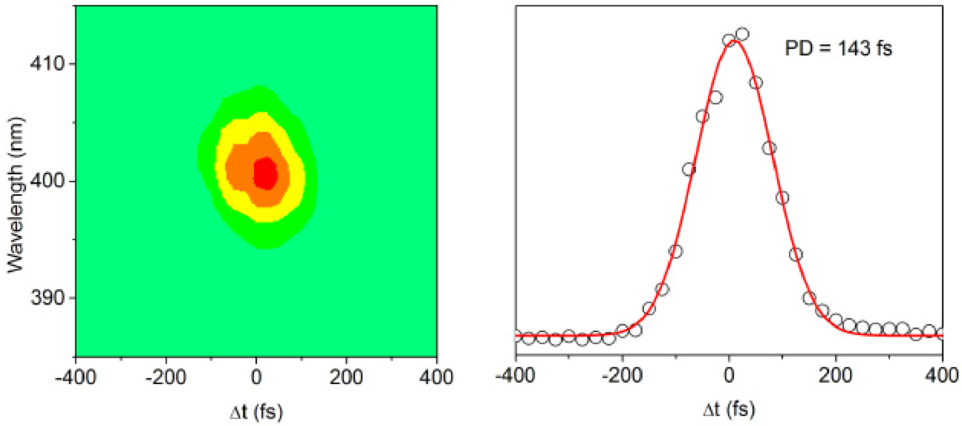

Figure 3.12: Plots of TG-FROG measurement of 400 nm pulse. A fit (red) of the integrated delay trace data (circles) yield a pulsewidth of 143 fs.

just a few minutes. The extra spectral information offered by FROG is not always needed for our application and the added pulse retrieval time hinders its use as a day-to-day diagnostic tool. Also, timing calibration measurements are performed in the spectrometer by cross correlation of the pump and probe beams. Cross correlation calibration wil be discussed in the data analysis section.

Molecular Beam Source

The vacuum system is diagramed in Fig 3.13 and consists of the high vacuum molecular beam (MB) source chamber, the ultra-high vacuum photoion photoelectron spectrometer chamber, and the associated rough vacuum backing system. In Fig 3.13, the MB source chamber is shown in a top view at left and the spectrometer is shown in a side view at right. In overview, a gaseous molecular beam of the sample molecule is generated at the nozzle in the inner chamber (IC) by expansion from a micrometer sized pinhole. The MB (red line) is collimated by two separate skimmers (S1 and S2) at the boundary of the IC and outer chamber (OC) before entering the spectrometer. The pump-probe laser pulses intersect the MB in the ionization region (yellow ring) of the spectrometer. Charged particles produced by photoionization are collected through several methods, including electrostatic extraction of ions and magnetic collection of photoelectrons and H-atoms. Multi-channel plate detectors (MCP; ED and ID) facilitate TOF measurements which are converted into mass or energy spectra for analysis of molecular photophysics.

The MB chamber is constructed of 0.5 inch thick aluminum and encompasses two differential pumping regions of overall dimensions 100 x 60 x 30 cm - a total volume of 1800 cm^3. The MB originates at the nozzle inside the inner chamber which is isolated by an inner wall of dimensions 80 x 50 x 30 cm. The chamber lid is detachable and allows removal of the inner wall for cleaning or for other MB configurations. Three removable panels on the lid allow access to the inner chamber for day to day operation. Several feedthrough flanges are placed along the vertical face of the outer chamber wall. The interchangeable flanges allow for several options including a viewport, electrical power, temperature measurement, and gas input. The lid, inner wall, access ports, and feedthrough flanges are all sealed by viton O-rings.

Two Varian VHS-6 diffusion pumps (DP1 and DP3) provide 4000 L s^{-1} pumping speed for the inner chamber, and one M4 diffusion pump (DP2) provides 1800 L s^{-1} pumping speed for the outer chamber. Pneumatically actuated gate valves isolate the diffusion pumps from the MB chamber. The three diffusion pump exhausts are combined into a single 6 inch outlet which is evacuated by BOC Edwards EH 1200 roots blower and E2M80 rotary pumps (total backing pump speed of 250 L s^{-1}). The inner and outer chamber base pressures of 5 x 10^{-7} and 1 x 10^{-6} Torr, respectively, are measured by separate iridium filament ionization gauges located near the entrance of each diffusion pump. The vacuum gauges are operated by a Varian Multigauge controller that is interfaced with a LabView based pressure monitoring program. An interlock system has been developed to protect from unwanted spikes in vacuum pressure during experimentation. The interlock shuts off the sample gas supply and closes several vacuum valves if a high pressure reading is measured by the Multigauge controller.

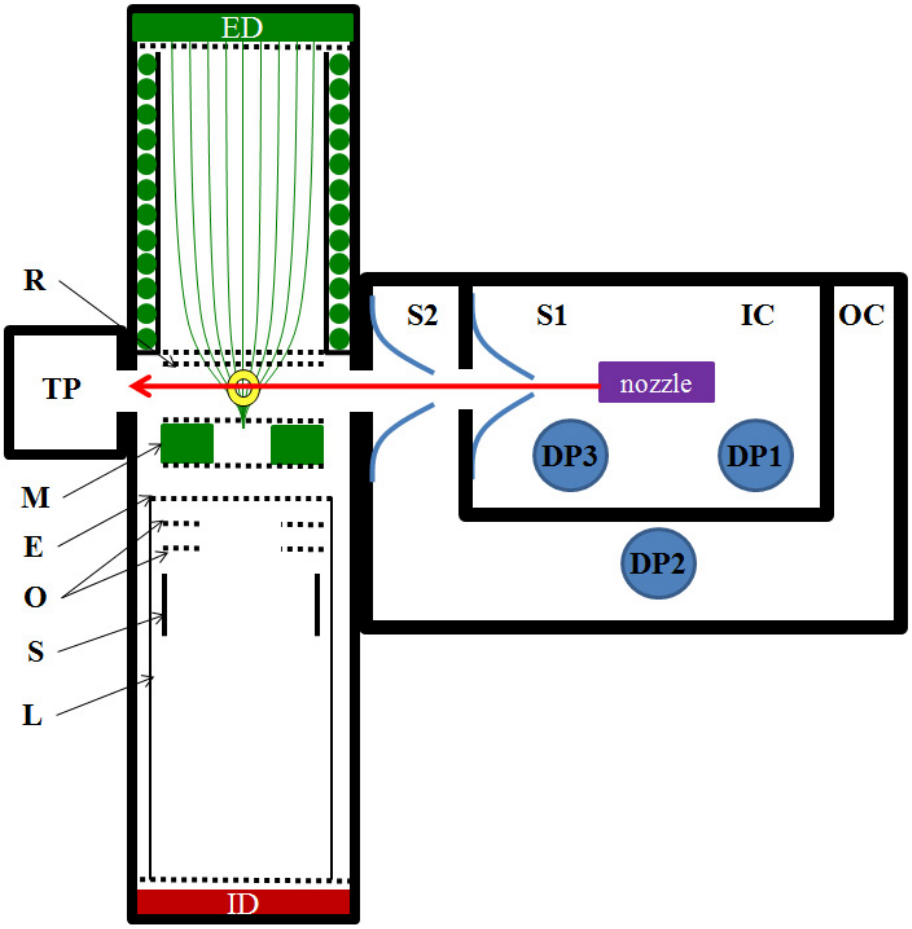

Figure 3.13: Schematic of molecular beam source (top view) and spectrometer (side view). The molecular beam (red line) originates from the nozzle and intersects pump-probe laser pulses in the ionization region (yellow ring). Other abbreviations are as follows: OC - outer chamber; IC - inner chamber; DP - diffusion pump; S1 and S2 - conical skimmers; ED - electron detector; ID - ion detector; TP - turbo pump; R - ion repeller; M - magnet; E - ion extractor; L - ion lenses; S - ion steering plates.

The high voltage spectrometer power is also stopped to protect the charged particle detector. A detailed description of the interlock system design and operation is given in Chp 9.

During experiment downtime, the chamber is maintained at rough vacuum as measured by several thermocouple gauges. The E2M80 maintains the diffusion pump system while the pneumatic gate valves are closed. A separate roughing line evacuates the main chamber and is pumped by a 1397 Welch pump. The roughing system is isolated in a separate mechanical room to eliminate oil vapor contamination of the optical setup.

The MB originates in the inner chamber at the nozzle assembly. A close-up diagram is shown in Fig 3.14 and a picture of the nozzle mounted in the inner chamber is shown in Panel 1 of Fig 3.15. The nozzle is basically a 2 inch long stainless steel cylinder with I.D. = 0.5 inch and O.D. = 1 inch. The MB sample gas source (GS) is supplied at one end of the nozzle (right side in Fig 3.14) through a removable O-ring sealed flange with Swagelok adapter connected to a 0.25 inch copper tube. An external needle valve controls the pressure/flow of the sample gas through one of the chamber wall feedthroughs and into the nozzle. A precision pinhole (PH) aperture is mounted in another O-ring sealed flange at the opposite end of the nozzle. PH diameters of 50 - 200 μm are used depending on the sample of interest. The MB is generated by continuous expansion from the high-pressure region (HPR) through the PH and into the inner chamber. A collimated beam enters the spectrometer after passing two conical skimmers of 3 mm (S1) and 5 mm (S2) diameter positioned at distances d_1 = 15 cm and d_2 = 45 cm from the PH. S1 and S2 are Model 2 electroformed curved skimmers manufactured by Beam Dynamics. Maximum pressures of 1 x 10^{-5} and 5 x 10^{-6} Torr are measured during operation of the MB. The MB passes S2 and enters the spectrometer region in which the laser photolysis occurs. S2 is mounted on a manual gate valve (GV) which isolates the spectrometer and MB chambers. This design allows the MB source to be vented to atmosphere while the spectrometer stays under vacuum. Changes may be made to the MB chamber several times during a single experiment

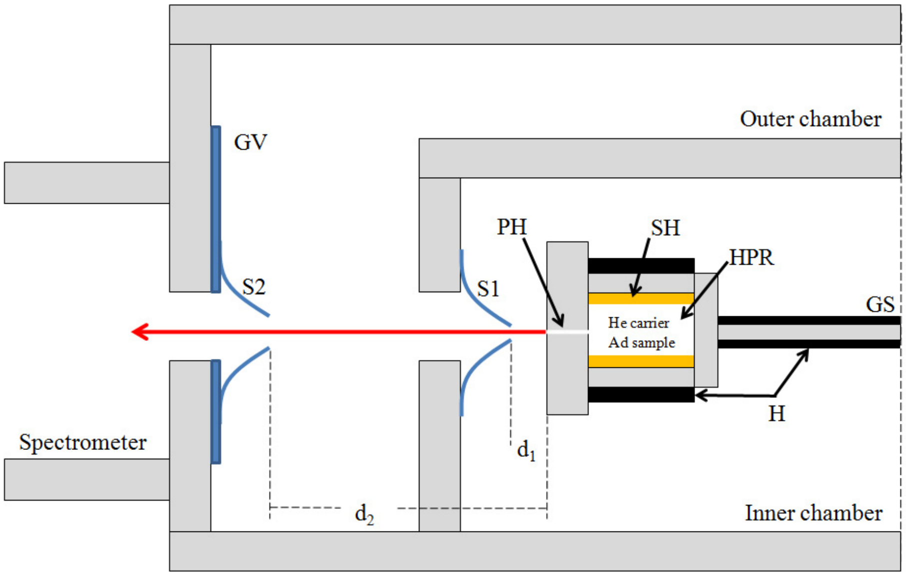

Figure 3.14: Expanded view of molecular beam generation. GS - gas source; H - heater; HPR - high pressure region; SH - sample holder; PH - pinhole; d_1 = 10 cm; d_2 = 40 cm; S_1 - skimmer 1; S_2 - skimmer 2; GV - manual gate valve.

and this design eliminates a lengthy pump down sequence which would be required if the spectrometer were vented each time.

A MB of gaseous samples, either 1, 3 butadiene (BD), ammonia (NH_3), or nitric oxide (NO), is formed using the technique described above. Typically, the sample gasses are diluted to 10 - 50% concentration with He carrier gas, and the mixture is sent directly to the nozzle from a high pressure source cylinder through a needle valve. However, generation of a gaseous MB from a solid sample, such as adenine, is more difficult. Many iterations of heating mechanisms and sample preparation were undertaken before substantial molecular density was achieved for an adenine MB. A picture of the adenine molecular beam set-up is shown in Fig 3.15. Approximately 0.1 g of adenine powder is placed inside a cylindrical quartz sample holder (SH) in the HPR. He carrier gas is maintained at $\sim$ 100 Torr in the HPR. A small amount of glass wool is placed in front of the PH to assure that adenine powder does not block the aperture due to dynamic pressure changes of the carrier gas. A

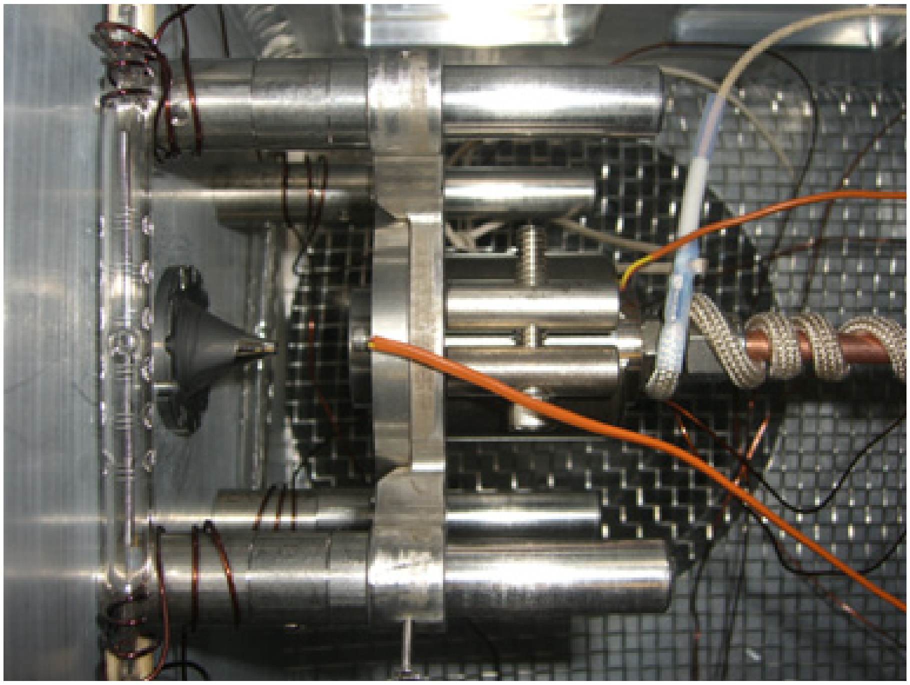

Figure 3.15: Picture of adenine molecular beam set-up. Note, halogen light and graphite coated skimmer.

resistive band heater (under screw) is placed around the length of the nozzle and a vacuum compatible rope heater is placed around the copper tube of the GS. Type K thermocouple temperature probes (orange) are placed near the pinhole and between the band heater and the nozzle body. The nozzle temperature is maintained at 175 - 200 °C by a temperature controller and SSR relay. This temperature range was selected based on previous reports [14 - 16] as well as our own mass spectra measurements which show little ionization signal at lower temperatures and significant parent fragmentation at higher temperatures. Two key developments that allowed the adenine measurements were the addition of two halogen bulbs near S1 and the coating of S1 with black graphite spray. The bulbs heat the pinhole exit and S1 such that no adenine gas can condense at these locations and the graphite spray increases the halogen light absorption, and therefore the temperature of S1.

A series of simple calculations will be carried out here and in the following paragraphs to estimate the molecular beam gas load (Q_M) in each vacuum region during a typical experiment. The formula Q = S * P is used to calculate the gas load where S is the pumping speed and P is the pressure. The base pressure gas load (Q_B) is determined when the MB is off, and the total gas load (Q_T) is determined when the MB is operating. The gas load due to the MB is calculated as the difference between total and base pressure gas loads

$$Q_M = Q_T \;\; Q_B.$$

Two subscripts are used in the following notation. The first refers to the chamber region (I - inner, O - outer, S - spectrometer), and the second refers to the experiment situation (B - base, T - total, M - MB only) The inner and outer chamber base pressures ($P_{IB} = 5$ x 10^{-7} Torr and $P_{OB} = 1$ x 10^{-6} Torr) and operating pressures ($P_{IT} = 1$ x 10^{-5} Torr and $P_{OT} = 5$ x 10^{-6} Torr) lead to gas loads of $Q_{IB} = 2$ x 10^{-3} Torr L s^{-1}, $Q_{OB} = 1.8$ x 10^{-3} Torr L s^{-1}, $Q_{IT} = 4$ x 10^{-2} Torr L s^{-1}, and $Q_{OT} = 9$ x 10^{-3} Torr L s^{-1}. The gas loads due to the MB are then $Q_{IM} = 3.8$ x 10^{-2} Torr L s^{-1} and $Q_{OM} = 7.2$ x 10^{-3} Torr L s^{-1}. These calculations show that most of the sample gas which expands from the pinhole is blocked at the first skimming stage and is pumped by the inner chamber diffusion pumps.

Time-of-flight Spectrometer

Pictures of the spectrometer constrruction are shown in Fig 3.16. Panel 1 shows a close-up of the ion optics stack, Panel 2 shows the ion optics and electron flight tube inside the spectrometer chamber, and Panel 3 shows a wide view of the entire assembly. The spectrometer body is a stainless steel ConFlat (CF) cube with two opposing linear flight tubes for ion and electron measurements (see Fig 3.13). CF flanges and copper gaskets seals allow for ultra-high vacuum (UHV) generation. The spectrometer is evacuated by a magnetically levitated turbo pump (Mitsubishi Heavy Industries FT-3301W; 2100 L s^{-1}) to a base pressure of $P_{SB} = 1$ x 10^{-9} Torr ($Q_{SB} = 2.1$ x 10^{-6} Torr L s^{-1}). The turbo pums connects to the large opening in Panel 3 of Fig 3.16. Care is taken to achieve such

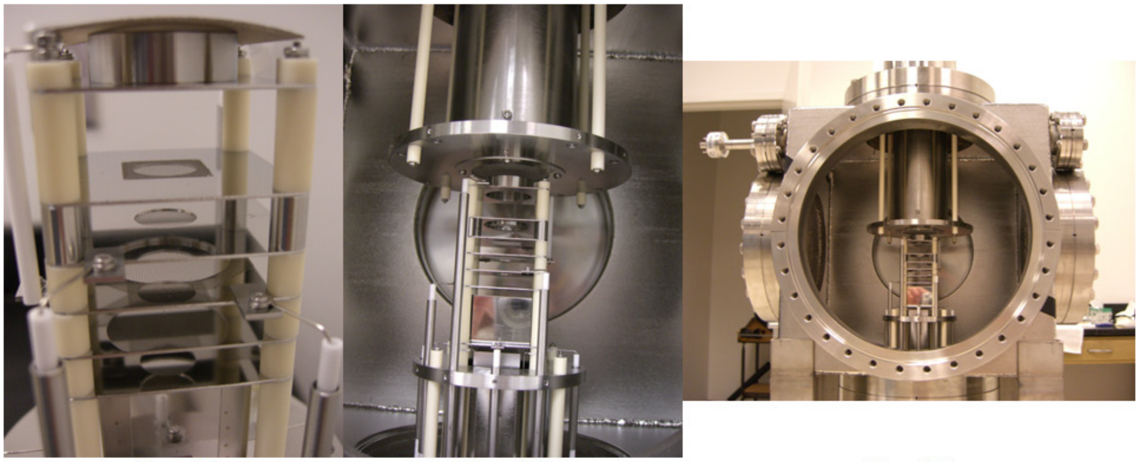

Panel 1 Panel 2 Panel 3

Figure 3.16: Pictures of spectrometer assembly. Panel 1 - ion optics stack; Panel 2 -ion optics and electron flight tube mounted inside the spectrometer; Panel 3 - wide view of spectrometer cube.

a low pressure because 1) photoionization experiments can be extremely sensitive to water and hydrocarbon contaminants, 2) the MCP detectors cannot be operated safely at higher pressures, and 3) the mean-free flight path must be at least the length of the ion flight tube (~1 m). During MB operation, a pressure of $P_{ST} = 3 \text{ x } 10^{-8}$ Torr is maintained ($Q_{ST} = 6.3 \text{ x } 10^{-5}$ Torr L s^{-1}). The molecular beam gas load in the spectrometer is then $Q_{SM} = 6.1 \text{ x } 10^{-5}$ Torr L s^{-1}. This value is two orders lower than Q_{OM} due to the second skimming stage.

The MB, laser beam path, and linear flight tubes lie on mutually orthogonal axes. The laser pulses pass through the spectrometer from right to left in Fig 3.16 by way of 1 inch diameter 3 mm thick Calcium Fluoride (CaF_2), Magnesium Fluoride (MgF_2), or UV fused silica (UVFS) windows. The three axes intersect at a common point inside the spectrometer ion optics called the ionization region (yellow ring in Fig 3.13). It is here that laser photolysis of the MB occurs and ionization products are directed toward MCP detectors for time-of-flight (TOF) measurements. A diagram of the ion optics is given in Fig 3.17 with the

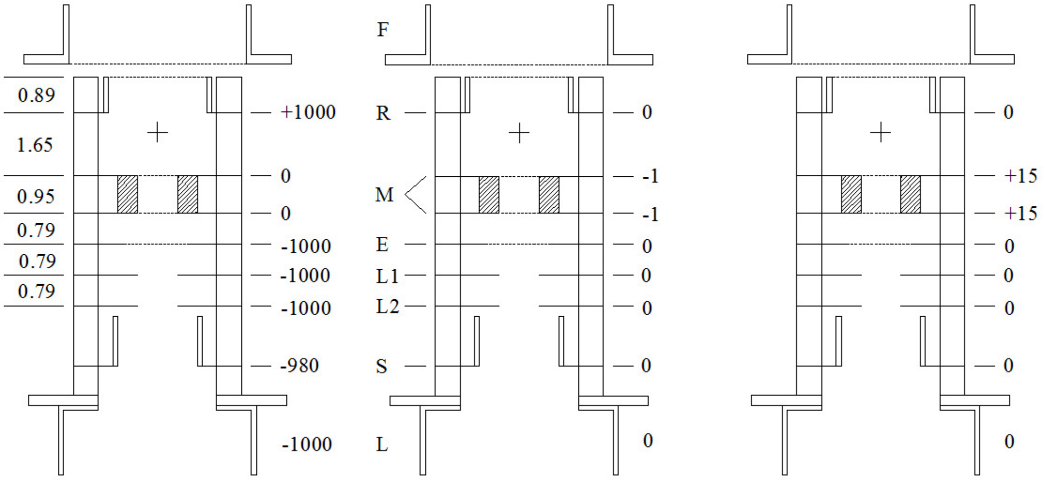

Figure 3.17: Schematic of ion optics stack. Dimensions are listed in cm at the far left. Important elements are labeled to the left of the center figure: F - electron flight tube; R - repeller; M - magnet; E - extractor; L1 - lens 1; L2 - lens 2; S - x, y steering; L - liner. Voltages applied for ion (left), electron (center), and H-atom (right) collection are given to the right of each figure.

ionization region marked by a cross. The ion optics stack (Fig 3.16 Panel 1) is comprised of several 4.5 cm square stainless steel electrodes which are electrically isolated by ceramic spacers (vertical white bars). Elements of the spectrometer are labeled in the center of Fig 3.17 where F - electron flight tube; R - repeller; M - magnet; E - extractor; L1 - lens 1; L2 - lens 2; S - x, y steering; L - liner.

The ion mass spectrometer design is based on the Wiley-McLaren [20] geometry, which is modified by inclusion of a permanent ring magnet (M). Typical ion collection voltages are given in the left side of Fig 3.17. Ions are accelerated downward (-$\vec{z}$) in two stages, 1) between R and M, and 2) between M and E, before entering the field-free flight tube. The magnet (M) and extractor (E) plates have steel meshes (dashed lines) at the center to allow ions to pass. Also, the repeller is a steel mesh that allows electrons and H-atoms to pass during magnetic bottle collection mode as described below. The liner (L) is a stainless steel tube that extends ~1 m to the ion detector. The liner and extractor (E) are set to the same voltage to create the field-free flight tube. The 25 mm diameter MCP ion detector entrance is held at -4.2 kV and a short (3 mm) acceleration occurs between the flight tube exit and the detector entrance. Secondary electrons created in the MCP are accelerated toward the grounded anode. The charge of a single ion is amplified within each MCP by a factor of at least 10^6. The amplified electrons reach the detector anode and produce a pulse of ~10 ns duration and ~-10 mV magnitude. Below the extraction grid lies two circular ion lenses (L1 and L2) and two steering plates (S). The ion lenses are generally set to the flight tube voltage and have no measurable effect on ion collection efficiency. The steering plates compensate for the molecular beam velocity in both x and y directions. The y steering plates lie parallel to the page and is omitted from Fig 3.17 for clarity; they are set to the liner voltage. The x-steering plates are charged within +50 V from the liner potential and are adjusted to optimize detection of high or low mass species as pertinent to each experiment.

Photoelectrons are collected and energy analyzed in a magnetic bottle spectrometer. The angular distribution of emitted electrons requires a wide angle collection mechanism in order to achieve appreciable signals. A collection efficiency of up to 50% has been achieved through similar magnetic bottle designs. [17, 18] One downside of using a magnetic bottle in many applications is the modest energy resolution of ~10 - 50 meV. [15, 19] However, resolution of this magnitude is not a limiting factor because our fs pulses have an energy bandwidth of ~100 meV; they are intended for high temporal resolution measurements instead of high energy resolution.

Our magnetic bottle design is based on the principles of Kruit and Read, [15] whereby a strong ring magnet (M) produces an inhomogeneous field used for steering electron trajectories into a solenoidal guiding field that carries them to the detector. Combination of the ring magnet and solenoid produces a bottle-shaped magnetic field that can be visualized as the green lines in Fig 3.13. The axially magnetized Samarium Cobalt (SmCo) cylindrical ring magnet is held between two steel grid electrodes within the ion optics. The SmCo ring produces a field strength of 0.5 T along the center axis. A maximum Lorentz turning force of up to 1 x 10^{-14} N can be experienced by 1 eV electrons emitted at the centerline with velocities normal to the axial field. As shown in the center of Fig 3.17, the magnet, all ion optics, and the electron flight tube (F) are held at ground potential to negate any electrostatic acceleration. In some applications, a small accelerating voltage (-1 V) is applied to the magnet electrodes to boost the electron collection efficiency. The effect of this acceleration is compensated for during the energy calibration procedure discussed below. Electrons are steered past the relepper grid an into the electron flight tube, which is comprised of a home-built solenoid surrounded by μ-metal magnetic shield. The aluminum solenoid is ∼75 cm long with I.D. = 2 inch. Approximately 1500 windings of Kapton insulated copper wire (green circles in Fig 3.13) run along the entire length and a magnetic field is produced by a 1 A current through the wire. Two secondary solenoidal loops of about 300 windings each are placed at the top and bottom of the solenoid for added control of electron flight paths. The solenoid field magnitude is relatively weak (∼0.01 T) and the μ-metal shield is required to block stray fields. Electrons follow a helical path around the solenoid field lines between the grounded electron flight tube entrance grid and the grounded MCP entrance. Secondary electrons created in the 40 mm diameter MCP are accelerated over +4.2 kV to the signal anode. The detector pulse is small in relation to the high voltage charge on the anode, and so must be isolated by capacitive coupling before signal processing and data collection.

H-atom KE measurements are also performed in the magnetic bottle with modification of the magnet voltage as shown in the right side of Fig 3.17. The Lorentz force on a 1 eV H-atom is at least an order of magnitude lower than the force on a 1 eV electron. The steering ability of the ring magnet and the guiding ability of the solenoid are therefore much weaker for H-atoms. An accelerating potential of ∼15 V is applied to the magnet electrodes to facilitate the collection of H-atoms near 1 eV emission energy. The work done by the electric field is compensated for during energy calibration and does not change the measured H-atom KE. The MCP entrance is held at -4.2 kV. A very short (3 mm) acceleration occurs between the grounded flight tube exit and the detector input. Secondary electrons created inside the MCP are accelerated from negative HV toward the grounded anode. Detector signals are measured from the grounded anode without capacitive coupling.

Data Acquisition and Analysis

In this section, details of detector signal processing and rendering of TOF spectra are discussed. Also, the data acquisition software and a typical time resolved measurement sequence are outlined. Finally, analysis of a general data set is presented and includes signal stability assessment, mass/energy conversion, timing calibration, and delay trace production.

All detector signals are sent through a Fisher Scientific M-6950 preamplifier. Photoelectron signals are obtained through capacitive coupling with the HV anode, whereas the photoion and H-atom signals are obtained from the anode without capacitive coupling. The 10x preamplifier gain is fixed and the baseline offset is set to zero. The fast response time (1 ns) of the preamplifier does not substantially distort the >10 ns wide detector pulses. The relatively inexpensive preamplifier also serves as a protection barrier between the detector and the data collection circuits. Following the preamplifier, pulses are fed into a FAST Comtech P7888-2 two-channel multiscaler card with integrated discriminator capable of 1 ns timing resolution and kHz acquisition rates. The multiscaler measures the time between a laser trigger and the detector pulse and constructs the TOF spectrum. A single TOF spectrum is taken as the sum over $\sim 1^3$ laser shots. Flight times of 1 μs, 10 μs, and 20 μs are typical for electrons, H-atoms, and ions, respectively. The laser trigger timing is offset from the actual arrival of the laser pulse at the ionization region and the creation of the ion. Therefore, the multiscaler does not directly measure the ion TOF, however the trigger/ionization timing offset is accounted for during calibration.

The multiscaler TOF readout is incorporated into a LabView based data acquisition program that controls the following time-resolved measurement sequence. First, the Newport model ILS-150-PP motorized delay stage is positioned to an appropriate pump-probe delay.

Second, a TOF spectrum is recorded as the average over a fixed number of laser shots. Third, the TOF spectrum is labeled by the pump-probe delay value and is saved/displayed by the scan program. Last, the delay position is changed and the entire sequence begins again until a TOF spectrum has been recorded at all predetermined delay positions. The program allows the Δt scan range, the Δt step size, and the laser shot averaging to be easily changed for each experiment. Additionally, the delay range can be traversed back and forth in several sweeps in order to eliminate signal instability due to slow long term drifts in laser power or molecular beam intensity. Each of the pump and probe beams creates time independent one-color ionization signal which must be subtracted for analysis of the 2-color dynamic signal. The scan program allows measurement of the pump-only and probe-only TOF spectra through the use of mechanical shutters, which block each beam independently. At each delay position a pump-probe spectra is recorded, followed by pump-only and then probe-only spectra. The one-color spectra are subtracted from the 2-color spectra during data analysis, as described below.

Raw data from a generic TRPES experiment are presented in Fig 3.18 to introduce some analysis methods that are used in TRPES, TRIY, and TR-TKER experiments throughout this thesis. The color contour plots represent the 2-D data obtained by the time and spectrally resolved measurement. Plots are presented with delay positions as the x-axis and TOF as the y-axis. The intensity scale in each plot goes from a blue minimum to a red maximum. The pump-probe, pump-only, probe-only, and 2-color spectra are shown from left to right. The 2-color plot is created by subtracting the pump-only and probe-only matrices directly from the pump-probe matrix. The pump-only and probe-only signal magnitudes are small compared to the 2-color signal. Still, slight differences are present between the pump-probe and the 2-color matrices. Six maxima, indicating the maximum ionization signal obtained when the pump and probe pulses are temporally synchronized ($\Delta t = 0$), are present in the 2-color matrix. This occurs once during each sweep, therefore the data in Fig 3.18 represents 6 sweeps of the Δt range. The sweep ranges are indicated (1 - 6) in the pump-probe matrix.

The 2-D raw data can be integrated over TOF to produce pump-probe delay traces, or it can be integrated over pump-probe delays to produce TOF spectra. Analysis of TOF spectra is discussed below. Delay traces can be used to assess the experiment stability. Integrating all TOF at each Δt yields the delay traces presented in the second row of Fig 3.18. Again, 6 sweeps are evident in the pump-probe and 2-color data and the delay step corresponding to Δt = 0 is marked in the pump-probe delay trace. The stability of the molecular beam intensity and laser power over the total measurement time (up to 12 hr. in some cases) is indicated by the Δt independent one-color signals. Intensity drifts that are approximately linear, as in Fig 3.18, are cancelled by the back-and-forth procedure of taking multiple sweeps. The data in Fig 3.18 is considered stable over all six sweeps. During data processing, it is possible to delete sweeps that do not fit the stability requirement and to analyze the remaining data.

A similar stability assessment procedure is performed for TRIY, TRPES, and TR-TKER measurements. The raw data is then converted from TOF to mass (TRIY) or energy (TRPES and TR-TKER) spectra. Analysis of each measurement type in relation to specific molecular photophysics is left for Chapters 4 - 6. Here, the conversion of TOF measurements into energy or mass spectra is discussed.

The photoelectron/H-atom TOF is determined by the velocity it obtains during ionization/dissociation. The KE of an emitted photoelectron/H-atom can be written as

$$\mathrm{KE} = \mathrm{E}_t - \mathrm{E}_\circ = 1/2\ \mathrm{m}\ \mathrm{v}^2 - \mathrm{E}_\circ,$$

where E_t is the measured total KE and $\mathrm{E}_\circ$ is the KE due to the molecular beam velocity and any stray fields in the spectrometer. The projectile velocity is simply d/TOF where d is the flight tube distance. The KE equation can then be rewritten as

$$\mathrm{KE} = \frac{md^2}{2(TOF-t_\circ)^2} - \mathrm{E}_\circ = \frac{IR}{(TOF-t_\circ)^2} - \mathrm{E}_\circ,$$

where $\mathrm{t}_\circ$ is the offset between the fast board trigger and the photoionization event, and the term (TOF - $\mathrm{t}_\circ$) is the actual photoelectron flight time. The term IR = m d^2 / 2 is an experimental constant called the instrument response. This equation is used to convert

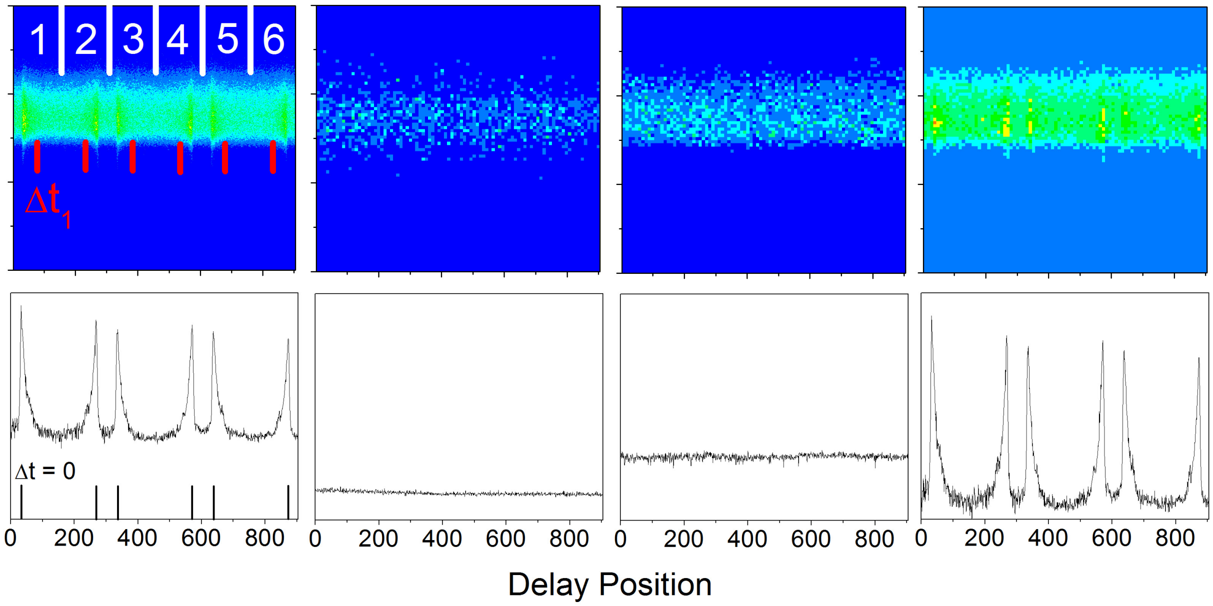

Figure 3.18: Example of raw data and stability assessment. Color contour plots are given in the top row and integrated delay traces in the bottom row. The pump-probe, pump-only, probe-only, and 2-color data are given from left to right.

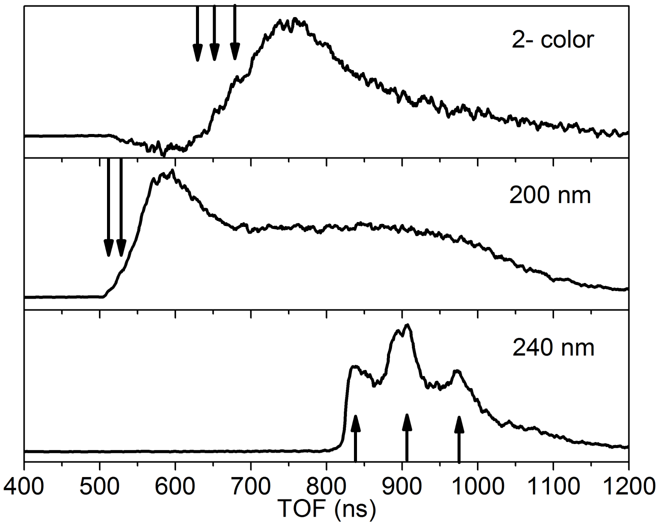

Figure 3.19: Photoelectron TOF to energy calibration scan of 1, 3 butadiene. 2-color (200 + 240 nm) (a), 200 nm (b), and 240 nm (c) ionization signals are shown separately.

TOF into energy spectra. Peaks in the calibration TOF spectrum are assigned to their known KE, and the resulting data is fit with the function above and the constants IR, t○, and $E_\circ$ are extracted. The constants are then used to convert each TOF to KE. Known KE values are obtained by different methods for the photoelectron and H-atom scans. During photoelectron energy calibration, peaks arising from ionization of 1, 3 butadiene (BD) [21] and nitric oxide (NO) [22] are assigned to published ionic vibrational energies. An example BD TOF spectrum is shown in Fig 3.19 with indication of each of the calibration peaks. Peaks with short TOF are difficult to distinguish because the TOF to KE conversion is quadratic in TOF. Therefore, the spacing between adjacent peaks decreases quadratically as the TOF decreases.

As discussed previously, H-atoms are emitted with KE ranging from zero up to a maximum of $E(h\nu_{pump})$ - $D_\circ$. The H-atom collection efficiency is boosted by an accelerating voltage (~15 V) applied between the magnet and the electron flight tube entrance. Therefore, H-atoms with zero dissociation energy enter the flight tube with KE due to the accelerating potential. The accelerating voltage is varied and the zero KE H-atom TOF is measured in order to produce TOF vs. energy data, which is then fit by the above equation. Again, the constants IR, $t_\circ$, and $E_\circ$ are extracted and are used to convert the TOF into H-atom KE spectra.

Ion mass spectra are obtained with the use of electrostatic acceleration instead of magnetic collection. Therefore the TOF to mass conversion proceeds differently than the TOF to energy conversion. Again, the TOF is determined by the velocity of each ion, but here the velocity is due to the accelerating potential instead of the emission energy. The ion KE can be written as

$$\mathrm{KE} = \mathrm{q\ V} = 1/2\ \mathrm{m\ v}^2,$$

where q is the ion charge and V is the accelerating potential. Substituting v = d/(TOF - $t_\circ$) and solving for m gives

$$\mathrm{m} = \frac{2qV(TOF-t_\circ)^2}{d^2} = \mathrm{IR}\ (TOF-t_\circ)^2,$$

where, $t_\circ$ is the trigger offset and IR = $(2qV/d)^2$ is the instrument response constant. Calibration mass vs. TOF data points are obtained from BD and NO as well as the parent of the molecule under study; the constants $t_\circ$ and IR are obtained from fits to this data. TOF spectra are then converted to mass spectra using the extracted constants.

In order to analyze population dynamics as a function of Δt, the raw data matrices must be collapsed into a single sweep of the Δt range. All TOF spectra recorded at a given Δt are added together during the collapse process, and a matrix representing a single sweep is produced as shown in Fig 3.20. In this example, the six spectra at Δt_1 in Fig 3.18 are collapsed into one spectrum in Fig 3.20. Here, the TOF spectrum had been converted into electron energy. Again, integrating all energies at each pump-probe delay produces a delay trace; however, this method neglects the rich spectroscopic information contained in the TRPES measurement. Instead, multiple delay traces can be produced by integrating small regions of the energy spectrum. Three such regions (D1, D2, and D3) are labeled in the contour plot of Fig 3.20, with the corresponding delay trace given at right. The x-axis is

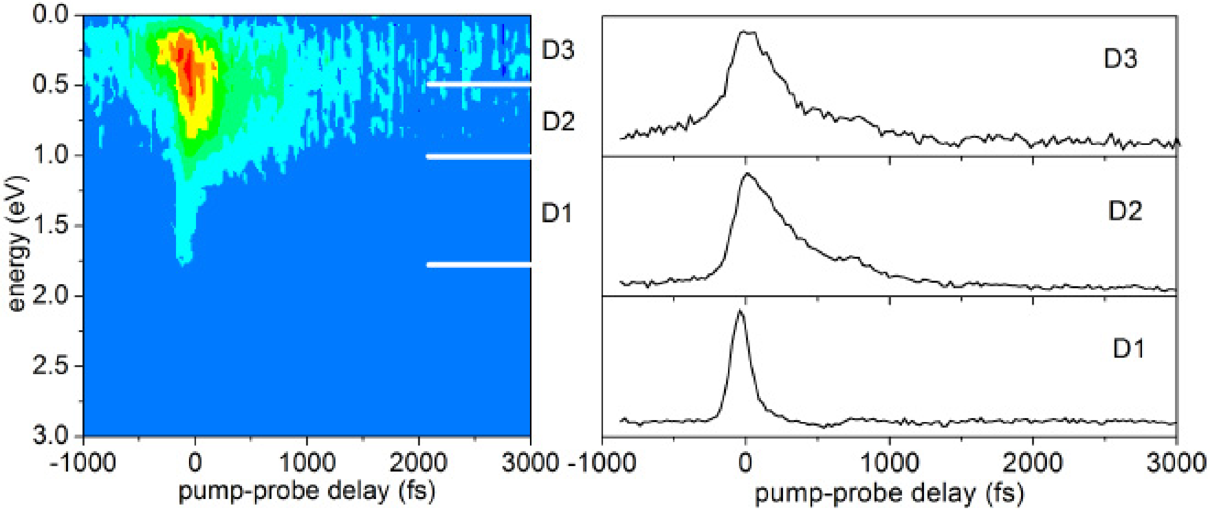

Figure 3.20: Example of collapsed photoelectron spectrum and associated delay traces. The delay traces are produced from the intervals indicated in the contour plot and reveal different dynamics for each energy region.

scaled by a value obtained from timing calibration scans, and the maximum intensity occurs near $\Delta t = 0$. Integration regions are selected differently for each experimental technique, and correspond to photoelectron energy (TRPES), ion mass (TRIY), or H-atom KE (TR-TKER). In this example, the integration regions can be associated with specific electronic states, and each delay trace reveals state dependent population dynamics. Here, three electronic excites states may be identified in Fig 3.18, and the corresponding delay traces reveal very different dynamics for each state, whereby the excited state lifetimes increase in the order D1 <D3 <D2. It is this simultaneous usage of spectroscopic and dynamic analysis that reveals the true power of time-resolved spectroscopy. The ammonia TRPES, TRIY, and TR-TKER experiments in Chapters 4 - 5 are analyzed by this method of producing delay traces for specific regions of the calibrated TOF spectrum.

The adenine TRPES data in Chapter 6 is analyzed by a 2-D global fitting routine, whereby the spectral and dynamic information is extracted simultaneously.

The 2-D matrix is fit with the equation

$$\mathrm{S(E,\ t)} = \sum_i I_i(E)[P_i(t) \bigotimes g(t)],$$

in a Levenberg-Marquardt optimization procedure. Here, S(E, t) is the energy, E, and time, t, dependent fit function. I_i(E) is the shape of the energy spectra of the ith channel, P_i(t) is the population of the ith channel at each pump-probe delay, t, and g(t) is the Gaussian instrument response function. The term in brackets gives the convoluted amplitude of each channel as a function of pump-probe delay. A global fit result example is given in Fig 3.21. Energy spectra are shown in the bottom panel and pump-probe delay traces are shown in the left panel. Three seperate spectral channels, I_i(E), are extracted and are shown as blue, wine, and olive lines in the bottom panel. The red line is the total fit. Pump-probe delay traces corresponding to each spectral channel are shown in the left panel. Inspection of the energy spectra shows one broad (blue) and one relatively narrow (wine) channel. The remaining channel (green) has very small overall magnitude. The 2-D matrix shows a broad feature that is limited to pump-probe delay times near Δt = 0 and a narrow channel that extends to longer times. The pump-probe traces of the broad and narrow energy spectra exhibit the same Δt dependence. Electronic excited states can be identified from the spectral information and corresponding lifetimes can be obtained from the dynamic information. Note that the global fitting routine has a large number of free parameters. Fits must be constrained by input of starting parameter values and, in some cases, by fixing several parameters. Choices of starting values and fixed parameters are determined by specific photophysical arguments as described in Chapter 6.

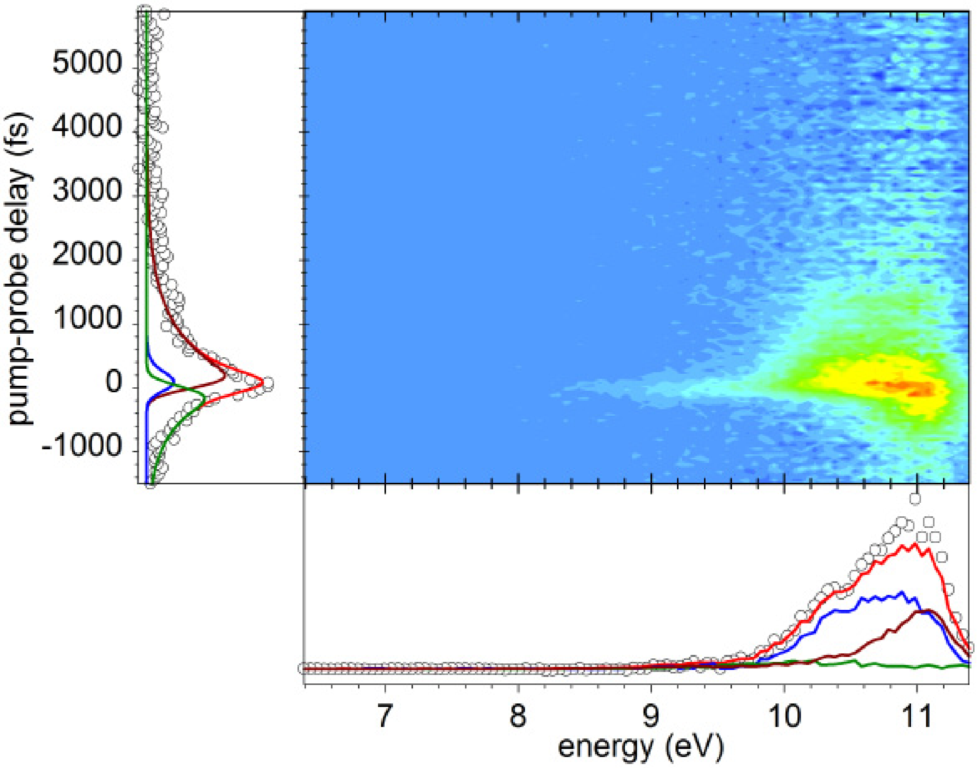

Figure 3.21: Example of global fitting of photoelectron data. Spectral (bottom) and dynamic (left) information is extracted simultaneously from the 2-D matrix (center). Three channels are represented by blue, wine, and green lines in both plots. Red is the total fit.

Surface Scattering Machine at the University of Hawaii

A separate set of experiments was conducted using the surface scattering machine [23, 24] at the University of Hawaii in collaboration with the NASA astrobiology institute. The purpose of these experiments was to investigate the survivability of adenine under interstellar radiation fields. The results were published in the Astrophysical Journal [25] and are included in Chapter 7. Details of the experimental setup and the design and construction of a high-temperature sublimation source are given here.

A diagram of the surface scattering machine is given in Fig 3.22. The apparatus consists of an ultra-high vacuum chamber with a liquid He refrigerated cold finger (black) and polished silver wafer (grey) at the center, two deposition arms mounted on linear translation stages (LTS), a Fourier transform infrared spectrometer (FTIR) and detector (DET), and a 5 keV electron source (SPECS). To simulate interstellar environments the vacuum chamber is baked out to pressures of 1 x 10^{-11} Torr and the cold finger is held at 10 K. The experiment is conducted in two phases, the condensation phase followed by the irradiation phase. During condensation, the adenine sample is sublimated at temperatures of $\sim$200 °C and the resulting vapor condenses onto the silver wafer where a thin ice is created. After condensation, the cold finger and silver wafer are rotated to face the electron source. This orientation also allows the infrared beam from the FTIR to reflect off the silver wafer and reach the detector. The makeup of the condensed ice is probed by the FTIR before and during irradiation from the 1 μA 5 keV electron source. The ice is irradiated for several hours during a single experiment. The FTIR measurements allow the degradation rate of adenine to be measured and for new products to be identified. Analysis of the FTIR data allows interstellar destruction rates to be calculated and decomposition reaction mechanisms to be proposed.

The surface scattering machine is a well established experiment operating at the University of Hawaii (see [23, 24] for example). The machine was modified by inclusion of the sublimation source during these experiments. Design and construction of the sublimation source

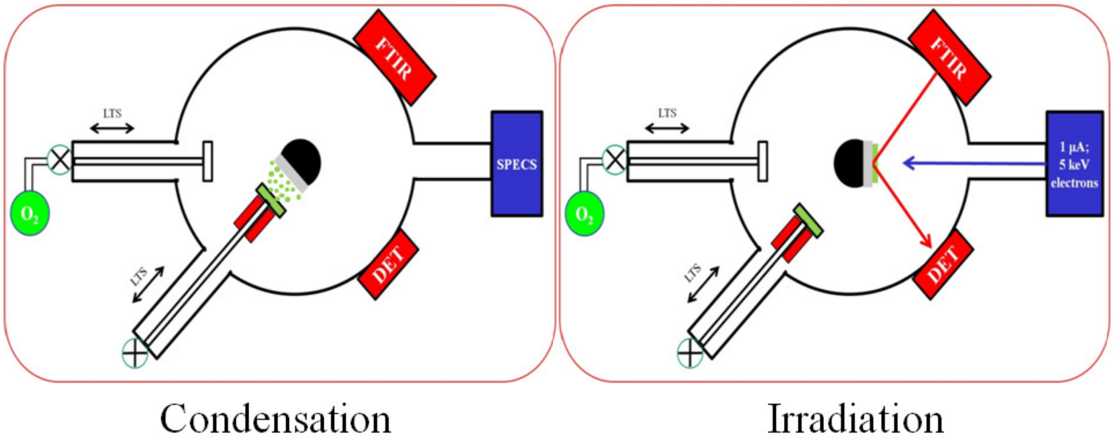

Figure 3.22: Diagram of the surface scattering machine. Condensation phase (left) and irradiation phase (right) are shown. Adenine vapor (green) condenses onto a silver wafer (grey) mounted on the cold finger (black) that is held at 10 K by recirculated liquid He. The resulting adenine ice is rotated toward the electron source (SPECS). The ice composition is monitired by FTIR during irradiation by 5 keV electrons.

was a major element in this experimental investigation. Important design considerations include: 1) mm precision position control, 2) 50 W power delivery, and 3) temperature measurement and control. All of these elements must be contained on a stand-alone ultra-high vacuum compatible platform that adapts easily to the original surface scattering machine. A picture of the completed sublimation source is given if Fig 3.23. The basic construction consists of three ConFlat (CF) vacuum flanges, a Tee piece with electric feedthroughs (EFT), a bellows style linear translation stage (LTS) and a CF coupler (C). The coupling is mounted directly to the surface scattering machine. Orientation of the sublimation arm within the machine can be seen in Fig 3.22. Adenine powder is held inside the sample holder (SH). A resistive heater is placed within the large copper band (BH) and a silicon diode temperature sensor (TS) is placed on the copper surface. The band heater and sample holder are slowly heated to ∼ 200 °C to create a large vapor pressure. The linear translation stage positions the sample holder within 3 mm of the refrigerated silver wafer deposition site. Adenine vapor condenses on the cold wafer over a 2 hr. heat/cool cycle. The sample holder is displaced from the cold finger before the silver wafer is rotated to face the irradiation source and the FTIR spectrometer.

The ice composition is probed by an FTIR spectrometer. The infrared beam passes through the sample, is reflected off the silver wafer, and passes the sample again before entering the detector. Adenine is identified through the measured absorption features that are compared to previous reports of adenine matrix isolation studies. [16] The original ice thickness is calculated from a modified Beer-Lambert law. [23] The ice is irradiated with 1 μA of 5 keV electrons for 3 hrs. as a simulation of the charged particle component of the galactic cosmic radiation (GCR) field. The FTIR operates continuously during irradiation and measures the degradation rate caused by the electron bombardment. Detailed analysis of the FTIR spectra in regard to calculating destruction rates is left for Chapter 7. Briefly, the FTIR absorption decreases due to adenine decomposition during irradiation. Decomposition rates are extracted and are used to calculate electron/adenine collision cross sections. These cross sections are scaled to account for the proton component of the GCR. Adenine lifetimes are calculated for specific astronomical environments from the scaled cross sections and the known proton flux in each environment.

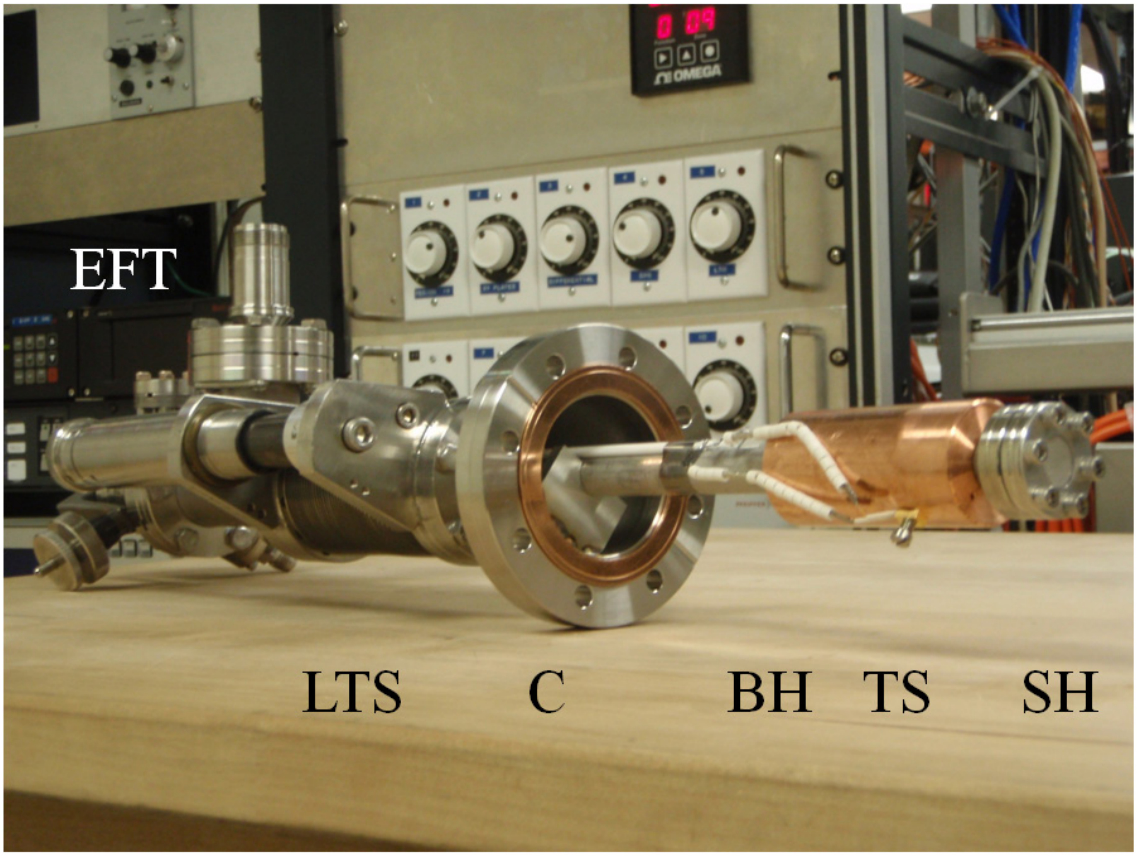

Figure 3.23: Picture of the adenine sublimation source. EFT - electric feedthrough; LTS - linear translation stage; C - CF coupling flange; BH - copper band heater; TS - silicon diode temperature sensor; SH - adenine sample holder.

3.3 REFERENCES

[1] H. Yu, N. L. Evans, V. G. Stavros and S. Ullrich 2012, Phys. Chem. Chem. Phys., 14, 6266.

[2] C. A. Williams, G. M. Roberts, H. Yu, N. L. Evans, S. Ullrich and V. G. Stavros 2012, J. Phys. Chem., 116, 2600.

[3] N. L. Evans, H. Yu, G. M. Roberts, V. G. Stavros and S. Ullrich 2012, Phys. Chem. Chem. Phys., 14, 10401.

[4] M. Seel and W. J. Domcke 1991, Chem. Phys., 95, 7806.

[5] M. Seel and W. J. Domcke 1991, Chem. Phys., 151, 59.

[6] J. Franck 1926, Transactions of the Faraday Society, 21, 536.

[7] E. Condon 1926, Physical Review, 28, 1182.

[8] R. L. Fork, B. I. Greene and C. V. Shank 1981, Appl. Phys. Lett., 38, 671.

[9] W. Sibbett, A. A. Lagatsky and C. T. A. Brown 2012, Optics Express, 20, 6989.

[10] D. E. Spence, P. N. Kean and W. Sibbett 1991, Opt. Lett., 16, 42.

[11] P. F. Moulton 1986, J. Opt. Soc. Am. B, 3.

[12] R. Trebino 2000, Frequency Resolved Optical gating: the Measurement of Ultrashort Laser Pulses, Kluwer Academic Publishers:Norwell, MA.

[13] H. Stark ed., 1987, Image Recovery: Theory and Application, Academic press:Orlando.

[14] D. P. Glavin, M. Schubert and J. L. Bada 2002, Anal. Chem., 74, 6408.

[15] H. W. Jochims, M. Schwell, H. Baumgartel and S. Leach 2005, Chem. Phys., 314, 263.

[16] M. J. Nowak, L. Lapinski, J. S. Kwiatkowski, and J. Leszczynski 1996, J. Phys. Chem., 100, 3527.

[17] P. Kruit, F. H. Read 1983, J. Phys. E: Sci. Instrum., 16, 313.

[18] T. Tsuboi, E. Y. Xu, Y. K. Bae and K. T. Gillen 1988, Rev. Sci. Instrum. 59, 1357.

[19] O. Cheshnovsky, S. H. Yang, C. L. Pettiette, M. J. Craycraft, and R. E. Smalley 1987, Rev. Sci. Instrum., 58, 2131.

[20] W. C. Wiley and I. H. McLaren, 1955, Rev. Sci. Instr., 26, 1150.

[21] J. D. H. Eland, Int. J. Mass Spectrom. Ion Phys.,1969, 2, 471.

[22] J. C. Miller and R. N. Compton 1981, J. Chem. Phys., 1, 22.

[23] C. J. Bennett, C. S., Jameison, A. M., Mebel and R. I. Kaiser 2004, Phys. Chem. Chem. Phys., 6, 735.

[24] C. S. Jamieson, A. M. Mebel and R. I. Kaiser 2006, ApJSS, 163, 184.

[25] N. L. Evans, C. J. Bennett, S. Ullrich and R. I. Kaiser 2011, ApJ, 730, 69.

CHAPTER 4

OBSERVATION OF ULTRAFAST NH_3 ($\tilde{A}$) STATE RELAXATION DYNAMICS USING A COMBINATION OF TIME-RESOLVED SPECTROSCOPY AND PHOTOPRODUCT DETECTION [1]

---

[1] N. L. Evans, H. Yu, G. M. Roberts, V. G. Stavros and S. Ullrich 2012, *Physical Chemistry Chemical Physics*, **14**, 10401.

Reprinted here with permission of the publisher.

4.1 ABSTRACT

The ultrafast excited state relaxation of ammonia is investigated by resonantly exciting specific vibrational modes of the electronically excited NH_3 ($\tilde{A}$) state using three complementary femtosecond (fs) pump-probe techniques: time-resolved photoelectron, ion-yield and photofragment translational spectroscopy. Ammonia can be seen as a prototypical system for studying non-adiabatic dynamics and therefore offers a benchmark species for demonstrating the advantages of combining the aforementioned techniques to probe excited state dynamics, whilst simultaneously illuminating new aspects of ammonias photochemistry. Time-resolved photoelectron spectroscopy (TRPES) provides direct spectroscopic evidence of σ^* mediated relaxation of the NH_3 ($\tilde{A}$) state which manifests itself as coupling of the umbrella (ν_2) and symmetric N - H stretch (ν_1) modes in the photoelectron spectra. Time-resolved ion yield (TRIY) and time-resolved photofragment translation spectroscopy (TRPTS) grant a measure of the dissociation dynamics through analysis of the H and NH_2 photodissociation co-fragments. Initial vibrational level dependent TRIY measurements reveal photoproduct formation times of between 190 and 230 fs. Measurement of H-atom photoproduct kinetic energies enables investigation into the competition between adiabatic and non-adiabatic dissociation channels at the NH_3 ($\tilde{A}$)/NH_3 ($\tilde{X}$) conical intersection and has shown that upon non-adiabatic dissociation into NH_2 ($\tilde{X}$) + H, the NH_2 ($\tilde{X}$) fragment is predominantly generated with significant fractions of internal vibrational energy.

4.2 INTRODUCTION

Over the years the excited state dynamics of ammonia have received considerable attention and have come to be regarded as a prototypical system in which non-adiabatic photochemistry can be studied. [1, 2] We aim to utilize ammonia as a simple model species in which to study σ^* mediated relaxation following excitation to its first electronically excited state. As put forth in the theoretical work of Sobolewski and Domcke, [3, 4] electronic excited states with notable σ^* character, centered at X - H bonds (where X = O or N), have been postulated to play an important role in efficient photoprotection of organic molecules. In general, $\pi/\mathrm{n}\sigma^*$ states are characterized by promotion of a π-type or n-type electron into a σ^* orbital and are repulsive along the X - H coordinate. At extended X - H bond lengths, a conical intersection (CI) is formed with the ground state, $S_\circ$, providing an efficient pathway for deactivation. σ^* mediated relaxation is seemingly ubiquitous in heteroaromatic molecules, including phenols, azoles, amines, N-heterocycles, and nitriles, [5, 6] and as such, obtaining direct spectroscopic evidence of $\pi/\mathrm{n}\sigma^*$ states and measuring associated timescales is of fundamental importance.

The neutral ground state of ammonia (NH_3 ($\tilde{X}$)) has a pyramidal equilibrium geometry (C_{3v} point group) and possesses ${}^1A_1'$ symmetry. The first excited electronic state (NH_3 ($\tilde{A}$)) is a ${}^1\mathrm{n}(3\mathrm{s}/\sigma^*)$ state with ${}^1A_2''$ symmetry and is populated by promotion of an electron from the nitrogen lone pair orbital $1a_2''$ into nitrogen centered Rydberg (3s) orbital in the vertical Franck-Condon (vFC) region, which then evolves into σ^* anti-bonding character upon elongation of an N-H bond; henceforth, termed a ${}^1\mathrm{n}\sigma^*$ state or simply, NH_3 ($\tilde{A}$). Additionally, the ${}^1\mathrm{n}\sigma^*$ manifold has a planar equilibrium geometry (D_{3h} symmetry). Upon NH_3 ($\tilde{A}$) excitation, the pyramidal to planar shift in equilibrium geometry is manifested in the UV band (170 - 215 nm) of ammonia's absorption spectrum as a long progression in the out-of-plane bend (umbrella) mode, ν_2'. [7-9] The NH_3 ($\tilde{A}$) absorption bands show no rotational fine structure and analysis of vibrational lineshapes has shown that dissociation of the $\nu_2' = 0$ - 6 levels occurs within 100 femtoseconds (fs). [7, 10]

A detailed model of NH_3 ($\tilde{A}$) dissociation has followed from various experimental techniques including laser induced fluorescence (LIF), [11-13] resonance enhanced multi-photon ionization photoelectron spectroscopy (REMPI-PES), [14] and H-atom photofragment translation spectroscopy (PTS). [15-19] The NH_3 ($\tilde{A}$) and NH_3 ($\tilde{X}$) potential energy surfaces have been calculated as a function of the out-of-plane bending angle, θ, and the H_2N-H bond distance, R_{N-H}. [15, 20] A schematic of a one-dimensional (1-D) cut through these electronic state surfaces at $\theta = 0°$ is presented in Fig 4.1. The NH_3 ($\tilde{A}$) state origin lies 5.73 eV above the NH_3 ($\tilde{X}$) minimum, [21,22] and is repulsive along the R_{N-H} coordinate (due to the increasing σ^* character) but has a small energetic barrier (0.3 0.4 eV) [23, 24] to N-H bond fission between the vFC excitation region and the diabatic dissociation asymptote. At elongated R_{N-H}, a NH_3 ($\tilde{A}$)/NH_3 ($\tilde{X}$) conical intersection (labeled CI1 in Fig 4.1) is present and provides a route back to NH_3 ($\tilde{X}$). Potentially, three relaxation pathways are in competition after NH_3 ($\tilde{A}$) excitation, as identified by the dotted grey arrows in Fig 4.1. Pathways 1 and 2 involve non-adiabatic crossing through CI1 at planar geometries ($\theta = 0°$). Path 1 results in (re)population of a vibrationally hot NH_3 ($\tilde{X}$) state, while path 2 correlates non-adiabatically with an amino radical (NH_2) in its electronic ground state, NH_2 ($\tilde{X}$), and a ground state H (^{2}S) photoproduct. Alternatively, path 3 involves adiabatic dissociation along the NH_3 ($\tilde{A}$ surface (at non-planar geometries) by avoiding non-adiabatic (vibronic) coupling at CI1 and produces an excited state amino radical, NH_2 ($\tilde{A}$), and H (^{2}S). NH_3 ($\tilde{A}$) dissociation (paths 2 and 3) is extremely efficient. In fact, vibronic absorption band contour analysis [10, 11, 25] and microwave-UV double resonance [26] experiments have set the NH_3 ($\tilde{A}$) dissociation time to be as short as 35 fs.

The NH_3 ($\tilde{A}$) potential energy barrier cannot be overcome for $\nu_2' < 2$ states. Measurement of high kinetic energy (KE) H-atoms after $\nu_2' = 0$ and 1 excitation lead Biesner et al. [15] to conclude that predissociation of these states occurs by tunneling through the barrier and leaves the NH_3 ($\tilde{X}$) fragment with very little internal (vibrational) energy. The NH_2 photofragment carries increasing amounts of vibrational energy as the initial excitation

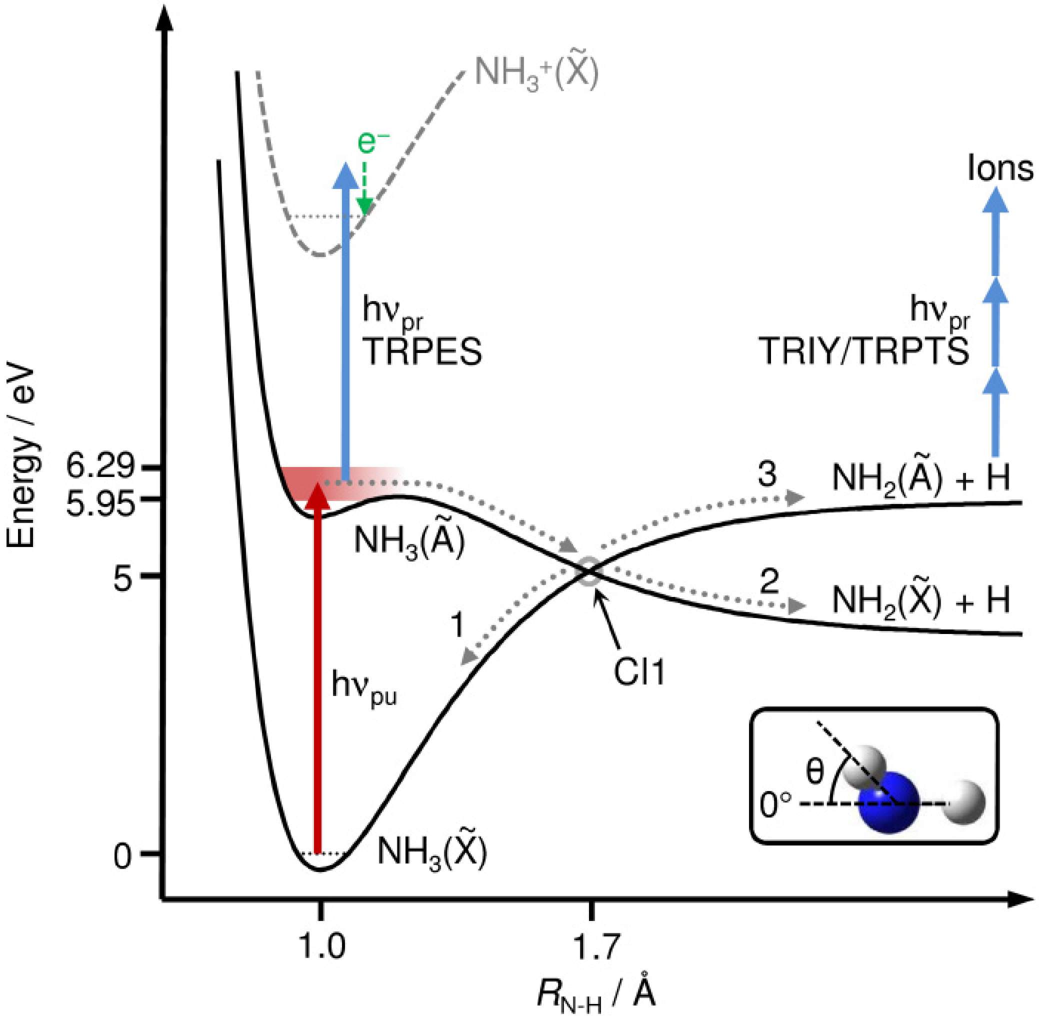

Figure 4.1: Schematic of a 1-D cut (at $\theta = 0°$, as defined on the molecular structure inset) through the multi-dimensional potential energy surfaces of the ground, NH_3 $(\tilde{X})$, and first excited, NH_3 $(\tilde{A})$, electronic states of ammonia, as a function of the H_2N-H coordinate, R_{N-H}. At R_{N-H} ~1.7 Å, a conical intersection between the NH_3 $(\tilde{A})$/NH_3 $(\tilde{X})$ states is formed (labeled CI1). Three relaxation paths are indicated by dotted arrows (labeled 1, 2 and 3), and details are given in the main text. The excitation range used in the experiments is indicated by the red shaded region, and is performed using fs pump pulses, $h\nu_{pu}$. Dynamics are monitored with time-delayed fs probe pulses, $h\nu_{pr}$, of varying energies (see main text for details) using either TRPES, TRIY or TRPTS techniques. Also shown is a schematic potential profile for the ground electronic state of the ammonia cation, NH_3^+ $(\tilde{X})$. NH_3 $(\tilde{A})$ ionization into NH_3^+ $(\tilde{X})$ in TRPES measurements yields ammonia cations in coincidence with photoelectrons, e$^-$, with defined kinetic energies.

energy increases. [16] The energetic threshold for the adiabatic dissociation channel (path 3, Fig 4.1), yielding NH_2 ($\tilde{A}$), is 6.02 eV. NH_2 ($\tilde{X}$) is the dominant photoproduct at low excitation energies ($<$ 6 eV; $\nu_2' < 3$). However, at higher excitation energies, current knowledge regarding the percentage of NH_3 ($\tilde{A}$) dissociation evolving into the NH_2 ($\tilde{A}$) + H channel is ambiguous. Reported values for NH_2 ($\tilde{A}$) yield after NH_3 ($\tilde{A}$) $\nu_2' = 6$ excitation (6.4 eV) vary from 2.5% [12] to 30%. [16] Crim and co-workers have demonstrated that the NH_2 ($\tilde{A}$) yield can be controlled by vibrational (pre)excitation of NH_3 ($\tilde{X}$), whereby population of the symmetric N-H stretch mode increases the NH_2 ($\tilde{A}$) formation and population of the anti-symmetric N-H stretch mode reduces the NH_2 ($\tilde{A}$) yield. [27, 28]

Although high resolution experiments, such as those discussed above, can provide intimate details regarding the excited state N-H bond fission process in NH_3, dissociation lifetimes remain difficult to determine accurately by these methods. Direct measurement of ammonia excited state lifetimes, via fs pump-probe spectroscopy, has been employed less widely. Time-resolved ion yield (TRIY) [29] and time-resolved photoelectron spectroscopy (TRPES) [30] studies of the high-lying NH_3 ($\tilde{E}$) state have reported a bi-exponential population decay with lifetimes of 1 ps and 60 fs, assigned to NH_3 ($\tilde{E}$)/NH_3 ($\tilde{A}$) and NH_3 ($\tilde{A}$)/NH_3 ($\tilde{X}$) transfer, respectively. More recently, the time-resolved velocity map ion imaging (TR-VMI) work by Wells et al. [19] has measured the H-atom KE distribution and emission timescales after NH_3 ($\tilde{A}$) $\nu_2' = 4$ excitation. These authors report a wide range of H-atom elimination timescales (50 - 250 fs) which increase with the portion of internal vibrational energy imparted to the NH_2 fragment.

In this work, we present new detailed studies of the photophysics of NH_3 following broadband excitation to the NH_3 ($\tilde{A}$) state, using a combination of TRPES, TRIY, and time-resolved photofragment translation spectroscopy (TRPTS) methodologies. Specifically, dynamics from the photoexcited NH_3 ($\tilde{A}$) $\nu_2' = 2$ - 5 levels have been studied to show the influence of the initially prepared vibronic energy level on the product formation timescales and energy disposal. We demonstrate how the combination of these three techniques allows a comprehensive picture of the excited state dynamics of NH_3 to be constructed and provides a direct measurement of the lifetimes for these processes.

4.3 EXPERIMENT

The experimental set up has been described in detail elsewhere. [31 - 33] It consists of a linear time-of-flight (TOF) mass spectrometer, a magnetic bottle energy spectrometer, and a fs laser system with UV conversion capabilities.

The TOF mass spectrometer consists of a typical Wiley-McLaren [34] configuration with ion repeller, extraction and acceleration grids, and field-free flight tube. The ion optics are modified to accommodate a permanent ring magnet, which is utilized by the magnetic bottle spectrometer, between two grounded extraction grids. Ions are extracted through the center of the ring magnet by applying a positive high voltage to the ion repeller and their flight time to the microchannel plate (MCP) detector is measured. Photoion TOF to mass conversion is performed through calibration scans with 1,3- butadiene (BD) and nitric oxide (NO).

Our magnetic bottle design follows the basic principles described by Kruit and Read [35] and is used for both photoelectron and H-atom KE measurements. A strong inhomogeneous magnetic field turns charged particle trajectories into a relatively weak solenoidal field which guides them through an electrostatic field-free flight tube to the detector. In TR-PES measurements, photoelectron flight times are measured and converted to photoelectron kinetic energies using well known transitions in BD and NO calibration gases. Subtracting the photoelectron kinetic energies from the total 2-color photon energy provides the electron binding energies. For use in TRPTS studies, a repelling potential of +12 V is applied to the extraction grids surrounding the ring magnet in order to boost the collection efficiency for photoionized H-atoms. H^+-ions will then carry energy imparted by the accelerating field and any KE obtained during dissociation. Conversion of TOF spectra into KE spectra is performed by varying the electrostatic potential and monitoring the TOF of the slowest H^+-ion detection. The slowest H^+-ions are assumed to have no KE from dissociation and their

TOF is assigned as the electrostatic energy alone. Calibration yields an energy spectrum containing both electrostatic and dissociation energy. We take the electrostatic energy as constant for all H^+-ions and directly subtract it to produce spectra of the dissociation energy only.

A 50 : 50 NH_3/He mixture (Airgas) is held at ∼200 Torr backing pressure behind a 200 μm diameter stainless steel pinhole. A continuous beam is formed by free expansion from the pinhole and is doubly skimmed before entering the ionization region of the spectrometer.

The optical layout is based on a commercially available fs oscillator/amplifier system (Coherent Inc., Mira 900 and Legend Elite HE). The amplifier output (1 kHz, 800 nm, 130 fs, 3.5 mJ/pulse) is split to produce two pulses at UV wavelengths that are aligned collinearly and focused onto the molecular beam (f = 50 cm). The relative timing between the two pulses is scanned with a motorized optical delay line and typical cross-correlations (IRF) of 230 fs are determined from BD and NO measurements.

Pump wavelengths, matching transitions to ν_2' levels in the NH_3 ($\tilde{A}$) state, are generated by tuning the oscillator/amplifier fundamental which is subsequently frequency converted in a BBO crystal based fourth harmonic set up. Pump pulses of typically 0.5 μJ/pulse promote excitation to the $\nu_2' = 2$ (208.5 nm; 5.95 eV), 3 (204.6 nm; 6.06 eV), 4 (200.8; 6.17 eV), and 5 (197.1; 6.29 eV) levels of NH_3 ($\tilde{A}$) as indicated by the vertical red arrow, labeled $h\nu_{pu}$, and the shaded red region in Fig 4.1 (also see Fig 4.2a). Identical pump pulses are used in TRPES, TRIY, and TRPTS experiments but probe pulses are specific to each detection method. Probe pulses at 240.2 and 243.1 nm are produced by optical parametric amplification (TOPAS-C).

In TRPES experiments, NH_3 ($\tilde{A}$) is probed using 240.2 nm (5.16 eV). This wavelength was selected such that (i) 1-photon absorption is non-resonant with NH_3 and NH_2 excited states, and (ii) the total $(1 + 1')$ photon energy is high enough above the vertical ionization potential (IP) of NH_3 (10.18 eV) to display a vibrational progression in the final cationic state, NH_3^+ ($\tilde{X}$). The total $(1 + 1')$ photon energy corresponds to the height of the arrows in

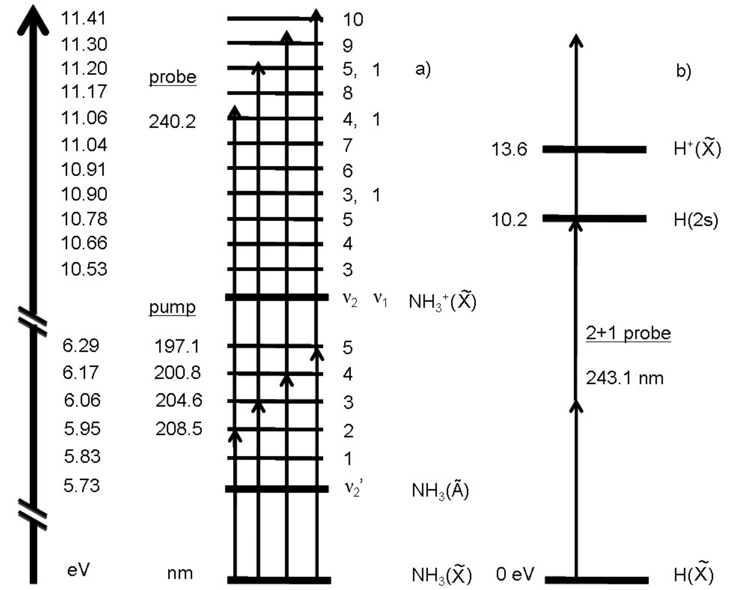

Figure 4.2: Pump-probe scheme for TRPES (a), TRIY (a, b), and TRPTS (a, b) experiments. Vertical arrows represent absorption of pump and probe photons. In TRPES (a), vibrational levels of NH_3 ($\tilde{A}$) are probed through ionization by 240.2 nm, and resulting photoelectrons are assigned to vibrational levels of NH_3^+ ($\tilde{X}$). In TRIY and TRPTS (b), photodissociated H-atoms are probed through (2 + 1) REMPI using 243.1 nm.

Fig 4.2a. Pump powers are kept low (∼3 μJ/pulse) as to avoid any 2-photon resonances with high-lying Rydberg states. Preferential 1-photon absorption of the pump is evidenced by the fact that no photoelectrons are detected during probe only photolysis or from multi-photon ionization (i.e. $(1 + 2')$ or $(1 + 3')$, instead of $(1 + 1')$).

In TRIY and TRPTS experiments, H-atoms from σ^* mediated dissociation are probed by (2 + 1) REMPI of the 2-photon allowed 2s ← 1s transition in atomic H at 243.1 nm (5.1 eV). Here, the probe power of ∼10 μJ/pulse is required in order to promote 3-photon ionization. In TRIY, the high-power probe has the added advantage of increasing the NH_2 photofragment signal. The vertical IP of NH_2 (12.0 eV) [36, 37] can only be reached by 3-photon absorption at this probe wavelength.

4.4 RESULTS AND DISCUSSION

Time-Resolved Photoelectron Spectroscopy

Presented in Fig 4.3 are photoelectron spectra of jet-cooled NH_3 resonantly excited to the $\nu_2' = 2$ (a), 3 (b), 4 (c), and 5 (d) vibrational levels of the NH_3 ($\tilde{A}$) state with fs pump pulses ($h\nu_{pu}$) centered at 208.5, 204.6, 200.8 and 197.1 nm, respectively, and probed with a constant non-resonant fs probe pulse ($h\nu_{pr}$) centered at 240.2 nm. Spectra in Fig 4.3 show 2-color only ($1 + 1'$) photoelectron signal integrated over the delay range $-100 < \Delta t < 100$ fs. We highlight that the mass spectrum shown as an inset in Fig 4.5 is typical of laser power and molecular beam conditions used during TRPES experiments and assures that collected photoelectrons are from photoionization of NH_3. Spectra are plotted with an arbitrary intensity scale versus the electron binding energy (BE) which is calculated as the total photon energy ($h\nu_{pu} + h\nu_{pr}$) minus the photoelectron KE. The highest BE cutoff of each spectrum, in the 11.11 - 11.45 eV range, signifies the total $h\nu_{pu} + h\nu_{pr}$ photon energy available. Plots are presented in this manner to afford assignment of photoelectron peaks to known vibronic levels in the cationic ground state, NH_3^+ ($\tilde{X}$). [14, 38 - 40] Four peaks are seen in each of the $\nu_2' = 2$ - 5 spectra - referred to as peaks i, ii, iii, and iv, from left to right within each panel of Fig 4.3 (see panel (b)). Peaks iii and iv are difficult to distinguish in the $\nu_2' = 2$ spectrum, and only appear as small shoulders on the high BE side of peak ii (see ESI Fig 1). In all spectra, an abrupt rise in photoelectron signal occurs at the lower BE side of peak i, and the peak intensities diminish as the BE increases. The average energy spacing of the peaks is ~0.2 eV. The relatively broad linewidth (~0.05 eV) is as expected, due to the 1 nm bandwidth (~0.03 eV at 200 nm) of the fs pump and probe pulses and the limited resolution of the magnetic bottle spectrometer.

The first excited state of ammonia is characterized by a long progression in the umbrella mode, [7 - 9] and based on Franck-Condon arguments the umbrella mode is expected to dominate the cationic spectrum as well. The vibrational energy levels of the NH_3^+ ($\tilde{X}$) umbrella

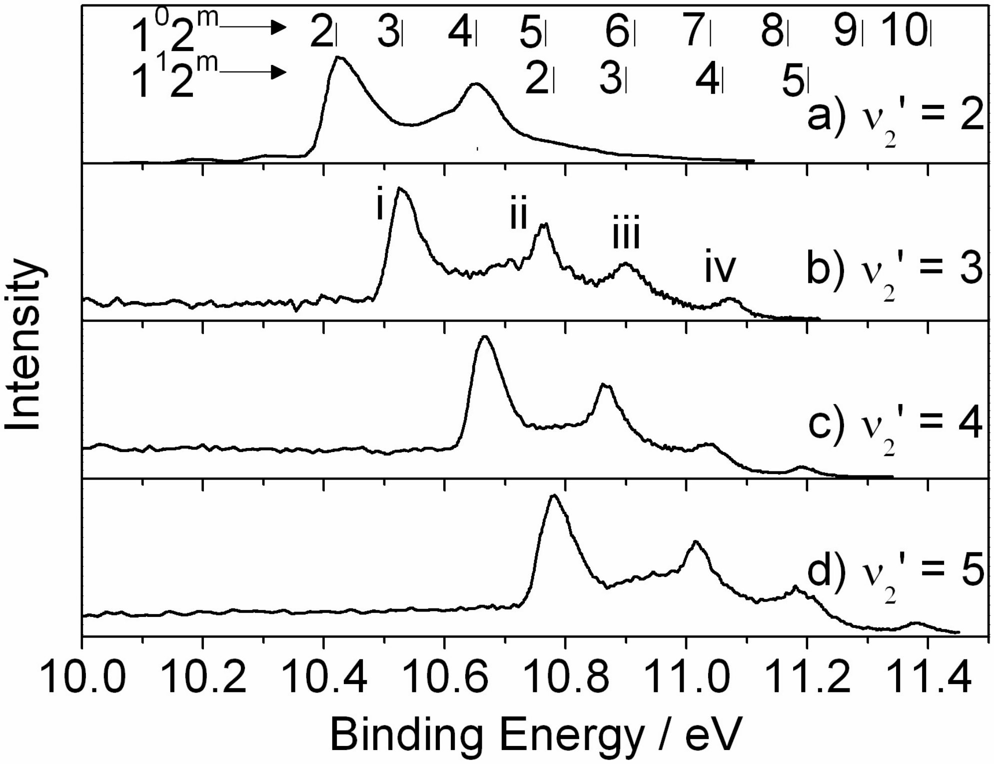

Figure 4.3: Photoelectron binding energy (BE) spectra recorded following resonant excitation of the $\nu_2' = 2$ (a), $\nu_2' = 3$ (b), $\nu_2' = 4$ (c), and $\nu_2' = 5$ (d) levels of the NH_3 $(\tilde{A})$ state and subsequent ionization into the NH_3^+ $(\tilde{X})$ cationic state with a 240.2 nm probe. Each panel shows the 2-color $(1 + 1')$ photoelectron signal integrated over $-100 < \Delta t < 100$ fs. Vibrational energy levels of NH_3^+ $(\tilde{X})$ are indicated at the top of panel (a) for assignment of photoelectron peaks. Progressions of m vibrational quanta in the cation's umbrella mode (ν_2) with either zero (1^02^m) or one (1^12^m) quanta in the cation's symmetric N - H stretch mode (ν_1) are identified.

mode (ν_2) have been determined with high precision by He(I) photoelectron spectroscopy (He(I)-PES) and zero electron kinetic energy (ZEKE) measurements. [38 - 40] The experimental values obtained by these methods (provided in Table 4.1) have a maximum error of ~2 meV and are used in labeling the $1^0 2^m$ progression in panel (a) of Fig 4.3. The most intense peak in each photoelectron spectrum (peak i) aligns well with the $1^0 2^m$ level of the final cationic state, where the number of quanta m in the cationic umbrella mode (ν_2) is equal to the number of initially excited ν_2' quanta in the NH$_3$ ($\tilde{A}$) state. This assignment suggests that the dominant ionization mechanism follows a $\Delta\nu_2$, $\Delta\nu_1 = 0$ propensity rule. This is in-line with earlier findings from fs REMPI-PES experiments on ionization from the NH$_3$ ($\tilde{A}$) state, [14] but differs from the observation of a $\Delta\nu_1 = 1$ rule observed after excitation to, and ionization from, the higher lying NH$_3$ ($\tilde{E}$) state. [30] Photoelectron peaks ii and iv are assigned to the umbrella progression in the cation, where only even 2^m quanta are present for ionization from $\nu_2' = 2$ and 4 levels, and only odd 2^m quanta are present for ionization from $\nu_2' = 3$ and 5 levels. This even/odd progression is evident in previous studies of 2-photon fs ionization of NH$_3$ ($\tilde{A}$). [14]

However, peak iii does not follow the simple umbrella mode progression evident in the case of previous non-resonant above threshold ionization measurements. [38 - 40] Relaxation along NH$_3$ ($\tilde{A}$) is expected to anharmonically couple two quanta in the umbrella mode with one quanta in the symmetric N-H stretch mode through the N-H dissociation coordinate. [11, 14, 16, 25] BE thresholds for ionization to the $1^1 2^2$ and $1^1 2^3$ levels in the NH$_3^+$ ($\tilde{X}$) cation have been identified at 10.76 eV and 10.90 eV, respectively, by REMPI-PES measurements. [14] The $1^1 2^2$ combination band may be expected to manifest as peak iii in the $\nu_2' = 2$ spectrum (Fig 4.3a), but peak intensities in this region of the spectrum do not enable a confident assignment. Yet, in the $\nu_2' = 3$ spectrum (Fig 4.3b), peak iii correlates well with the anticipated BE of the $1^1 2^3$ combination mode, allowing a more justified peak assignment. To our knowledge, $1^1 2^4$ and $1^1 2^5$ combination bands, expected after $\nu_2' = 4$ and 5 excitation, are not described in the literature. We assign peak iii in panels (c) and (d) of Fig 4.3

Table 4.1: Relevant energies for excitation from NH_3 ($\tilde{X}$) into NH_3 ($\tilde{A}$) (top) and NH_3^+ ($\tilde{X}$) (bottom) vibrational levels. NH_3 ($\tilde{A}$) ν_2' are umbrella vibrations of the excited state, [22] and NH_3^+ ($\tilde{X}$) ν_2 are umbrella vibrations in the cation. [38] ν_1 labels the symmetric N-H stretch in NH_3^+ ($\tilde{X}$). Cationic states are labeled 1^n2^m, where n and m are quanta in ν_1 and ν_2, respectively.

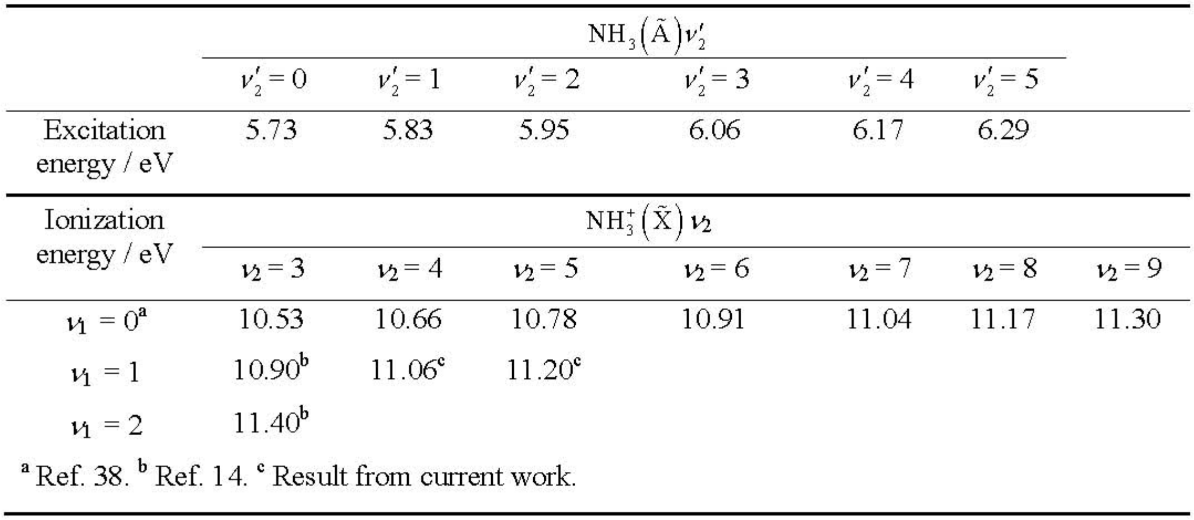

	$NH_3(\tilde{A})\nu_2'$						
	$\nu_2' = 0$	$\nu_2' = 1$	$\nu_2' = 2$	$\nu_2' = 3$	$\nu_2' = 4$	$\nu_2' = 5$	
Excitation energy / eV	5.73	5.83	5.95	6.06	6.17	6.29	
Ionization energy / eV	$NH_3^+(\tilde{X})\,\nu_2$						
	$\nu_2 = 3$	$\nu_2 = 4$	$\nu_2 = 5$	$\nu_2 = 6$	$\nu_2 = 7$	$\nu_2 = 8$	$\nu_2 = 9$
$\nu_1 = 0^a$	10.53	10.66	10.78	10.91	11.04	11.17	11.30
$\nu_1 = 1$	10.90^b	11.06^c	11.20^c				
$\nu_1 = 2$	11.40^b						

[a] Ref. 38. [b] Ref. 14. [c] Result from current work.

as the 1^12^4 and 1^12^5 levels, respectively, based on: (i) analogy with the $\nu_2' = 3$ spectrum; and (ii) the propensity rules for ionization into the 1^02^m progression (discussed above) do not adhere with the appearance of peak iii. The cationic ground state vibrational energy levels measured here are 11.06 (1^12^4) and 11.18 eV (1^12^5) (see Table 4.1). The presence of combination bands in our photoelectron spectra provide spectroscopic evidence of coupling between the umbrella mode (associated with pyramidal to planar geometry changes upon photoexcitation to the NH_3 ($\tilde{A}$) state) and the symmetric N-H stretch mode that promotes relaxation along the NH_3 ($\tilde{A}$) state (possessing $^1n\sigma^*$ character). We also highlight that the absence of a combination band peak (peak iii) in the $\nu_2' = 2$ spectrum may suggest that R_{N-H} elongation is suppressed as the initial excitation energy approaches the energetic threshold of the potential barrier to N-H dissociation in the NH_3 ($\tilde{A}$) state (see schematic potentials in Fig 4.1).

Having assigned the features in the photoelectron spectra of the NH_3 ($\tilde{A}$) state, we now turn to analysis of the temporal evolution of these spectra. Decay profiles for each photoelectron band are obtained by integrating signal over a 0.2 eV wide window, around the center of each peak, at each pump-probe delay, Δt. A representative decay profile is shown in Fig 4.4 for the NH_3 ($\tilde{A}$) $\nu_2' = 3 \rightarrow NH_3^+$ ($\tilde{X}$) $1^0 2^3$ ionization channel. In total, 14 transients are obtained (one for each NH_3 ($\tilde{A}$) ν_2' = x $\rightarrow NH_3^+$ ($\tilde{X}$) $1^n 2^m$ ionization channel, where x, n, and m are the number of quanta in initial ν_2' and final ν_1 and ν_2 modes, respectively) and are analyzed as described below. Data and fits for the remaining ionization channels are not shown here, but are provided in the ESI. All time profiles show nearly zero intensity for Δt < -500 fs and Δt > 500 fs, indicating that NH_3 ($\tilde{A}$) relaxation is indeed ultrafast. A single exponential decay function convoluted with the Gaussian IRF (fixed FWHM = 230 fs) is used to fit these data. The fitting routine yields extremely short decay constants, $\tau_D < 75$ fs, for each of the 14 photoelectron transients. Ionization from a specific ν_2' level can yield up to four different final cationic states, as determined from the aforementioned analysis of the photoelectron spectra in Fig 4.1. Within our (temporal) error, the extracted decay constants for photoionization from specific ν_2' levels are independent of the vibrational configurations populated in the final cation state. We report the decay time ($\tau_D < 75$ fs) as an upper limit because accurate determination of shorter timescales is not possible with our instruments timing resolution. Measured decay times are in-line with expectations from rotationally resolved linewidth measurements (~35 fs) [10] and the time-resolved photoelectron/photoion coincidence (PEPICO) experiments (~40 fs) [41] on NH_3 ($\tilde{A}$). Whilst, TRIY [29] and TRPES [30] measurements have identified a lifetime of ~60 fs for the NH_3 ($\tilde{A}$) state, following non-adiabatic coupling from the initially populated NH_3 ($\tilde{E}$) $\nu_2' = 2$ state (which occurs on the order of ps).

During TRPES measurements, photoelectron signal is recorded only if (i) the probe photon provides enough energy to at least access the ionic ground state, and (ii) there is good vFC overlap between neutral and ionic states. These conditions are met by our probe pulse

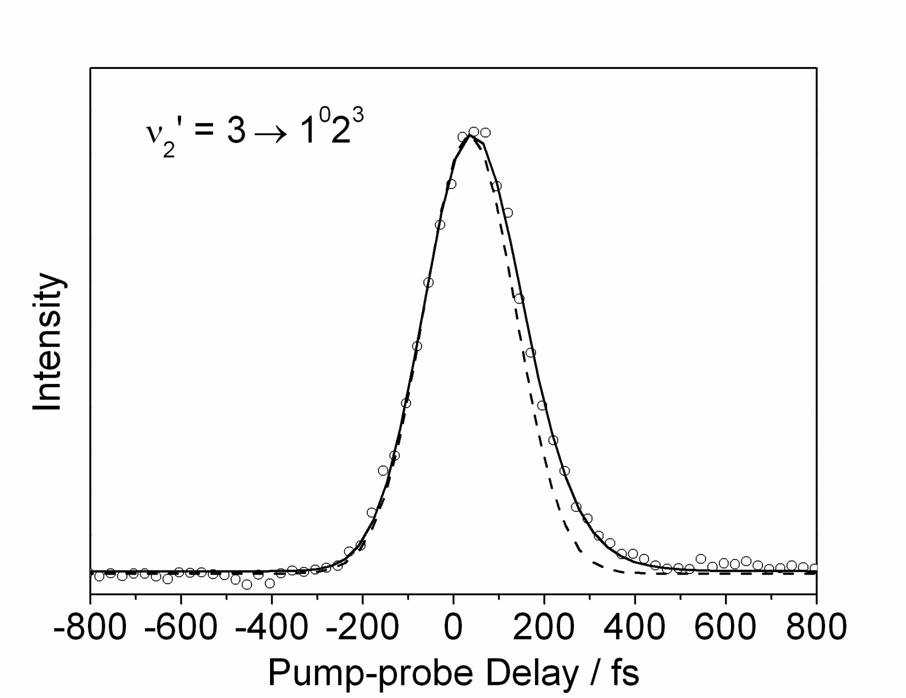

Figure 4.4: Photoelectron signal transient (circles) for NH_3 ($\tilde{A}$) $\nu_2' = 3 \rightarrow NH_3^+$ ($\tilde{X}$) 1^02^3 ionization (peak i in Fig 3(b)). Best fit line (solid) is an exponential decay convoluted with a fixed width (FWHM = 230 fs) Gaussian IRF (dash).

at the time of initial excitation. However, it is likely that the vFC overlap with the final NH_3^+ ($\tilde{X}$) state is diminished once the wavepacket leaves the vFC region and crosses the potential barrier along the N-H stretch coordinate of NH_3 ($\tilde{A}$): this is represented by the schematic potential energy profiles of the neutral excited state and ground cationic states in Fig 4.1. Additionally, the NH_3^+ ($\tilde{X}$) state potential energy, and hence the ionization energy of NH_3 ($\tilde{A}$), will increase with extended R_{N-H} and at some point before CI1 our probe is no longer able to ionize neutral ammonia due the increase in vertical IP. These issues are inherent to TRPES experiments on neutral species [42, 43] and in the case here, will ultimately manifest as underestimation of the true NH_3 ($\tilde{A}$) lifetime. In recent years however, some progress has been made to circumvent this issue with the aid of high energy fs probe pulses (produced by high harmonic generation methods), capable of 1-photon electron detachment, enabling ionization of the evolving wavepacket along the entire reaction coordinate. [44, 45] A comparison of the TRPES NH_3 ($\tilde{A}$) decay times with the H and NH_2 photofragment formation times is given in the succeeding sections and supports the interpretation presented here.

Time-Resolved Ion Yield

Analysis of TRPES data determined that population in NH_3 ($\tilde{A}$) moves out of the vFC excitation region and toward CI1 within 75 fs. At this point the molecule may potentially return to a vibrationally excited NH_3 ($\tilde{X}$) state (Path 1 in Fig 4.1). Alternatively, reactive flux may evolve towards N-H bond fission through either non-adiabatic or adiabatic dissociation channels (Paths 2 and 3 in Fig 4.1, respectively). This section focuses on measuring the timescales for H and NH_2 photofragment formation using TRIY. The $\nu_2' = 2$ - 5 levels of NH_3 ($\tilde{A}$) are resonantly excited by UV fs pump pulses, and photoproducts are then probed by a time-delayed UV pulse. Here, a high-power (10 μJ/pulse) 243.1 nm probe has been selected specifically to promote (2 + 1) REMPI of H-atoms through the 2-photon allowed 2s ← 1s transition. The high-power probe has the added advantage of promoting non-resonant multi-photon ionization of the NH_2 co-fragment. This pump-probe scheme allows direct measurement of H and NH_2 photofragment formation timescales as described below.

Presented in Fig 4.5 are results from TRIY experiments using a 204.6 nm pump to populate the NH_3 ($\tilde{A}$) $\nu_2' = 3$ state. Data for excitation to other ν_2' levels in NH_3 ($\tilde{A}$) are available in the ESI. Mass spectra are shown in Fig 4.5a using a high (main) and low-power (inset) 243.1 nm probe. Both spectra are produced by integrating over all positive pump-probe delays ($0 < \Delta t < 2000$ fs) in order to show transient species present during different Δt regimes in a single plot. The low-power probe mass spectrum (inset) is typical of the pump-probe powers used during TRPES and is shown here to assure that NH_3 ($\tilde{A}$) is the primary source of the photoelectrons analyzed in Section 3.1. The inset shows a dominant parent (NH_3^+) signal at 17 amu with peaks at 16 and 18 amu accounting for $< 1\%$ of the total signal.

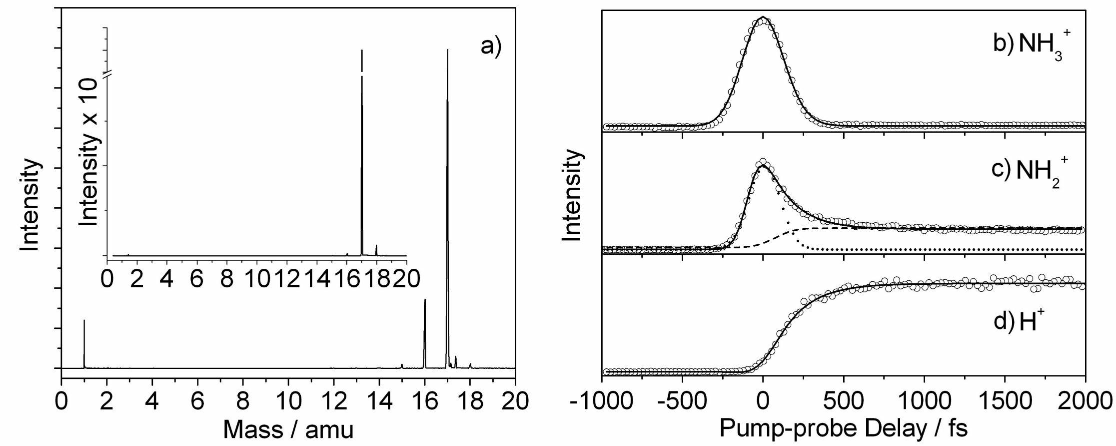

Figure 4.5: Results from TRIY measurements of the $\nu_2' = 3$ level of NH$_3$ ($\tilde{A}$). Mass spectra for high (10μJ/pulse; main) and low (2 μJ/pulse; inset) power 243.1 nm probes are shown in panel (a). Transient data (circles) for NH_3^+ (b), NH_2^+ (c) and H^+ (d) and fits (solid lines) are used in analysis of dissociation dynamics as described in the text. The IRF (dotted line) and rise functions (dashed line) are indicated in panel (c).

Significant fragment signals are evident in the high-power mass spectrum. Peaks at 1, 15, 16, and 17 amu are assigned as H^+, NH^+, NH_2^+, and NH_3^+, respectively. Possible sources of the 18 amu peak are: (i) NH_3 isotopes; (ii) NH_4^+; and (iii) contamination from H_2O^+. It is important to note that photofragmentation signals at 1, 15, and 16 amu can arise from multiple sources including excited state fragmentation and multi-photon dissociative ionization. [32, 33] The 10 μJ/pulse 243.1 nm probe was selected here to promote (2 + 1) REMPI of neutral H, and 3-photon absorption by other species is therefore also expected. Highly vibrationally excited cationic states of NH_3^+ are created upon 3-photon ionization which may subsequently dissociate (dissociative ionization). We are able to differentiate between these two processes and must isolate the ion signal arising from excited state fragmentation by analyzing the emission timescales as described below.

Also presented in Fig 4.5 are time-dependent ion yield profiles for NH_3^+ (b), NH_2^+ (c), and H^+ (d). Transient profiles are obtained by integrating a 1 amu wide gate, positioned around the center of each peak, at all pump-probe delays, Δt. Excited state relaxation dynamics, leading to each photoproduct, are extracted from fits to these delay traces. The NH^+ transient cannot be analyzed here due to extremely low signal levels. We do however note that, sequential H loss is presumed as the most likely source of NH^+ and its appearance is therefore not directly associated with NH_3 ($\tilde{A}$) state relaxation. The NH_3^+ transient is reminiscent of the TRPES trace shown in Fig 4.4 and is fit accordingly - using a single exponential decay convoluted with the IRF. Decay constants from NH_3^+ TRIY traces are determined for the $\nu_2' = 2$ - 5 levels of NH_3 ($\tilde{A}$) as $\tau_D < 75$ fs. TRPES data reported in Section 3.1 identified NH_3 ($\tilde{A}$) ionization into as many as four different vibrational levels of the cationic ground state, NH_3^+ ($\tilde{X}$). The decay constant obtained by TRIY is considered an average over ionization into all possible final cationic states and, as expected, agrees with the τ_D time constants extracted from TRPES measurements, which have been interpreted as the timescale required for excited state flux to move out of the vFC excitation window rather than a measurement of the true NH_3 ($\tilde{A}$) state lifetime.

Transients for NH_2^+ and H^+ show a very different profile than that of the NH_3^+ parent. The former two transients are related to σ^* mediated N-H dissociation, and fits to these data allow the dissociation dynamics to be extracted. In Fig 4.5d, the H^+ transient shows a steady rise near $\Delta t = 0$ fs which plateaus after a few hundred fs. This trace is fit using an exponential rise function convoluted with the IRF. The extracted rise constant, τ_R, provides a direct measure of the time from initial excitation to H-atom emission. Appearance time constants for H-atom formation, following initial excitation to $\nu_2' = 2$ ($\tau_R = 226$ fs), $\nu_2' = 3$ ($\tau_R = 217$ fs), $\nu_2' = 4$ ($\tau_R = 208$ fs), and $\nu_2' = 5$ ($\tau_R = 193$ fs) levels, decrease as the initial excitation energy increases. We attribute this trend to an increased accessibility of CI1 as the excitation energy increases. In general, H-atom emission should occur on a timescale similar to the observed NH_3 ($\tilde{A}$) lifetime (population decay). Values for τ_R are nearly three times as long as the measurement of τ_D in Section 3.1 - further evidence that TRPES underestimates the NH_3 ($\tilde{A}$) lifetime due to the loss of the vFC ionization window. The H-atom formation times reported here are an average over all possible H-atom KE channels and do not allow a discussion of the fraction of internal energy imparted to the NH_2 co-fragment during dissociation. KE resolved H-atom transients are presented in Section 3.3, and a thorough discussion relating to competition between the non-adiabatic and adiabatic dissociation channels is reserved until then.

NH_2 is born here as a co-fragment to the H-atom discussed above, and should in principle follow the same appearance dynamics. However, the NH_2^+ delay trace (Fig 4.5c) is quite different from that of H^+. A baseline offset, between positive and negative pump-probe times, is present and suggests that some component of the NH_2^+ transient can be modeled with a step function - as in the H^+ transient fits. Additionally, a large peak in NH_2^+ signal is present around $\Delta t = 0$ which then rapidly decays by $\Delta t = 200$ fs - evidence of another process leading to NH_2 (or directly to NH_2^+). As a result, the NH_2^+ trace is fit with a combination of exponential decay and rise functions convoluted with the IRF. Due to the strong convolution between decay and rise functions in the $\Delta t < 300$ fs region, many combinations of τ_D and τ_R are able to fit the data. Therefore, in an effort to reduce the amount of phasespace sampled during the fit procedure, we have chosen to fix τ_R to the value obtained from the associated H^+ trace and allow τ_D to be fit. Extracted values for τ_D are again, less than 75 fs for excitation to NH_3 ($\tilde{A}$) $\nu_2' = 2$ - 5 - in reasonable agreement with the NH_3 ($\tilde{A}$) relaxation times obtained from TRPES in Section 3.1 and from the NH_3^+ TRIY data described above. We can then associate this peak, around $\Delta t = 0$ in Fig 4.5b, with an NH_2^+ formation process occurring within the NH_3 ($\tilde{A}$) state lifetime, and similar to previous interpretations of TRIY data in larger heteroaromatic molecules, this peak is assigned as multi-photon dissociative ionization via the NH_3 ($\tilde{A}$) state. [32, 33] As described above, this fragmentation occurs from a cationic state and is not a measure of the excited state dynamics under study here. In addition to this dissociative ionization mechanism, fragmentation of neutral NH_3 from the NH_3 ($\tilde{A}$) state leads to neutral NH_2 radicals, the timescale for which is ascribed to τ_R. We do highlight, however, that the overlap between the rise function and the rapid decay associated with dissociative ionization, makes it challenging to extract a value for τ_R from fully free fits to the NH_2^+ decay trace alone. Fixing τ_R to the H-atom appearance time produces acceptable fits of the NH_2^+ transient.

Time-Resolved Photofragment Translation Spectroscopy

N-H dissociation originating from the NH_3 ($\tilde{A}$) state can take place by passing through CI1 (non-adiabatic dissociation) or by avoiding it (adiabatic dissociation), as shown by paths 2 and 3 in Fig 4.1. NH_2 ($\tilde{X}$) and high KE H-atoms are created if non-adiabatic dissociation takes place at CI1, while excited NH_2 ($\tilde{A}$) and low KE H-atoms are created by avoiding CI1 (via a non-planar NH_3 geometry). Time-resolved measurement of the H-atom KEs is thus an excellent tool to determine the relative importance (and timescales) for N-H dissociation via these two mechanisms. To this end, we have recorded time-resolved H-atom KE spectra for initial UV excitation to the $\nu_2' = 2$ - 5 levels of NH_3 ($\tilde{A}$).

The TRPTS measurements result in two dimensional data which is time and energy resolved. This 2-D data can be integrated in either dimension to produce the plots in Fig 4.6 and Fig 4.7. TRPTS spectra at all pump wavelengths are integrated over $500 < \Delta t < 2000$ fs to produce the H-atom KE spectra presented in Fig 4.6. The H^+ transient obtained from TRIY measurements (Fig 4.5d) plateaus before $\Delta t = 500$ fs, and these energy spectra are therefore representative of the steady-state product distribution. Before $\Delta t = 500$ fs, the H-atom KE spectra display a time dependence which is utilized in the analysis of dissociation timescales given below. All spectra have been normalized so the relative yield of high and low energy H-atoms at differing pump energies may be investigated. Each spectrum displays a sharp peak between 0.05 and 0.07 eV followed by a long tail which extends beyond 1.5 eV. An interesting trend is evident in the 0.3 - 1.0 eV range. H-atom signal in this range decreases with increasing pump energy - evidence that the fraction of internal energy partitioned into

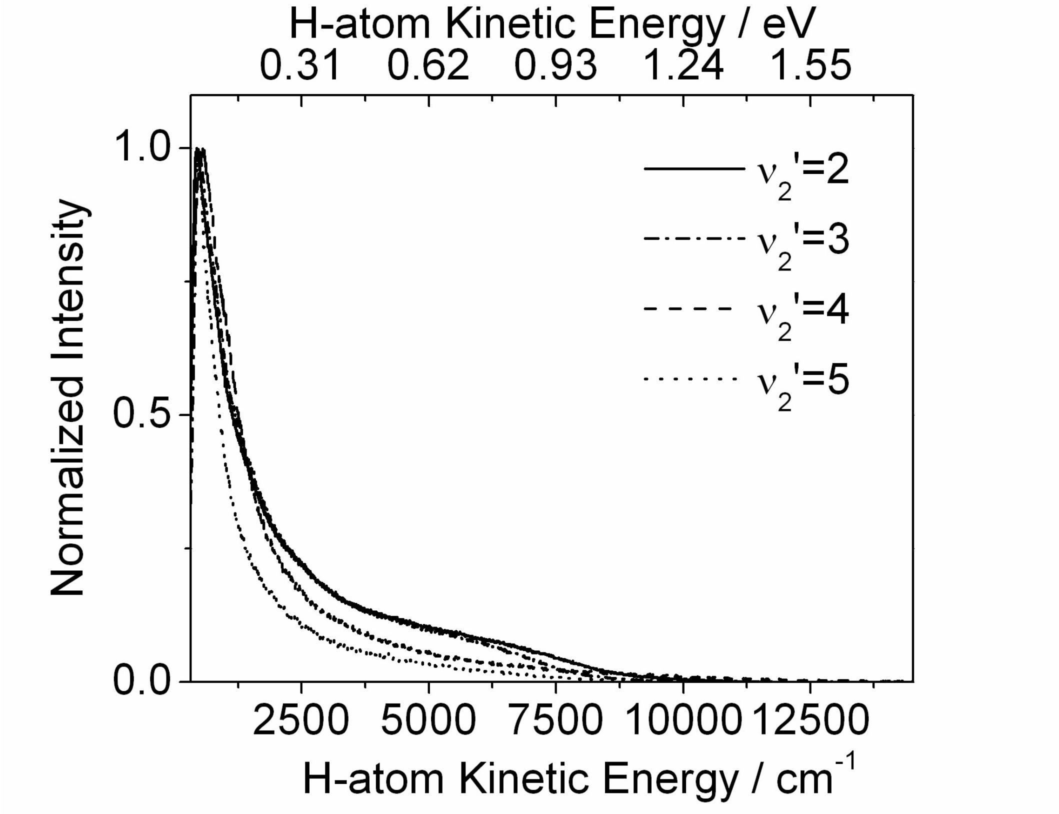

Figure 4.6: H-atom KE spectra after photodissociation from ν_2' vibrational levels of NH_3 ($\tilde{A}$), populated by wavelengths between 195 and 208 nm. The high KE H-atom signal (0.3 - 1.0 eV) is enhanced for $\nu_2' = 2$ and 3 levels.

NH_2 increases with increasing pump energy. This conclusion is supported by previous PTS studies of NH_3 ($\tilde{A}$) $\nu_2' = 0$ - 6 photodissociation. [16]

In general, any internal energy imparted to NH_3 ($\tilde{A}$), in excess of the dissociation energy, $D_\circ$, will be partitioned between dissociating co-fragments. In ammonia, this additional energy is distributed between H-atom KE, NH_2 KE (negligible within our energy resolution), and NH_2 internal energy. Measurement of H-atom KE then allows determination of NH_2 internal energy states, and H-atom KE spectra can be converted into NH_2 internal energy spectra by subtracting the H-atom KE from the total available photon energy (defined by $h\nu_{pu}$). The maximum available H-atom KE, KE_{max}, can be calculated for excitation to each

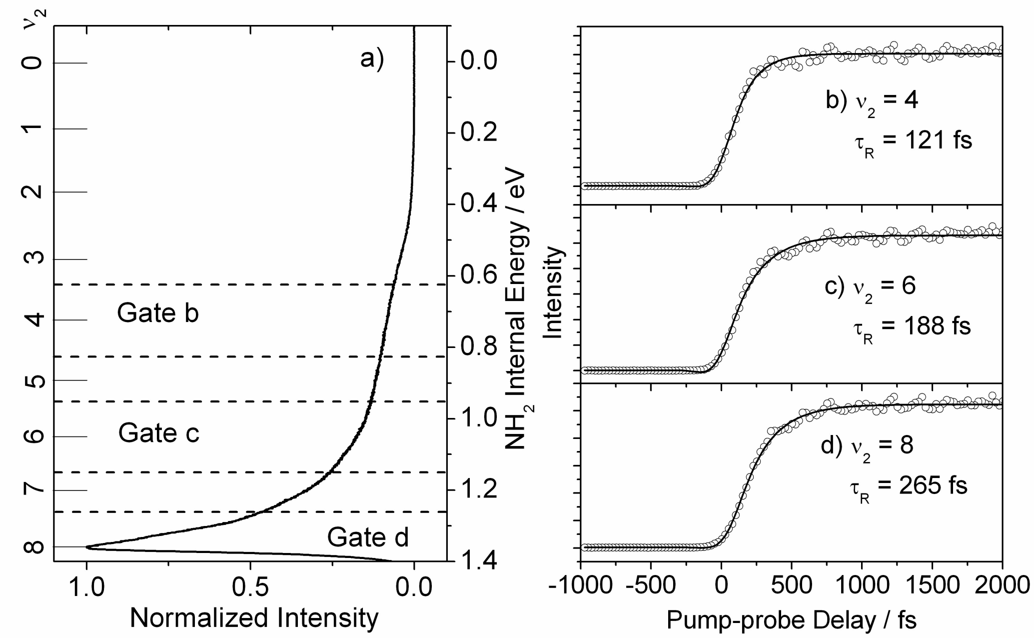

Figure 4.7: NH_2 internal energy spectra (a) and H^+ transients (b) - (d) for 204.6 nm excitation of the $\nu_2' = 3$ level of NH_3 ($\tilde{A}$). Each transient (b) - (d) corresponds to different quanta of vibrational energy carried away by the NH_2 fragment as determined from (a). Transients (b) - (d) are obtained by integrating NH_2 internal energy spectra, recorded at each Δt, over the respective gates labeled in (a). Fits (solid lines) to these data (circles) are used to analyze excited state dynamics as described in the text.

ν_2' level from KE_{max} = $h\nu_{pu}$ - $D_\circ$, where $D_\circ$ is the adiabatic H_2N-H dissociation energy (previously determined as 4.64 eV [15]). The $\nu_2' = 3$ H-atom KE spectrum is converted to an NH_2 internal energy spectrum and is presented in Fig 4.7a. Vibrational energy levels of the bending mode (ν_2) in the NH_2 ($\tilde{X}$) photoproducts [46 - 48] are identified by ticks in Fig 4.7a and are used to extract final-state dependent emission lifetimes.

Timescales for the production of NH_2 carrying a distribution of quanta in its ν_2 bend mode can be extracted from the delay traces presented in Fig 4.7 b - d following excitation at 204.6 nm to the $\nu_2' = 3$ level of the NH_3 ($\tilde{A}$) state. Data and fits for the ν_2 = 4, 6, and

8 product state levels of NH_2 ($\tilde{X}$) are given in Fig 4.7 b - d. This data set is presented here to illustrate general features which may also be obtained for excitation at other pump wavelengths (contained in the ESI). Delay traces are produced from TRPTS spectra by integrating a gate (shown in Fig 4.7a) around each NH_2 ($\tilde{X}$) ν_2 level, at each pump-probe delay. Reliable fits of the $\nu_2 = 0$, 1 and 2 levels are not obtained due to the extremely low signal levels at small NH_2 internal energies (see Fig 4.7a). Fitting results are given in Table 4.2 for $\nu_2 = 3$ - 9 states of NH_2 ($\tilde{X}$). The $\nu_2 = 9$ level of NH_2 ($\tilde{X}$) lies 1.5 eV above $D_\circ$ (total energy of 6.15 eV). [46] Excitation of $\nu_2' = 2$ and 3 levels of NH_3 ($\tilde{A}$) around 5.95 and 6.06 eV does not provide enough energy to populate this level and hence, transients for these product states are not obtained. All transients in Fig 4.7 show negligible intensity at $\Delta t < 0$ fs, followed by a steep rise which plateaus near $\Delta t = 500$ fs. As with the H^+ TRIY data (Fig 4.5d), these transients are fit with an exponential step function convoluted with the IRF. The H-atom emission timescale is again measured by τ_R - all of which fall in the < 75 - 346 fs range. Within each pump wavelength, the H-atom formation time increases as a function of increasing NH_2 internal energy. This is a trend recently observed in TR-VMI experiments following excitation to NH_3 ($\tilde{A}$) $\nu_2' = 4$. [19] The shortest H-atom appearance times measured here correlate with NH_2 fragments carrying very little internal vibrational energy.

Dissociation leading to H-atoms with high KEs and NH_2 fragments with low amounts of vibrational energy results from non-adiabatic crossing at CI1 (path 2, Fig 4.1). CI1 occurs at planar geometry of the NH_3 parent and vibronic coupling into path 2 at CI1 is expected to be ultrafast since out-of-plane distortion of NH_3 ($\tilde{A}$) is limited. Our measurements show that NH_2 products with high fractions of vibrational energy are formed on a timescale up to five times as long as products with minimal internal vibrational energy. Excited state trajectories which avoid non-adiabatic coupling at CI1, or bypass it via highly non-planar geometries, are a possible source of the observed NH_2 photofragments with large amounts of internal energy. [1, 2, 16] The average lifetime measured by TRPTS is obtained from

Table 4.2: Exponential rise time constants, τ_R obtained from fits to H-atom KE transients (see Fig 4.7 b - d). ν_2' refers to the initially excited level in the NH_3 ($\tilde{A}$) state and ν_2 refers to the bending mode vibrational levels of NH_3 ($\tilde{X}$) photoproducts. All values reported in units of fs with a ± 20 fs error.

	ν_2'			
ν_2	2	3	4	5
3	<75	84	82	138
4	<75	121	115	182
5	104	155	132	211
6	143	188	162	229
7	178	214	181	232
8	238	265	219	273
9	…	…	263	346
τ_A	150	173	162	236

fitting of transient profiles derived by integrating all H-atom KEs, for comparison to results reported in Section 3.2. The average dissociation time, τ_A = 150 - 236 fs, is reported in Table 4.2. TRPTS measurements of τ_A generally (except for the $\nu_2' = 5$ level) underestimate measurements made by TRIY. We note however, that the collection efficiency of our magnetic bottle spectrometer is not uniform across all H-atom KEs, which is not the case in TRIY measurements, and the observation of a shortened dissociation time is taken as evidence that the collection efficiency of our magnetic bottle is biased towards detection of high KE H-atoms.

4.5 CONCLUSIONS

The relaxation dynamics of resonantly excited ν_2' = 2 - 5 vibrational levels of NH_3 ($\tilde{A}$) have been investigated using three complementary UV fs pump-probe techniques: TRPES, TRIY and TRPTS. Time-resolved photoelectron spectra give direct spectroscopic evidence of σ^* mediated relaxation of the NH_3 ($\tilde{A}$) state. This manifests itself as coupling between the umbrella mode, associated with a pyramidal-to-planar geometric shift upon NH_3 ($\tilde{A}$) state excitation, and the symmetric N-H stretch mode along the σ^* relaxation coordinate. Time constants of < 75 fs are extracted from the TRPES spectra and correspond to motion of the excited state wavepacket out of the vertical Franck-Condon window with NH_3^+ ($\tilde{X}$) rather than a true measurement of the NH_3 ($\tilde{A}$) state lifetime. Evolution of reactive flux along the N-H dissociation pathways of the NH_3 ($\tilde{A}$) potential energy surface yields H-atom and NH_2 photoproducts. Formation timescales, together with their energy distributions, are investigated by TRIY and TRPTS. These measurements reveal H-atom elimination times of < 75 fs to 350 fs, which increase with the amount of internal energy partitioned into the NH_2 co-fragment. Analysis of H-atom KE spectra shows that NH_2 is predominantly formed with significant amounts of vibrational excitation in the ν_2 bending mode. Vibronic level dependent time constants extracted from TRPTS measurements can be considered an upper limit for the corresponding NH_3 ($\tilde{A}$) lifetimes whereas TRPES provides a lower limit.

4.6 ACKNOWLEDGEMENTS

S.U and V.G.S would like to thank the NSF and EPSRC for grants (NSF-CHE-0924456 and EP/H003401) which have been awarded through the International Collaboration in Chemistry Program. V.G.S would also like to thank the Royal Society for a University Research Fellowship. G.M.R thanks the Leverhulme trust for a postdoctoral research fellowship.

4.7 REFERENCES

[1] C. A. de Lange, in Advances in Chemical Physics, ed. I. Prigogine and S. A. Rice, John Wiley and Sons, Inc., New York, 2001, vol. 117, p. 1.

[2] M. N. R. Ashfold, D. H. Mordaunt and S. H. S. Wilson, in Advances in Photochemistry, ed. D. C. Neckers, D. H. Volman and G. von Bunau, John Wiley and Sons, Inc., New York, 1996, vol. 21, p. 217.

[3] A. L. Sobolewski, W. Domcke, C. Dedonder-Lardeux and C. Jouvet, Phys. Chem. Chem. Phys., 2002, 4, 1093.

[4] A. L. Sobolewski and W. Domcke, Chem. Phys., 2000, 259, 181.

[5] M. N. R. Ashfold, G. A. King, D.Murdock, M.G.D.Nix, T.A.A. Oliver and A. G. Sage, Phys. Chem. Chem. Phys., 2010, 12, 1218.

[6] M. N. R. Ashfold, B. Cronin, A. L. Devine, R. N. Dixon and M. G. D. Nix, Science, 2006, 312, 1637.

[7] A. E. Douglas, Discuss. Faraday Soc., 1963, 35, 158.

[8] V. Vaida, M. I. McCarthy, P. C. Engelking, P. Rosmus, H.-J. Werner and P. Botschwina, J. Chem. Phys., 1987, 86, 6669.

[9] J. H. Glowina, S. J. Riley, S. D. Colson and G. C. Nieman, J. Chem. Phys., 1980, 73, 4296.

[10] L. D. Ziegler, J. Chem. Phys., 1985, 82, 664.

[11] M. N. R. Ashfold, C. L. Bennett and R. N. Dixon, Chem. Phys., 1985, 93, 293.

[12] V. M. Donnelly, A. P. Baranovski and J. R. McDonald, Chem. Phys., 1979, 43, 271.

[13] E. L. Woodbridge, M. N. R. Ashfold and S. R. Leone, J. Chem. Phys., 1991, 94, 4195.

[14] J. Xie, B. Jiang, G. Li, S. Yang, J. Xu, G. Sha, D. Xu, N. Lou and C. Zhang, Faraday Discuss., 2000, 115, 127.

[15] J. Biesner, L. Schnieder, J. Schmeer, G. Ahlers, X. Xie, K. H. Welge, M. N. R. Ashfold and R. N. Dixon, J. Chem. Phys., 1988, 88, 3607.

[16] J. Biesner, L. Schnieder, G. Ahlers, X. Xie, K. H. Welge, M. N. R. Ashfold and R. N. Dixon, J. Chem. Phys., 1989, 91, 2901.

[17] D. H. Mordaunt, M. N. R. Ashfold and R. N. Dixon, J. Chem. Phys., 1996, 104, 6460.

[18] D. H. Mordaunt, R. N. Dixon and M. N. R. Ashfold, J. Chem. Phys., 1996, 104, 6472.

[19] K. L. Wells, G. Perriam and V. G. Stavros, J. Chem. Phys., 2009, 130, 074308.

[20] M. I. McCarthy, P. Rosmus, H.-J. Werner, P. Botschwina and V. Vaida, J. Chem. Phys., 1987, 86, 6693.

[21] G. C. Nieman and S. D. Colson, J. Chem. Phys., 1978, 68, 5656; 1979, 71, 571.

[22] J. H. Glowina, S. J. Riley, S. D. Colson and G. C. Nieman, J. Chem. Phys., 1980, 73, 4296.

[23] R. Polak, I. Paidarova, V. Spirko and P. J. kuntz, Int. J. Quantum Chem., 1996, 57, 429.

[24] H. Akagi, K. Yokoyama and A. Yokoyama, J. Chem. Phys., 2003, 118, 3600.

[25] M. N. R. Ashfold, C. L. Bennett and R. N. Dixon, Faraday Discuss. Chem. Soc., 1986, 82, 163.

[26] S. A. Henck, M. A. Mason, W. B. Yan, K. K. Lehmann and S. L. Coy, J. Chem. Phys., 1995, 102, 4783.

[27] A. Bach, J. M. Hutchison, R. J. Holiday and F. Fleming Crim, J. Chem. Phys., 2002, 116, 9315.

[28] M. L. House, Y. H. Yoon and F. F. Crim, Mol. Phys., 2008, 106, 1127.

[29] S. H. Yin, H. P. Liu, J. Y. Zhang, B. Jiang, D. A. Xu, L. Wang, G. H. Sha and N. Q. Lou, Chem. Phys. Lett., 2002, 356, 227.

[30] H. P. Liu, S. H. Yin, J. Y. Zhang, L. Wang, B. Jiang and N. Q. Lou, Phys. Rev. A: At., Mol., Opt. Phys., 2006, 74, 053418.

[31] N. L. Evans and S. Ullrich, J. Phys. Chem. A, 2010, 114, 11225.

[32] C. A. Williams, G. M. Roberts, H. Yu, N. L. Evans, S. Ullrich and V. G. Stavros, J. Phys. Chem. A., 2012, 116, 2600.

[33] H. Yu, N. L. Evans, V. G. Stavros and S. Ullrich, Phys. Chem. Chem. Phys., 2012, 14, 6266.

[34] W. C. Wiley and I. H. McLaren, Rev. Sci. Instrum., 1955, 26, 1150.

[35] P. Kruit and F. H. Read, J. Phys. E: Sci. Instrum., 1983, 16, 313.

[36] S. J. Dunlavey, J. M. Dyke, N. Jonathan and A. Morris, Mol. Phys., 1980, 39, 1121.

[37] R. Locht, C. Servais, M. Ligot, F. Derwa and J. Momigny, Chem. Phys., 1988, 123, 443.

[38] G. Reiser, W. Habenicht and K. Muller-Dethlefs, J. Chem. Phys., 1993, 98, 8462.

[39] R. Locht, B. Leyh, W. Denzer, G. Hagenow and H. Baumgartel, Chem. Phys., 1991, 155, 407.

[40] R. Locht, K. Hottmann, G. Hagenow, W. Denzer and H. Baumgartel, Chem. Phys. Lett., 1992, 190, 124.

[41] V. Stert, W. Radloff, Th. Freudenberg, F. Noack, I. V. Hertel, C. Jouvet, C. Dedonder-Lardeux and D. Solgadi, Europhys. Lett., 1997, 40, 515.

[42] M. Barbatti and S. Ullrich, Phys. Chem. Chem. Phys., 2011, 13, 15492.

[43] R. Crespo-Otero, M. Barbatti, H. Yu, N. L. Evans and S. Ullrich, Chem. Phys. Chem., 2011, 12, 3365.

[44] L. Nugent-Glandorf, M. Scheer, D. A. Samuels, A. M. Mulhisen, E. R. Grant, X. Yang, V. M. Bierbaum and S. R. Leone, Phys. Rev. Lett., 2001, 87, 193002.

[45] L. Nugent-Glandorf, M. Scheer, D. A. Samuels, V. M. Bierbaum and S. R. Leone, Rev. Sci. Instrum., 2002, 73, 1875.

[46] S. Zhou, Z. Li, D. Xie, S. Y. Lin and H. Guo, J. Chem. Phys., 2009, 130, 184307.

[47] A. Alijah and D. Duxbury, J. Mol. Spectrosc., 2002, 211, 16.

[48] W. Gabriel, G. Chambaud, P. Rosmus, S. Carter and N. C. Handy, Mol. Phys., 1994, 81, 1445.

CHAPTER 5

OBSERVATION OF ULTRAFAST NH_3 ($\tilde{A}$) STATE TUNNELING USING A COMBINATION OF TIME-RESOLVED PHOTOELECTON AND H-ATOM KINETIC ENERGY SPECTROSCOPY [2]

---

[2] N. L. Evans, H. Yu, A. S. Chatterley, G. M. Roberts, V. G. Stavros and S. Ullrich
To be submitted to *Physical Chemistry Chemical Physics*

5.1 ABSTRACT

We have investigated photodissociation of NH_3 ($\tilde{A}$) from low-lying levels of the ν_2' umbrella mode, in order to observe the effect of quantum tunneling through the NH_3 ($\tilde{A}$) dissociation barrier. Two techniques, time-resolved photoelectron spectroscopy (TR-PES) and time-resolved total kinetic energy release (TR-TKER) spectroscopy, have been utilized to directly measure: vibrational level dependent excited state lifetimes; H-atom appearance times; and photoproduct final energy distributions. The photoelectron spectra reveal that excited state relaxation by N-H bond elongation results from a coupling between the umbrella and symmetric stretch modes of NH_3 ($\tilde{A}$). Excited state lifetimes measured by TR-PES increase following photoexcitation of $\nu_2' = 0$ and 1 ($\tau_A = 131$ fs and $\tau_A = 165$ fs respectively) and decrease with $\nu_2' = 2$ and 3 ($\tau_A = 81$ fs and $\tau_A <$50 fs respectively).The H-atom TR-TKER data reveal NH_2 internal energy distributions, which favor large amounts of vibrational excitation in the NH2 bend (ν_2). Interestingly, from the TKER spectra, we also observe a low internal energy feature in the NH_2 following excitation of $\nu_2' = 0$ and 2 levels which is absent in the $\nu_2' = 1$ and 3 levels. We propose that this is evidence of tunneling through an *effective* dissociation barrier, whose magnitude is dependent on the out-of-plane angle. Average H-atom appearance times show the same ν_2' dependence as the TR-PES measurements. Furthermore, H-atom appearance times for specific vibrational levels of the NH_2 co-fragment are extracted from the TR-TKER spectra.

5.2 INTRODUCTION

The ultraviolet (UV) region of the absorption spectrum of ammonia contains a single long progression, which is attributed to the out-of-plane umbrella mode, ν_2'. This progression reflects the change in the minimum energy geometry structure from pyramidal in the ground electronic state, NH_3 ($\tilde{X}$), to trigonal planar in the first excited electronic state, NH_3 ($\tilde{A}$). [1 - 4] The absence of a progression in the N-H stretch, and the broad absorption bands attributed to ν_2', indicate fast predissociation of vibrational levels of NH_3 ($\tilde{A}$). [2, 5 - 7] Many aspects of predissociation, can be understood in term of the properties of the ground and excited state potential energy surfaces (PES), which can be determined through multi-dimensional calculations. [8 - 12] A sketch is given for NH_3 ($\tilde{X}$), NH_3 ($\tilde{A}$), and NH_3^+ ($\tilde{A}$) as a function of the N-H stretch coordinate, R_{N-H}, in Fig 5.1. The NH_3 ($\tilde{A}$) PES has an energetic minimum at 5.73 eV [3] and is repulsive along the R_{N-H} coordinate. The exact topography of the NH_3 ($\tilde{A}$) dissociation barrier, lying near 1.4 Å, is dependent on computational method [9] but is known to have a minimum at planar geometries (reported values are between 1900 - 3600 cm^{-1} above the origin), increasing steeply with the out-of-plane angle (θ). This is illustrated by the dashed PESs shown for NH_3 ($\tilde{A}$) in Fig 5.1, with increasing deviation from planarity. At extended R_{N-H} and at planar geometries (C_2v), there is a conical intersection (CI) between the NH_3 ($\tilde{X}$) and NH_3 ($\tilde{A}$) states, leading to competition between the adiabatic and non-adiabatic dissociation channels which produce, NH_2 ($\tilde{A}$) + H and NH_2 ($\tilde{X}$) + H photoproducts, respectively. The PES topography leads to interesting vibrational level dependent dynamics, including competition between adiabatic and non-adiabatic dissociation following photoexcitation above the barrier and dissociation through quantum tunneling following excitation below the barrier.

High resolution absorption linewidth measurements, [3, 7] time-resolved photoproduct emission spectroscopy, [13 - 15] and full quantum dynamics calculations [16 - 18] performed on recent high-level PES [11, 12] provide overwhelming evidence that above barrier dissociation

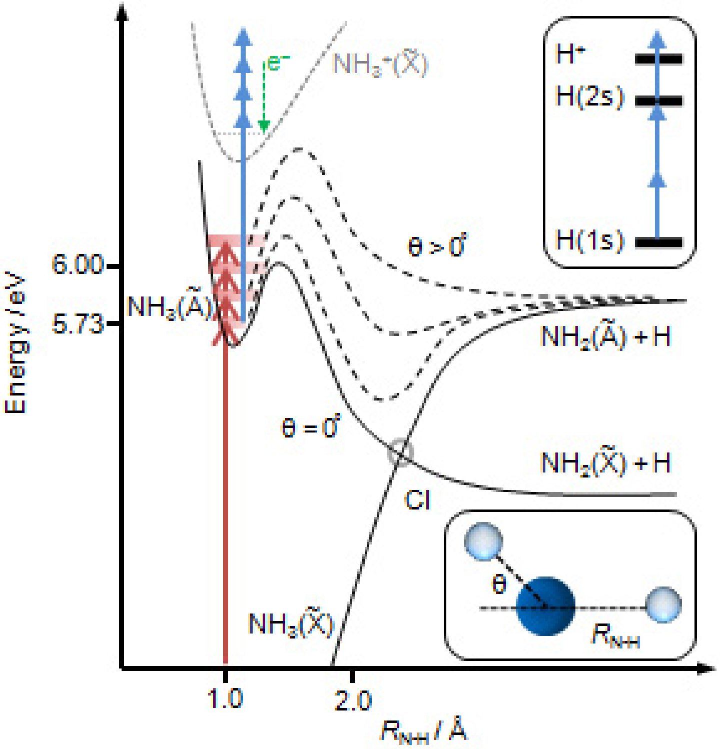

Figure 5.1: Schematic of NH_3 ($\tilde{X}$), NH_3 ($\tilde{A}$), and NH_3^+ ($\tilde{A}$) theoretical potential energy surfaces [11] as a function of R_{N-H}. Atomic geometry is defined in the inset. Solid lines represent the barrier minimum occurring at planar geometries ($\theta = 0$); dashed lines represent the *effective* dissociation barrier experienced as θ increases. The NH_3 ($\tilde{X}$)/NH_3 ($\tilde{A}$) CI is indicated by the grey circle. Red arrows represent resonant excitation of $\nu_2' = 0$ - 3 levels of NH_3 ($\tilde{A}$). Blue arrows represent ionization of NH_3 in TR-PES (left) and 2 + 1 REMPI of H in TR-TKER (right).

occurs within 75 fs of initial excitation, and that the dissociation time decreases as the excitation energy increases. At excitation energies below 6.02 eV, [19] the CI captures trajectories and non-adiabatic vibrational coupling with the NH_2 ($\tilde{X}$) state occurs. H-atom emission energy measurements [13, 19, 20] reveal that internal energy imparted to the NH_2 ($\tilde{X}$) fragment increases with the excitation energy, eventually leading to NH_2 ($\tilde{A}$) following excitation above 6.02 eV. [19, 20] As the adiabatic path becomes energetically available, the CI can be avoided *via* non-planar trajectories. The percentage of products increases from approximately 5 to 25% following photoexcitation across the $\nu_2' = 3$ - 6 series, [19] and reports of NH_2 ($\tilde{A}$) yield from the $\nu_2' = 6$ level vary from 2.5 to 25%. [19] Dissociation branching ratios can be controlled by population of NH_3 ground state vibrational levels, [22, 23] whereby pre-excitation of the symmetric stretch favors NH_2 ($\tilde{A}$) products and pre-excitation of the anti-symmetric stretch favors NH_2 ($\tilde{X}$) products.

The $\nu_2' = 0$ (5.73 eV) and 1 (5.83 eV) levels lie below the barrier and dissociation occurs by quantum tunneling, whereas the $\nu_2' = 2$ (5.95 eV) level is located at or below the barrier depending on which method is used to calculate the barrier height. [9] Previous experimental evidence of tunneling dynamics has come from linewidth [3, 7] and NH_2 internal energy [19, 20] measurements. On energetic grounds alone, one may anticipate dissociation times to decrease as the excitation energy increases relative to the dissociation barrier. However, linewidth measurements reveal that $\nu_2' = 1$ has a longer lifetime than $\nu_2' = 0$. [3, 7] This behavior is also observed in recent quantum dynamics calculations [16 -18] and is explained as tunneling through an *effective* barrier whose height is dependent on θ. The planar $\nu_2' = 0$ level encounters the barrier minimum and can tunnel more easily than can the $\nu_2' = 1$ level, which experiences an elevated dissociation barrier at non-planar geometries.

In this paper we have extended our previous measurements [13] of $\nu_2' = 2$ - 5 photoexcitation to include the $\nu_2' = 0$ - 3 levels of NH_3 ($\tilde{A}$), in order to investigate varying dynamics due to tunneling through the dissociation barrier. The use of time-resolved photoelectron spectroscopy (TR-PES) allows us to directly measure ν_2' dependent lifetimes. Time-resolved total kinetic energy release (TR-TKER) spectroscopy enables us to probe H-atom appearance times, and to correlate these H-atoms with specific ν_2 levels of NH_2 - an extension of the frequency resolved H-atom energy emission measurements. [19, 20]

5.3 EXPERIMENT

The experimental apparatus used for the present TR-PES and TR-TKER measurements has been described previously. [13, 24 - 26] Briefly, a molecular beam is generated by continuous expansion of a 50/50 mixture of He and NH_3.The molecular beam is intersected by a UV fs pump pulse, which resonantly excites specific vibrational levels of NH_3 ($\tilde{A}$). A time-delayed probe either ionizes the parent molecule or H-atom products. The pump and probe steps are represented in the schematic shown in Fig 5.1 by the red and blue arrows respectively. A magnetic bottle spectrometer facilitates kinetic energy measurements of photoelectrons (TR-PES) or H-ions (TR-TKER). Operation of the spectrometer is identical to that described in REF 13 however; a new method for generation of deep UV (DUV) pump pulses is employed.

Whereas in our previous study the fourth harmonic of the Ti:Sapphire fundamental was tuned from the oscillator, we now use an external mixing set up for our optical parametric amplifier (OPA, TOPAS-C) to achieve the wider tunability range necessary for these measurements. Here, the fundamental wavelength is fixed at 800 nm and the tunable (275 - 296 nm) OPA output is externally mixed with 650 μJ/pulse of 800 nm, in a type I BBO crystal to create the DUV pump pulses centered at 204.9, 208.7, 212.6 and 216.4 nm for excitation of the $\nu_2' = 3$, 2, 1 and 0 levels, respectively. The OPA output conversion efficiency is around 20% for all pump wavelengths, providing typical pump energies of 0.5 μJ/ pulse.

Probe pulses at 243.1 nm are produced in a second OPA (Coherent OPERA) for use in both TR-PES and TR-TKER experiments. This wavelength is chosen because: a) it is 2-photon resonant with the 2s state of H-atoms; and b) the total pump + probe energy (in the range 10.8 -11.1 eV) is able to access several vibrational levels of the NH_3^+ ($\tilde{A}$) cation - allowing for observation of a vibrational progression in the TR-PES spectra. Here, the probe power is kept low (∼3 μJ/pulse) to eliminate multiphoton absorption in favor of 1 + 1′ photon ionization. In TR-TKER, H-atoms are ionized by 2 + 1 resonance enhanced multiphoton ionization (REMPI) via the 2s ← 1s transition. Given the multiphoton nature of the REMPI transition, a high power probe (∼8 μJ/pulse) is required to promote the 3-photon ionization.

Calibration scans allow: 1) definition of zero pump-probe delay ($\Delta t = 0$); 2) measurement of the Gaussian instrument response function (IRF) width; and 3) conversion of time-of-flight (TOF) measurements into electron and H-atom kinetic energy (KE) spectra. Pump-probe cross correlations recorded in 1, 3-butadiene (BD) and pyrrole indicate the delay position corresponding to $\Delta t = 0$ and the IRF, which has a full width at half maximum (FWHM) of 230 fs. The extremely short lifetimes (<50 fs) of these calibration gasses justifies their use for IRF determination. [27, 28] Known ionic state energies of BD [29] are used for photoelectron TOF to KE conversion. H-atom KE calibration is performed by varying the small acceleration voltage as described in detail in REF 13.

5.4 RESULTS AND DISCUSSION

TR-PES Measurements

In TR-PES, ν_2' vibrational levels of the NH_3 ($\tilde{A}$) state are resonantly excited with DUV pump pulses and are then one-photon ionized by a low power time-delayed probe centered at 243.1 nm. The resulting photoelectrons are collected and energy analyzed in a magnetic bottle spectrometer. Photoelectron energy spectra are obtained over the pump-probe delay range -500 <Δt <1000 fs in 25 fs intervals. The resulting two-dimensional (2-D) data provide both spectroscopic and dynamic information to be used in the analysis of NH_3 ($\tilde{A}$) state photophysics as described below.

Photoelectron KE spectra following photoexcitation to each ν_2' level are obtained by integrating each photoelectron spectrum in the pump-probe delay region -100 <Δt <100 fs

- the range in which ultrafast relaxation occurs, and then summing these spectra together. KEs are converted into electron binding energy (BE) by subtracting the measured electron KE from the total (1 + 1$'$) pump-probe energy (BE = hν_{pu} + hν_{pr} - KE$_{e-}$). Presented from top to bottom in Fig 5.2 are photoelectron spectra as a function of BE, obtained after excitation of $\nu_2' = 0$ - 3 vibrational levels of NH_3 ($\tilde{A}$). Spectra in Fig 5.2 show 2-color only (1 + 1$'$) photoelectron signal obtained after background subtraction, in which pump-alone and probe-along signal has been subtracted from the measured 2-colour photoelectron signal. In each spectrum, four distinct photoelectron peaks are evident and are referred to as peaks i, ii, iii, and iv from left to right within each spectrum (see labels in panel b of Fig 5.2). The broad linewidth (up to 0.1 eV) of peaks i - iv is due to the spectral bandwidth of our fs pump and probe pulses and is not indicative of the excited state lifetime. In comparison, high resolution measurements yield a FWHM linewidth of ~0.02 eV. [3, 7] A relatively weak feature is observed between peaks i and ii that may be attributed to hot band transitions. The NH_3 ($\tilde{A}$) state room temperature absorption spectrum [3] displays split peaks for the ν_2' = 0 - 3 levels which are not present in the jet-cooled spectrum. It is possible to excite these hot bands with the wide bandwidth fs excitation pulse.

Spectra are presented in terms of BE to afford assignment to known vibrational levels of the ground state, NH_3^+ ($\tilde{X}$), of the cation. Experimental [13, 30, 31] and theoretical [32, 33] values are reported for relevant NH_3^+ ($\tilde{X}$) levels in Table 5.1 and are indicated in the top panel of Fig 5.2. Peaks i, ii, and iv are spaced by ~0.2 eV, the spacing decreasing slightly across the series (peak i to peak iv), a result of anharmonicity in the umbrella mode. Based on Frank-Condon calculations, [34] the transition probability should be a maximum between the initially excited umbrella mode (ν_2') of NH_3 ($\tilde{A}$) and the umbrella mode (ν_2) in the cation. These two arguments allow us to assign peaks i, ii, and iv to umbrella vibrations in the cation. The umbrella progression ($1^0 2^m$) of NH_3^+ ($\tilde{X}$) is indicated in Fig 5.2a and shows that our assignments align nicely with known [13, 30 - 33] vibrational levels in the cation. In each panel, peak i corresponds to the $1^0 2^m$ cationic level, where m is the number of ν_2'

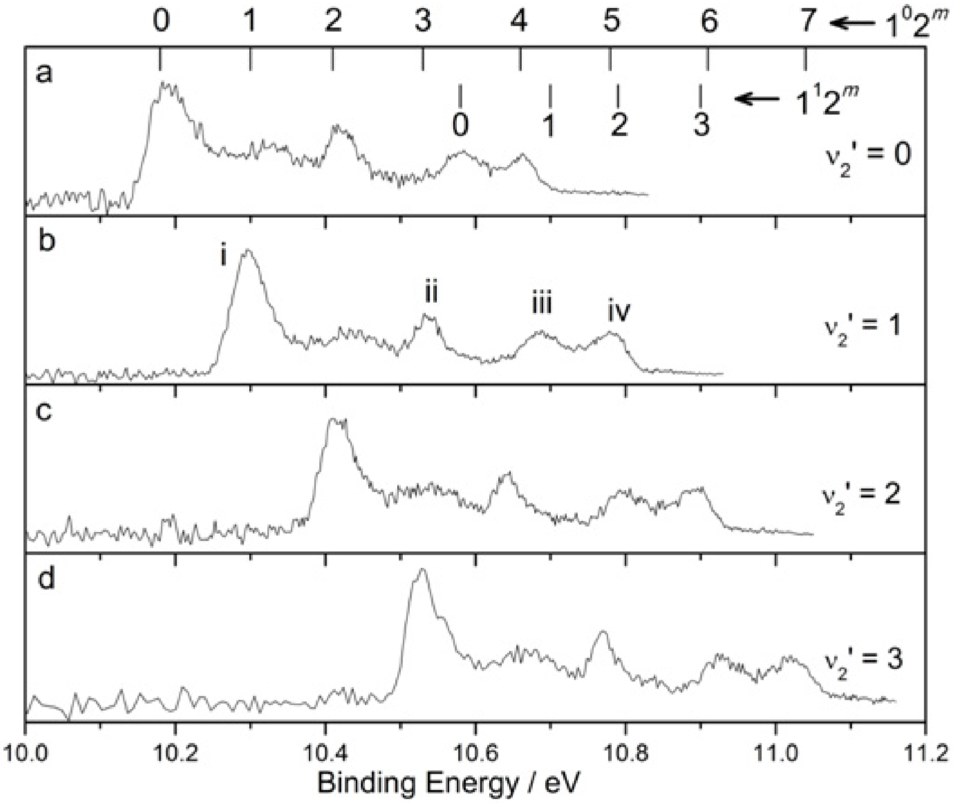

Figure 5.2: Photoelectron spectra obtained after resonant excitation to $\nu_2' = 0$ (a), 1 (b), 2 (c), and 3 (d) vibrational levels of NH_3 ($\tilde{A}$) with UV fs pulses centered at 216.4 (a), 212.6 (b), 208.5 (c), and 204.6 nm (d). Umbrella (ν_2) and stretch (ν_1) progressions of the NH_3^+ ($\tilde{X}$) cation are labeled at the top of panel (a).

quanta in the initially excited NH_3 ($\tilde{A}$) state. For example, peak i in the $\nu_2' = 0$ spectrum corresponds to $1^0 2^0$. This assignment follows the $\Delta\nu_1$, $\Delta\nu_2 = 0$ ionization propensity rule observed in previous fs studies of the NH_3 ($\tilde{A}$) intermediate state. [13, 30] Peak ii is assigned as $1^0 2^{m+2}$ and peak iv is assigned as $1^0 2^{m+4}$. The even (or odd) progression in NH_3^+ ($\tilde{X}$), is determined by the initially exited even (or odd) ν_2' level of NH_3 ($\tilde{A}$). The progression of two quanta in the umbrella mode is also in-line with previous fs studies. [13, 30]

Peak iii does not fall into the two quanta umbrella progression of peaks i, ii, and iv. However, relaxation along the N-H coordinate is known to anharmonically couple two umbrella quanta with one quantum of N-H stretch (ν_1), [13, 19, 30] and we can assign peak iii to a umbrella/stretch combination vibration. The combination bands having one quantum of stretch, $1^1 2^m$, are also shown in Fig 5.2a. Peak iii in each spectrum aligns nicely with the $1^1 2^m$ combination mode where m is the initially excited vibrational level (i.e. peak iii in the $\nu_2' = 2$ spectrum corresponds to $1^1 2^2$). Again, a $\Delta\nu_2 = 0$ ionization propensity rule is observed. In assigning these combination bands, we have provided clear spectroscopic evidence of relaxation along the N-H stretch coordinate following photoexcitation of NH_3 ($\tilde{A}$). One-photon, above threshold ionization experiments do not access NH_3 ($\tilde{A}$), and thus do not reveal the combination mode because relaxation along N-H is eliminated. [35, 36, 37] Previous two-photon ZEKE, [31] REMPI-PES, [30] and TR-PES [13] experiments *via* the NH_3 ($\tilde{A}$) intermediate state have directly identified this umbrella/stretch coupling.

To investigate the relaxation dynamics following photoexcitation of NH_3 ($\tilde{A}$), the 2-D TR-PES data can be integrated over specific peaks in the BE spectra to produce pump-probe delay transients. Representative transients are shown in Fig 5.3, for the lowest BE peak following photoexcitation of $\nu_2' = 0$ - 3. The integration ranges are 10.10 - 10.25 eV ($\nu_2' = 0$), 10.25 -10.37 eV ($\nu_2' = 1$), 10.37 - 10.48 eV ($\nu_2' = 2$), and 10.48 - 10.60 eV ($\nu_2' = 3$). The data (circles) represent the dynamical evolution of the NH_3 ($\tilde{A}$) excited state population over time delays $-500 < \Delta t < 1000$ fs. Transients for peaks ii, iii, and iv have also been obtained and are identical to those in Fig 5.3. These traces are not presented here for

Table 5.1: Vibrational energy levels in the NH_3^+ ($\tilde{X}$) cation, where ν_1 and ν_2 correspond to the symmetric stretch and umbrella vibrations, respectively. Cationic states are labeled 1^n2^m, where n and m are quanta in ν_1 and ν_2, respectively. a. - Ref 31, b. - Refs 32 and 33, c. - Ref 30, d. - Ref 13

	$NH_3^+(\tilde{X})$							
	$\nu_2=0$	$\nu_2=1$	$\nu_2=2$	$\nu_2=3$	$\nu_2=4$	$\nu_2=5$	$\nu_2=6$	$\nu_2=7$
$\nu_1=0^a$	10.18	10.30	10.41	10.53	10.66	10.78	10.91	11.04
$\nu_1=1$	10.58^b	10.70^b	10.79^c	10.90^c	11.06^d	11.20^d		

clarity, but are available in the electronic supplementary material (ESM), with results from fits to all data included in Table 5.2. All transients are fit with a Gaussian convoluted to an exponential decay function. The Gaussian (blue lines in Fig 5.3) is centered at Δt = 0 and has a fixed width (FWHM = 230 fs) corresponding to our IRF. The decay constants, τ_D, and all amplitudes are obtained through least squares fitting. Results for τ_D are compiled in Table 5.2. Preliminary fits with FWHM and Δt = 0 relaxed allow us to estimate a ± 20 fs error in the extracted decay constants. Within each ν_2' level, the decay constants are considered to be the same for each photoelectron peak - evidence that the NH_3 ($\tilde{A}$) relaxation time is independent of the final cationic state. Further discussion will be in regard to the average decay constant, τ_A, for each level. Our previous TR-PES experiment [13] reported lifetimes of <75 fs for $\nu_2' = 2$ and 3 levels, and our current results for τ_A are in agreement with this value.

We can now discuss the significance of the decay constant in relation to the NH_3 ($\tilde{A}$) state lifetime. The NH_3 ($\tilde{A}$) lifetime is considered as the time from initial excitation until the wavepacket reaches the CI. At this point the wavepacket may return to the ground state or continue through to dissociation along adiabatic or non-adiabatic paths (see Fig 5.1). Photoelectron signal is obtained only when the probe photon has enough energy to photode-

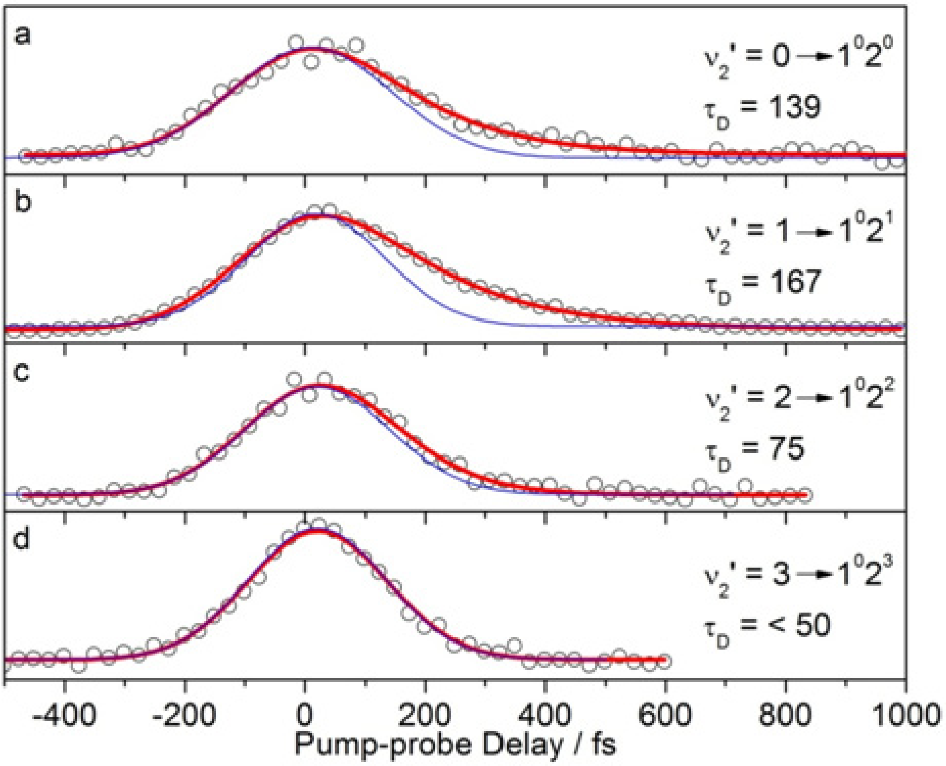

Figure 5.3: Pump-probe delay traces for peak i in the photoelectron spectra of Fig 5.2. Ionization from $\nu_2' = 0$ - 3 intermediate levels are presented from top to bottom. Data (circles) are obtained in increments of 25 fs. Fits (red) are made with an exponential decay function convoluted with a fixed width Gaussian IRF (blue). Decay constants (τ_D) are extracted from fits and used for analysis of NH_3 ($\tilde{A}$) relaxation rates.

Table 5.2: Exponential decay constants, τ_D, are obtained from fits to pump-probe decay traces. ν_2' is the initially excited level of NH_3 ($\tilde{A}$) and the peak labels refer to BE peaks from the photoelectron energy spectra (Fig 5.2). All values are in fs with ± 20 fs error.

	$\nu_2' = 0$	$\nu_2' = 1$	$\nu_2' = 2$	$\nu_2' = 3$
peak i	139	167	75	<50
peak ii	130	166	76	<50
peak iii	135	164	79	<50
peak iv	122	161	92	<50
τ_A	131	165	81	<50

tach from NH_3 ($\tilde{A}$). The NH_3^+ ($\tilde{X}$) PES rises steeply along the N-H coordinate [32, 38] and at some point before the CI our probe does not have enough energy to photodetach to this state - the ionization window is lost. This has been observed previously in UV photoionization experiments on other molecules, which exhibit a dissociative intermediate electronic state. [39, 40] It is thus entirely possible that the ionization window loss may result in underestimating the true excited state lifetime. Comparison of our TR-PES results to lifetimes obtained from frequency resolved measurements does not clearly show this relationship. Collating results from two absorption linewidth experiments [3, 7] provides lifetimes of 93, 149, 128, and 61 fs for the $\nu_2' = 0$, 1, 2, and 3 levels, respectively. In comparison, our measurements yield lifetimes of 131, 165, 81 and <50 fs for the $\nu_2' = 0$, 1, 2 and 3 levels respectively. Our measurements therefore do not allow us to estimate the point at which the ionization window is lost. For comparison, time-resolved UV photoionization experiment using VMI [14] report a lifetime of <50 fs for the $\nu_2' = 4$ level.

Values for τ_A increase from $\nu_2' = 0$ to $\nu_2' = 1$ and then decrease at higher ν_2' levels. The lifetime trend, as a function of ν_2', is similar to the linewidth measurements [3, 7] and full-dimensional quantum dynamics calculations. [16 - 18] NH_3 ($\tilde{A}$) lifetimes decrease with photoexcitation of increasing ν_2' levels because the dissociation barrier is more easily surmounted and the CI is quickly accessed as more energy is initially deposited. [3, 7, 13, 16 - 19] The $\nu_2' = 0$ and 1 level minima lie below the dissociation barrier; the CI can only be reached by tunneling through the barrier. Following the ν_2' lifetime trend discussed above, one may expect tunneling from the $\nu_2' = 0$ level to be slower than from the $\nu_2' = 1$ level. However, the barrier height increases steeply as the out-of-plane angle, θ, increases. A node at $\theta = 0°$ in the $\nu_2' = 1$ wavefunction restricts purely planar geometries while the $\nu_2' = 0$ wavefunction has large amplitude at $\theta = 0°$. The first vibrational level then experiences a larger *effective* barrier (at non-planar geometries) than does the zeroth level and the tunneling rate is reduced. Previous experimental [3, 7] and theoretical [16 - 18] evidence of this lifetime behavior near the barrier strengthens our reasoning as well as the analysis of H-atom appearance times discussed below.

TR-TKER Measurements

Photoexcitation of ammonia below 6.02 eV leads to extremely efficient [41] non-adiabatic dissociation, resulting in NH_2 ($\tilde{X}$) + H co-fragments. Using TR-TKER spectroscopy allows us to directly measure the appearance times of H-atoms and thus enables us to clock the dissociation dynamics directly. Further, energy analysis of the H-atom photoproducts allows us to extract NH_2 internal energy dependent dissociation timescales, providing a more comprehensive picture of NH_3 ($\tilde{A}$) state photophysics.

H-atom KE spectra obtained following photoexcitation and then dissociation from the ν_2' = 0 (blue), 1 (green), 2 (red) and 3 (black) levels of NH_3 ($\tilde{A}$) are shown in Fig 5.4. Each KE spectrum is produced by integrating the 2-D TKER data over pump-probe delays 500 $<\Delta$t $<$3500 fs, as this reveals the steady state H-atom KE distributions (see Fig 5.6). Variations of the H-atom KE spectra in the range 0 $<\Delta$t $<$500 fs will be utilized to extract details about the fast dissociation dynamics from the NH_3 ($\tilde{A}$) state in the following analysis. All spectra have been normalized to allow comparison of relative H-atom intensities at differing KE. It is important to note that the overall H-atom signal intensity increases across the $\nu_2' = 0$ - 3 series due to: a) NH_3 ($\tilde{A}$) ← NH_3 ($\tilde{X}$) absorption cross sections increase across this series; [1 - 5] and b) the barrier to dissociation along the N-H coordinate on the NH_3 ($\tilde{A}$) PES cannot be overcome following photoexcitation to $\nu_2' = 0$ or 1, with dissociation occurring only through tunneling. The low absorption of the $\nu_2' = 0$ level produces extremely small signal levels, as evidenced by the noise in the H-atom KE spectrum (blue). Each spectrum is dominated by signal at low KE, which drops quickly above 0.25 eV - evidence that low energy H-atoms are the preferred dissociation products. Care must be taken when making photophysical arguments based on signal intensities collected in a magnetic bottle, due to the KE dependent collection efficiency. However, collection of high KE species is favored [42] and the enhanced low KE signal in our spectra must therefore arise from the dissociation event itself, instead of from a collection efficiency artifact. We note that the steep signal drop at H-atom energies below 0.05 eV *is* indicative of the magnetic bottles collection characteristics instead of the dissociation. Comparison to H-atom KE measurements made by high resolution ns photofragment translational spectroscopy (PTS) [19, 20] and fs velocity map ion imaging (VMI) [14] techniques provides confidence in our overall assignment of H-atom KE spectra. As in the ns PTS measurements, a high energy feature arises at 0.5 - 1.0 eV in the $\nu_2' = 0$ and 2 levels which is absent in the other levels. In general, high KE H-atom emission decreases with increasing excitation in ν_2', [13, 19] but the observation of high KE H-atoms following photoexcitation of $\nu_2' = 0$ and 2 in the current measurements can be attributed to dissociation through tunneling. Final product energy distributions associated with tunneling are discussed in terms of energy imparted to the NH_2 co-fragment below.

Energy conservation arguments allow us to transform the H-atom KE spectra into NH_2 internal energy spectra. Following photoexcitation of the NH_3 ($\tilde{A}$) state, initial excitation energy in excess of the dissociation limit, $D_\circ$, is shared between H and NH_2 co-fragments. The NH_2 KE can be a maximum of 5% of the total energy and we therefore consider only

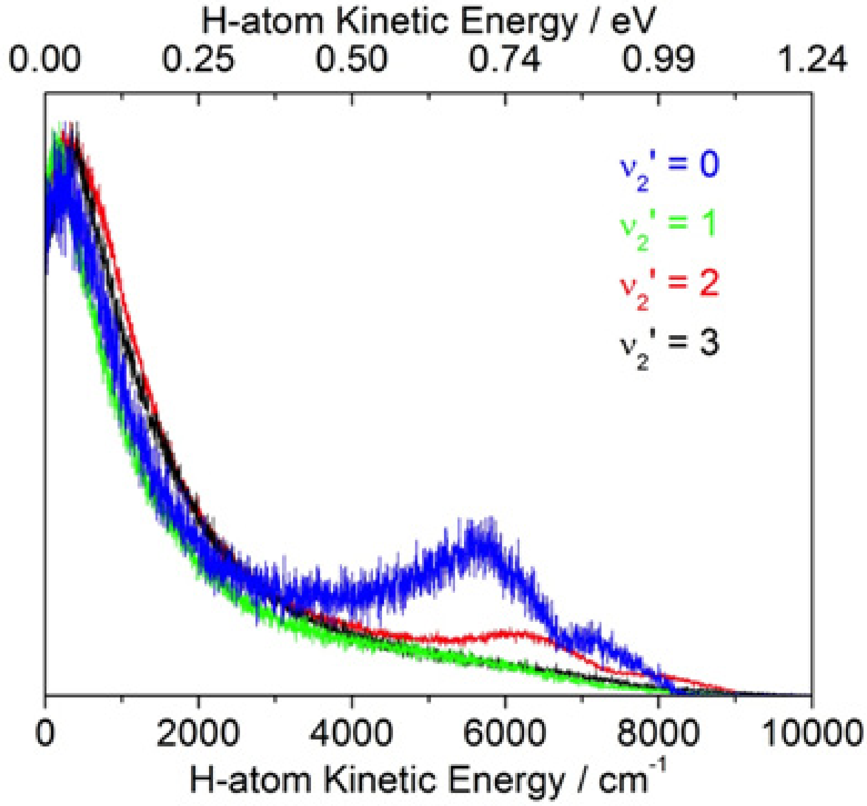

Figure 5.4: H-atom KE spectra obtained after dissociation from $\nu_2' = 0$, (blue), 1 (green), 2 (red), and 3 (black) vibrational levels of the NH_3 $(\tilde{A})$ state.

H-atom KE and NH_2 internal energy. The NH_2 internal energy is calculated by, $E(NH_{2int}) = E(h\nu_{pump}) - D_\circ - KE(H)$, where $E(h\nu_{pump})$ is the pump photon energy, $D_\circ = 4.64$ eV [20] is the dissociation energy, and KE(H) is the measured H-atom KE. In Fig 5.5 we present NH_2 internal energy spectra for each ν_2' level for discussion of the NH_2 final state energy distribution. The maximum available energy, $E_{max} = E(h\nu_{pump}) - D_\circ$, is indicated for each level (small vertical arrow) and the steep drop is again due to the magnetic bottle collection efficiency. By comparison of Figs 5.4 and 5.5, one can clearly see that the large amplitude low KE H-atom signal, is associated with NH_2 fragments carrying over 0.9 eV of internal energy. In general, this internal energy may be distributed over rotational, vibrational, and/or electronic modes. Our discussion will focus on internal energy partitioned into vibrational modes of NH_2 $(\tilde{X})$ because: a) our experiment lacks rotational resolution due to the spectral bandwidth of the fs excitation pulse; and b) we consider all products to be in the NH_2 $(\tilde{X})$ state, as the adiabatic dissociation channel is not active until the excitation energy is above 6.02 eV ($\nu_2' = 3$) and NH_2 $(\tilde{A})$ yield from this ν_2' level is less than 10%. [18, 19] Labels for the bend vibrational progression, ν_2 , of NH_2 $(\tilde{X})$ are placed at the top of Fig 5.5. [43 - 45] The low NH_2 internal energy signal is enhanced in the $\nu_2' = 0$ and 2 spectra relative to the $\nu_2' = 1$ and 3 spectra. This behavior has been observed previously [19, 20] and was rationalized on the basis that the $\nu_2' = 0$ and 2 levels traverse the CI at planar geometries - leaving little NH_2 vibrational energy. The node at $\theta = 0$ in the $\nu_2' = 1$ and 3 wavefunctions prevents strictly planar dissociation, and angular acceleration caused by approaching the CI from non-planar geometries imparts more vibrational energy into the NH_2 fragment.

We are now able to discuss the timescales for N-H dissociation, leading to specific vibrational levels populated in the NH_2 co-fragment. Dynamical information is extracted from fits to pump-probe transients, which are produced for each NH_2 vibrational level by integrating specific regions of the internal energy spectra for all pump-probe delays. Fig 5.6 shows the NH_2 internal energy spectrum (panel a) following photoexcitation of the $\nu_2' = 0$ level and three representative delay traces (panels b, c, and d) produced from the shaded

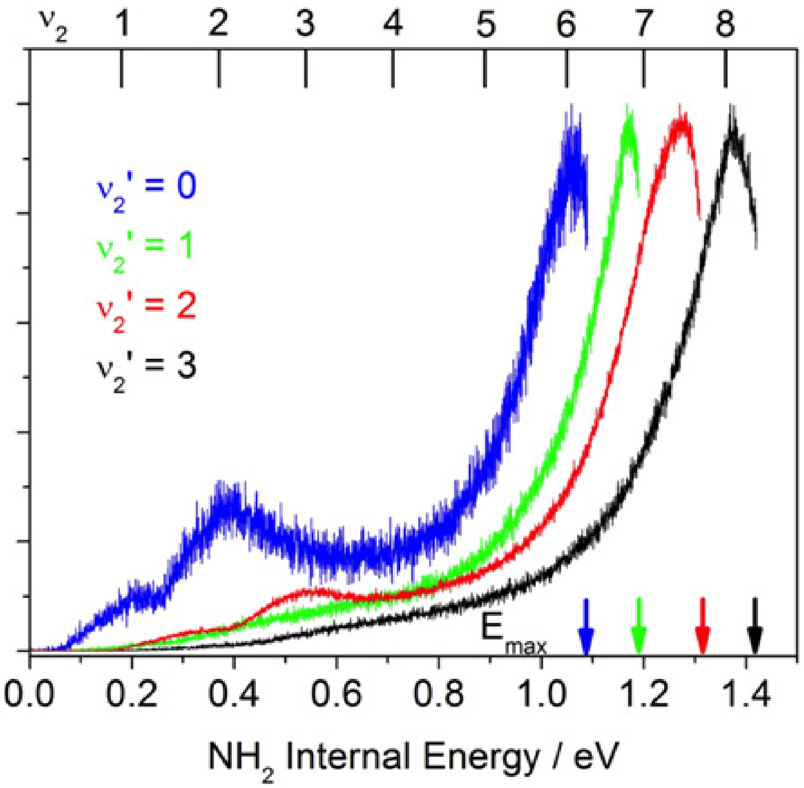

Figure 5.5: NH_2 ($\tilde{X}$) internal energy spectra, converted from H-atom KE measurements displayed in Fig 5.4. Labels for the bend progression in NH_2 ($\tilde{X}$) are labeled at top. [42 - 44] Note the low energy feature near $\nu_2 = 2$ and 3 in the $\nu_2' = 0$ and 2 spectra, respectively which is absent in the $\nu_2' = 1$ and 3 spectra.

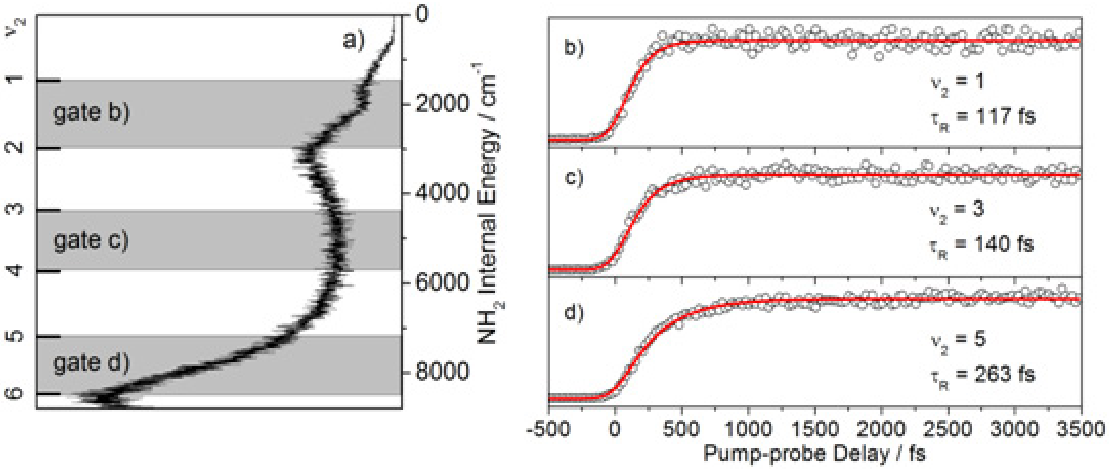

Figure 5.6: NH$_2$ ($\tilde{X}$) internal energy spectrum (a) and vibrational level (ν_2) dependent transients (b, c, d) following excitation of $\nu_2' = 0$ in the NH$_3$ ($\tilde{A}$) state. Transients are obtained by integrating over the shaded gates marked in panel (a) at each pump-probe delay. The red lines are fits to the data (circles). See text for details.

integration regions. The transient for a specific ν_2 level of NH$_2$ is generated by integrating the region from the origin of that specific level up to the origin of the next vibrational level. For example, gate b) in Fig 5.6 corresponds to the $\nu_2 = 1$ level. Within this energy range, molecules are considered to reside in the $\nu_2 = 1$ level with some rotational excitation, but not enough energy to reach the higher $\nu_2 = 2$ level. In total, 26 transients are produced from the $\nu_2' = 0$ - 3 levels of the NH$_3$ ($\tilde{A}$) state. All data and fits are available in the ESM. Representative transients are shown in Fig 5.6. All transients display zero signal at negative Δt, a distinct rise near Δt = 0 and a plateau before Δt = 750 fs. All transients are fit with a Gaussian convoluted with an exponential step function. As in the TR-PES fits, Δt = 0 and a FWHM = 230 fs are fixed in our fitting algorithm, while other fit parameters, including the step amplitude and the exponential time constant, τ_R, are extracted in a least squares fitting algorithm. Values for ν_2 dependent time constants are compiled in Table 5.3 for each ν_2' level of the NH$_3$ ($\tilde{A}$) state.

Table 5.3: Rise constants, τ_R (in fs with ±20 fs error), extracted from fits to the H-atom transients. NH_3 $(\tilde{A})$ ν_2' is the initially excited level and NH_2 $(\tilde{X})$ ν_2 is the final product level as deduced from H-atom KE measurements. τ_A is the intensity weighted average rise constant obtained by integrating across all NH_2 internal energies.

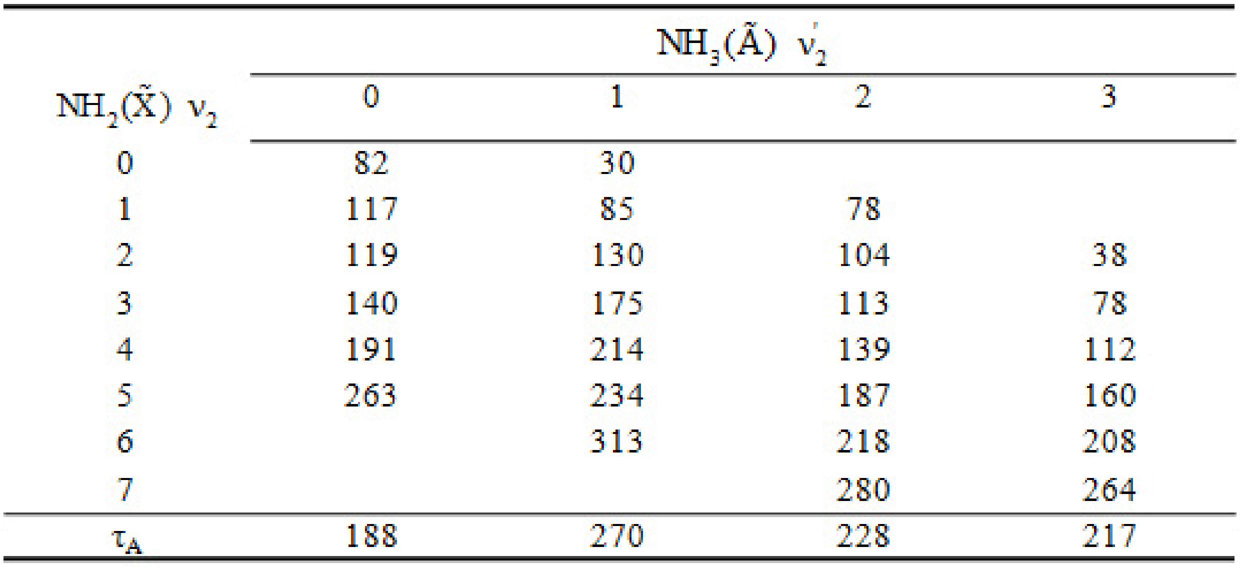

	$NH_3(\tilde{A})$ ν_2'			
$NH_2(\tilde{X})$ ν_2	0	1	2	3
0	82	30		
1	117	85	78	
2	119	130	104	38
3	140	175	113	78
4	191	214	139	112
5	263	234	187	160
6		313	218	208
7			280	264
τ_A	188	270	228	217

The H-ion signal level is due to both a) the H-atom population, and b) the 243.1 nm REMPI (2 +1) photoionization efficiency. The latter is constant and we can associate the H^+ signal level with the real time H-atom population instead of an artifact due to a change in ionization efficiency. Extracted time constants are then considered a direct measure of the H-atom elimination, and therefore the dissociation, timescales. An interpretation of the time constants allows one to understand the dissociation dynamics when NH_3 is prepared near the energetic barrier on the state.

Discussion of the dissociation times reported in Table 5.3 will proceed by inspecting their dependence on both the final NH_2 $(\tilde{X})$ ν_2 level and the initially excited NH_3 $(\tilde{A})$ ν_2' level. First, note the trend of lengthening timescales as energy in the ν_2 mode increases. Within each NH_3 $(\tilde{A})$ ν_2' level, the dissociation timescale increases by ~200 fs from the lowest to highest NH_2 $(\tilde{X})$ ν_2 level. Previous time-resolved studies have shown the same trend for higher ν_2' levels of NH_3 ($\tilde{A}$). [13, 14] Our analysis of NH_2 internal energy spectra has centered on the CI behaving like a funnel for NH_3 ($\tilde{A}$) trajectories leading to NH_2 ($\tilde{X}$) + H products. The CI causes acceleration of out-of-plane trajectories as they reach the exit channel and NH_2 is given large amounts of internal vibrational energy. As the out-of-plane angle increases, so too does the energy imparted to the NH_2 fragment. If we consider planar dissociation as a direct path along the NH_3 ($\tilde{A}$) PES, then non-planar dissociation can be viewed as taking an indirect path. Indirect dissociation pathways sample more of the NH_3 ($\tilde{A}$) PES before reaching the CI and causes elongation of dissociation times observed in our NH_2 vibrational level dependent data.

To continue our analysis of timescales reported in Table 5.3 we note the trend in timescales as a function of ν_2'. It is in this trend that we expect to see influence of tunneling through the energetic barrier on NH_3 ($\tilde{A}$) dissociation times. The average dissociation time, τ_A, is obtained by integrating all NH_2 internal energies for each ν_2' level. Values for τ_A are higher than the results for τ_D obtained by TR-PES. We correlate this discrepancy to: 1) the TR-PES measurements may slightly underestimate the H-atom elimination timescale due to the ionization window loss along the R_{N-H} coordinate as described above, and 2) the additional time required for the wavepacket to move from the CI to the dissociation limit. The general trend in rise times observed in the TR-PES experiment is preserved by τ_A, whereby an increase is observed from the zeroth level to the first and then a decrease again at higher levels. Both $\nu_2' = 0$ and 1 are below the dissociation barrier, $\nu_2' = 2$ is at the barrier, and $\nu_2' = 3$ is above the barrier. [9] We consider the $\nu_2' = 2$ and 3 levels to pass over the barrier and move towards the CI without tunneling. Both $\nu_2' = 0$ and 1 levels must tunnel through the barrier. We account for this lifetime trend by noting again that the barrier rises steeply with the out-of-plane angle. The excited state flux in the planar geometry ($\nu_2' = 0$ level) will then encounter a smaller potential than excited state flux in the non-planar geometry ($\nu_2' =$ 1 level). As such, tunneling at planar geometries will proceed more quickly than tunneling through non-planar geometries; ergo τ_A = 188 fs ($\nu_2' = 0$) whilst τ_A= 270 fs ($\nu_2' = 1$).

5.5 CONCLUSIONS

TR-PES and TR-TKER have been used to investigate dissociation dynamics of the NH_3 ($\tilde{A}$) state in $\nu_2' = 0$ - 3 vibrational levels. This study serves to extend our previous measurements [13] to observe varying dynamics due to tunneling through the NH_3 ($\tilde{A}$) state potential energy barrier. Relaxation along the N-H stretch coordinate is revealed as an umbrella/stretch combination band identified in the photoelectron spectra. The ν_2' dependent NH_3 ($\tilde{A}$) excited state relaxation times measured by TR-PES and H-atom emission times measured by TR-TKER reveal an increase from the zeroth level to the first and a decrease at higher levels. This trend is interpreted as tunneling from the zeroth and first vibrational levels through a barrier whose height is dependent on the out-of-plane angle. Further, TR-TKER results show a low NH_2 internal energy feature in the $\nu_2' = 0$ and 2 spectra which is indicative of planar dissociation geometries reaching the NH_3 ($\tilde{X}$)/NH_3 ($\tilde{A}$) CI. Absence of this feature in the $\nu_2' = 1$ and 3 spectra is due to non-planar trajectories being funneled through the CI while imparting rotational and vibrational energy to the NH_2 product.

5.6 REFERENCES

[1] S. W. Leifson, Astrophys. J, 1926, 63, 73.

[2] A. E. Douglas, Discuss.Faraday Soc., 1963, 35, 158.

[3] V. Vaida, M. I. McCarthy, P. C. Engelking, P. Rosmus, H. J. Werner and P. Botschwina, J. Chem. Phys., 1987, 86, 6669.

[4] J. H. Glowina, S.J. Riley, S.D. Colson and G. C. Nieman, J. Chem. Phys., 1980, 73, 4296.

[5] A. D. Walsh and P. Warsop, Trans. Faraday Soc., 1961,57, 345.

[6] R. N. Dixon, Chem. Phys. Lett., 1988,147, 377.

[7] L. D. Ziegler, J. Chem. Phys., 1985, 82, 664.

[8] M. I. McCarthy, P. Rosmus, H. J. Werner, P. Botschwina and V. Vaida, J. Chem. Phys., 1987, 86, 6693.

[9] H. Akagi, K. Yokoyama and A. Yokoyama, J. Chem. Phys., 2003, 118, 3600.

[10] S. Nangia and D. G. Truhlar, J. Chem. Phys., 2006, 124, 124309.

[11] Z. H. Li, R. Valero and D. G. Truhlar, Theor. Chem. Acc., 2007, 118, 9.

[12] X. Zhu, J. Ma, D. R. Yarkony, and H. Guo, J. Chem. Phys., 2012, 136, 234301.

[13] N. L. Evans, H. Yu, G. M. Roberts, V. G. Stavros and S. Ullrich, Phys. Chem. Chem .Phys., 2012, 14, 104.

[14] K. L. Wells, G. Perriam and V. G. Stavros, J. Chem. Phys., 2009, 130, 074308.

[15] S. H. Yin, H. P. Liu, J. Y. Zhang, B. Jiang, D. A. Xu, L. Wang, G. H. Sha and N. Q. Lou, Chem. Phys. Lett., 2002, 356, 227.

[16] W. Lai, S. Y. Lin, D. Xie, and H. Guo, J. Chem. Phys., 2008,129, 154311.

[17] K. Giri, E. Chapman, C. S. Sanz, and G. Worth, J. Chem. Phys., 2011, 135, 044311.

[18] J. Ma, X. Zhu, H. Guo, and D. R. Yarkony,J. Chem. Phys., 2012, 137, 22A541.

[19] J. Biesner, L. Schnieder, G. Ahlers, X. Xie, K. H. Welge, M. N. R. Ashfold and R. N. Dixon, J. Chem. Phys., 1989, 91, 2901.

[20] J. Biesner, L. Schnieder, J. Schmeer, G. Ahlers, X. Xie, K. H. Welge, M. N. R. Ashfold and R. N. Dixon, J. Chem. Phys., 1988, 88, 3607.

[21] V. M. Donnelly, A. P. Baranovski and J. R. McDonald, Chem. Phys., 1979, 43, 271.

[22] M. L. House, Y. H. Yoon and F. F. Crim, Mol. Phys., 2008, 106, 1127.

[23] A. Bach, J. M. Hutchinson, R. J. Holiday and F. F. Crim, J. Chem. Phys., 2002, 116, 9315.

[24] N. L. Evans and S. Ullrich,J. Phys. Chem. A., 2010, 114, 11225.

[25] C. A. Williams, G. M. Roberts, H. Yu, N. L. Evans, S. Ullrich and V. G. Stavros, J. Phys. Chem. A., 2012, 116, 2600.

[26] H. Yu, N. L. Evans, V. G. Stavros and S. Ullrich, Phys. Chem. Chem. Phys., 2012, 14, 6266.

[27] G. M. Roberts, C. A. Williams, H. Yu, A. S. Chatterley, J. D. Young, S. Ullrich and V. G. Stavros, Faraday Discuss., 2013, DOI: 10.1039/C3FD20140B

[28] S-H Lee, K-C Tang, I. Chen, M. Schmitt, J. P. Shaffer, T. Schultz, J. G. Underwood, M. Z. Zgierski, and A. Stolow, J. Phys. Chem. A, 2002, 106, 8979.

[29] J. D. H. Eland, Int. J. Mass Spectrom. Ion Phys.,1969, 2, 471.

[30] J. Xie, B. Jiang, G. Li, S. Yang, J. Xu, G. Sha, D. Xu, N. Lou and C. Zhang, Faraday Discuss., 2000, 115, 127.

[31] G. Reiser, W. Habenicht and K. Mller-Dethlefs, J. Chem. Phys., 1993, 98, 8462.

[32] W. P. Kraemer and V. Spirko, J. Molec. Spectrosc., 1992, 153, 276.

[33] C. Leonard, S. Carter and N. C. Handy, Phys. Chem. Chem .Phys., 2002, 4, 4087.

[34] A. Peluso, R. Borrelli and A. Capobianco, J. Phys. Chem., 2009, 113, 14831.

[35] W. Habenicht, G. Reiser and K. Mller-Dethlefs, J. Chem. Phys., 1991, 95, 4809.

[36] R. Locht, B. Leyh, W. Denzer, G. Hagenow and H. Baumgartel, Chem. Phys., 1991, 155, 407.

[37] R. Locht, K. Hottmann, G. Hagenow, W. Denzer and H. Baumgartel, Chem. Phys. Lett., 1992, 190, 124.

[38] S. N. Yurchenko, W. Thiel, M. Carvajal andP. Jensen, 2008, Chem. Phys., 346, 146.

[39] M. Barbatti and S. Ullrich, Phys. Chem. Chem. Phys., 2011, 13, 15492.

[40] R. Crespo-Otero, M. Barbatti, H. Yu, N. L. Evans and S. Ullrich, Chem. Phys. Chem., 2011, 12, 3365.

[41] W. E. Groth, U. Schurath and R. N. Schindler, J. Phys. Chem., 1968,72, 3914.

[42] P. Kruit and F. H. Read, J. Phys. E., 1983, 16, 313.

[43] S. Zhou, Z. Li, D. Xie, S. Y. Lin and H. Guo, J. Chem. Phys., 2009, 130, 184307.

[44] A. Alijah and D. Duxbury, J. Mol. Spectrosc., 2002, 211, 16.

[45] W. Gabriel, G. Chambaud, P. Rosmus, S. Carter and N. C. Handy, Mol. Phys., 1994, 81, 1445.

CHAPTER 6

WAVELENGTH DEPENDENCE OF ELECTRONIC RELAXATION IN ISOLATED ADENINE USING UV FEMTOSECOND TIME-RESOLVED PHOTOELECTRON SPECTROSCOPY [3]

---

[3] N. L. Evans and S. Ullrich 2010, *Journal of Physical Chemistry*, **114**, 11225.
Reprinted here with permission of the publisher.

6.1 ABSTRACT

Electronic relaxation pathways in photoexcited nucleobases have received much theoretical and experimental attention due to their underlying importance to the UV photostability of these biomolecules. Multiple mechanisms with different energetic onsets have been proposed by ab initio calculations yet the majority of experiments to date have only probed the photophysics at a few selected excitation energies. We present femtosecond time-resolved photoelectron spectra (TRPES) of the DNA base adenine in a molecular beam at multiple excitation energies between 4.7 - 6.2 eV. The two-dimensional TRPES data is fit globally to extract lifetimes and decay associated spectra for unambiguous identification of states participating in the relaxation. Furthermore, the corresponding amplitude ratios are indicative of the relative importance of competing pathways. We adopt the following mechanism for the electronic relaxation of isolated adenine; initially the $S_2(\pi\pi^*)$ state is populated by all excitation wavelengths and decays quickly within 100 fs. For excitation energies below ~5.2 eV, the $S_2(\pi\pi^*) \rightarrow S_1(n\pi^*) \rightarrow S_\circ$ pathway dominates the deactivation process. The $S_1(n\pi^*) \rightarrow S_\circ$ lifetime (1032 - 700 fs) displays a trend toward shorter time constants with increasing excitation energy. On the basis of relative amplitude ratios, an additional relaxation channel is identified at excitation energies above 5.2 eV.

6.2 INTRODUCTION

Extraterrestrial ultraviolet (UV) light is a major cause of radiation induced molecular processing on both the prebiotic and present day Earth. The absence of significant atmospheric shielding on the early Earth caused photodestruction of molecules which were not inherently stable under intense UV radiation. However, photostable organic molecules were ubiquitous and were able to participate in the complex molecular evolution which lead to the formation of life. [1] Incorporation of the nucleic acid bases, adenine, cytosine, guanine, thymine, and uracil, into our genetic code may be an important example of this selection methodology, as isolated nucleobases have displayed remarkable photostability. Due to the significance of nucleic acids as the genetic coding material, the photophysics of nucleobases has received considerable theoretical and experimental attention which has recently been reviewed. [2] Singlet excited states of nucleobases are populated upon UV absorption, and their UV photostability relies on relaxation mechanisms which convert this electronic energy into vibrational energy, the later being easily quenched in solution. [3] Electronic relaxation must occur on an ultrafast time scale in order to dominate over photochemical processes which could lead to destruction of the molecule. The UV photophysics of the purine base adenine (Fig 6.1) has been detailed in a recent review, [4] and is therefore discussed only briefly here.

The UV vapor phase absorption spectrum of adenine [5] as relevant to this work extends from approximately 300 to 200 nm with maxima at ∼250 and ∼207 nm. High resolution spectroscopies [6 - 8] have identified a number of low-lying excited states of nπ^*, $\pi\pi^*$, and $\pi\sigma^*$ character in this region. The resonance-enhanced multi-photon ionization (REMPI) spectrum displays discrete transitions near 36000 cm^{-1} which evolve into a broad featureless band above 37000 cm^{-1}. [6] These spectral observations are indicative of fast radiationless decays following S$_2(\pi\pi^*)$ excitation, and quantum chemical calculations have predicted several excited state relaxation pathways to describe these mechanisms. The most commonly discussed relaxation pathways are those of Broo [9] and Domcke et al. [10, 11], Broo sug-

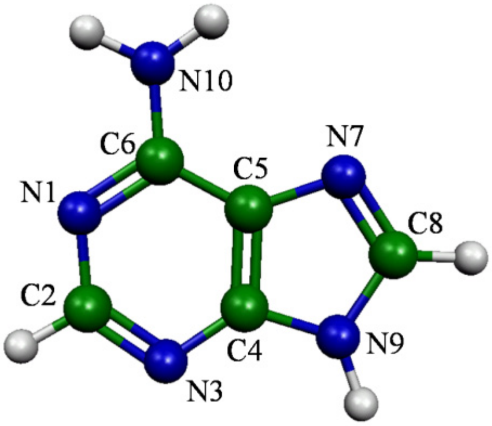

Figure 6.1: Structure and standard numbering of N(9)-H adenine.

gests a nearly barrierless two-step $S_2(\pi\pi^*)\rightarrow S_1(n\pi^*)\rightarrow S_\circ$ relaxation along a six-membered ring-puckering coordinate. Alternatively, Domcke and co-workers have identified a conical intersection between the $S_2(\pi\pi^*)$ and $S_3(\pi\sigma^*)$ states which occurs ~0.5 eV above the $S_2(\pi\pi^*)$ band origin. Photoexcited adenine then efficiently relaxes, along the repulsive $S_3(\pi\sigma^*)$ state, to the ground state via large amplitude N(9)-H motion. Additional pathways have been proposed with various onsets and barriers and include $S_1(n\pi^*)$ mediated decays, [12 - 16] a five-membered ring opening at the C(8)-N(9) bond involving a valence type $\pi\sigma^*$ state, [17] a $\pi\sigma^*$ state associated with N-H dissociation at the amino group, [15, 17] and direct $S_2(\pi\pi^*)$ to $S_\circ$ conversion through C(2) out-of-plane twisting of the six membered ring. [12, 15, 17 - 21] While quantum chemical calculations can, in general, suggest potential electronic relaxation pathways based on crossings between potential energy surfaces, the prediction of dynamical processes, and hence the significance of different pathways remains challenging. [22 - 24].

Great experimental effort has been put forth to clarify the quantum yield and energetic onset of each relaxation pathway. A two-step mechanism involving one short- and one long-lived state is widely accepted, and $S_1(n\pi^*)$ is commonly identified as the long-lived state having a lifetime of several hundred fs to a few ps. [2, 4, 25 - 30]. The short-lived state has a lifetime generally reported as less than 100 fs [2, 4, 25 - 29] and can be attributed to the initially excited $S_2(\pi\pi^*)$ state. However, contribution of the $S_3(\pi\sigma^*)$ pathway to the photophysical properties of adenine and its energetic onset are still heavily discussed. The $S_3(\pi\sigma^*)$ state is generally difficult to detect as it is dark in absorption and is expected to undergo ultrafast dynamics due to its repulsive character. 9-methyl adenine has been used as an indirect probe of $S_3(\pi\sigma^*)\rightarrow S_\circ$ relaxation via several experimental approaches including: time-resolved ion yield (TRIY), time-resolved photoelectron spectroscopy (TRPES), and hydrogen (H) atom detection. Methyl substitution at the N(9)-H coordinate alters the $S_2(\pi\pi^*)\rightarrow S_3(\pi\sigma^*)\rightarrow S_\circ$ relaxation pathway [31] and hence may result in increased excited state lifetimes, photoelectron spectral changes and altered N(9)-H fragmentation dynamics. TRIY measurements at 267 nm excitation [28] reveal a double-exponential decay with lifetimes of 100 fs and 1.1 ps before and 110 fs and 1.3 ps after methylation. The authors consider these lifetimes as essentially unchanged and conclude that the $S_3(\pi\sigma^*)$ state does not participate in the relaxation of adenine after 267 nm excitation. A combined TRIY and TRPES [29] experiment of 9-methyl adenine also reports no evidence of $S_3(\pi\sigma^*)$ at 267 nm. However, photoelectron spectral differences which are apparent between adenine and 9-methyl adenine in a different TRPES [25] study support the presence of the $S_3(\pi\sigma^*)$ state at the same excitation wavelength. Similarly, TRPES measurements of adenine report the participation of $S_3(\pi\sigma^*)$ at 266 nm but not at 250 or 277 nm based on wavelength dependent spectral changes. [26, 27] Relaxation along the repulsive $S_3(\pi\sigma^*)$ potential energy surface can result in ejection of H atoms from the N(9) position. These H atoms can be distinguished from H atoms that boil off of the vibrationally hot ground state by their fast and narrow velocity distribution and short appearance times following excitation. Although the quantum yield is expected to be small, [15] experiments have identified fast H atoms at several different excitation energies. The most comprehensive H atom detection study to date [32] reports participation of the $S_3(\pi\sigma^*)$ relaxation channel at excitation wavelengths in the 226 - 233 nm range. As noted by the authors, this is contradictory to results of similar experiments that attribute H atoms observed at 266 [33, 34] and 243 nm [35] excitation wavelengths to the $S_3(\pi\sigma^*)$ pathway.

From the brief discussion above, it becomes apparent that inconsistencies remain regarding the respective onsets and branching ratios of competing pathways involved in electronic relaxation of adenine. Given a possibly universal role of the σ^* channel in deactivation processes of numerous heteroatomic molecules [36] (e.g. azoles and phenols), further investigations of the adenine relaxation dynamics are certainly warranted. We aim to resolve some of the inconsistencies described above in an extensive wavelength dependency study using TRPES. TRPES is particularly well suited for the study of electronic excited state dynamics in biomolecules, [37] as it simultaneously provides both spectrally and time-resolved information. In TRPES, an isolated molecule is excited by a pump laser pulse and is probed through photoionization by a time-delayed probe pulse. Changes in the photoelectron spectrum, observed as the delay between pump and probe pulses is scanned, can be associated with electronic configurational changes during relaxation. Lifetimes of the participating excited states can then be extracted from the time-evolution of individual channels in the photoelectron spectrum. Another advantage of using TRPES is that states, such as $S_3(\pi\sigma^*)$, which are dark in absorption, can be probed as ionization is always allowed. We apply UV fs TRPES in a broad wavelength dependency study of the electronic relaxation mechanisms of the DNA base adenine. We identify pathways accessible at excitation wavelengths between 200 - 265 nm, extract their wavelength-dependent lifetimes and comment on their relative importance.

6.3 EXPERIMENT

The experimental set up employed for the present study consists of a fs laser system with UV conversion capabilities, gaseous molecular beam source, TOF ion mass and magnetic bottle photoelectron energy spectrometers.

The commercially available (Coherent Inc.) fs laser system consists of a diode pumped Ti:Sa oscillator (MIRA Optima 900) and a regenerative amplifier (Legend Elite HE) with 800 nm output (3.2 W, 11 nm bandwidth, 140 fs pulse duration measured by intensity autocorrelation) at 1 kHz repetition rate. UV pump and probe pulses are created from the amplifier output in subsequent frequency conversion steps. For use as the probe, the fourth harmonic of the amplifier fundamental is produced in a custom-built set up based on second harmonic and sum-frequency generation. Tunable UV (238 - 267 nm) pump pulses are created by an optical parametric amplifier (Coherent Inc. OperA), and are time-delayed relative to the probe pulses via an optical delay line. Pump and probe pulses, with typical pulse energies of 3.0 and 0.5 μJ, respectively, are focused (f = 50, 75 cm) collinearly into the interaction region of our time-of-flight spectrometer through a UV fused silica window. We present results from TRPES experiments using pump wavelengths of 265.1, 259.9, 251.3, 246.0, 238.1, and 200.5 nm.

The vacuum system consists of two parts: a high vacuum molecular beam source chamber and an ultra-high vacuum photoelectron photoion coincidence (PEPICO) spectrometer. The molecular beam source chamber is divided into two differential pumping stages by a removable inner wall. The first stage is equipped with two Varian VHS-6 diffusion pumps (4000 l/s pumping speed total), and contains a stainless steel nozzle assembly for generation of the molecular beam. The beam is skimmed at the inner wall by a 3 mm diameter conical skimmer before entering the outer chamber which is evacuated by a Varian M6 diffusion pump (1800 l/s). The stainless steel molecular beam nozzle consists of a cylindrical cavity with backing gas inlet and 200 m pinhole aperture on opposing ends. The pinhole is positioned 15 cm from the first skimmer. Adenine powder (Sigma >99.9%) is held in the cavity where it is isolated from metallic contact by quartz glass. To create sufficient vapor pressure the sample and nozzle assembly are heated to 190 - 220 °C. Adenine vapor and helium (He) backing gas, maintained at 150 Torr, undergo continuous supersonic co-expansion through the pinhole. Before entering the PEPICO spectrometer, the molecular beam passes a second skimmer (5 mm diameter) which is mounted 30 cm after the first skimmer on an ultra-high vacuum gate valve separating the spectrometer from the source chamber. The molecular beam and fs time-delayed pump and probe pulses intersect in the ionization region of the PEPICO spectrometer, which is evacuated by a Mitsubishi Heavy Industries magnetically levitated turbo pump (MHI FT-3301W) (2100 l/s).

The magnetic bottle photoelectron spectrometer is based on an axially magnetized permanent ring magnet that produces a strong, divergent field in the ionization region which is overlapped with a relatively weak homogenous field produced by a solenoid surrounding the electron flight tube. Photoelectron trajectories are parallelized by the ring magnet field, and follow the solenoidal field toward a 40 mm diameter multi-channel plate (MCP) detector. The ring magnet is incorporated into the ion optics of the linear time-of-flight mass spectrometer and ions are extracted through the center hole of the magnet. Photoion and photoelectron TOF spectra are recorded by a two-channel multiscaler card (FAST Comtech P7888-2). LabView-based data acquisition software reads the multiscaler output, positions the optical delay stage, and operates shutters in the pump and probe beams. TOF spectra are recorded at each pump-probe delay according to the following measurement sequence: (1) position optical delay stage; (2) record pump-probe two-color TOF spectrum; (3) close pump beam shutter and record probe-only one-color TOF spectrum; (4) close probe beam shutter and record pump-only one-color TOF spectrum. Both pump and probe beams produce one-color ionization signals which are considered as background and are measured *in situ* by chopping each beam and recording a TOF spectrum. This background is then directly subtracted from the total signal to reveal only the two-color contribution. Each TOF spectrum is recorded for $\sim 10^4$ laser pulses to eliminate shot-to-shot laser instabilities, and the delay range is scanned back and forth several times to eliminate slow drifts in molecular beam intensity. Electron energy calibration is performed using 1,3 butadiene (BD) and nitric oxide (NO) which both have well resolved transitions in the energy range of interest. [38, 39] Energy resolution is estimated to be $\sim$0.05 eV for 1 eV photoelectrons and is comparable to the resolution limit due to the laser bandwidth (~1 nm at λ = 200 - 267 nm). Time-resolved scans of the calibration gasses are used to locate the temporal overlap of the pulses, which is referred to as $T_\circ$, and the full-width at half-max (FWHM) of the laser cross-correlation, which is generally 260 ± 20 fs inside the PEPICO spectrometer. The FWHM defines the timing resolution of our experiments and is also referred to as the instrument response function.

6.4 RESULTS AND DISCUSSION

Time-resolved Photoelectron Spectroscopy

Presented in column a), of Fig 6.2 are TRPES spectra recorded at pump wavelengths of (top to bottom) 265.1, 259.9, 251.3, 246.0, 238.1, and 200.5 nm. A 200 nm probe is used for all pump wavelengths. All plots are shown, after one-color background signals have been subtracted, as pump-probe delay versus electron binding energy (total photon energy minus electron kinetic energy). Similar time-evolution is observed in TRPES spectra at all pump wavelengths whereby a broad band is evident within 150 fs of $T_\circ$ in the 8 - 12 eV range, and shifts to 9.5 - 12 eV at longer delay times. Thus, at positive delay times two channels with differing spectral profile are needed to fit the short- and long-lived bands in the 2-D data. Both bands shift toward higher binding energy with increasing excitation energy due to the additional vibrational energy added above the excited state origin. Also noticeable is that the relative contribution at negative pump-probe delays (i.e. probe-pump) from 200 nm excitation signal is smallest at wavelengths near adenines absorption maximum (~250 nm) and increases toward the edge of the absorption curve. This is perhaps most evident in the delay traces in column d) where the cyan and magenta curves represent the negative delay channel amplitudes. While the relative amplitude of the probe-pump channel may vary significantly, the spectrum and dynamics are expected to be identical for all TRPES spectra except for a wavelength dependent total energy cut off. Hence, the 200 + 200 nm

TRPES experiment presented in row 6 of Fig 6.2 provides essential information about this channel.

Global fits are prepared of our TRPES spectra whereby lifetimes and decay associated spectra are extracted for each of the participating electronic states. Fitting the 2-D data is particularly challenging in the region near $T_\circ$ due to fast dynamics which occur within the time-resolution of our experiment and overlapping spectral features of multiple decay channels. Fortunately, several fit parameters can be determined independently and are used as constraints in the 2-D global fit. The width of the instrument response function and $T_\circ$ are available from photoelectron calibration scans of BD and NO as mentioned above. At delays longer than 250 fs, spectra are integrated over the 9.5 - 12 eV band where a single channel is isolated. The resulting decay curve is fit using a single exponential convoluted with a Gaussian having the width of the instrument response function. Extracted decay constants listed in Table 6.1 range from 731 to 1032 fs, and are used as fixed time constants for a long-lived channel in the global fitting procedure. At negative delay times, the probe-pump photoelectron signal in data sets 1a) - 5a) of Fig 6.2 originates from 200 nm photoexciation (probe pulse) with ionization at the various UV wavelengths (pump pulse). A 2-D global fit of the symmetric 200 + 200 nm TRPES data (6a) allows us to extract time constants for 200 nm photoexcitation with more confidence than simply including a probe-pump channel(s) in the global analysis of the TRPES scans 1a) - 5a). The 200 + 200 nm TRPES data also clearly indicate the presence of two decay channels which are otherwise obscured. Global fits are shown in plots 6b) and 6c) of Fig 6.2, and reveal a short- and long-lived channel having decay constants of 35 ± 20 and 700 ± 50 fs, respectively. Probe-pump time constants are fixed to these values in the 2-D fits at longer excitation wavelengths. TRPES scans at excitation wavelengths 238 nm and longer are fit using three channels of fixed decay constants (one long positive, one long negative, and one short negative) as described above and one short-lived positive channel with variable decay time. Decay associated spectra of all four channels are fit simultaneously, and are shown in columns b) and c) of Fig 6.2 for the two channels present

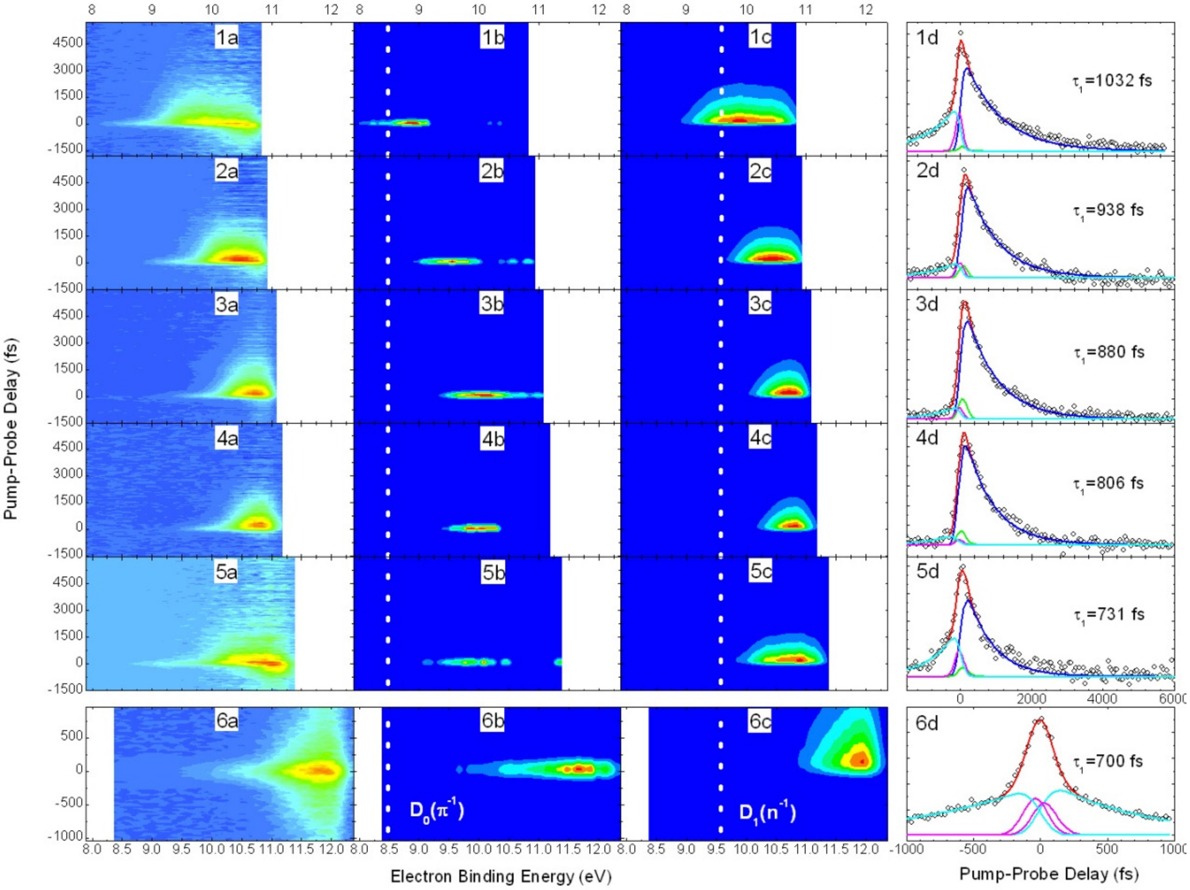

Figure 6.2: TRPES scans of adenine at (1) 265.1, (2) 259.9, (3) 251.3, (4) 246.0, (5) 238.1, and (6) 200.5 nm pump wavelengths and 200.5 nm probe. Experimental data (a) and 2-D decay associated spectra of the two relevant pump-probe channels ((b), (c)) extracted from fits are shown on a comon electron binding energy axis. Dashed lines in (b) and (c) represent vertical ionization energies from He(I) photoelectron spectroscopy of the $D_\circ(\pi^{-1})$ and $D_1(n^{-1})$ ionic states, respectively. Energy-integrated decay traces for all four channels are shown in (d): ○ is total photoelectron signal; red is total fit; green and blue are short- and long-lived pump-probe channels; magenta and cyan are short- and long-lived probe-pump channels

at positive pump-probe delays. Decay constants of the short-lived state are extracted from the 2-D fits 1b) - 5b) and are included in Table 6.1. A large error (>50%) is associated with these time constants as they are within the timing resolution of our experiment. Energy integration of the 2-D fits yields the decay profiles shown in column d).

Electronic excited states are identified from our photoelectron spectra through *ab initio* Koopmans'-like ionization correlations: [27] $S_1(n\pi^*) \rightarrow D_1(n^{-1})$, $S_2(\pi\pi^*) \rightarrow D_0(\pi^{-1})$, and $S_3(\pi\sigma^*) \rightarrow D_0(\pi^{-1})$. Vertical ionization energies, $D_0 = 8.48$ eV and $D_1 = 9.58$ eV, are known from He(I) photoelectron spectroscopy, [40] and are indicated as dashed lines in columns b) and c) of Fig 6.2. In rigid aromatic systems with similar ground and excited state geometries, we expect the observed TRPES ionization potentials to be comparable to the He(I) values but shifted by the vibrational energy deposited into the excited state. [37] This effect is in fact nicely visible as the decay associated spectra of the short- and long-lived channels in columns b) and c) of Fig 6.2 shift toward higher binding energy with increasing pump photon energy. Taking these shifts into account, we assign the photoelectron spectra as follows: The short-lived channel displays ionization into $D_0(\pi^{-1})$ which is associated with the $S_2(\pi\pi^*)$ state. Unfortunately, the $S_2(\pi\pi^*)$ and $S_3(\pi\sigma^*)$ states share the same ionization correlations. However, only $S_2(\pi\pi^*)$ is bright in absorption, and is therefore initially excited by the pump pulse. The dark $S_3(\pi\sigma^*)$ state can only be indirectly populated via excited state decay. Therefore, in the following discussion we nominally refer to $S_2(\pi\pi^*)$ as the short-lived state, but at this point cannot explicitly exclude contributions to the short-lived channel from $S_3(\pi\sigma^*)$. The long-lived state shows ionization into $D_1(n^{-1})$, and hence is assigned to the $S_1(n\pi^*)$ state. The short- and long-lived channels of the 200 nm pump TRPES spectrum are similarly assigned to $S_2(\pi\pi^*)$ and $S_1(n\pi^*)$, respectively. Although additional $\pi\pi^*$ states above $S_2(\pi\pi^*)$ may be accessible at 200 nm this assignment is adopted based on observed systematic shifts due to vibrational excitation. Assignments and extracted decay constants are compiled in Table 6.1.

Table 6.1: Excited-state decay lifetimes of adenine extracted from TRPES spectra.[a]

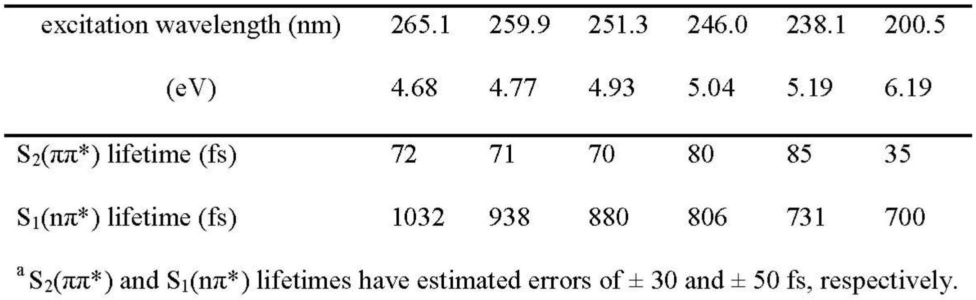

excitation wavelength (nm)	265.1	259.9	251.3	246.0	238.1	200.5
(eV)	4.68	4.77	4.93	5.04	5.19	6.19
$S_2(\pi\pi^*)$ lifetime (fs)	72	71	70	80	85	35
$S_1(n\pi^*)$ lifetime (fs)	1032	938	880	806	731	700

[a] $S_2(\pi\pi^*)$ and $S_1(n\pi^*)$ lifetimes have estimated errors of ± 30 and ± 50 fs, respectively.

The most evident observation in Table 6.1 is a steady trend toward shorter $S_1(n\pi^*)$ lifetimes as the excitation energy increases. Exciting $S_2(\pi\pi^*)$ with energy above the band origin results in a vibrationally active electronic state. A $S_1(n\pi^*)$ state populated from decay of such an $S_2(\pi\pi^*)$ state will also be highly vibrationally excited. Additional S_1/S_0 conical intersections may become accessible at high vibrational levels and account for the lifetime trend we observe. A similar lifetime trend may be expected for the $S_2(\pi\pi^*)$ state, however the short-lived time constants are within our laser cross-correlation and, hence our timing-resolution, and do not allow us to identify such a trend.

Relative contributions from each channel can be determined through inspection of the decay curve amplitudes shown in column d) of Fig 6.2. Comparison of the $S_1(n\pi^*)$:$S_2(\pi\pi^*)$ amplitude ratio at different excitation wavelengths allows us to determine the significance of each decay channel. Excitation wavelengths of 238 nm and longer all show a similar ∼10:1 ratio, but at 200 nm excitation this ratio is ∼1:1. Based on this observation, we conclude that relaxation is dominated by the $S_2(\pi\pi^*)\rightarrow S_1(n\pi^*)\rightarrow S_0$ pathway at long wavelengths, and that an additional pathway is accessible at excitation energies above 5.2 eV. Electronic spectra of the short-lived channel obtained at 200 nm excitation are significantly broadened in relation to spectra from longer pump wavelengths. The photoelectron signal slowly increases from around 9.5 eV toward its peak around 11.8 eV. This band shape is consistent with a Franck-

Condon progression of a large amplitude N(9)-H stretch motion as expected for relaxation along the repulsive $S_3(\pi\sigma^*)$ channel. Assignment of the photoelectron signal around 11.8 eV to ionization of higher $\pi\pi^*$ states into higher ionic states of π^{-1} character is also plausible, but would not explain the broadened photoelectron band shape.

Based on the above interpretation of our wavelength-dependent TRPES study we develop the following coherent picture to explain the UV photophysics of adenine. All pump wavelengths (200 - 265 nm) initially excite the $S_2(\pi\pi^*)$ state which decays to $S_1(n\pi^*)$ within 100 fs. The $S_1(n\pi^*)\rightarrow S_0$ deactivation occurs on a much longer time scale (700 - 1032 fs) which noticeably decreases with increasing vibrational excitation. This is most likely due to additional S_1/S_0 conical intersections accessible at high excitation energies. Based on the wavelength-dependent changes in channel amplitude ratios we conclude that relaxation to the ground state is dominated by a $S_2(\pi\pi^*)\rightarrow S_1(n\pi^*)\rightarrow S_\circ$ pathway for excitation energies below 5.2 eV, and that an additional pathway is accessible at higher energies and becomes a very significant contributor to the relaxation processes. Our tentative assignment of this additional channel to $S_2(\pi\pi^*)\rightarrow S_3(\pi\sigma^*)\rightarrow S_\circ$ is consistent with observed changes in the photoelectron band shape of the short-lived signal.

It is imperative to discuss our model within the bounds of previously published experimental and theoretical results. Our excited state assignment of the $S_2(\pi\pi^*)$ and $S_1(n\pi^*)$ states is based on vibrational shifts from known cationic ionization potentials and *ab initio* ionization correlations similar to previous TRPES studies. [25 - 27, 29] This is in agreement with various theoretical studies that propose a $S_2(\pi\pi^*)\rightarrow S_1(n\pi^*)\rightarrow S_\circ$ relaxation pathway. [9, 12 - 14] TRIY [28, 30] and TRPES [25 - 27] experiments using 266 nm excitation report $S_1(n\pi^*)$ lifetimes ranging from 750 to 1010 fs and at longer excitation wavelengths (277 nm) this time constant increases to several ps. [8, 26, 27] This supports the wavelength-dependent lifetime trend observed from our data. The fast dynamics of the $S_2(\pi\pi^*)$ generally occur within the experimental timing-resolution of most pump-probe experiments. Lifetimes are typically reported as less than 100 fs within large confidence intervals and further support our results. [25 - 28] An extensive mixed quantum-classical dynamics calculation by Lischka et al. [22] nicely reproduces the short and long time constants of this two step relaxation; another dynamics calculation by Chin et al. [16] predicts an excess energy dependent trend for the nπ^* excited state lifetimes. It is also noteworthy that 2-aminopurine, a constitutional isomer of adenine (6-aminopurine), displays very different photophysical properties, i.e. long lifetimes and high fluorescence quantum yields, due to a different electronic structure and relative ordering of electronically excited states. In 2-aminopurine, as opposed to adenine, the lowest electronically excited state is of $\pi\pi^*$ character. Excitation to the first $\pi\pi^*$ state is followed by geometric relaxation from the Franck-Condon region to the $\pi\pi^*$ minimum from where the system undergoes radiative deactivation to the ground state or alternatively has to pass a barrier to reach a higher-lying conical intersection with the ground state; [21] a $\pi\pi^*\rightarrow$ n$\pi^*\rightarrow$S$_\circ$ pathway analogous to adenine is unavailable.

We now turn our attention to discussion of S$_3(\pi\sigma^*)$ participation in the electronic relaxation of adenine. The S$_3(\pi\sigma^*)\rightarrow$S$_\circ$ conical intersection is predicted to be near 5 eV. [10] However, various experimental techniques employed to specifically probe this relaxation channel provide widely varying onset energies. TRPES studies of adenine report S$_3(\pi\sigma^*)$ participation at 267 nm (4.64 eV) but not at 250 nm (4.96 eV) [26, 27] and are further supported by TRPES methylation studies [25] that found evidence of this pathway at 267 nm. Selectively perturbing S$_3(\pi\sigma^*)$ via methylation would seem to give firm evidence of this relaxation channel. However, H atom detection experiments have also reported very different onsets of S$_2(\pi\pi^*)\rightarrow$S$_3(\pi\sigma^*)\rightarrow$S$_0$, ranging from 267 - 226 nm (4.64 - 5.49 eV), using the same substitution techniques. [32 - 35] Our results loosely assign this onset to be above 5.2 eV in accordance with Refs. [10, 32] but in contrast to Refs. [33 - 35].

Time-resolved Total Kinetic Energy Release Spectroscopy

This section contains supplementary data that was not included in the adenine TRPES publication. Here, results from TR-TKER measurements of adenine provide further evidence that the extra relaxation channel available above 5.2 eV excitation energy is in fact the theoretically predicted $S_3(\pi\sigma^*)$ channel.

The TR-TKER measurement technique is detailed in the ammonia experiment Chapters 3 and 4. The DUV pump wavelength generation technique of Chapter 4 is used here to provide the 0.3 μJ/pulse pump at 200 nm. The ~8 μJ/pulse 243 nm probe ionizes H-atoms through 2 + 1 photon REMPI. TOF to KE conversion and pump-probe delay timing calibration were performed as in Chapter 3. Adenine molecular beam generation is the same as in the experimental section of this chapter. The 2-D TR-TKER data is both time and energy resolved, and can be integrated in either dimension to provide the plots described below.

Figure 6.3 shows H-atom KE spectra obtained by integrating all spectra at Δt >500 fs. A low kinetic energy (low-KE) feature is located near 0.25 eV and a high kinetic energy (high-KE) feature is located near 1.20 eV. Previous measurements on adenine report low-KE H-atoms near 0.22 eV [32, 34] and high-KE H-atoms in the range 1.10 [32] - 1.22 [34]. Small differences are attributed to the use of slightly different excitation wavelengths, but our spectra are in general agreement with previous reports. H-atoms emitted *via* the dissociative $S_3(\pi\sigma^*)$ state are expected to carry KE of ~8000 cm^{-1}. [12, 15, 34] Presence of the high-KE H-atom feature is then clear spectroscopic evidence of $S_3(\pi\sigma^*)$ dissociation after 200 nm excitation. The low-KE H-atom component is associated with statistical decay due to multiphoton excitation of high lying excited states.

Figure 6.4 shows pump-probe delay traces for three regions of the H-atom KE spectrum. The delay traces are produced by integrating the 2-D TR-TKER data over specific KE regions (see vertical lines in Fig 6.3) at all pump-probe delays. Delay traces for the low-KE and high-KE H-atom regions and for the entire KE spectrum are shown in Fig 6.4. Each delay trace displays zero H-atom signal at Δt <0 fs followed by a step near Δt = 0 fs which reaches a plateau near Δt = 500 fs. Delay trace fits are made with a single exponential step convoluted by the Gaussian instrument response function of fixed FWHM = 230 fs.

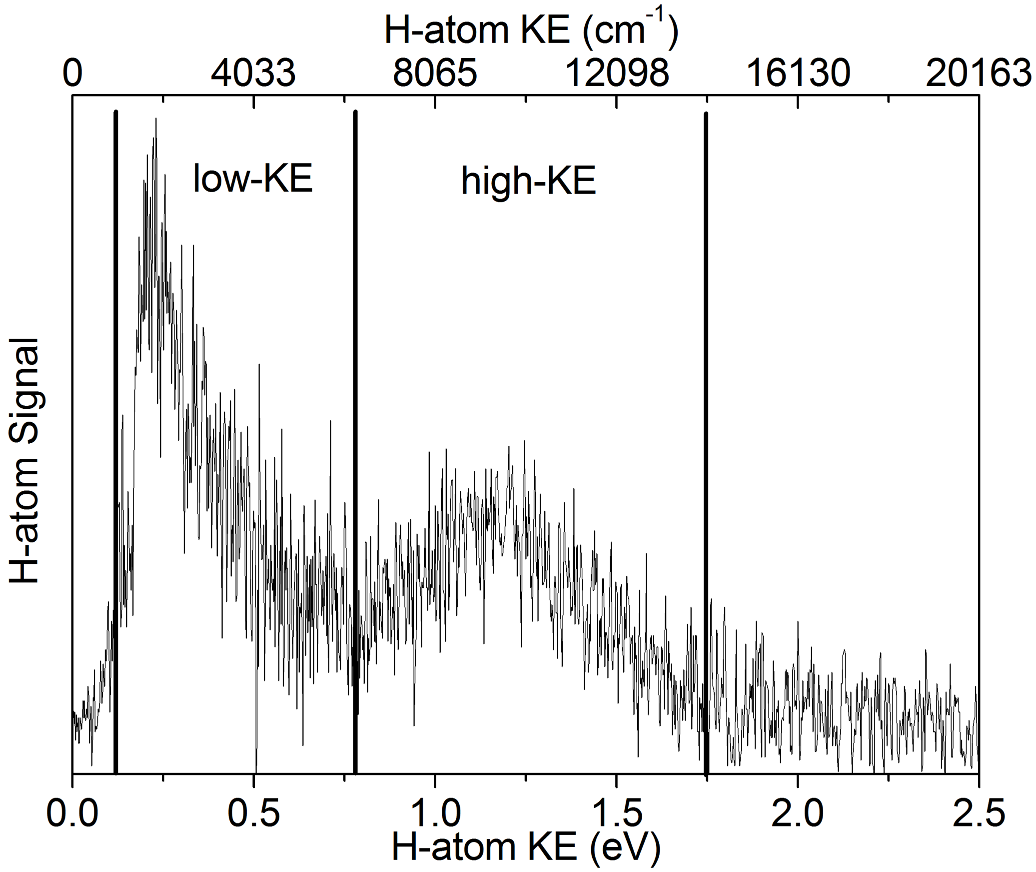

Figure 6.3: H-atom KE spectrum obtained from 200 nm excitation of adenine and time-delayed 243 REMPI probe. Spectrum obtained from integration of Δt >500 fs. Low-KE and high-KE features are evidence of statistical and $S_3(\pi\sigma^*)$ mediated H-dissociation, respectively. Indicated integration regions allow production of pump-probe delay traces for each dissociation mechanism.

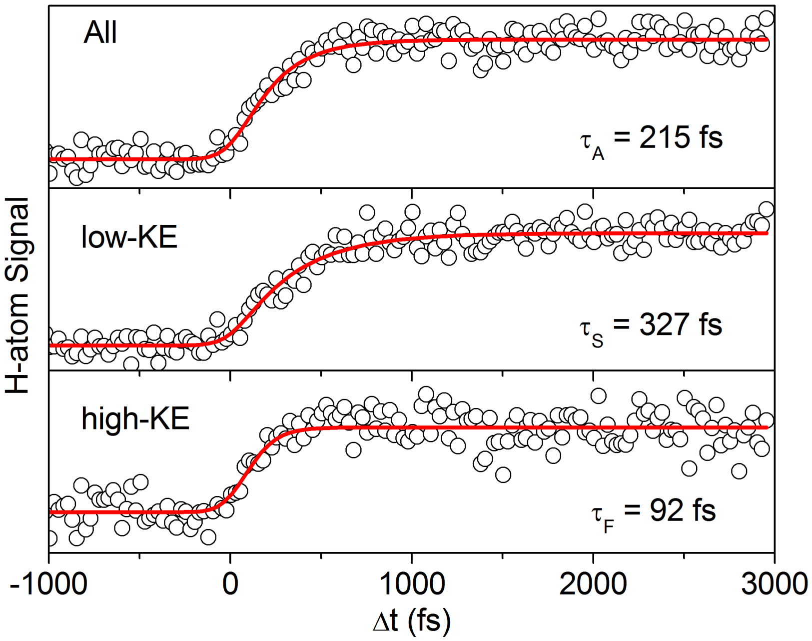

Figure 6.4: Pump-probe delay traces from TR-TKER measurement of adenine H-atom dissociation timescales. Integration over the low-KE and high-KE regions indicated in Fig 6.3 produces the delay traces in the lower two panels. Integration of all KE produces the top trace. Exponential rise constants for each fit are listed within each panel.

The point along the x-axis where the rise function begins ($\Delta t = 0$ fs) is allowed to vary within ±10 fs of zero. Exponential rise constants, τ, are extracted and represent the H-atom emission timescales for each region of the KE spectrum. The time constant error is ±20 fs as determined by preliminary fits with a variable value of $\Delta t = 0$. Having already assigned the low- and high-KE features allows discussion of dissociation timescales for each relaxation mechanism. Time constants for all energies (τ_A), low-KE (τ_L), and high-KE (τ_H) H-atoms are listed in Fig 6.4. The statistical decay of high lying excited states yields low-KE H-atoms on a timescale of $\tau_L = 327$ fs. Dissociation through the $S_3(\pi\sigma^*)$ excited state yields high-KE H-atoms on a timescale of $\tau_H = 92$ fs. The value of $\tau_A = 215$ fs is a signal intensity weighted average of the high-KE and low-KE components.

These TR-TKER measurements are an improvement over recent TRIY measurements of H-atom emission from adenine. In the work by Wells et al. [34] the total integrated H-atom signal was collected by mass spectroscopy and the delay trace was fit with the sum of two exponential step functions (τ_1 = 110 ±63 fs and τ_2 = 265 ±135 fs). Analysis of methylated adenines allowed these authors to assign the short time constant (τ_1) to $S_3(\pi\sigma^*)$ dissociation and the long time constant (τ_2) to statistical decay. Note, the relatively large error bars, which may be associated with fitting a single H-atom delay trace with two rise functions. Here, H-atoms from statistical and $S_3(\pi\sigma^*)$ dissociation are differentiated by KE and their emission timescales are measured separately. Our result is within the error of the previous report but is considered a more direct measurement of the dissociation timescale for each product and our values have much improved error bars.

6.5 CONCLUSIONS

Femtosecond TRPES spectra of the DNA base adenine isolated in a molecular beam have been presented at six excitation wavelengths between 265 - 200 nm (4.7 - 6.2 eV) in an effort to determine the energetic appearances and relative significance of competing electronic excited state relaxation pathways. The following model for ultrafast electronic relaxation has been proposed. At excitation energies below 5.2 eV, a $S_2(\pi\pi^*) \rightarrow S_1(n\pi^*) \rightarrow S_\circ$ relaxation mechanism dominates which populates the $S_1(n\pi^*)$ state in less than 100 fs. The $S_1(n\pi^*)$ state lifetime decreases from 1032 to 700 fs as excess vibrational energy is deposited into the the initially excited $S_2(\pi\pi^*)$ state and consequently additional S_1/S_0 conical intersections become energetically accessible. Observed changes in $S_1(n\pi^*)$:$S_2(\pi\pi^*)$ amplitude ratios indicate that an additional channel may significantly account for relaxation processes after photoexcitation above 5.2 eV. This additional channel has a lifetime of less than 100 fs and is consistent with the theoretically predicted $S_2(\pi\pi^*) \rightarrow S_3(\pi\sigma^*) \rightarrow S_\circ$ pathway.

Subsequent measurement of H-atom emission by TR-TKER has provided further evidence that the additional relaxation channel available above 5.2 eV is in fact due to the $S_3(\pi\sigma^*)$

state. H-atom KE spectra reveal a high-KE component within the energy range expected from calculations of $S_3(\pi\sigma^*)$ dissociation. This high-KE feature has a characteristic emission time of $\tau_H = 92 \pm 20$ fs which is further evidence of prompt dissociation along the N-H stretch coordinate of the $S_3(\pi\sigma^*)$ state.

6.6 ACKNOWLEDGEMENTS

Acknowledgement is made to the National Science Foundation (Award No. CHE-0924456) and the Donors of the American Chemical Society Petroleum Research Fund (ACS-PRF No. 44110-G6) for partial support of this research. The authors also thank the UGA Instrument Shop and R. M. Jordan Company for their help with design and construction of our PEPICO spectrometer and H. Yu, A. N. Brouillette, and W. M. Potter for their assistance.

6.7 REFERENCES

[1] Balucani, N. Int. J. Mol. Sci. 2009, 10, 2304-2335.

[2] Crespo-Hernandez, C. E.; Cohen, B.; Hare, P. M.; Kohler, B. Chem. Rev. 2004, 104, 1977-2019.

[3] Pecourt , J. -M. L.; Peon, J.; Kohler, B. J. Am. Chem. Soc. 2001, 123, 10370-10378.

[4] Bisgaard, C. Z.; Satzger, H.; Ullrich S.; Stolow, A. Chem. Phys. Chem. 2009, 10, 101-110.

[5] Clark, L. B.; Peschel, G. G.; Tinoco Jr., I. J. Phys. Chem. 1965, 69, 3615-3618.

[6] Kim, N. J.; Jeong, G.; Kim, Y. S.; Sung, J.; Kim, S. K.; Park, Y. D. J. Chem. Phys., 2000, 113, 10051-10055.

[7] Nir, E.; Plutzer, C.; Kleinermanns, K.; de Vries, M. Eur. Phys. J. D 2002, 20, 317-329.

[8] Luhrs, D. C.; Viallon, J.; Fischer, I. Phys. Chem. Chem. Phys. 2001, 3, 1827-1831.

[9] Broo, A. J. Phys. Chem. A 1998, 102, 526-531.

[10] Sobolewski, A. L.; Domcke, W. Eur. Phys. J. D 2002, 20, 369-374.

[11] Chung, W. C.; Lan, Z. G.; Ohtsuki, Y.; Shimakura, N.; Domcke, W.; Fujimura, Y. Phys. Chem. Chem. Phys. 2007, 9, 2075-2084.

[12] Perun, S.; Sobolewski, A. L.; Domcke, W. J. Am. Chem. Soc. 2005, 127, 6257-6265.

[13] Marian, C. M. J. Chem. Phys. 2005, 122, 104314-13.

[14] Lei, Y. B.; Yuan, S. A.; Dou, Y. S.; Wang, Y. B.; Wen, Z. Y. J. Phys. Chem. A 2008, 112, 8497-8504.

[15] Conti, I.; Garavelli, M.; Orlandi, G. J. Am. Chem. Soc. 2009, 131, 16108-16118.

[16] Chin, C. H.; Mebel, A. M.; Kim, G. S.; Baek, K. Y.; Hayashi, M.; Liang, K. K.; Lin, S. H. Chem. Phys. Lett. 2007, 445, 361-369.

[17] Perun, S.; Sobolewski, A. L.; Domcke, W. Chem. Phys. 2005, 313, 107-112.

[18] Zgierski, M. Z.; Patchkovskii, S.; Lim, E. C. Can. J. Chem. 2007, 85, 124-134.

[19] Chen, H.; Li, S. H. J. Phys. Chem. A 2005, 109, 8443-8446.

[20] Blancafort, L. J. Am. Chem. Soc. 2006, 128, 210-219.

[21] Serrano-Andres, L.; Merchan, M.; Borin, A. C. Proc. Natl. Acad. Sci. USA 2006, 103, 8691-8696.

[22] Barbatti, M.; Lischka, H. J. Am. Chem. Soc. 2008, 130, 6831-6839.

[23] Hudock, H. R.; Levine, B. G.; Thompson, A. L.; Satzger, H.; Townsend, D.; Gador, N.; Ullrich, S.; Stolow, A.; Martinez, T. J. J. Phys. Chem. A 2007, 111, 8500-8508.

[24] Fabiano, E.; Thiel, W. J. Phys. Chem. A 2008, 112, 6859-6863.

[25] Satzger, H.; Townsend, D.; Zgierski, M. Z.; Patchkovskii, S.; Ullrich, S.; Stolow, A. Proc. Natl. Acad. Sci. U.S.A. 2006, 103, 10196-10201.

[26] Ullrich, S.; Schultz, T.; Zgierski, M. Z.; Stolow, A. Phys. Chem. Chem. Phys. 2004, 6, 2796-2801.

[27] Ullrich, S.; Schultz, T.; Zgierski, M. Z.; Stolow, A. J. Am. Chem. Soc. 2004, 126, 2262-2263.

[28] Canuel, C.; Mons, M.; Piuzzi, F.; Tardivel, B.; Dimicoli, I.; Elhanine, M. J. Chem. Phys. 2005, 122, 074316-6.

[29] Canuel, C.; Elhanine, M.; Mons, M.; Piuzzi, F.; Tardivel, B.; Dimicoli, I. Phys. Chem. Chem. Phys. 2006, 8, 3978-3987.

[30] Kang, H.; Lee, K. T.; Jung, B.; Ko, Y. J.; Kim, S. K. J. Am. Chem. Soc. 2002, 124, 12958-12959.

[31] Bronsted Nielsen, S.; Solling, T. I. Chem. Phys. Chem. 2005, 6, 1276-1281.

[32] Nix, M. G. D.; Devine; A. L.; Cronin, B.; Ashfold, M. N. R. J. Chem. Phys. 2007, 126, 124312-10.

[33] Zierhut, M.; Roth, W.; Fischer, I. Phys. Chem. Chem. Phys. 2004, 6, 5178-5183.

[34] Wells, K. L.; Roberts, G. M.; Stavros, V. G. Chem. Phys. Lett. 2007, 446, 20-24.

[35] Hunig, I.; Plutzer, C.; Seefeld, K. A.; Louwenich, D.; Nispel, M.; Kleinermanns, K. Chem. Phys. Chem. 2004, 5, 1427-1431.

[36] Ashfold, M. N. R.; King, G. A.; Murdock, D.; Nix, M. G. D.; Oliver, T. A. A.; Sage, A. G. Phys. Chem. Chem. Phys. 2010, 12, 1218-1238.

[37] Stolow, A. Annu. Rev. Phys. Chem. 2003, 54, 89-119.

[38] Eland, J. H. D. Int. J. Mass Spec. and Ion Phys. 1969, 2, 471-484.

[39] Miller, J. C.; Compton, R. N. J. Chem. Phys. 1981, 1, 22-29.

[40] Peng, S.; Padva, A.; LeBreton, P. R. Proc. Natl. Acad. Sci. U.S.A. 1976, 73, 2966-2968.

CHAPTER 7

ON THE INTERACTION OF ADENINE WITH IONIZING RADIATION - MECHANISTICAL STUDIES AND ASTROBIOLOGICAL IMPLICATIONS [4]

---

[4] N. L. Evans, C. J. Bennett, S. Ullrich and R. I. Kaiser 2011, *Astrophysical Journal*, **730**, 69. Reprinted here with permision of the publisher.

7.1 ABSTRACT

The chemical inventory available on the prebiotic Earth was likely derived from both terrestrial and extraterrestrial sources. A complete description of which extraterrestrial molecules may have seeded early Earth is therefore necessary to fully understand the prebiotic chemical evolution which led to life. Galactic cosmic rays (GCRs) are expected to cause both the formation and destruction of important biomolecules - including nucleic acid bases such as adenine - in the interstellar medium (ISM) in both the gas-phase and within ices condensed on interstellar grains. The interstellar ultraviolet (UV) component is expected to photochemically degrade gas-phase adenine on a timescale of only several years. However, the destruction rate is expected to be significantly reduced when adenine is shielded within the ices of interstellar grains or even in dense molecular clouds. In these UV-shielded environments, biomolecule destruction by the energetic charged particle component of the GCR becomes important as it is not fully attenuated. Presented here are results on the destruction rate of the nucleobase adenine in the solid state at 10 K by energetic electrons, as generated in the track of cosmic ray particles as they penetrate interstellar ices. When both UV and energetic charged particle destructive processes are taken into account, the half-life of adenine within dense interstellar clouds is found to be 6 Myr which is on the order of the lifetime of star-forming molecular cloud. We also discuss chemical reaction pathways within the ices to explain the production of observed species, including the formation of nitriles (R-C=N), epoxides (C-O-C), and carbonyl functions (R-C=O).

7.2 INTRODUCTION

Deoxyribonucleic acid (DNA) and ribonucleic acid (RNA) - today responsible for storing and passing on our genetic information - are complex organic polymers composed of nitrogen-rich heterocyclic (N-heterocyclic) nucleobases attached to a sugar-phosphate backbone. Discussion still continues as to whether life first evolved in an “RNA world” as proposed by Gilbert [43] or whether self-replicating proteins evolved first, and later learned to use DNA/RNA to safe-guard sensitive genetic information. [53, 63, 96] The subsequent transition from either starting scenario to the DNA/RNA/protein world of extant life is yet to be fully understood. [35, 40, 80, 91] However, it is certain that organisms began accumulating and replicating DNA/RNA at some point along the evolutionary timeline. [32, 47] Hence, it is a necessity that to have been incorporated into DNA/RNA, the purine (adenine and guanine) and pyrimidine (cytosine, thymine, and uracil) nucleobases must have been readily available. Despite a significant research endeavor, terrestrial nucleobase origins are still unclear; also, it is unknown whether they were metabolized specifically for use in DNA/RNA or if they were simply part of the prebiotic organic inventory; if it is the latter case, it is essential to determine their formation and destruction mechanisms and subsequently how abundant they may have been on the primordial Earth.

The pioneering work of Miller [73] provided the first evidence that complex organics such as amino acids, sugars, and nucleic acid precursors could be created by electric discharge in a primordial Earth-like environment, and this work was the motivation for many successive experiments in the following decades. The synthesis of adenine ($C_5N_5H_5$; Fig 7.1) from concentrated ammonium cyanide solutions, heated to 80 - 90 °C, was first demonstrated by Oro and co-workers. [81, 82] Nucleobase formation has been reported under various terrestrial conditions [14, 52, 65, 90, 98]; however due to low yields and susceptibility to hydrolysis, [66, 101] the accumulation of a large quantity of terrestrially synthesized nucleobases remains troublesome.

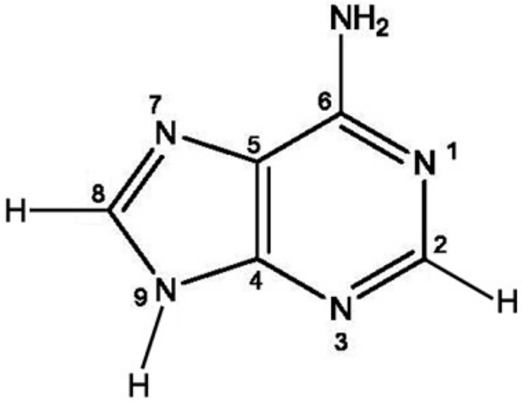

Figure 7.1: N(9)-H tautomer of the nucleic acid base adenine ($C_5N_5H_5$)

The organic inventory available on the early Earth was likely augmented by several exogenous sources [27, 29, 46] including atmospheric impact-shock synthesis [4, 39] and direct delivery of intact organics amidst comets, meteorites, [29] and interplanetary dust particles (IDP). [2] Chyba & Sagan [28] have compared the mass influx rate of organics by endogenous and exogenous sources, and report that for a presumably non-reducing terrestrial atmosphere ($[H_2]/[CO_2] \leq 0.1$) the influx of IDPs was the predominant source of prebiotic organics. It has been estimated that during the time period where life is thought to have begun - between 4.2 Gyr and 3.9 Gyr ago - up to 10^{18} kg of intact organic material could have been brought to the Earth via IDPs. [17] A detailed investigation of how biologically important interstellar molecules may form, their rates of production, and their survival lifetimes must therefore be undertaken in an effort to further understand the chemical composition of IDPs and therefore the chemical environment on the prebiotic Earth.

Let us consider the formation of N-heterocyclic nucleobases, and more specifically adenine, in the interstellar medium. The synthesis of adenine via gas-phase pathways in diffuse molecular clouds by hydrogen cyanide (HCN) oligomerization has been suggested. [24, 36, 41, 44] However, the HCN dimerization rate, [103] the inclusion of nitrogen into aromatic rings [93] and the presence of large reaction barriers [97] are significant factors which may limit the gas-phase production of adenine within such environments. Astronomical observations [25, 26, 108] have yet to identify adenine or its N-heterocyclic precursors in the gas-phase.

It is perhaps more likely that adenine may form in the solid state either inside, or on the surfaces of interstellar grains within molecular clouds. These small (up to a few 100 nm) icy grains exist at low temperatures, down to 10 K, and typically consist of a silicate/carbonaceous core covered with simple volatiles which have frozen out of the ISM; predominantly water (H_2O), but other detected species include carbon monoxide (CO), carbon dioxide (CO_2), ammonia (NH_3), methane (CH_4), formaldehyde (H_2CO), methanol (CH_3OH), and carbonyl sulfide (OCS). [42] These molecules serve as precursor species to the formation of more complex species as these ices are known to be chemically processed by both the charged particle and UV photon components of the Galactic Cosmic Radiation (GCR). Laboratory experiments studying these phenomena, have shown that both amino acids and nucleobases are created by UV photolysis, [11, 75, 77, 78, 79, 102] electron irradiation, [23, 51, 64] proton (H^+) irradiation, [62] and highly-charged heavy ion irradiation [89] of interstellar ice analogs. In addition, much of the cosmic carbon ($\sim$20 %) available to participate in adenine synthesis may already be incorporated into structurally similar species, such as polycyclic aromatic hydrocarbons (PAH), [1, 36] and N-heterocyclic PAHs, [72] which are expected to be abundant within the interstellar medium, and may also condense onto cold interstellar grains. [12] Similarly, radiation induced chemistry on these PAH-like grain surfaces and inside grain cavities is known to produce complex organics [22, 95] increasing the likelihood that grains are indeed a plausible location for interstellar nucleobase formation. In fact, there is evidence of extraterrestrial biologically important molecules in meteorites (for a review see [15]) including the discovery of the nucleobase uracil within the Murchison meteorite. [71]

However, in order to determine whether or not these molecules could have seeded the primordial Earth, we need to understand how likely it is that they could survive the harsh irradiation field experienced not only in the ISM, but also from the sun within our solar system. The survivability of nucleobases and their precursors in interstellar ice analogs under UV radiation has been discussed previously. [79, 87, 88] The main conclusions drawn from this work are that, i) decay half-lives of heterocyclic molecules decrease with the number of nitrogen atoms in the ring, ii) nucleobase half-lives are short at 1 AU from the Sun (hrs) or in diffuse clouds (yrs) where they are unshielded from the UV radiation, and iii) half-lives are greatly increased (106 yrs) in UV shielded environments such as dense clouds. These findings cannot exclude the possibility that nucleobases formed in UV shielded environments can survive over the lifetime of a typical dark cloud such as Taurus Molecular Cloud 1 (TMC-1). Dense molecular clouds and icy grain mantles serve to shield molecules from UV destruction, but do not shield from energetic charged particles of the GCR which are able to penetrate deep into these environments, and biomolecules which are formed here are subject to their destructive influence. Here, we report on the degradation rate of adenine ices at 10 K under simulated GCR conditions in an attempt to estimate the survivability of this important biomolecule under radiation by the charged particle component of the GCR. In addition, data on the reaction of oxygen atoms to chemically degrade adenine in extraterrestrial icy grains are presented.

7.3 EXPERIMENT

The experiments were conducted using the surface scattering machine at the University of Hawaii [5, 55] which was modified to accommodate a biomolecule sublimation source. Within the main vacuum chamber, held at 8.0 x 10^{-11} Torr, adenine powder (Sigma $\geq$ 99 %) is placed in a cylindrical stainless steel sample holder which is positioned 6 mm in front of a highly polished silver wafer maintained at 11.4 ± 0.3 K by a two-stage closed cycle helium refrigerator. The sample holder is surrounded by an oxygen-free high conductivity (OFHC) copper cylinder to which a programmable 50 W cartridge heater and a silicone diode temperature sensor are attached. The sample oven is heated to 443 K at 1 K min^{-1}

and is allowed to cool to 383 K in a 4 hour process during which, the sublimating adenine molecules are deposited onto the cooled silver target. To determine the adenine sample thickness; the column density, N, in molecules cm^{-2}, is calculated according to Bennett et al.. [5] The absorption intensity in cm^{-1} is obtained by taking the area under a Gaussian fit of each spectral feature, and the frequency dependent absorption coefficients are taken from the theoretical (B3LYP/6-31G(d,p)) values of Nowak et al.. [76] The pre-irradiation column density, $N_\circ = 8.10 \pm 0.76 \times 10^{16}$ molecules cm^{-2} of adenine, and the ice thickness, $d = N_\circ M/N_A\rho = 122 \pm 14$ nm, are derived by taking the average values from all identified bands between 1750 - 750 cm^{-1} (see Table 7.1); here, $M = 135.1$ amu and $\rho = 1.49$ g cm^{-3} [60] are the molecular mass and density of adenine, respectively; N_A is Avogadros number.

Test experiments determined that the close proximity of the oven to the silver wafer does not increase the wafer temperature, and that adenine vapor condenses on the silver wafer only at oven temperatures above 403 K. This assures that no thermal decomposition occurs during the deposition sequence. Note, that in order to remove water being deposited in our ice - which could serve as a potential contaminant during the experiment - the adenine sample was located inside the vacuum chamber during the bake-out procedure of the vessel, whereby it was typically held for 36 hours at 343 K; this temperature is below the reported sublimation temperature of adenine. [45, 56, 76] Previous experiments [38, 109] have verified that thermal decomposition is negligible at the sublimation temperatures used here; and further, that the N(9)-H tautomer is the dominant species in the gas-phase. [19, 67]

Besides the pure adenine samples, some early work has also been carried out to investigate how oxygen atoms may react to degrade adenine, whereby a 500 nm thick layer of molecular oxygen (O_2) is condensed on top of the adenine ice. A secondary deposition arm was used to co-condense molecular oxygen in order to prevent reactions between the oxygen and the adenine, which remains hot in the sample oven. The molecular oxygen layer was added to both a neat adenine ice and one which had already undergone the standard irradiation sequence.

The standard irradiation procedure is as follows. All neat adenine samples are irradiated for 3 hours with 5 keV electrons emitted from a SPECS model EQ 22-35 electron gun operating at a filament current of 1 μA, and all oxygen-covered adenine samples were irradiated for 2 hours with electron energy and current identical to the neat adenine experiments. The EQ 22-35 has a 78.8 % extraction efficiency and a 3.2 ± 0.3 cm^2 surface of the silver wafer is irradiated; the electron flux is then, ϕ = 1.54 x 10^{12} electrons cm^{-2} s^{-1}. The chemical processing of the adenine ices is monitored on line and *in situ* by a Thermoelectron 6700 FTIR. Spectra (194 scans from 6000 - 400 cm^{-1} at 2 cm^{-1} resolution) are continuously recorded during irradiation in 1.6 min intervals. After being kept isothermally at 11 K without further irradiation for 30 minutes, the samples are heated to room temperature at a rate of 0.5 K min^{-1}.

7.4 RESULTS

The infrared spectrum of the adenine ice prior to irradiation is shown in Fig 7.2 (black line); mode assignments are taken from the argon matrix isolation experiments of Nowak et al. [76] and are listed in Table 7.1. Large frequency red-shifts, up to 60 cm^{-1}, are seen for the ν_6, ν_8, ν_{10}, ν_{17}, ν_{19}, ν_{24} modes; all of which involve hydrogen (H) atom or amino group (NH_2) motion. These shifts are caused by intermolecular adenine-adenine interactions, which are absent in the argon matrix isolation experiments. Apart from these shifts, our peak positions agree exceptionally well with the matrix isolation studies. Upon electron irradiation, the absorption intensity decreases by at least 25 % for all modes as can be visualized in Fig 7.2. The absorption intensity of several prominent modes, including ν_{11}, ν_{14}, ν_{16}, and ν_{25}, is monitored throughout the irradiation in order to quantify the decomposition kinetics of the adenine ice. Column densities for each characteristic mode are calculated according to Bennett et al. [5] and are plotted versus irradiation time in Fig 7.3.

Table 7.1: Infrared absorptions of adenine ice at 10 K prior to irradiation, along with corresponding assignments of the observed bands.

Frequency (cm^{-1})	Frequency[a] (cm^{-1})	Mode[b]	Characterization[b]
1681	1639, 1633	ν_6	β NH$_2$ scis (28), ν C6N10 (21), ν C5C6 (19)
1609	1612	ν_7	ν N3C4 (27), ν C5C6 (12)
1506		ν_8	β NH$_2$(48), ν C4C5 (12)
1456	1474	ν_{10}	ν C6N1 (24), β C2H (27), ν C6N10 (13), β NH$_2$ scis (12), ν C2N3 (12)
1420	1419	ν_{11}	ν C4C5 (27), ν C4N9 (21)
1368	1345	ν_{13}	ν N9C8 (20), β C8H (13), β N9H (10), ν C6N1 (10)
1335	1328	ν_{14}	ν N1C2 (31), ν C5N7 (19), β C2H (11)
1309	1290	ν_{15}	ν C2N3 (43), ν C5N7 (13), ν N1C2 (10)
1255	1240	ν_{16}	β C8H (36), ν N7C8 (16), β N9H (10)
1160	1229	ν_{17}	β NH$_2$ rock (26), ν C5N7 (22)
1126	1127	ν_{18}	ν C4N9 (20), β r4 (10), ν C6N10 (10)
1021	1061, 1032	ν_{19}	ν C8N9 (55), β N9H (32)
944	927	ν_{22}	β r4 (42), β r5 (32), ν C4C5 (11)
914	887	ν_{23}	β R1 (49), β R3 (15)
850	848	ν_{24}	γ C8H (90)
800	802	ν_{25}	τ R1 (46), τ r4 (20), γ C6N10 (19), γ C8H (15)
723	717	ν_{26}	ν N3C4 (20), β r4 (14), ν C5N7 (11), ν C4N9 (10)

[a] values taken from Ar matrix isolation experiments of Nowak et al. (1996).

[b] assignments taken from B3LYP/6-31 G(d,p) calculations of Nowak et al. (1996).

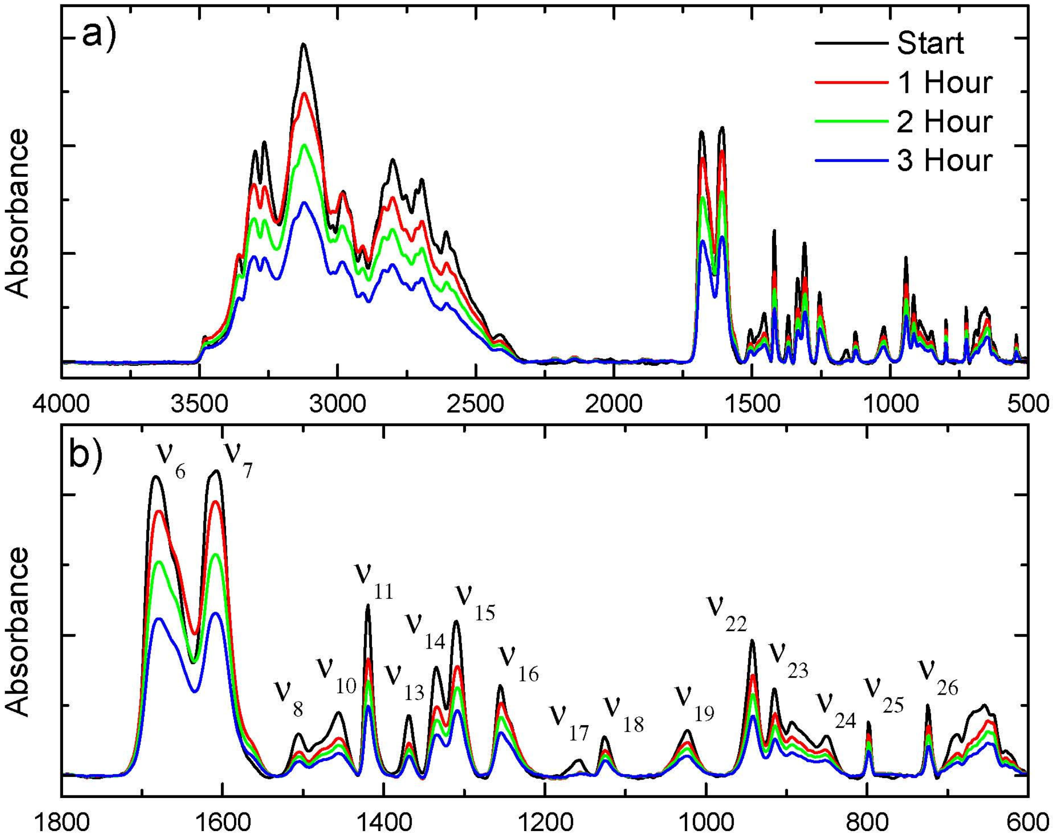

Figure 7.2: FTIR spectra: (a) 4000 - 500 cm^{-1} and (b) 1800 - 600 cm $^{-1}$ of adenine at 11 K in 1 hr intervals of electron irradiation. Mode assignments from Nowak et al.[76] are shown in panel (b). Characteristic ν_{11}, ν_{14}, ν_{16}, and ν_{25} modes are utilized to extract decay rate constants.

These data are fit with a unimolecular decomposition of the adenine via (pseudo) first-order kinetics [105] as quantified via equation (1)

$$N(t) = N_{\circ}e^{-k_i t} \ (1)$$

with $N(t)$ being the column density at a time t, $N_{\circ}$ the initial column density, and k_i is the decay constant of the ith mode. These fits yield the decay parameters (in s^{-1}) of $k_1 = 1.48 \pm 0.14 \times 10^{-4}$, $k_2 = 1.51 \pm 0.25 \times 10^{-4}$, $k_3 = 1.40 \pm 0.37 \times 10^{-4}$, and $k_4 = 2.21 \pm 0.71 \times 10^{-4}$ for the ν_{11}, ν_{14}, ν_{16}, and ν_{25} modes, respectively. From these values, the average decay constant, $k_a = 1.65 \pm 0.37 \times 10^{-4}$ s^{-1} is obtained for use in subsequent calculations.

The solid state and gas-phase decomposition of adenine may be expected to proceed by similar mechanisms. In the gas-phase, mass spectroscopy has identified the loss of successive hydrogen cyanide (HCN) or hydrogen isocyanide (HNC) units as the main fragmentation pathway for several irradiation sources including 70 eV electrons, [94] 6 - 22 eV photons, [56] 56 keV Ar^{8+} ions, [70] and 3 keV Cl^{+} ions. [18] However, absorption lines of HCN/HNC could not be observed due to the complexity of the adenine parent spectrum. The ν_1 C-H stretch of HCN at 3306 cm^{-1} [99] and the ν_1 N-H stretch of HNC at 3620 cm^{-1} [74] are not observed as they arise in a region where severe spectral broadening is present due to intermolecular adenine-adenine interactions. The ν_2 bending mode of HCN at 721 cm^{-1} [99] is not detected due to overlap with the ν_{26} mode of adenine. The ν_2 bending mode of HNC at 477 cm^{-1} [74] is at the edge of the FTIR detection range and could not be resolved due to poor signal-noise ratios. The ν_3 C≡N stretch of HCN at 2098 cm^{-1}, [99] and the ν_3 C=N stretch of HNC at 2029 cm^{-1} [74] are in a region where the adenine spectrum is featureless, but both of these modes are very weak in absorption and are also not detected.

While HCN/HNC absorptions are not visible in our spectrum we do see evidence of one novel band which arises during neat adenine irradiation at 2235 cm^{-1} and is assigned as an R-C≡N mode. [104] The saturated heterocyclic adenine parent will inevitably produce unsaturated bonds after electron impact fragmentation, and CN radicals within our ice are able to bond at these positions to yield the R-C≡N product. This mechanism for R-C≡N

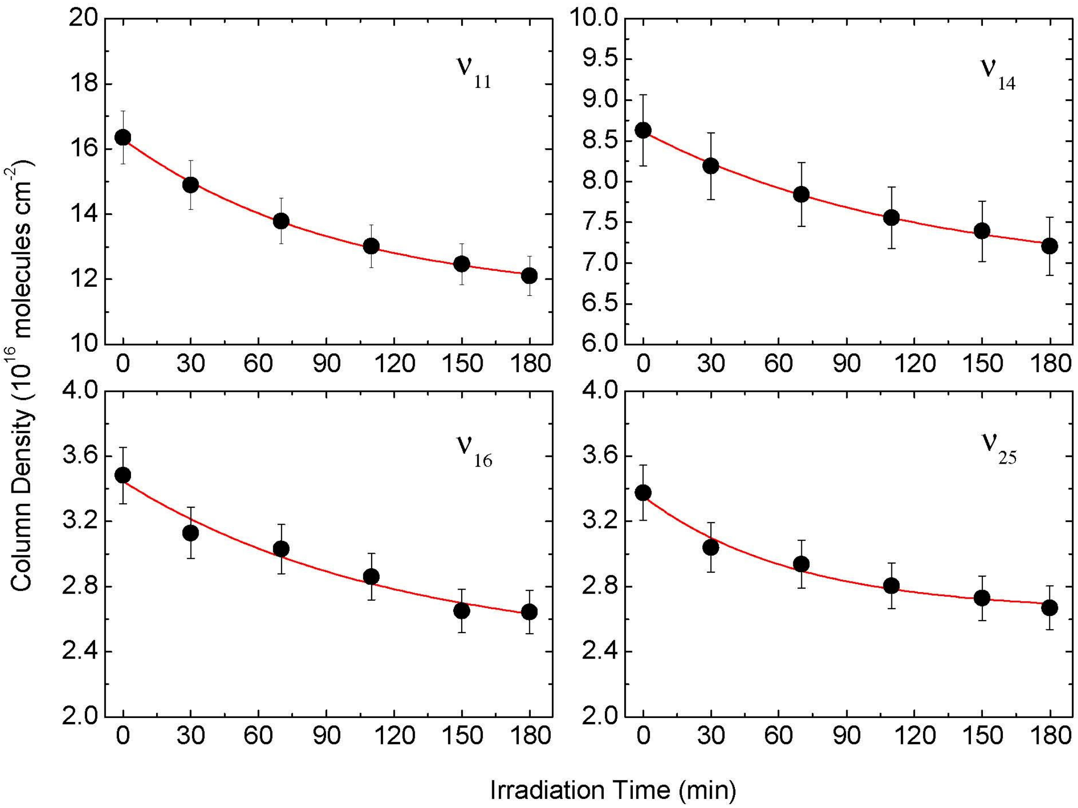

Figure 7.3: Calculated column densities of the ν_{11}, ν_{14}, ν_{16}, and ν_{25} modes plotted *vs.* irradiation time. Fits, shown in red, are used to determine the half-life of adenine under cosmic proton flux (see text for a detailed discussion).

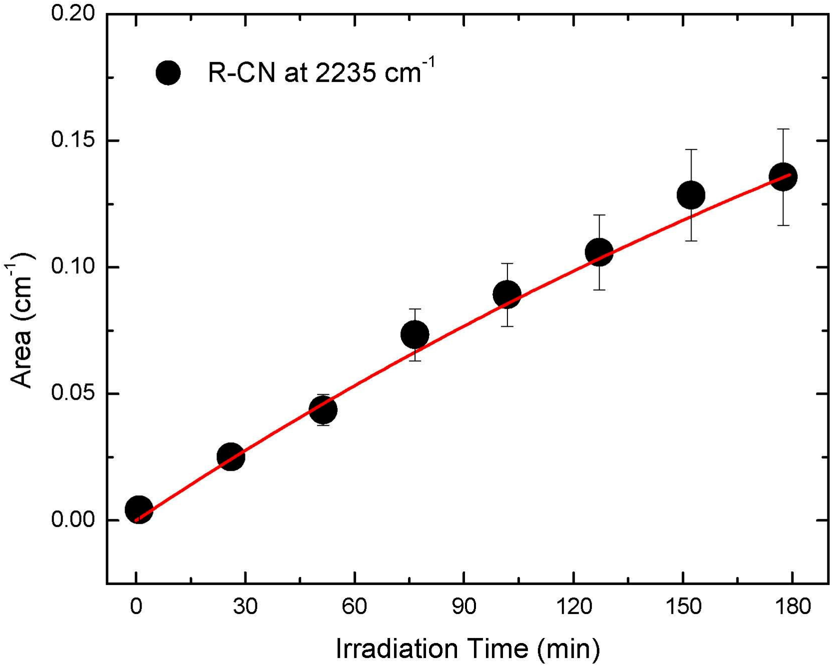

Figure 7.4: Absorption intensity rise profile and first-order fit of R-C≡N peak observed at 2235 cm^{-1} during neat adenine irradiation.

production is adopted based on previous experimental work involving cyano radical reactions with unsaturated compounds (acetylene, ethylene, methylacetylene, allene, dimethlyacetylene, and benzene) similar to adenine, [3] as well as propylene, [49] and diacetylene, [110] whereby the nearly barrierless addition of the cyano radical to these species is reported. The band at 2235 cm^{-1} displays a first-order rise profile, which is plotted as a function of irradiation time in Fig 7.4 along with a first-order fit (see Eq. 1); this yields a production rate of the R-C≡N feature of 4.53 ± 0.58 x 10^{-5} s^{-1}.

We would now like to briefly address the irradiation of the oxygen-covered adenine ices. FTIR spectra of pre-irradiated oxygen-covered adenine ice during 2 hr of 5 keV electron irradiation are presented in Fig 7.5. Upon electron irradiation oxygen-covered adenine ices show less than 3 % degradation of the characteristic adenine bands, and exponential column density decay profiles could not be extracted as in the adenine only irradiation experiments discussed above. This is evidence of the protection afforded by thin layers of molecular oxygen to molecules formed inside interstellar icy grains. Bands of ozone (O_3) appear at 702 (ν_2), 1035 (ν_3), and 2108 ($\nu_1 + \nu_3$) cm^{-1} during irradiation; this serves as confirmation that energetic electrons are interacting with oxygen molecules on the adenine ice, which dissociate into atomic oxygen, and subsequently react with molecular oxygen forming ozone. [6] The R-C≡N mode at 2235 cm^{-1} seen during the irradiation of pure adenine is also observed here; additional absorption features unique to this experiment arise at 1871, 1750, 1610, 1242, and 737 cm^{-1}. As these absorption bands were not identified within irradiated ices of pure adenine, or pure molecular oxygen, we associate them with oxygen-bearing species formed as a result of reactions between these two ice components. The temporal rise profile of all oxygen bearing products is seen in Fig 7.6 to be very distinct from those of ozone, and R-C≡N (Fig 7.4). Here, the profiles of the oxygen-bearing species initially rise very slowly; after approximately 75 min, a steeper rise is observed. Note that these are oxygen-bearing species, and the oxygen atoms necessary for the chemical reaction are formed via unimolecular decomposition of molecular oxygen, [6] which is deposited on top of the adenine layer. Therefore, the locations of the oxygen source and oxygen sinks are spatially separated. Consequently, we attribute this time delay to the time needed for oxygen atoms to diffuse through the molecular oxygen layer before reaching the adenine ice. Note that these oxygen atoms can be generated with excess energy of a few eV from molecular oxygen; [31] this excess energy helps to overcome the activation energy necessary to diffuse through the ice, but also to react with the adenine molecule. The bands at 1871 and 1750 cm^{-1} are characteristic of a CO stretch, indicating the formation of a carbonyl group (C=O). [104] We are also able to determine the formation of epoxides as evidenced by the bands at 737 (asymmetric C-O-C ring breathing), 1242 (symmetric C-O-C ring breathing), and 1610 cm^{-1} (aromatic ring buckling). [7, 50, 68, 104, 107]

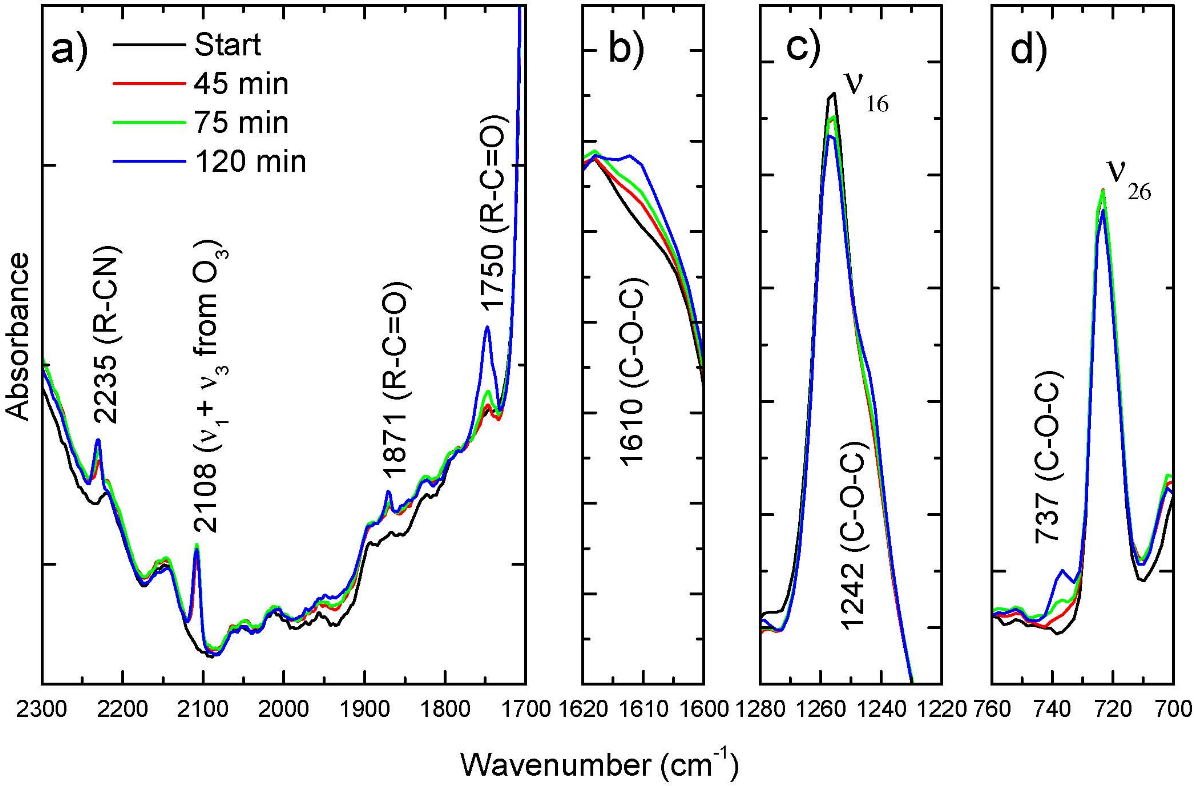

Figure 7.5: FTIR spectra (a) 2300 - 1700 cm^{-1}, (b) 1620 - 1600 cm^{-1}, (c) 1280 - 1220 cm $^{-1}$, and (d) 760 - 700 cm^{-1} of pre-irradiated oxygen-covered adenine at 11 K during electron irradiation at 5 keV. Assignment of ozone is taken from Bennett et al.; [7] assignment of other bands from Socrates. [104]

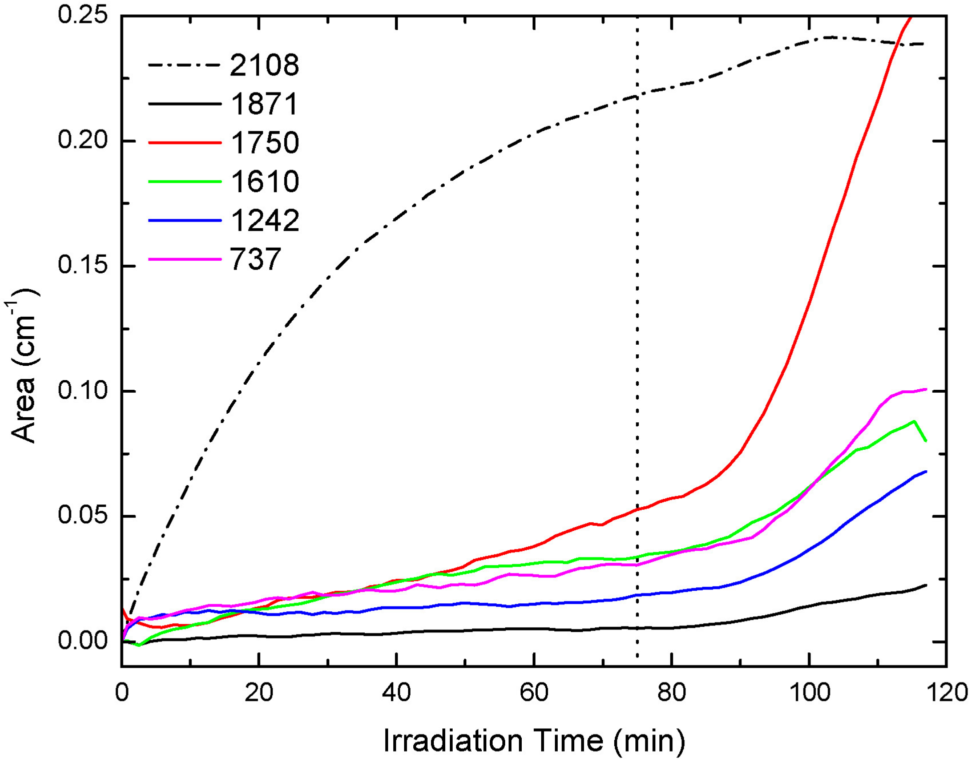

Figure 7.6: Absorption intensity rise profiles of products observed during oxygen-covered adenine ice irradiation. Irradiation products include: R-C=O (carbonyl group) at 1871 cm^{-1} (black) and 1750 cm^{-1} (red); C-O-C (epoxide) at 1610 cm^{-1} (green), 1242 cm^{-1} (blue) and 737 cm^{-1} (magenta); ozone at 2108 cm^{-1} (dashed). Vertical dotted line indicates beginning of oxygen atom interaction with adenine.

7.5 DISCUSSION

The discussion is divided into two parts. First, we have quantified the destruction of the adenine molecule, and determined its half-life within several different interstellar environments (3.5.1). Secondly, the formation of new molecules (RCN, epoxides, carbonyl functions) within the ices is investigated, and reaction mechanisms are proposed (3.5.2).

Destruction of Adenine

It is important to stress that our experiments monitored the destruction of adenine by energetic electrons; our kinetic analysis suggests decay rates of k_a =1.65 ± 0.37 x 10^{-4} s^{-1}. It is important to transfer these findings to real astrobiologically relevant environments. This is addressed by quantifying the survivability of adenine within the solar system and in several interstellar environments by calculating the half-life using a similar approach to that carried out by Peeters et al.. [87]

First, we calculate the electron destruction cross section of a single electron passing through our ice, whereby, $\sigma = 1.07 \pm 0.24$ x 10^{-16} cm^2, according to, $\sigma = k_a/\phi$, where $\phi = 1.54$ x 10^{12} electrons cm^{-2} s^{-1} is the laboratory electron flux and k_a is the average decay parameter derived in the results section. The stated error results from uncertainties in fitting the decay parameter. It is noted that the destructive cross sections for keV electrons refer to inelastic scattering processes. Experimentally determined cross section data in this energy range is scarce, as noted by Blanco & Garcia, [13] who calculated the inelastic cross section for scattering of 5 keV electrons from gaseous adenine using the screening-corrected additivity-rule (SCAR) and reported $\sigma_{in} = 1.67$ x 10^{-16} cm^2. However, two experimental studies of interest are mentioned here. Isaacson [54] measured the inelastic scattering of 25 keV electrons from gaseous adenine and found a cross section of $\sigma_{in} = 3.6$ x 10^{-17} cm^2, and total dissociative cross sections on the order of 10^{-17} cm^2 are reported for scattering of low energy electrons (a few eV) from thin films of adenine. [85] Our electron destruction cross section results are in general agreement with these findings.

Secondly, it is necessary to scale the calculated electron destruction cross section of our keV electrons to an effective destruction cross section for the MeV proton component of the GCR. The validity of simulating proton irradiation with keV electron impact has been discussed in detail previously, [10, 55, 57, 58] and is based on calculations of energy loss mechanisms as protons and electrons pass through a solid. Linear energy transfer (LET) is a measure of the energy deposited into a material per unit distance as energetic particles travel through it, and is used here to quantify the destructive effect of ionizing radiation. Ion trajectory simulations using the SRIM/TRIM code [112] reveal that the LET_{H^+} of 0.001, 1.0 and 10 MeV protons in solid adenine is 21.9, 34.8 and 6.4 keV $\mu\mathrm{m}^{-1}$, with 85.6, 99.9, and 99.9 % of this energy loss proceeding though inelastic electronic interactions with the target molecules, respectively; this leads to electronic excited states of the molecules, unimolecular decomposition, and/or free secondary electrons. Secondary electrons are generated with energies up to a few keV, [69] and are therefore directly modeled by our radiation source. The LET_{e^-} of a 5 keV electron as it traverses our ice is calculated to be 3.62 keV $\mu\mathrm{m}^{-1}$ using the CASINO code. [33] Therefore, the LET of a single electron does not directly translate to the same radiation damage caused by a single energetic proton, so electron destruction cross sections are scaled by the ratio (LET_{H^+} /LET_{e^-}) to give an effective destruction cross section, σ_{eff}, which more accurately models damage from protons at particular energies; results are summarized in Table 7.2. An advantage of employing this scaling method is that it allows simulation of the dominating inelastic electronic transfer processes of protons at multiple energies with a monoenergetic electron source.

In order to determine the cosmic survivability of adenine in astrobiologically relevant radiation environments, the decay half-life is calculated according to equation (2):

$$\mathrm{t}_{1/2} = \ln\,(2)\ /\ \sigma_{eff}\phi_p\ (2),$$

where σ_{eff} is the effective electron destruction cross section and ϕ_p is the proton flux in each specific environment. In this scenario, it is assumed that a given amount of adenine is initially present and that no additional production pathways are present. Thus, given the reported flux of protons within a particular astronomical environment, which are taken as the values reported by Palumbo et al. [84] we are able to estimate the half-life of adenine. At a distance of 1 AU the flux for 1 keV H^+ nuclei from the solar wind is given as $\phi_p = 3.0 \text{ x } 10^8 \text{ cm}^{-2} \text{ s}^{-1}$; combined with an averaged flux of 1 MeV H^+ nuclei from solar flares is given as $\phi_p = 3.2 \;\; 10^2 \text{ cm}^{-2} \text{ s}^{-1}$. The contribution from galactic cosmic rays adds a further $\phi_p = 10 \text{ cm}^{-2} \text{ s}^{-1}$ of 1 MeV H^+ nuclei. Meanwhile, at a distance of 40 AU - a typical orbital distance for a Kuiper belt object - the contribution from galactic cosmic rays is unchanged, but all other values are scaled by the relationship r^{-2}. Considering next the interstellar environments, we adopt values of $\phi_p = 1.8 \text{ cm}^{-2} \text{ s}^{-1}$ of 1 MeV H^+ nuclei for the diffuse ISM (DISM; where visual extinction, A $\leq$ 1 mag) and $\phi_p = 1.0 \text{ cm}^{-2} \text{ s}^{-1}$ of 1 MeV H^+ nuclei for dense clouds (DC; A $>$ 5 mag). The half-life of adenine in each environment due to the individual proton destruction processes is calculated and reported in Table 7.2. However, molecules in the ISM are subject to destruction by both proton and UV irradiation, and discussions of cosmic survivability must consider both processes; here we take UV half-lives as reported by Peeters et al.. [87] The total half-life of adenine is then calculated according to equation (3) where destruction due to UV photons, 1 keV H^+ and 1 MeV H^+ nuclei are treated as three independent processes:

$$\frac{1}{T_{1/2}} = \Sigma_i \frac{1}{t_i} \text{ (3)},$$

where $T_{1/2}$ is the total half-life and t_i is the half-life due to the ith destruction process. Effective cross sections, fluxes, individually calculated half-lives from each contributing radiation source, as well as total half-lives, are compiled in Table 7.2 for each astronomical environment considered here.

Half-lives within the solar system at 1 AU and 40 AU from the sun are essentially determined by the UV flux within these environments; inclusion of the additional proton induced

Table 7.2: Calculated half-lives of adenine within our solar system (at distances of 1 and 40 AU), as well as in the interstellar medium. (DC - dense cloud; DISM - diffuse interstellar medium).[a]

Radiation Source	σ_{eff}	Flux				Half-life			
		1 AU	40 AU	DC	DISM	1 AU	40 AU	DC	DISM
	(cm^2 per molecule)	cm^{-2} s^{-1}	cm^{-2} s^{-1}	cm^{-2} s^{-1}	cm^{-2} s^{-1}	(s)	(yr)	(Myr)	(Myr)
1 MeV H^+……...	1.03×10^{-15} [b]	3.3×10^{2} [c]	2.1×10^{-1} [d]	1.0 [c]	1.8 [c]	2.04×10^{12}	1.02×10^{8}	21.3	11.9
1 keV H^+………	6.48×10^{-16} [b]	3.0×10^{8} [c]	1.9×10^{5} [d]	-	-	3.57×10^{6}	1.79×10^{2}	-	-
UV [e]……………	2.7×10^{-18}	3.0×10^{13}	1.9×10^{10} [d]	1.0×10^{3}	1.0×10^{8}	8.65×10^{3}	4.28×10^{-1} [d]	8.27	8.27×10^{-5}
Total	-	-	-	-	-	8.63×10^{3}	4.27×10^{-1}	5.97	8.27×10^{-5}

[a] Also shown are the effective destruction cross sections (σ_{eff}), and the relevant fluxes of each irradiation source in each astrophysical environment.

[b] Effective cross sections calculated by scaling the 5 keV electron destruction cross section by the energy loss ratio (LET_{H^+}/LET_e).

[c] Combined contribution from GCRs and solar flares estimated from Palumbo et al. (2008).

[d] Scaled from the value at 1 AU, using $1/r^2$ at a distance of 40 AU for a typical Kuiper belt object.

[e] Values taken from Peeters et al. (2003).

destruction rates reduces the lifetime of adenine by only 0.29% and 0.24 %, respectively. While the decreased UV flux at 40 AU does enhance the expected half-life of adenine by a factor of 1.56 x 10^3, it is still relatively short on astronomical timescales, and the survivability of unshielded adenine remains unlikely. A similar situation is found for the DISM, where the photon flux is found to be eight orders of magnitude larger than the proton flux, leading to a half-life of only 82.7 years - the same value as reported when UV radiation alone is taken into account. [87] However, in a DC the UV flux can be attenuated by a factor of up to 10^5 [92] and it is here that the destruction of adenine by MeV protons becomes significant. Indeed, the proton (21.3 Myr) and UV (8.2 Myr) half-lives are within a factor of $\sim$ 3, and the total half-life (5.9 Myr) is $\sim$30 % shorter than the UV-only half-life. Of significant astrobiological interest is the fact that while our result decreases the overall lifetime of adenine in DCs it does not exclude the possibility that adenine should remain relatively abundant over the lifetime of typical molecular clouds. As an example, let us consider the case of the cold, dense interstellar cloud TMC-1, which is estimated to be 6 Myr old. [30] Assuming uniform UV shielding throughout the cloud, one would expect 50

% of the initially available adenine to still be present. This result is valid within our initial assumption that adenine begins at some initial concentration and is subsequently degraded by both UV photons and energetic protons without taking into account the accompanying production mechanisms, which is of course an over-simplification of the realistic scenario. In fact, these irradiation sources are likely to also be processing these ices and contributing to the production of adenine within these ices, as adenine has been observed to form within irradiated ices in laboratory experiments simulating these environments (see introduction). It is likely that both production and destruction mechanisms for adenine are in competition with one another; it is anticipated that a steady-state abundance of adenine will be reached for each particular astronomical environment.

Formation of New Products

Having commented on the destruction rates of adenine, we are now discussing possible reaction products, i.e. the spectroscopically detected nitriles, epoxides, and carbonyl functions evident upon irradiation of adenine and oxygen ices. In pure adenine ices, it is important to note that the destruction rate ($1.65 \pm 0.37 \times 10^{-4}$ s^{-1}) is - within the error limits - a factor of about three higher than the production rate of the R-C≡N ($0.45 \pm 0.06 \times 10^{-4}$ s^{-1}), and also, that nitriles were the only new reaction product formed in the solid state. On the other hand, as discussed, gas-phase studies provide compelling evidence for the formation of HCN/HNC. [18, 56, 70, 94] How can these results be combined into a coherent picture? We propose that in the solid state, a unimolecular decomposition of adenine leads to the formation of CN radicals; the formation of radicals in the unimolecular decomposition of organic molecules with energetic electrons is well established, for instance the formation of CH_3O and CH_2OH radicals in the decomposition of methanol (CH_3OH). [9] The cyano radical can react within a matrix cage to add without barrier to the aromatic adenine molecule across either a carbon, or nitrogen atom leading to the formation of a generic doublet radical intermediate; it is not feasible to assign the exact location to which the cyano radical adds since the reaction is not conducted under single collision conditions as in crossed beam experiments. [59] Nevertheless, it is conceivable that this newly formed doublet radical can either (1) react with hydrogen atoms in the ice to form a closed shell nitrile, or (2) if there is an H atom bound to the carbon atom which is attacked by the cyano radical - such as at the C2 and C8 positions of adenine - it could also be possible for this hydrogen atom to be emitted during the process thus maintaining the aromaticity of the molecule; this in turn also forms a closed shell nitrile whereby a hydrogen atom was replaced by a CN group. Note that the interaction of energetic electrons with any organic molecule such as methanol, [9] methane, [8] ethane, [61] and methylamine [51] leads to the formation of mobile hydrogen atoms in the solid ices even at 10 K - so does adenine. In this proposed mechanism, one adenine molecule is consumed by unimolecular decomposition forming the cyano radical, whereas this radical adds to the π system of a second adenine molecule. So in total, we would expect - if the formation of the nitriles is the only reactive pathway - that the decay rate constant is a factor of two higher than the rate constant associated with the formation of the nitrile. A comparison of these rate constants of 1.65 ± 0.37 x 10^{-4} s^{-1} versus 0.45 ± 0.06 x 10^{-4} s^{-1} shows that this tendency is actually observed.

We are turning our attention now to the oxygen-bearing molecules. It is expected that supra-thermal oxygen atoms liberated from the dissociation of molecular oxygen - which are electrophilic - can add to the π electron density of the aromatic adenine molecule; similar processes have previously been observed for benzene. Here, the reactions have been studied in the gas-phase at room temperature and up to 1,000 K, where oxygen atoms were generated by photolysis of nitrous oxide (N_2O), [16, 106] and within argon matrices held at 12 K where oxygen atoms were produced from the photolysis of ozone. [86] In these studies, a wide range of products were observed including: alcohols (phenol), epoxides (benzene oxide which may isomerize to oxepin, where the oxygen is formally incorporated into the ring structure), ketones (2,4-cyclohexadienone), ketenes (hexa-1,3,5-trien-1-one), and the formation of 5-membered rings (cyclopentadiene) which is accompanied by the evolution of gaseous carbon monoxide; infrared vibrational analysis additionally supports the production of aldehydes. More specifically, our studies indicate that we observe the presence of an epoxide group, as evidenced by infrared bands appearing at 737 cm^{-1} (asymmetric C-O-C ring breathing), 1242 cm^{-1} (symmetric C-O-C ring breathing), and 1610 cm^{-1} (aromatic ring buckling). [6, 50, 68, 104, 107] The epoxide formation is explained by the initial addition of an oxygen atom to a carbon atom leading to an O-C_a-C_b diradical which can then ring-close to form the epoxide; this can likely occur across the C4-C5 and/or C5-C6 atoms. Secondly, the features at 1871 and 1750 cm^{-1} are characteristic of the formation of a carbonyl group (C=O). Whilst the previous studies on benzene have lead to the possibility of ring-opening reactions, we also consider what may happen if the oxygen atom again attacks a carbon atom with hydrogen bound to it (i.e. C_a is C2 or C8); here, in both cases the migration of the hydrogen atom from C_a to the adjacent atom (which may be carbon or nitrogen) would yield a ketone structure. Indeed, there are several studies to suggest that the C8-oxidation of adenine can occur readily. [48] The formation of both epoxides and carbonyls has been demonstrated previously in low temperature irradiation experiments; for example, the reaction of ethylene (C_2H_4) with oxygen atoms produced from both ozone [50] and carbon dioxide [6] leads to the formation of both ethylene oxide (c-C_2H_4O) and acetaldehyde (CH_3CHO). These studies support our proposed reactions mechanisms.

7.6 ASTROPHYSICAL IMPLICATIONS

The nucleic acid base molecule adenine is thought to be synthesized from readily available molecules in the ISM by both gas-phase processes, and in the solid state on icy grains, initiated by the UV and charged particle component of the GCR. This radiation will simultaneously act to degrade adenine, and the competition between synthesis and degradation rates is expected to afford some steady state abundance within astronomical environments. Destruction due to UV photons and charged particles in the GCR must both be considered; here results on the destruction rate of adenine by simulated proton irradiation is presented and combined with previously reported UV destruction rates in an effort to determine the overall survivability of this important terrestrial biomolecule. Our discussion has neglected the competing formation rates and therefore the abundances we predict are likely to be underestimated.

Within our solar system, the half-life of adenine, due to proton and UV irradiation is less than 0.5 yr. Due to such short half-lives predicted at 1 AU (Table 7.2), or even at 40 AU, how could adenine, and other complex biomolecules, have survived to seed the early Earth? In their study of the UV destruction of adenine, Peeters et al. [87] also investigated the lifetime of the amino acid glycine, and found the lifetime to be a factor or 4.5 times lower than that of adenine meaning that the survival of this species over the age of our solar system would be even more unlikely. It is surprising then, that the analysis of comet-exposed materials from NASAs stardust mission - obtained when it flew within 234 km of the surface of comet 81P/Wild 2 - found that traces of glycine were present. [20, 37] The comet itself has a volume of nearly 75 km^3 and is believed to have had a stable orbit within the Kuiper belt (∼40 AU) since the birth of the solar system. An encounter with Jupiter in 1974 has disturbed its orbit, bringing it into a dynamic orbit within the inner solar system, whereby it orbits roughly once every six years passing as close as 1.86 AU from the sun [21, 100] An orbit so close to the sun has caused the surface of the comet to become active; the additional heating causes the sublimation of volatiles. The outer layers of the comet began sublimating in the few hours prior to the Stardust flyby, and collected materials are thought to be from the interior of the comet; the pristine material that the solar system was formed from. The outer layers of the comet were able to sufficiently shield the fragile glycine molecule from the harsh irradiation environment of our solar system over the 4.5 billion years since its formation.

The penetration depth for both UV photons, as well as charged particles is highly dependant upon the energy. Orzechowska et al. [83] carried out an in-depth study of the UV photolysis of amino acids embedded within a water ice matrix at 100 K, and found that the penetration depth of UV photons within water ice is ∼1 μm at 163 nm (7.6 eV), ∼1 cm at 180 nm (6.9 eV), and up to 1 m at 200 - 300 nm (4.1 - 6.2 eV). The half-life of glycine, isolated in water ice only 1.6 mm thick, was found to increase by two orders over the unshielded half-life of around 0.5 hr determined by Peeters et al.. [87] Using the SRIM/TRIM code, the calculated penetration depth for protons in water ice is again energy dependant whereby 1 keV H^+ nuclei penetrate only ∼34 nm, 1 MeV H^+ nuclei are able to penetrate ∼18 μm, and very high energy 1 GeV H^+ nuclei can penetrate around 3.2 m. Thus, just the few outer meters of any icy solar system body, such as a comet, should provide satisfactory shielding for the survival of large amounts of complex biomolecules.

In our solar system and in the DISM, the UV destruction of adenine dominates; the half-life is on the order of years, and accumulation of adenine is considered unlikely. However, it has been shown by Peeters et al., [87] that in UV shielded environments such as DCs, the half-life due to UV radiation is 8.3 Myr which would favor the accumulation of adenine. However, the fast proton component of the GCR is not attenuated in these environments, and when this is taken into account, the additional destruction of adenine from MeV protons reduces the overall lifetime by nearly 30 % to ∼6 Myr; approximately the lifetime of a star forming molecular cloud. Therefore, half of any initial adenine population would remain present over the lifetime of a typical dark cloud such as TMC-1. Further, it is noted that the destructive effects of both UV photons and high energy charged particles are reduced by the outer layers of icy grains, or icy bodies. In the later case, it is expected that only the outer few meters would be effectively processed; the underlying material should be unprocessed over the age of our solar system meaning that the abundance of adenine as well as other biomolecules would be unaltered from their composition within the pre-solar interstellar cloud from which our solar system formed. Hence, it is considered very likely that large icy bodies enabled the survival of biologically important species, which could occasionally be perturbed into the inner solar system to seed the primordial Earth.

Also, we have shown that in oxygen-bearing ices, two competing chemical pathways can lead to the destruction of adenine via reactions with atomic oxygen inside ices at 10 K to form epoxides and carbonyls. It should be noted that although oxygen atoms are released from molecular oxygen in the present experiments, additional oxygen sources exist in real interstellar ices that can likely form epoxides and carbonyls. Here, previous investigations on the interaction of low temperature ices with energetic electrons in our group suggested that water (H_2O) can also undergo fragmentation upon radiolysis to form excited state oxygen atoms plus molecular hydrogen (H_2) via retro-insertion. [111] Likewise, a retro-insertion mechanism in methanol (CH_3OH) exposed to energetic electrons leads to electronically excited oxygen atoms and methane (CH_4). [9] Finally, depending on the ice matrix conditions, carbon monoxide (CO) can also be fragmented to a carbon and an oxygen atom. [10] Therefore, each of these suprathermal oxygen atoms could react with embedded adenine molecules. It is therefore desirable for future work to incorporate the effects of different matrix compositions on the decomposition rates of adenine to fully understand its survivability within these environments.

7.7 ACKNOWLEDGEMENTS

NLE and SU acknowledge the Donors of the American Chemical Society Petroleum Research Fund (grant ACS-PRF#44110-G6) and the National Science Foundation (award #CHE-0924456) for partial support of this research. NLE would like to thank the Franklin College of Arts and Sciences and the Department of Physics and Astronomy at the University of Georgia for covering travel expenses. CJB and RIK thank the National Aeronautics Space Administration (NASA Astrobiology Institute under Cooperative Agreement no. NNA09DA77A issued through the Office of Space Science).

7.8 REFERENCES

[1] Allamandola, L. J., Tielens, A. G. G. M., & Barker, J. R. 1989, ApJSS, 71, 733

[2] Anders, E. 1989, Nature, 342, 255

[3] Balucani, N., Asvany, O., Huang, L. C. L., Lee, Y. T., Kaiser, R. I., Osamura, Y., & Bettinger H. F. 2000, Ap. J., 545, 892

[4] Bar-Nun, A., Bar-Nun, N., Bauer, S. H. & Sagan, C. 1970, Science, 168, 470

[5] Bennett, C. J., Jameison, C. S., Mebel, A.M., & Kaiser, R. I. 2004, PCCP, 6, 735

[6] Bennett, C. J., & Kaiser, R. I. 2005, ApJ, 635, 1362

[7] Bennett, C. J., Osamura, Y., Lebar, M. D., & Kaiser, R. I. 2005, ApJ, 634, 698

[8] Bennett, C. J., Jamieson, C. S., Osamura, Y., & Kaiser, R.I. 2006, ApJ, 653, 792

[9] Bennett, C. J., Chen, S.-H., Sun, B.-J., Chang, A. H. H., & Kaiser, R. I. 2007, ApJ, 660, 1588

[10] Bennett, C. J., Jameison, C. S., & Kaiser, R. I. 2009, ApJSS, 182, 1

[11] Bernstein, M. P., Dworkin, J. P., Sandford, S. A., Cooper, G. W., & Allamandola, L. J. 2002, Nature, 416, 401

[12] Bernstein, M. P., Sandford, S. A., & Allamandola, L. J. 2005, ApJSS, 161, 53

[13] Blanco, F., & Garcia, G. 2007, Physics Letters A, 360, 707

[14] Borquez, E., Cleaves, H. J., Lazcano, A., & Miller, S. L. 2005, Orig. Life Evol. Biosph., 35, 79

[15] Botta, O., & Bada, J. 2002, Surveys Geophys., 23, 411

[16] Boocock, G., & Cvetanovic, R. J. 1961, Can. J. Chem., 39, 2436

[17] Brack, A. 1999, Adv. Space Res., 24, 417

[18] Bredy, R., Bernard, J., Chen, L., Montagne, G., Li, B., & Martin, S. 2009, J. Chem. Phys., 130, 114305

[19] Brown, R. D., Godfrey, P. D., McNaughton, D., & Pierlot, A. P. 1989, Chem. Phys. Letters, 156, 61

[20] Brownlee, D. et al. 2004, Science, 304, 1764

[21] Brownlee, D. et al. 2006, Science, 314, 1711

[22] Cecchi-Pestellini, C., Scappini, F., Saija, R., Iati, M. A., Giusto, A., Aiello, S., Borghese, F., & Denti, P. 2004, International Journal of Astrobiology, 3, 287

[23] Caceres, D., Bertin, M., Lafosse, A., Domaracka, A., Pliszka, D., & Azaria, A. 2006, AIP Conference Proceedings, 876, 112

[24] Chakrabarti, S., & Chakrabarti, S. K. 2000, A&A, 354, L6

[25] Charnley, S. B., Ehrenfreund, P., & Kuan, Y. -J. 2001, Spectrochem. Acta A. 57, 685.

[26] Charnley, S. B., et al. 2005, Adv. Space. Res., 36, 137

[27] Chyba, C. F. 1990, Nature, 348, 113

[28] Chyba, C. F., & Sagan, C. 1992, Nature, 355, 125

[29] Chyba, C. F., Thomas, P. J., Brookshaw, L., & Sagan, C. 1990, Science, 249, 366

[30] Cohen, M., & Kuhi, L. W. 1979, ApJS, 41, 743

[31] Cosby, P. C. 1993, J. Chem. Phys., 98, 9560

[32] Darnell, J. E., & Doolittle, W. F. 1986, Proc. Natl. Acad. Sci. USA, 83, 1271

[33] Drouin, D., Couture, A. R., Gauvin, R., Hovington, P., Horny, P., & Demers, H. 2001,

[34] Monte Carlo Simulation of Electron Trajectory in Solids (CASINO) ver. 2.42 ; (Sherbrooke: Univ. Sherbrooke)

[35] Dworkin, J. P., Lazcano, A., & Miller, S. L. 2003, Journal of Theoretical Biology, 222, 127

[36] Ehrenfreund, P., & Charnley, S. B. 2000, Ann. Rev. Astron. Astrophys., 38, 427

[37] Elsila, J. E., Glavin, D. P., & Dworkin, J. P. 2010, Astrobiology Science Conference, League City, TX; Lunar and Planetary Institute: Houston, TX, 2010, Abstract #5105.

[38] Evans, N. L., & Ullrich, S. U. 2010, J. Phys. Chem. A, in press

[39] Fegley, B., Prinn, R. G., Hartman, H., & Watkins, G. H. 1986, Nature, 319, 305

[40] Freeland, S. J., Knight, R. D., & Landweber, L. F. 1999, Science, 286, 690

[41] Ghosh, K. K., & Ghosh, S. N. 1980, Life Sci. Space Res., 18, 37

[42] Gibb, E. L., Whittet, D. C. B., Boogert, A. C. A., & Tielens, A. G. G. M. 2004, ApJSS, 151, 35

[43] Gilbert, W. 1986, Nature, 319, 618

[44] Glaser, R., Hodgen, B., Farrelly, D., & McKee, E. 2007, Astrobiology, 7, 455

[45] Glavin, D. P., Schubert, M., & Bada, J. L. 2002, Anal. Chem., 74, 6408

[46] Greenberg, J. M. 1989, Adv. Space Res., 9, 15

[47] Griffith, R. W. 2009, Orig. Life Evol. Biosph., 39, 517

[48] Gu, J., Tian, A., Li, W. K., & Wong, N. B. 2000, J. Phys. Chem., 104, 10698

[49] Gu, X., Zhang, F., & Kaiser, R. I. 2008, J. Phys. Chem. A, 112, 9607

[50] Hawkins, M., & Andrews, L. 1983, J. Am. Chem. Soc., 105, 2523

[51] Holtom, P. D., Bennett, C. J., Osamura, Y., Mason, N. J., & Kaiser, R. I. 2005, ApJ, 626, 940

[52] Hill, A., & Orgel, L. E. 2002, Orig. Life Evol. Biosph., 32, 99

[53] Ikehara, K. 1999, Seibutsu Kagaku, 51, 43

[54] Isaacson, M. 1972, J. Chem. Phys., 56, 1813

[55] Jamieson, C. S., Mebel, A. M., & Kaiser, R. I. 2006, ApJSS, 163, 184

[56] Jochims, H. W., Schwell, M., Baumgrtel, H., & Leach, S. 2005, Chem. Phys., 314, 263

[57] Kaiser, R. I., Eich, G., Gabrysch, A., & Roessler, K. 1997, ApJ, 484, 487

[58] Kaiser, R. I., & Roessler, K. 1998, ApJ, 503, 959

[59] Kaiser, R. I., Ochsenfeld, C., Stranges, D., Head-Gordon, M., & Lee, Y. T. 1998, Faraday Discuss, 109, 183

[60] Kilday, M. V. 1978, J. Res. Nat. Bur. Stand., 83, 347

[61] Kim, Y. S., Bennett, C. J., Chen, L.-H., OBrien, K., & Kaiser, R. I. 2010, ApJ, 711, 744

[62] Kobayashi, K., Kasamatsu, T., Kaneko, T., Koike, J., Oshima,T., Saito, T., & Yanagawa, H. 1995, Adv. Space Res. 16, 21

[63] Lacey, J. C., Cook, G. W., & Mullins, D. W. 1999, Biochem. Mol. Biol., 12, 398

[64] Lafosse, A., Bertin, M., Domaracka, A., Pliszka, D., Illenberger, E., & Azria, R. 2006, Phys. Chem. Chem. Phys. 8, 5564.

[65] Levy, M., & Miller, S. L. 1999, J. Mol. Evol., 48, 631

[66] Levy, M., & Miller, S. L. 1998, Proc. Natl. Acad. Sci. USA, 95, 7933

[67] Lin, J., Yu, C., Peng, S., Akiyama, I., Li, K., Kao Lee, L., & LeBreton, P. R. 1980, J. Am. Chem. Soc., 102, 4627

[68] Liu, J., Xu, T., & Fu, Y. 2005, J. Non-cryst. solids, 351, 3050

[69] Magee, J. L., & Chatterjee, A. 1987, in Radiation Chemistry: Principles and Applications, ed. Farhataziz & M. A. J. Rodgers (New York: VCH)

[70] Martin, S., Bredy, R., Allouche, A. R., Bernard, J., Salmoun, A., Li, B., & Chen L. 2008, Phys. Rev. A, 77, 062513

[71] Martins, Z., Botta, O., Fogel, M. L., Sephton, M. A., Glavin, D. P., Watson, J. S., Dworkin, J. P., Schwartz, A. W. & Ehrenfreund, P. 2008, Earth and Planetary Science Letters, 270, 130

[72] Mattioda, A. L., Hudgins, D. M., Bauschlicher, C. W., Rosi, M., & Allamandola, L. J. 2003, J. Phys. Chem. A, 107, 1486

[73] Miller, S. L. 1953, Science, 117, 528

[74] Milligan, D. E., & Jacox, M. E. 1967, J. Chem. Phys., 47, 278

[75] Munoz Caro, G. M., Meierhenrich, U. J., Schutte, W. A., Barbier, B., Arcones Segovia, A., Rosenbauer, H., Thiemann, W. H. P., Brack, A., & Greenberg, J. M. 2002, Nature, 416, 403

[76] Nowak, M. J., Lapinski, L., Kwiatkowski, J.S., & Leszczynski, J. 1996, J. Phys. Chem., 100, 3527

[77] Nuevo, M., Chen, Y. -J., Yih, T. S., Ip, W. -H., Fung, H. -S., Cheng, C. -Y., Tsai, H. -R., & Wu, C. -Y. R. 2007, Adv. Space Res., 40, 1628

[78] Nuevo, M., Auger, G., Blanot, D., & dHendecourt, L. 2008, Orig. Life Evol. Biosph., 38, 37

[79] Nuevo, M., Milam, S. N., Sandford, S. A., Elsila, J. E., & Dworkin, J. P. 2009, Astrobiology, 9, 683

[80] Orgel, L. E. 2004, Crit. Rev. Biochem. Mol. Biol., 39, 99

[81] Oro, J. 1960, J. Biochim. Biophys. Res. Commun., 2, 407

[82] Oro, J., & Kimball, A. P. 1962, Arch. Biochem. Biophys., 96, 293

[83] Orzechowska, G. E., Goguen, J. D., Johnson, P. V., Tsapin, A., & Kanik, I. 2007, Icarus, 187, 584

[84] Palumbo, M. E., Baratta, G. A., Fulvio, D., Garozzo, M., Gomis, O., Leto, G., Spinella, F., & Strazzulla, G. 2008, J. Physics: Conference Series, 101, 1

[85] Panajotovic, R., Michaud, M., & Sanche, L. 2007, PCCP, 9, 138

[86] Parker, J. K., & Davis, S. R. 1999. J. Am. Chem. Soc., 121, 4271

[87] Peeters, Z., Botta, O.,Charnley, S. B., Ruiterkamp, R., & Ehrenfreund, P. 2003, ApJ, 593, L129

[88] Peeters, Z., Botta, O., Charnley, S. B., Kisiel, Z., Kuan, Y. -J., & Ehrenfreund, P. 2005, A&A, 433, 583

[89] Pilling, S., Seperuelo Duarte, E., da Silveira, E. F., Balanzat, E., Rothard, H., Domararcka, A., & Boduch, 2009, e-print Archive, Astrophysics, 1

[90] Ponnamperuma, C., Lemmon, R. M., Mariner, R., & Calvin, M. 1963, Proc. Natl. Acad. Sci. USA, 49, 737

[91] Poole, A. M., Jeffares, D. C., & Penny, D. 1998, J. Mol. Evol., 46, 1

[92] Prasad, S., & Tarafdar, S. P. 1983, ApJ, 267, 603

[93] Ricci, A., Bauschlicher, C. W., & Bakes, E. L. O. 2001, Icarus, 154, 516

[94] Rice, J. M., & Dudek, G. O. 1997, JACS, 89, 2719

[95] Rimola, A., & Uglieno, P. 2009, PCCP, 11, 2497

[96] Rode, B. M. 1999, Peptides, 20, 773

[97] Roy, D., Najafian, K., & Schleyer, P. v-R. 2007, PNAS., 104, 17272

[98] Saladino, R., Crestini, C., Costanzo, G., Negri, R., & Di Mauro, E. 2001, Bioorganic & Medicinal Chemistry, 9, 1249

[99] Satoshi, K.,Takayanagi, M., & Nakata, M. 1997, J. Mol. Structure, 413-414, 365

[100] Sekanina, Z., & Yeomans, D. K. 1985, Astron. J. 85, 2335

[101] Shapiro, R. 1995, Orig. Life Evol. Biosph., 25, 83

[102] Simakov, M. B., & Kuzicheva, E. A. 2005, Adv. Space Res., 36, 190

[103] Smith, I. W. M., Talbi, D., & Herbst, E. 2001, Astron. Astrophys., 369, 611

[104] Socrates, G. 2001, Infrared and Raman Characteristic Group Frequencies (3rd ed.; John Wiley & Sons, Inc.)

[105] Steinfeld, J. I., Francisco, J. S., & Hase, W. L. 1989, Chemical Kinetics and Dynamics (Prentice Hall)

[106] Taatjes, C. A., Osborn, D. L., Selby, T. M., Meloni, G., Trevitt, A. J., Epifanovsky, E., Krylov, A. I., Sirjean, B., Dames, E., & Wang, H. 2010, J. Phys. Chem. A, 114, 3355

[107] Tait, J. F. K., Edwards, H. G. M., Farwell, D. W., & Yarwood, J. 1995, Spectrochimica Acta Pt. A., 51, 2101.

[108] Tielens, A. G. G. M. 2008, ARA&A, 46, 289

[109] Ullrich, S., Schultz, T., Zgierski, M. Z., & Stolow, A. 2004, PCCP, 6, 2796

[110] Zhang, F., Kim, S., Kaiser, R. I., Jamal, A., & Mebel, A. 2009, J. Chem. Phys., 130, 234308

[111] Zheng, W., Jewitt, D., & Kaiser, R. I. 2006, ApJ, 639, 534

[112] Ziegler, J. F., Biersack, J. P., & Littmark, V. 1985, The Stopping and Range of Ions in Solids (New York: Permagon)

CHAPTER 8

CONCLUSIONS

The electronic excited state dynamics of ammonia and adenine have been investigated by ultrafast time-resolved photoelectron and photoion spectroscopy. Mapping the internal energy redistribution mechanisms which link the excited and ground electronic states is crucial to understanding the UV photostability of these molecules. Further, knowledge of adenine's photoprotection mechanisms can give insight into why it (and other heterocyclic biomolecules) was incorpatated into living organisms during the pre-ozone layer period of biogenesis on the early Earth.

One, more specific, goal of this investigation is to clarify the energetic onset of the $S_3(\pi\sigma^*)$ relaxation channel in adenine. This σ^*-mediated relaxation path is important because it is extremely efficient and operates in a host of biomolecules. Similarly, ammonia's first excited state, NH_3 ($\tilde{A}$), is an $n\pi^*$ state which is used here as a model of the $S_3(\pi\sigma^*)$ state in adenine. Electronic relaxation following resonant excitation of $\nu_2' = 0$ - 5 vibrational levels of NH_3 ($\tilde{A}$) is measured by TRIY, TRPES, and TR-TKER in Chapters 4 - 5. TR-TKER measurements reveal that N-H bond dissociation occurs from all ν_2' levels within 250 fs of initial excitation and predominantly yields low-KE H-atoms. H-atom KE spectra show that dissociation timescales increase as energy imparted to the NH_2 co-fragment increases. This behavior is explained on the basis that non-planar passage through the NH_3 ($\tilde{A}$)/NH_3 ($\tilde{X}$) conical intersection yields high energy NH_2 co-fragments and the non-planar trajectories evolve slowly in comparison to planar dissociation paths. The NH_3 ($\tilde{A}$) potential energy surface has a small energetic barrier which affords an excellent opportunity to observe dissociation by quantum tunneling. TRIY, TRPES, and TR-TKER measurements show that the NH_3 ($\tilde{A}$) lifetime and H-atom dissociation time decreases as quanta in the initially excited vibrational level is increased above $\nu_2' = 2$. However, an interesting lifetime trend is observed for excitation of lower vibrational levels, in which the $\nu_2' = 1$ level has a longer lifetime than the $\nu_2' =$ 0 or 2 levels. Also, TR-TKER measurements of the $\nu_2' = 0$ and 2 levels reveal a low NH_2 internal energy feature that is absent from the $\nu_2' = 1$ measurement. The lifetime trend and NH_2 internal energy observations are indicative of dissociation by quantum tunneling through the NH_3 ($\tilde{A}$) state potential energy barrier. The magnitude of the barrier is known to increase as the out-of-plane bend angle increases. Tunneling by non-planar geometries is therefore more difficult, and slower, than tunneling by planar geometries. The $\nu_2' = 0$ and 2 wavefunctions have substantial planar character and encounter the barrier minimum, while the $\nu_2' = 1$ wavefunction has a node at planar geometry and encounters an elevated *effective* dissociation barrier at non-planar geometries. The low NH_2 internal energy feature in the ν_2' $= 0$ and 2 measurements is due to these planar geometries following a direct path through the conical intersection beofore reaching the dissociation limit.

An excitation wavelength dependent study of adenine is presented in Chapter 6. Experiment and theory generally agree that bi-modal relaxation of adenine occurs on timescales of 0.1 and 1 ps. However, identification of specific excited states involved in the relaxation has been under dispute. Here, TRPES measurements indicate a $S_2(\pi\pi^*) \rightarrow S_1(n\pi^*) \rightarrow S_\circ$ relaxation pathway after excitation below 5.2 eV. The $S_2(\pi\pi^*) \rightarrow S_1(n\pi^*)$ transfer occurs within 100 fs of initial excitation. The relaxation time of $S_1(n\pi^*)$ decreases from 1032 to 700 fs as the excitation energy increases from 4.7 to 6.2 eV. An additional relaxation path is observed after excitation above 5.2 eV. Analysis of spectral amplitude ratios and relaxation timescales indicate this additional path which is consistent with the thoretically predicted $S_3(\pi\sigma^*)$ relaxation channel. Measurement of the H-atom KE distribution following 200 nm excitation reveals a feature that arises within 100 fs of initial excitation near 1.25 eV - in agreement with the theoretically predicted $S_3(\pi\sigma^*)$ dissociation energy. Combining this energetic and dynamic information lends additional strength to the argument that the additional channel, open above 5.2 eV excitation energy, observed by TRPES is in fact due to participation of the $S_3(\pi\sigma^*)$ state.

An investigation of the interstellar survivability of adenine has been conducted in collaboration with the NASA astrobiology institute at the University of Hawaii. Measurement of 5 keV electron interaction with thin films of adenine at 10 K allows calculation of the adenine destruction rate due to the charged particle component of the Galactic Cosmic Radiation. The total destruction rate is calculated in several astrophysical environments by including the measured charged particle destruction rate and the previously reported UV destruction rate. Within the solar system and in diffuse molecular clouds, the UV radiation field dominates and adenine is expected to survive on the timescale of several years. However, in UV shielded environments, such as dense molecular clouds and on the surface of interstellar icy grains, inclusion of charged particle destruction reduces the lifetime of adenine by up to 30% from the UV destruction lifetime. Still, the total lifetime of adenine in UV shielded environments is near 10 Gyr. Further, the lifetime of adenine is increased by several orders of magnitude when shielded by a thin layer of molecular oxygen - a typical environment on icy grains. The lifetime of adenine is similar to the lifetime of star forming molecular clouds. It is then likely that adenine could survive within small icy grains during star formation and may have been subsequently deposited onto planetary bodies.

In summary, the well-studied molecule ammonia has been used as a model to test three time-resolved spectroscopy techniques (TRIY, TRPES, and TR-TKER). The experimental signature of σ^*-mediated H-atom dissociation and evidence of quantum tunneling were obtained. Investigation of adenine determined that several electronic excited state relaxation mechanisms operate simultaneously, including the important $\pi\sigma^*$ pathway. The relaxation mechanisms are able to redistribute electronic energy on sub-ps timescales and effectively protect adenine from UV photodestruction. The photoprotection afforded by these relaxation mechanisms may have allowed adenine to be incorporated into living organisms during the time of biogenesis. The adenine available on Earth during biogenesis likely derived from many sources. Investigation of adenine destruction rates in several astrophysical environments has determined that the delivery of extraterrestrial adenine in small icy grains contributed to the terrestrial abundance.

CHAPTER 9

APPENDIX I - VACUUM INTERLOCK SYSTEM

The interlock system has two main components which are described in this section. Vacuum pressures are continuously monitored by taking readings from the Varian Multiauge controller through a LabView vi. The LabView vi is interfaced to a set of computer controlled solid-state relays (SSR) which control the power to various vacuum system components (ie. pumps, valves, electronics). If a pressure is recorded above the upper limit values given in Table 9.1, then the SSR are switched off in an appropriate order to safely shut-down the vacuum system. The pressure monitoring system and LabView vi will be described first, and the SSR circuitry will be described second.

9.1 PRESSURE MONITOR PROGRAM

All TC and IG are connected to a Varian multi-gauge controller, and readings are taken using the Pressure4.vi LabView program. A picture of the LabView front panel and block diagram are presented as Figs 9.1 and 9.2, respectively. Annotations within the program serve to describe each routine in more detail. The pressure measurement sequence is written inside a WHILE LOOP which runs until the program is stopped manually or a pressure is recorded above the threshold value and the interlock system is engaged. During each measurement sequence, readings are taken from the Multigauge and displayed on the front panel. Also, on the front panel are CONTROLS for the pressure threshold values and the time to wait between measurement loops. There are four different pressure monitoring schemes which can be selected from the LabView dropdown menu (interlock is selected in

Table 9.1: Typical vacuum pressures. Given in units of Torr. Base pressure is obtained with all pumps on and no molecular beam. Normal operation is with molecular beam on. Upper limit is threshold for interlock activation. Standby made is rough vacuum only.

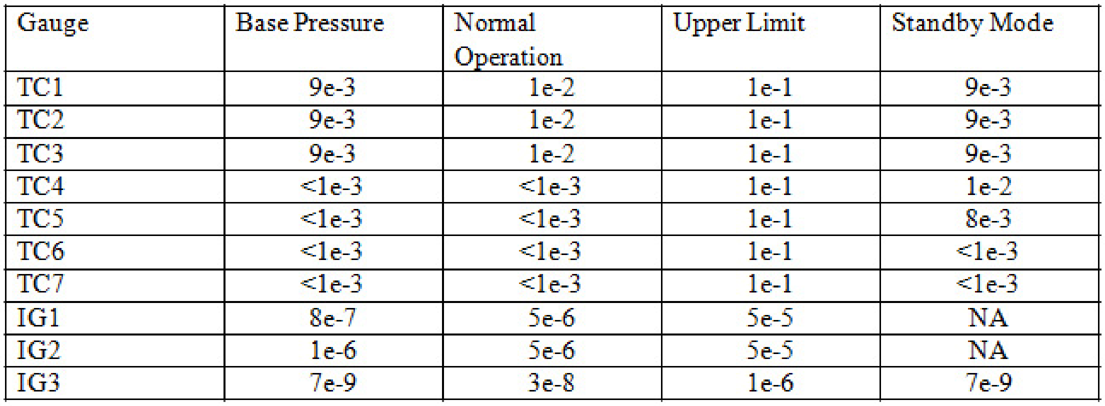

Gauge	Base Pressure	Normal Operation	Upper Limit	Standby Mode
TC1	9e-3	1e-2	1e-1	9e-3
TC2	9e-3	1e-2	1e-1	9e-3
TC3	9e-3	1e-2	1e-1	9e-3
TC4	<1e-3	<1e-3	1e-1	1e-2
TC5	<1e-3	<1e-3	1e-1	8e-3
TC6	<1e-3	<1e-3	1e-1	<1e-3
TC7	<1e-3	<1e-3	1e-1	<1e-3
IG1	8e-7	5e-6	5e-5	NA
IG2	1e-6	5e-6	5e-5	NA
IG3	7e-9	3e-8	1e-6	7e-9

Fig 9.1. Each scheme involves different gauges being active as is appropriate for different operation conditions and is controlled by a separate panel in the case structure shown at left of Fig 9.1. A description of each scheme is given below.

Scheme 1 —OVERNIGHT —TC 1-5 and IG 3 are active —used when diffusion pumps are off and gate valves are closed.

Scheme 2 —EXPERIMENT —TC 1-3 and IG 1-3 are active —used when diffusion pumps are on and gate valves are open.

Scheme 3 —ALL ON —all gauges are active, interlock is not active —used during venting or pump-down periods.

Scheme 4 —INTERLOCK —all gauges and interlock are active —used during data collection.

Each scheme has a common routine for getting the pressure readings from the Multigauge, although the specific gauges which are monitored are different in each scheme. Pressures are obtained through the get pressures.vi sub-vi which is executed, inside each scheme, once

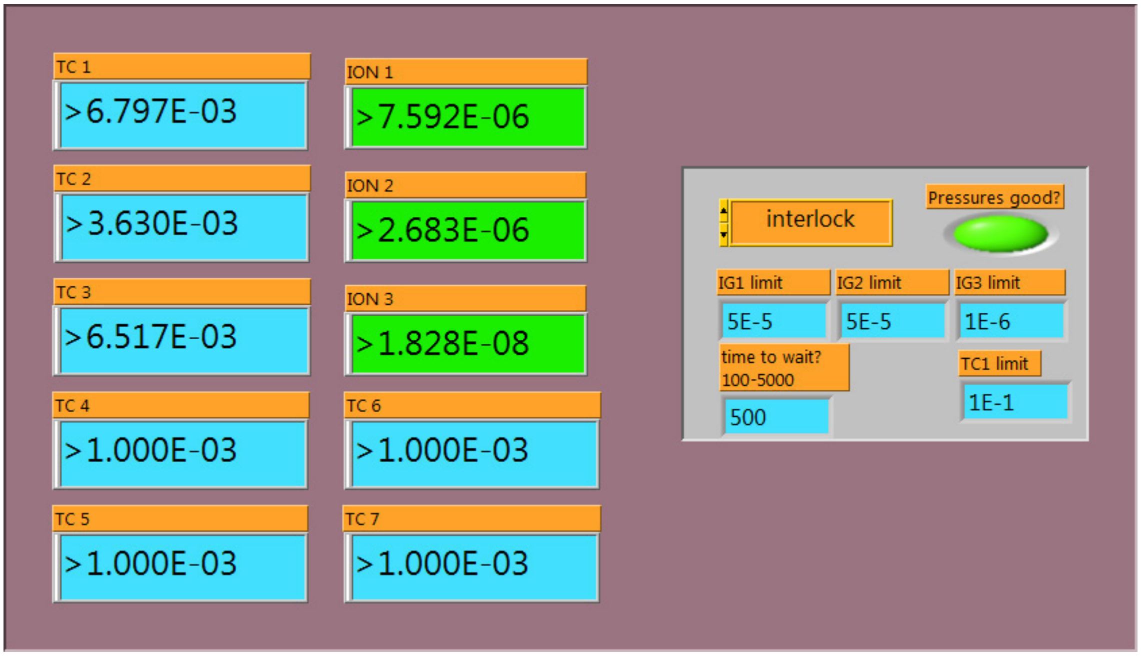

TC 1: >6.797E-03
TC 2: >3.630E-03
TC 3: >6.517E-03
TC 4: >1.000E-03
TC 5: >1.000E-03
ION 1: >7.592E-06
ION 2: >2.683E-06
ION 3: >1.828E-08
TC 6: >1.000E-03
TC 7: >1.000E-03
interlock
Pressures good?
IG1 limit: 5E-5
IG2 limit: 5E-5
IG3 limit: 1E-6
time to wait? 100-5000: 500
TC1 limit: 1E-1

Figure 9.1: Front panel of LabView pressure monitoring program. Thermocouple (TC) and ion gauge (IG) readouts are obtained from Multigauge controller. Several measurement schemes can be selected from the dropdown menu. The interlock scheme is currently selected.

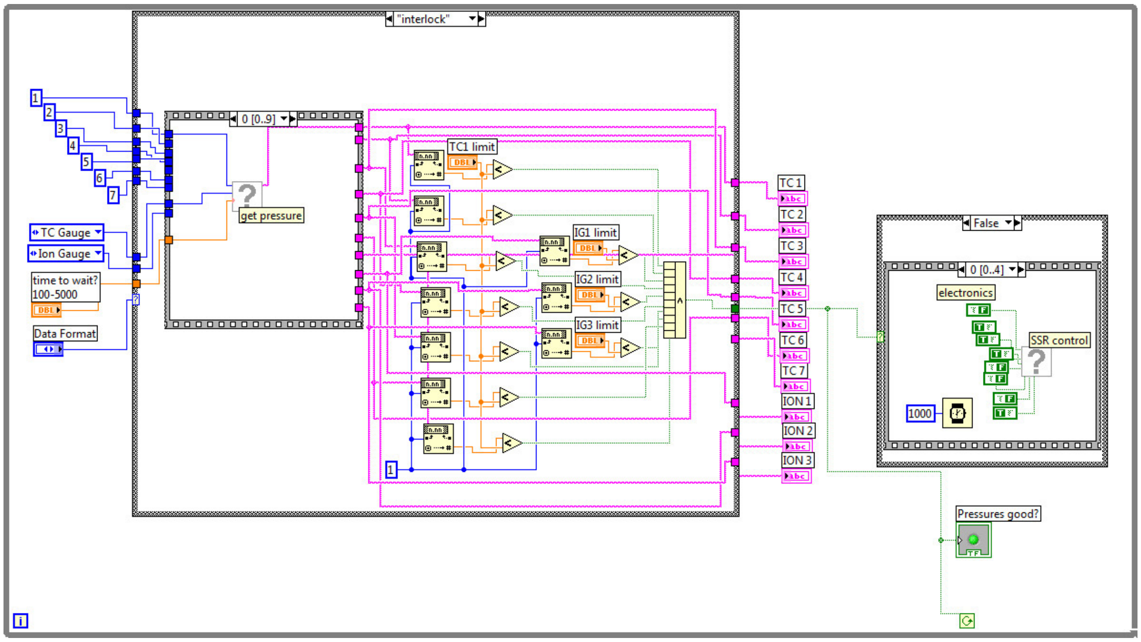

Figure 9.2: Block diagram of LabView pressure monitoring program. The Multigauge interface sub-vi 'get pressures' is located in the left sequence. Comparison of measured pressures with threshold values occurs in the center. Activation of the SSR is controlled by boolean operators connected to the sub-vi 'SSR control'.

for each active gauge. This sub-vi initializes and queries the Multigauge through a serial communication port and requires only the GAUGE TYPE and CHANNEL NUMBER as inputs. The case structure for each scheme has these inputs set to read the appropriate gauges for each monitoring scheme. Pressure readings are displayed on the front panel once each time all active gauges are queried. Scheme 4 is the only scheme in which the interlock feature is active. The interlock routine compares the pressure reading returned from the Multigauge to the threshold value and activates the SSR if necessary. The boolean pressure comparison is done inside the interlock loop, and the SSR control sub-vi is contained in the true/false panel at right of Fig 9.1. If all pressures are below the upper limit (or scheme 1, 2, or 3 is selected) then 'true' is returned and all SSR remain active. If any pressure is recorded above the upper limit then 'false' is returned from the boolean function and the SSR control starts deactivating relays. The SSR control sub-vi contains all the SSR-LabView serial communication commands and requires only on/off switches for each SSR as input. If 'false' is returned by the pressure comparison routine then the SSR are turned off in a sequence that protects the vacuum system and spectrometer.

9.2 INTERLOCK AND SSR CONTROL

The computer-controlled SSR board switches off the power to vacuum system and electronic components in the following sequence:

1. Electronics rack multi-outlet
2. Source-gas valve
3. Diffusion pump gate valve and roughing valve
4. Heater and transducer multi-outlet
5. Diffusion pumps

Table 9.2: Assignment of SSR relays. MO - multi-outlet.

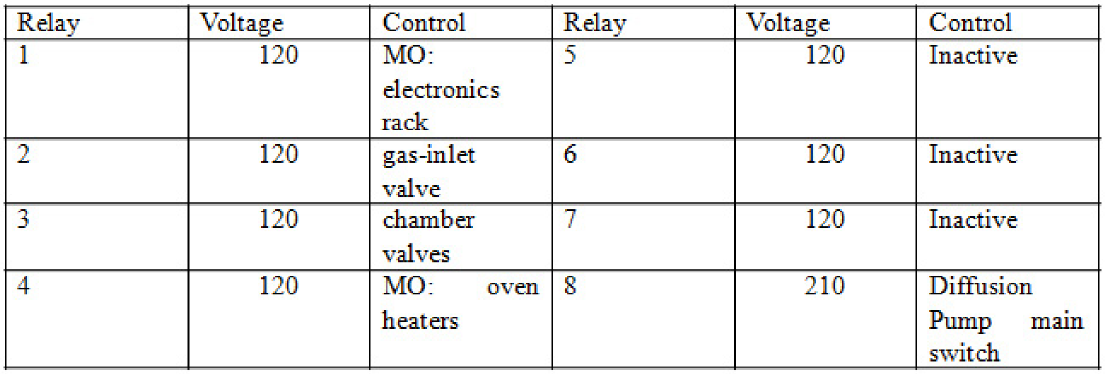

Relay	Voltage	Control	Relay	Voltage	Control
1	120	MO: electronics rack	5	120	Inactive
2	120	gas-inlet valve	6	120	Inactive
3	120	chamber valves	7	120	Inactive
4	120	MO: oven heaters	8	210	Diffusion Pump main switch

The SSR card was purchased from www.controlanything.com and is comprised of 8 relays which are rated for 30 A at 220 V. The relays are powered and controlled by an additional board which supports the 12 V power supply and serial port communication connections. Fig 9.3 shows the 10” x 10” x 4” interlock box in which the relay and control cards are mounted with 2 power bars and 4 external duplex outlets. Relays 1-7 are wired to supply 120 V to outlets 1-7. Currently, relays 5-7 are unused, relays 1 and 4 are connected to separate multi-outlets (MO) (power strips) which can support various devices, relay 2 is hard wired to control the source gas inlet valve, relay 3 controls the main chamber power which operates the gate valves and roughing valves, and relay 8 is hard wired to the main 220 V switch which controls the diffusion pump power. Table 9.2 gives a list of which device is controlled by which relay.

DO NOT PLUG THE POWER BAR SUPPLY AND THE

RELAY POWER INTO THE SAME OUTLET!

A POWER FEEDBACK LOOP CAUSES THE CIRCUIT TO SHORT!

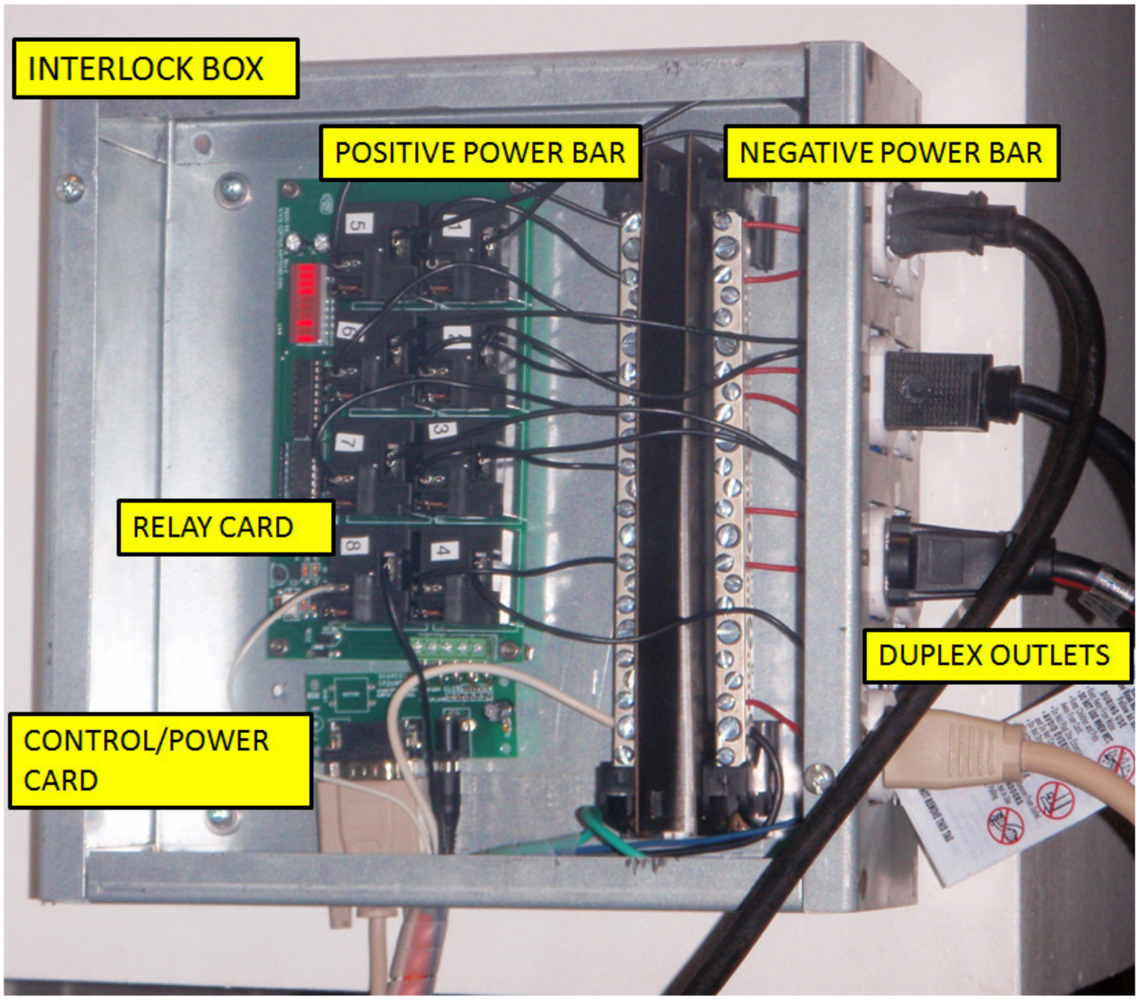

Figure 9.3: Picture of interlock box. Description of labeled elements is given in the text.

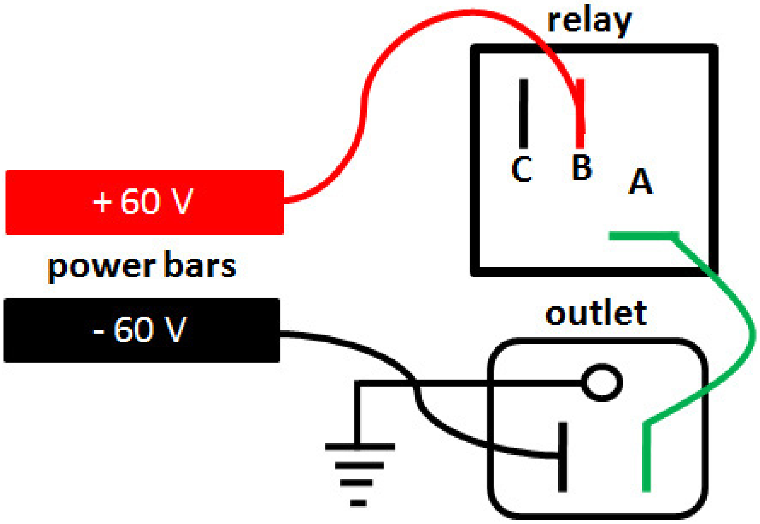

Figure 9.4: 120 V SSR wiring diagram.

Relays 1-7 are all wired identically to supply 120 V to outlets 1-7. A wiring diagram for one 120 V SSR is shown in Fig 9.4. Each relay has three connections labeled A, B, and C. A and B are connected when the relay is active, and A and C are connected when the relay is inactive. The power bars are wired to the high (thick white wire in Fig 9.3) and low (thick black wire in Fig 9.3) voltage coming from a 120 V wall socket, with the ground (thick green wire in Fig 9.3) wired to the outlet ground. Relay 1-7 all get their 120 V power from the power bars, but each is wired to a separate outlet. When the relay is active the outlet sees + 60 V from connector A and —60 V from the low voltage power bar, thus 120 V. When the relay is inactive the outlet sees 0 V from connector B and is therefore inactive.

A diagram of the 220 V diffusion pump circuitry is given in Fig 9.5. The interlock system modifies the original chamber circuitry only by inclusion of SSR 8 into the main 220 V switch circuit. In Fig 9.5, the 220 V high and low current supplies are contained in the large black box mounted at the bottom of the vacuum chamber front panel. The black boxes in Figure 6 are power relays which, when active, connect the high current supply to the diffusion pump heaters. The current box and power relays supply high current to the diffusion pumps

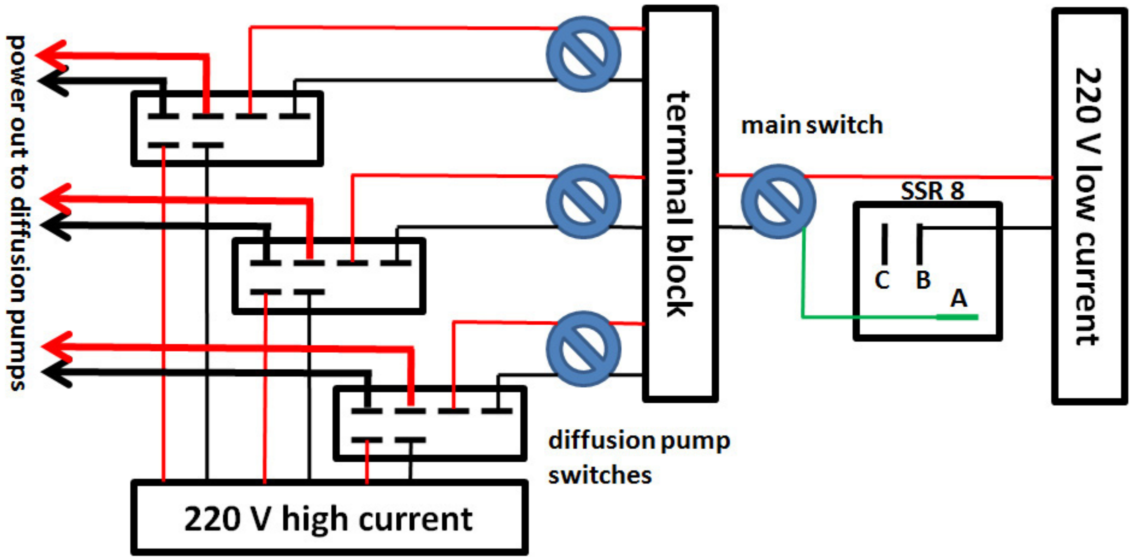

Figure 9.5: 220 V SSR wiring diagram.

without having it run through the switches. The power relays, and thus the diffusion pumps, are activated in the following manner:

1. SSR 8 is activated and the low current 220 V supply is connected to the main chamber switch.

2. The main chamber switch is turned on and the terminal bar and all three diffusion pump switches are charged.

3. Each diffusion pump switch is turned on and the corresponding power relay is activated.

4. High current flows to the diffusion pump heaters.

Disabling SSR 8 or the main chamber switch will cause the terminal bar to be uncharged. Disabling any diffusion pump switch will deactivate the corresponding power. Either of the above actions will disable the diffusion pump. Check the voltage on both sides of each switch to determine where the circuit is broken.

9.3 RESTARTING VACUUM SYSTEM

The interlock system may deactivate because of either an over threshold pressure measurement and the interlock was tripped, or the SSR card is malfunctioning. If deactivated because of a pressure warning, the system simply needs to be shut-down and the pressure monitoring program needs to be restarted. If the SSR card is malfunctioning the interlock box must be disengaged and the system can be operated on alternate power. Both situations are described here.

When the Pressure4.vi program is restarted all the relays immediately become active again. If devices connected to the SSR are left on when the SSR are reactivated, then sudden current surges could damage the devices. Also, if chamber valves are opened or closed improperly when the SSR are reactivated then pressure bursts can damage the vacuum system. In the event that the interlock is activated and the relays are tripped, there are several steps which must be followed before the vacuum system can be restarted safely. Perform the following steps to reactivate all SSR using the Pressure4.vi.

1. Close manual gate valve to isolate spectrometer.
2. Close diffusion pump gate valves.
3. Switch diffusion pump power off.
4. Close chamber roughing valves.
5. Close source-gas cutoff valve and evacuate gas manifold.
6. Turn off HV power supplies at front panel.
7. Start Pressure4.voi in ALL ON mode.
8. Verify TC pressures before opening any chamber valves.

Restarting Pressure4.vi in ALL ON mode allows you to verify that all TC pressures are in the 1^{-2} Torr range before opening the roughing valves. It is then safe to resume normal operations.

The interlock system can be disengaged in two ways. The first, very simple, method is to choose scheme 1, scheme 2, or scheme 3 from the Pressure4.vi front panel dropdown menu. This will stop the pressure comparison routine and all SSR (except SSR 5-7 which are unused) will remain active. This method should be used during experimental set-up, during chamber venting/ pump down, and during standby periods only.

STOP!!! VERIFY THAT ALL VALVES ARE CLOSED AND THAT ALL POWER TO THE CHAMBER IS TURNED OFF BEFORE DISCONNECTING ANY WIRING AT THE INTERLOCK BOX - INCLUDING THE 120 V AND 220 V MAIN POWER FROM THE WALL.

The second method to disengage the interlock system should be used if the SSR card is malfunctioning and involves powering each component from an alternative source which bypasses the SSR card. The 120 V circuits which plug into the duplex outlets can easily be plugged into another lab circuit. Switch all chamber valves to the closed position and turn all HV power supplies off at the front panel before connecting any plug to alternative power. The 220 V diffusion pump circuit must be rewired to bypass SSR 8, but this operation is quite easy. Fig 9.3 shows a black and white wire connected to SSR 8. The white wire is colored green in Fig 9.5. The black wire is connected to the 220 V low current supply, and the white wire is connected to the 220 V main chamber switch. To bypass SSR 8, disconnect the black wire at SSR 8 and the white wire at the chamber switch. Then connect the black wire to the switch where the white wire was just disconnected. The vacuum chamber should be operational once the main power is turned back on.